Single-Shot Holographic Readout of an Atom Interferometer

Andrew Rae MacKellar

Experimental Quantum Optics and Photonics Group
Department of Physics and SUPA

University of Strathclyde

A thesis presented in the fulfilment of the requirements for the degree of

Doctor of Philosophy

2017

This thesis is the result of the author's original research. It has been composed by the author and has not been previously submitted for examination which has led to the award of a degree.

Signed:

Date:

Abstract

Atom interferometry is a precision measurement technique that encodes information in the phase of atomic wavefunctions, using matter-wave interference to project the encoded phase information onto some relatively easy-to-measure property at the interferometer output, like the fractional atomic population in a specific momentum or internal state. Atoms are perturbed by influences to which photons are insensitive, offering atom interferometers excellent sensitivity and access to physics outwith the range of conventional optical interferometers. As such, for probing of fundamental physics such as QED corrections, atoms are an obvious test bed.

The primary focus of this thesis is the construction and development of an atom interferometer capable of performing single-shot measurements of the fine-structure constant using a holographic readout technique. This achievement allows the holographic interferometer an increased data acquisition rate on the order of 700-times that a conventional configuration.

As an interfering medium we use a Bose-Einstein condensate containing around $\sim 10^5$ ^{87}Rb atoms. We coherently manipulate the momentum of these atoms with the scattering of photons from an optical lattice with fully controllable intensity. We have developed a numerical toolbox capable of calculating optical-lattice pulse-sequences to generate arbitrary atom-optical operations such as mirrors, and beam-splitters, experimentally demonstrated with an efficiency of $99.97 \pm 0.03\,\%$. We have used these atom-optics to create experimental atom interferometers with various applications, shown here in the cases of a magnetic gradiometer and in measurements of recoil frequency. This latter configuration has been used to perform a measurement of the fine-structure constant with a fractional uncertainty of 6500 ppm in a single shot, with a clear pathway to reduce this uncertainty to 2300 ppm per shot, whilst the increased speed of the holographic interferometer allows a corresponding reduction in uncertainty to 60 ppm within a twelve hour integration period.

Acknowledgements

Well, that PhD turned out to be quite the rollercoaster. When I started I didn't quite understand what I was letting myself in for. Now, at the end, I realise that whilst it's great having good advisors around when everything works and data is flowing, it's only in the difficult times when stuff goes wrong that you really discover just *how* good your advisors are. I can now honestly say that I have two of the best.

Griff and Erling, you've gone above and beyond to take care of me for the last few years. You have shown me such patience and trust, and stuck your neck out for me more times than I dare to count. In all this time you have never failed to impress on me your belief that I have what it takes to succeed. I'm not so foolish as to miss the opportunities that you've given me access to. I'll do my best to make the most of them.

Billy, you weird and wonderful man: we first met four years ago, nearly to the day, and became friends nigh-on instantaneously. Since then we have spent more time together than the average married couple, and somehow managed to disarm any potential arguments with jokes and pranks and a ridiculous 80's music cover band. From day one you've shown me the ropes, taught me how to run our ridiculous experiment, and filled the lab with mostly good and occasionally terrible music.

Jim, your skill as a physicist made training you in the experiment incredibly easy. I'm astonished at how quickly you adapted to the lab, and more selfishly I'm really glad that you took on all of the workload so I could get this thesis written.

Aidan, Jon, Stuart, and Bruno; you've offered advice and knowledge and given me feedback far more useful than my terrible prose deserved. The group is significantly enhanced by your inclusion in it.

My office-mates, past and present: Chris, Calum, Jan, Vicki, Rachel, Arvind, Jim, Billy. Good office-mates are hard to find, unless you look in my office, because it's been filled with them for years. Best. Office. Ever. Accept no substitutes.

Johnny, you played the same bass-line for three minutes while I did a guitar-solo all over it, and also significantly increased the funk quota in my life. For these things you will eternally have my gratitude.

When I first joined the Experimental Quantum Optics and Photonics group it had far fewer people in it. Now there are a zillion of you, and you're all doing amazing things that I barely understand. This is a great place, and I'm proud I was a part of it.

My friends and family, those who are still here and those who aren't. I'll try to make you proud.

Contents

Abstract **ii**
Acknowledgements **iii**
Contents **iv**
List of Figures **viii**
1 Introduction & Background **1**
  1.1 Atom interferometry 1
    1.1.1 Optical interferometry 1
    1.1.2 Matter-waves 1
    1.1.3 Atom-optics 2
    1.1.4 Matter-wave interferometry 2
  1.2 The fine-structure constant 3
    1.2.1 History 3
    1.2.2 In tests of the stability of fundamental constants 3
    1.2.3 Redefinition of the SI system of units 4
    1.2.4 Measurement of the fine-structure constant 4
  1.3 Thesis Outline 7
2 Experimental setup **8**
  2.1 Overview 8
  2.2 Beam preparation 10
    2.2.1 Useful atomic transitions 10
    2.2.2 Laser preparation optics 11
    2.2.3 Laser frequency locking 13
  2.3 Atomic manipulation 15
    2.3.1 Overview 15
    2.3.2 2D MOT 16
    2.3.3 3D MOT 17
    2.3.4 Optical pumping 18
    2.3.5 Magnetic transport 19
    2.3.6 Forced RF evaporation 20
    2.3.7 Hybrid optical trap 21
    2.3.8 Interferometry beams 22

- 2.4 Signal detection . . . 28
  - 2.4.1 Overview . . . 28
  - 2.4.2 3D MOT Fluorescence . . . 29
  - 2.4.3 Absorption imaging . . . 30
  - 2.4.4 Contrast interferometry . . . 30
- **3 Atom-Optics** **32**
- 3.1 Introduction . . . 32
- 3.2 Experimental setup . . . 33
- 3.3 Theory and system modelling . . . 34
- 3.4 Model testing . . . 35
  - 3.4.1 Optical lattice calibration . . . 35
- 3.5 Optimising a high-fidelity atom-optic . . . 37
  - 3.5.1 Designing a first-order beam splitter pulse sequence . . . 37
  - 3.5.2 Testing first-order splitting efficiency . . . 39
- 3.6 Reflection pulse efficiency . . . 42
- 3.7 Second order atom-optics . . . 45
  - 3.7.1 Second order atom beam-splitting . . . 45
  - 3.7.2 Second order atom mirrors . . . 47
- 3.8 Targeted operations . . . 49
  - 3.8.1 Four-port quatter . . . 49
- **4 Atom Interferometry** **50**
- 4.1 Introduction . . . 50
- 4.2 Optical interferometry . . . 51
  - 4.2.1 Optical phase . . . 51
  - 4.2.2 Sagnac interferometry . . . 53
- 4.3 Atom interferometers . . . 56
  - 4.3.1 Enhanced sensitivity . . . 56
  - 4.3.2 Phase shifts . . . 57
- 4.4 Interferometer geometry . . . 59
  - 4.4.1 Two-arm interferometry . . . 60
  - 4.4.2 Three-arm interferometry . . . 61
- 4.5 Homodyne interferometry . . . 62
  - 4.5.1 Background . . . 62
  - 4.5.2 Gradiometry . . . 63
  - 4.5.3 Experimental gradiometer . . . 65
- 4.6 Heterodyne interferometry . . . 72
  - 4.6.1 Theory & Background . . . 72
  - 4.6.2 Experimental realisation . . . 74
  - 4.6.3 Fine structure constant . . . 75

4.7 Interferometer beam angle . . . 77
  4.7.1 How do we measure the beam angle? . . . 77
  4.7.2 How do we fix it? . . . 80

5 Contrast Interferometry 81

5.1 Background and Theory . . . 81
  5.1.1 Motivation . . . 81
  5.1.2 Theory and concepts . . . 82
5.2 Experimental realisation . . . 87
  5.2.1 First detection and confirmation of a contrast signal . . . 87
  5.2.2 Contrast signal decay and probe intensity . . . 91
  5.2.3 Detection with a Single-Photon Counting Module . . . 92
5.3 Extracting information from single-shot data . . . 94
  5.3.1 Numerical Model Fitting . . . 94
  5.3.2 Data dominated by Poisson noise . . . 95
  5.3.3 Inferring error bars from single-shot photon-counts . . . 96
  5.3.4 Maximum Likelihood fitting for data dominated by Poisson noise 99
5.4 Contrast measurement of α . . . 105
  5.4.1 Interferometer configuration . . . 105
  5.4.2 Extracting α information from contrast interferometer data . . . 106

6 Advanced techniques 108

6.1 Introduction . . . 108
6.2 Mean field effects . . . 108
  6.2.1 Introduction and background . . . 108
  6.2.2 Observation of frequency chirp in GPE simulation . . . 116
  6.2.3 Observation of frequency chirp in Contrast data . . . 118
6.3 Higher-order scattering . . . 123
  6.3.1 Motivation . . . 123
  6.3.2 Viability of the second order Contrast signal . . . 123
  6.3.3 Holographic ‘beat’ measurements . . . 124
  6.3.4 Experimental realisation . . . 126
6.4 Combining multiple measurements . . . 130
  6.4.1 Motivation and background . . . 130
  6.4.2 Fisher information . . . 131

7 Conclusions and Future Work 135

7.1 Conclusions . . . 135
7.2 Future Work . . . 136
  7.2.1 Interferometer beam angle . . . 136
  7.2.2 Data analysis . . . 136
  7.2.3 Beam-splitters . . . 137

7.2.4 Higher-order scattering 137
7.2.5 Mean-field chirp 137
A Appendix 138
A.1 Useful physical constants 138
A.2 Analytical theory for off-resonant scattering 138
A.3 Atom Gradiometer Theory 142
Bibliography 147

List of Figures

List of Figures **viii**

1.1 CODATA 2014 alpha measurement comparison. 5
1.2 Comparison of the best two CODATA 2014 alpha measurements. . . . 6

2.1 Optics table schematic overview. 9
2.2 Experimental laser transitions. 10
2.3 Laser beam preparation layout overview. 12
2.4 Saturated spectroscopy around the cooling transition. 13
2.5 Saturated spectroscopy around the repump transition. 14
2.6 Overview of science chamber. 15
2.7 2D MOT 16
2.8 3D MOT 17
2.9 Optical pumping. 18
2.10 Transport to QP. 19
2.11 Forced Radio Frequency (RF) evaporation 20
2.12 Hybrid magnetic-crossed-dipole ‘tilt’ trap. 21
2.13 Atom-optics. 22
2.14 Optics table layout of interferometry beam preparation. 23
2.15 Saturated spectroscopy around the 85 repump transition. 24
2.16 Longitudinal alignment of the atom-optics beams. 25
2.17 Longitudinal alignment of the atom-optics beams. 26
2.18 Interferometry beam alignment. 26
2.19 Overview of signal detection apparatus. 28

3.1 Experimental configuration for atom-optical grating. 34
3.2 Calibration of lattice depth by fitting data with a numerical simulation. 37
3.3 Numerical simulation of splitter pulse efficiency. 39
3.4 Experimental efficiency of $|{+2\hbar k}\rangle{+}|{-2\hbar k}\rangle$ ‘splitter’ pulse sequence. 40
3.5 Data versus theory comparison for time evolution of an optimised splitter pulse. 41
3.6 Numerical simulation mapping of reflection pulse parameters. 42
3.7 Overview of interferometer sequence and fringes. 44

3.8 Numerically simulated efficiency map of a $|{+4\hbar k}\rangle{+}|{-4\hbar k}\rangle$ splitter pulse sequence. 46
3.9 Numerically simulated efficiency map of a $|{\pm 4\hbar k}\rangle$ splitter pulse sequence. 47
3.10 Data versus theory for the time evolution of a numerically optimised $|{+4\hbar k}\rangle{\leftrightarrow}|{-4\hbar k}\rangle$ mirror pulse sequence. 48
3.11 Experimental data of four-port quitter operation. 49

4.1 Optical Mach-Zehnder interferometer principle of operation. 53
4.2 Optical Sagnac interferometer schematic. 55
4.3 Resonant 'Bragg' Mach-Zehnder atom interferometer principle of operation. 59
4.4 Mach-Zehnder atom interferometer with off-resonant optics. 60
4.5 Off-resonant 'two-arm' interferometer fringe contrast. 61
4.6 Off-resonant 'three-arm' interferometer geometry. 62
4.7 Magnetic gradiometetry principle of operation. 64
4.8 Magnetic gradient coil calibration 66
4.9 Magnetic gradiometry coil calibration. 67
4.10 Schematic of AC Stark shifts in an interferometer 69
4.11 Measured output of two-arm magnetic gradiometer. 71
4.12 A single numerically integrated interferometer shot. 72
4.13 A numerically integrated interferometer fringe. 73
4.14 Experiment output of three-arm interferometer. 75
4.15 Principle of trilateration. 78
4.16 Trilateration of our interferometer beam angle. 79

5.1 Contrast interferometer geometries. 83
5.2 Generation of the Phase-Contrast signal. 85
5.3 A 2D GPE simulation of the atomic density wave. 86
5.4 First confirmation of contrast interferometer signal. 88
5.5 Asymmetrical mode population after the Contrast readout. 89
5.6 Contrast signal as viewed by APD voltage. 92
5.7 Contrast signal as measured by SPCM. 93
5.8 Extraction of Bayesian probability from a binomial distribution. . . . 96
5.9 Calculation of Bayesian probability from a Poisson distribution. . . . 98
5.10 Single-shot error bars. 99
5.11 Error calculation for Poisson fit algorithm. 102
5.12 Uncertainty scaling with variation in data binning. 104
5.13 Experimental contrast interferometer sequence. 105
5.14 Short CI alpha measurement. 106

6.1 Phase accumulation of a BEC during dipole trap release. 109
6.2 Expansion of BEC over time after dipole trap release. 111
6.3 Influence of phase chirps on our BEC hologram. 112
6.4 Expansion of BEC fringes after some dipole expansion time. 113
6.5 Expected contrast signal frequency and frequency chirp. 115
6.6 Frequency chirp analysis of 2D GPE simulation. 117
6.7 Frequency chirp theory plots versus experimental data. 118
6.8 Poisson fit algorithm with frequency chirp. 120
6.9 Linearity of frequency chirp in 2D GPE. 121
6.10 The Talbot carpet of a $p = (+4, +2, -2, -4)\hbar k$ contrast interferometer. 125
6.11 The experimental realisation of the ‘beat-note’ contrast interferometer. 126
6.12 Finite-Difference Time-Domain simulation of holographic Contrast signal mechanism 128
6.13 GPE simulation of the ‘beat-note’ contrast interferometer. 129
6.14 Fisher information of the Contrast signal model 133

Chapter 1

Introduction & Background

1.1 Atom interferometry

1.1.1 Optical interferometry

Interferometry is a measurement technique that uses the interference of waves, mapping information contained in the phase of those waves to some easy-to-measure output [1]. In the case of optical interferometers, the waves in question are phase-coherent light, where the interferometer measure a difference in the optical path length of light within the interferometer [2]. The optical interferometer is a detection method that has been at the forefront of precision measurement for many years; for example in the attempt to detect a medium (the ‘lumineferous ether’) through which light travels in the Michelson-Morley experiment [3], the absence of which contributed to the body of evidence that inspired the development of Special Relativity [4].

Despite the age of the technology, optical interferometers are still used in an applied sense to detect rotation rates in optical gyroscopes [5, 6], where the finite speed of light allows the gyroscope to change orientation while the light is within the interferometer optical path [7]. Optical interferometers are still also used in state-of-the-art fundamental physics: they form the basis of the LIGO observatories [8] that last year made the first detection of gravitational waves [9], a key prediction of General Relativity [10].

1.1.2 Matter-waves

Wave properties are not exclusive to light: in 1923 Louis de Broglie proposed that matter could also exhibit a wave-light nature [11], with a wavelength determined by a particle’s momentum in the relation

$$\lambda = h/p \,, \tag{1.1}$$

where h is the Planck constant, p is the momentum of the particle, and λ is the de Broglie wavelength: the distance over which the phase of the particle rotates by 2π. This wave-nature and phase allows for the interference of matter-waves, generating interference fringes analogous to optical fringes that can be directly imaged in some atom interferometers [12–14].

1.1.3 Atom-optics

Optical interferometers use optical elements such as mirrors and beam-splitters to coherently split incoming light into two (or more) spatially distinct optical paths, allowing one path to interact with some phase-altering event, before overlapping this measurement light beam with an unperturbed reference beam on a beam-splitter. In this way the interference of the phases of the measurement and reference beams map the phase information to the light intensity at the interferometers output ports. Interferometry with matter-waves, such as atoms, also requires elements that can coherently manipulate the momentum (or sometimes, internal state) of those particles [15].

1.1.4 Matter-wave interferometry

The earliest matter-wave-optics used the diffraction of particle beams from periodic nano-structures, with the diffraction of an electron beam from a nickel crystal [15, 16] in 1927, and the diffraction of He atoms from a LiF crystal lattice in 1930 [15, 17]. Diffraction from *fabricated* objects was demonstrated with an electron-beam interferometer in 1952 [18–20], and with neutron interferometers in 1974 [21, 22]. The diffraction of *atoms* from fabricated objects was demonstrated with a single $20\,\mu\mathrm{m}$-wide transmission slit in 1969 [23], and from material transmission-grating with $200\,\mathrm{nm}$-wide slits in 1988 [24], with the first atom-interferometers using matter-transmission-gratings being experimentally demonstrated in 1991 [14, 25], and modern fabrication techniques allowing for gratings constructed of a single atomic layer [26].

The first proposal of a grating made of light came as early as 1933 [27], where an incoming beam of electrons would be partially coherently scattered from a standing-wave of light by stimulated Compton-scattering. Whilst the first demonstration of this effect was not demonstrated with electrons until 2001 [28], the use of such ‘optical gratings’ for atom-interferometry emerged in 1995 [29, 30]. Since then atom interferometry has grown into a wide range of applications, with interferometers capable of detecting rotations [31–35], AC Stark shifts [36], prospecting [37], magnetic fields [38], gravitational accelerations [39–41], leading the way to applied sensors such as magnetometry, gravimetry, inertial navigation [42], and rotation and inertial force sensing [34, 43–45].

The technology remains at the forefront of fundamental physics, having been used to make direct measurements of gravitational field curvature [41], tests of atom and neutron neutrality [46], Newton's gravitational constant [47], the equivalence principle [48], and the fine-structure constant α [49–54].

1.2 The fine-structure constant

1.2.1 History

The fine-structure constant is a dimensionless fundamental physical constant, which is generally quoted as its inverse $\alpha^{-1} \approx 137$, where $\alpha = e^2/4\pi\epsilon_0\hbar c$. The fine-structure constant was originally introduced by Sommerfeld in 1916 in an attempt to explain the 'fine-structure' in the spectral lines of Hydrogen [55], from which the constant derives its name.

Whilst the Sommerfeld model was ultimately superseded by the Dirac model [56], the fine-structure constant remained prominent with the 1947 discovery of splitting of the $2S_{1/2}$ and $2P_{1/2}$ spectral lines of Hydrogen [57, 58]. The Lamb shift was explained by way of vacuum fluctuations [59], in which the fine-structure constant appears. These vacuum fluctuations contribute to the anomalous gyromagnetic factor of leptons [60], where α appears as a correction term to the mechanical mass $(\sim (e^2/\hbar c)m_0)$ (where $\alpha = e^2/\hbar c$ in cgs units).

The ubiquitous appearance of α in the 1998 CODATA recommended values of the fundamental physical constants [61] emphasises the relevance of the constant whenever the electromagnetic interaction is present [62].

In modern physics the fine-structure constant retains its importance (1) as a cornerstone in the redefinition of the SI system of units [63], (2) as a key parameter in quantum electrodynamics [52, 64, 65], and (3) as a test of the stability of fundamental constants [66].

1.2.2 In tests of the stability of fundamental constants

Atomic and molecular structure is dominated by the values of the proton-to-electron mass ratio [67,68] and the fine-structure constant [68,69]. The two values of these two constants are such that atoms are stable, that heavy elements can form in late-stage heavy stars, and that carbon chemistry exists [70].

The gross structure of the universe is so strongly coupled to these constants that a shift in values by a small fraction of a percent would dramatically alter the evolution of the universe [70]. Whether some as-yet unknown physics constrains these values to exist within this window, or their values are some co-incidence is an open question in physics [68]. Aimed at this question, searches are underway to determine the stability of these constants; experiments aim to, for example, search for drifts in these fundamental constants in time [68].

1.2.3 Redefinition of the SI system of units

Within the current definition of the SI system of units many constants are determined by experiment and so are quoted with some associated uncertainty [71]. Planck's constant, for example, has been determined using Watt balances to measure the ratio h/M, defining a value of h with a prototype mass defined as the kilogram [72–74]. Likewise, the Ampere is defined by the permeability of vacuum, the Kelvin by the triple-point temperature of water, and the mole by the molar mass of carbon-12 [63].

The objective of the SI redefinition is to relate the system of units to universal fundamental constants in nature [63,75,76]. The kilogram will then be defined relative to Planck's constant, the ampere to the elementary charge, the Kelvin to the Boltzmann constant, and the mole to Avogadro's constant. The values these constants will be chosen as fixed values of effectively identical magnitude to their current values [63]. In this context the fine-structure constant will become a cornerstone of the SI; since many of the remaining constants are related by way of α [53], the reliability of its measurement will be crucial [75,76].

1.2.4 Measurement of the fine-structure constant

At the time of writing, the 'best value' of the fine-structure constant is quoted by The Committee on Data for Science and Technology (CODATA) [77] in the article *CODATA recommended values of the fundamental physical constants: 2014* [71]. Figure 1.1 shows the 2014 CODATA [71] comparison of the most precise determinations of the fine-structure constant from a variety of sources. These sources include those measuring the von-Klitzing constant (R_K [72, 78–83]), the proton gyromagnetic ratio ($\Gamma'_{\mathrm{p}-90}(\mathrm{lo})$ [84–86]), muonium transition frequencies ($\Delta\nu_\mathrm{Mu}$ [87, 88]), the ratio h/m_X by way of atom interferometry for the atomic species X = Cs and Rb [52, 89], and the anomalous magnetic moment of the electron a_e [64, 90].

The most precise determination of the fine structure constant is derived from the measurement of the anomalous magnetic moment of the electron a_e (Harvard-08 [64, 91]), where α appears as a power series in the value of the electron magnetic moment [65].

The second most precise method to date determines the ratio h/m [89] by recasting the fine-structure constant in the form

$$\alpha^2 = \frac{2R_\infty}{c}\frac{A_r(\mathrm{X})}{A_r(\mathrm{e})}\frac{h}{m_\mathrm{X}} \,. \tag{1.2}$$

Here the Rydberg constant (R_∞) is known with a precision of 5×10^{-12} [92, 93], the particle-to-electron-mass-ratio $A_r(\mathrm{X})/A_r(\mathrm{e})$ to 4.4×10^{-10} for ^{87}Rb [52, 94, 95], and c is defined as $299792458\,\mathrm{m\,s^{-1}}$ [71]. This makes h/m_x the least well known value in Equation 1.2.

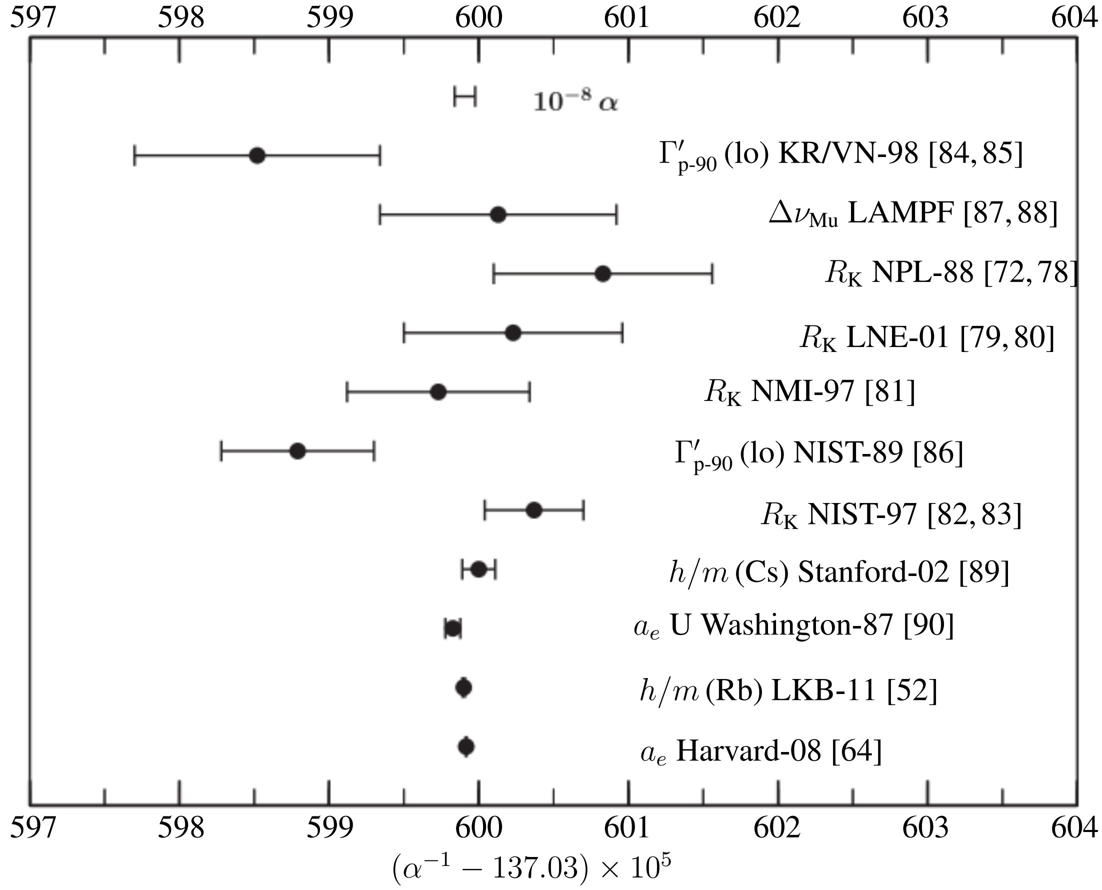

Figure 1.1: Figure adapted from [71]. Shown is the CODATA 2014 comparison of the most precisely determined values of the fine-structure constant from various experimental efforts.

The ratio h/m_{X} is determined by measuring the phase oscillation of an atom X recoiling from collision with a photon of wavevector $k = 2\pi/\lambda$, where the 'recoil frequency' is defined as $\omega_r = E_r/\hbar = \hbar k^2/2m_{\text{X}}$. This recoil frequency is measured by way of atom interferometry (h/m (Rb) LKB-11 [52]), returning a value of $\alpha = 0.00115965218113(84)$ (or 0.62 ppb) [52]. More recent improvements by the Müller group have reduced this error to 0.25 ppb [96].

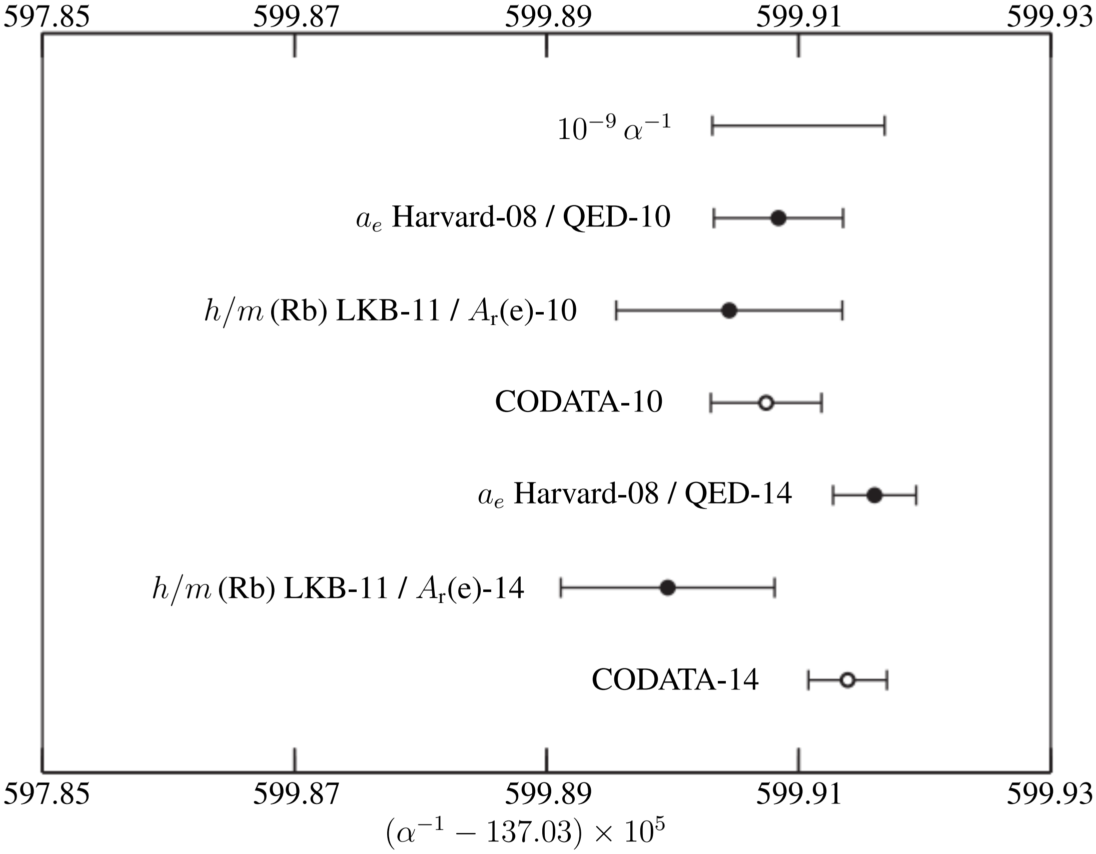

Figure 1.2: The CODATA 2014 determination of the fine-structure constant is dominated by the Harvard-08 and LKB-11 results. These two measurements rely on knowledge of the a_e QED expression and the value of $A_\mathrm{r}(\mathrm{e})$, respectively. Shown here are the determined values of α using the 2010 and 2014 recommended instances of a_e and $A_\mathrm{r}(\mathrm{e})$, in comparison with the recommended value of α in each year. Figure adapted from [71].

The current best value as quoted by CODATA (2014) has an associated uncertainty $\delta\alpha = 2.3 \times 10^{-10}$ [71], which is essentially determined from these two experiments a_e and h/m_X; the relatively poor precision of the other experimental values renders their weighting much lower [71]. It is important to note that these determinations of α are not entirely independent; they both rely on other measurements. Figure 1.2 shows a comparison of the values determined using these two experiments as quoted in CODATA 2010 [97] and CODATA 2014 [71], where the two experiments' inferred α values are shown using the 2010 and 2014 values for the a_e QED expression and value of $A_\mathrm{r}(\mathrm{e})$ [71].

1.3 Thesis Outline

This thesis reports on the progress of our Bose-Einstein condensate (BEC) atom interferometer: the generation of a BEC, the coherent optical control of the BEC atoms to generate atom-optical elements, the use of these tools to generate an atom interferometer, and the subsequent development and results of our single-shot holographic atom interferometer.

I give an overview of the experimental setup in Chapter 2. Since much of the experiment was constructed before my arrival and is described in detail in the PhD theses of Aline Dinkelaker [98] and Billy Robertson [99], I restrict this description to a more functional report on the procedure by which we cool ^{87}Rb atoms to Bose-Einstein condensation, how we coherently control these BEC atoms within our interferometer methods, and how we obtain signals from these interferometers.

Our atom-optics are described in Chapter 3. I begin by motivating the choice of our off-resonant atom-optics, before giving a brief background in the theory and literature of the physics involved. I then describe the numerical procedure by which we generate atom-optic pulse sequences, the use of these as a tool for optical-grating calibration, and the generation and testing of atom-optic operations.

In Chapter 4 I introduce interferometry in more detail, describing the importance of phase initially using optical interferometry as an example. This is then compared with a similar description of the operation of atom interferometers. I then describe the various configurations that our atom interferometer can operate in, using specific examples of magnetic gradiometry and a measurement of our interferometer recoil frequency. This recoil frequency measurement is used to find a determination of the fine-structure constant α.

Chapter 5 introduces the concept of single-shot ‘contrast-interferometry’. After describing the background theory, I recount the development of the contrast interferometer, with our initial struggle to obtain a contrast signal, then the development of the experiment until it was capable of performing single-shot measurements. I describe our first contrast signal, and how we confirmed that this really was the signal we were looking for. Following is a description of our data extraction method. This begins with a general description of data-fitting, and the problems that our low-photon-count-data present. I then describe the solution we found, followed by some example fits to our experimental data in a second determination of the fine-structure constant.

Chapter 6 contains a number of nuances that are important to consider with the contrast-interferometer. Here I describe the influence of mean-field interactions in the contrast interferometry signal which manifests as a frequency chirp. We then move on to higher-order ‘beat-note’ contrast interferometry. I then describe some advantages of our measurement technique, combining multiple contrast measurements, and the Fisher information contained within a single shot.

Chapter 2

Experimental setup

2.1 Overview

To perform atom interferometry with an ^{87}Rb Bose-Einstein condensate (BEC), we require a source of atoms in addition to the ability to trap and cool those atoms in a controlled way to sub-micro-Kelvin temperatures. Laser trapping and cooling of neutral atoms is now an established and robust technology with more than twenty years having passed since the first BECs were created [100–103]. Moreover, much of the apparatus used in our experiment to create a Bose-Einstein Condensate was already constructed before my arrival. I will therefore forego description of many of the details of our experimental apparatus, and direct enquiring minds to the PhD theses of Dr. Aline Dinkelaker [98] (construction of the atom cooling and trapping apparatus) and of Dr. Billy Robertson [99] (current generation experiment and generation of a BEC). I will instead provide a brief overview of the experimental procedure focussing only on details which are later pertinent to our measurement techniques.

Figure 2.1 shows an overview of the experiment optics table, which is effectively split into three sections: (1) laser beam preparation, (2) atom manipulation, and (3) contrast signal detection. We generate laser light with the use of Extended-Cavity Diode Lasers (ECDL) [99], locking the laser frequency to features in a saturated spectroscopy signal. Various pickoffs are taken from these beams to match our requirements for laser cooling, repumping, imaging, optical pumping, atom-optics, and the contrast interferometer probe (see Section 5.1.2). Individual beam frequency and intensity are controlled by way of Acousto-Optical Modulators (AOM), and polarisations set with half-wavelength and quarter-wavelength waveplates as required. The beams are then fibre-coupled to the atom manipulation section, where a 2D Magneto-Optical Trap (MOT) is used as a bright source of atoms to feed a 3D MOT. The MOT cooled atoms are then further cooled with forced Radio-Frequency evaporation, and then cooled further still with a hybrid magnetic and optical-crossed-dipole trap until Bose-Einstein Condensation. At this time the interferometer is primed and ready for interferometry.

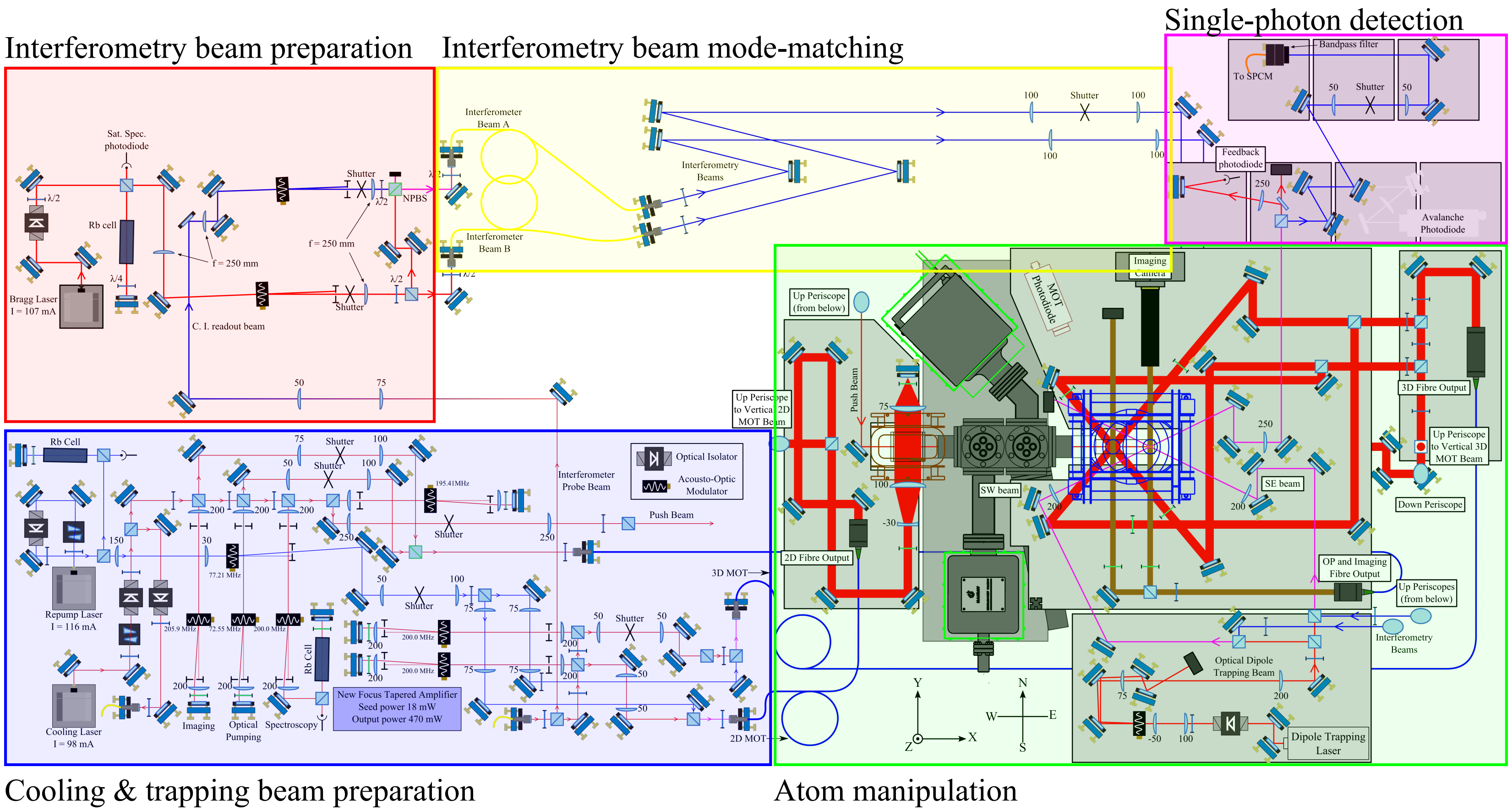

Figure 2.1: An overview of the experimental optics bench. The left side of the table is concerned with preparation of the laser light used in trapping and cooling (blue) and in atom-optics (red). The right side contains the atomic containment apparatus and science cell (green), as well as contrast signal measurement (purple). Figure adapted from [99]. Each subsection is shown in closer detail in Figures 2.3 (Cooling & Trapping preparation), 2.14 (Interferometry beam preparation), 2.16 (Interferometry beam mode-matching), 2.19 (Atom manipulation & Single-photon detection).

2.2 Beam preparation

2.2.1 Useful atomic transitions

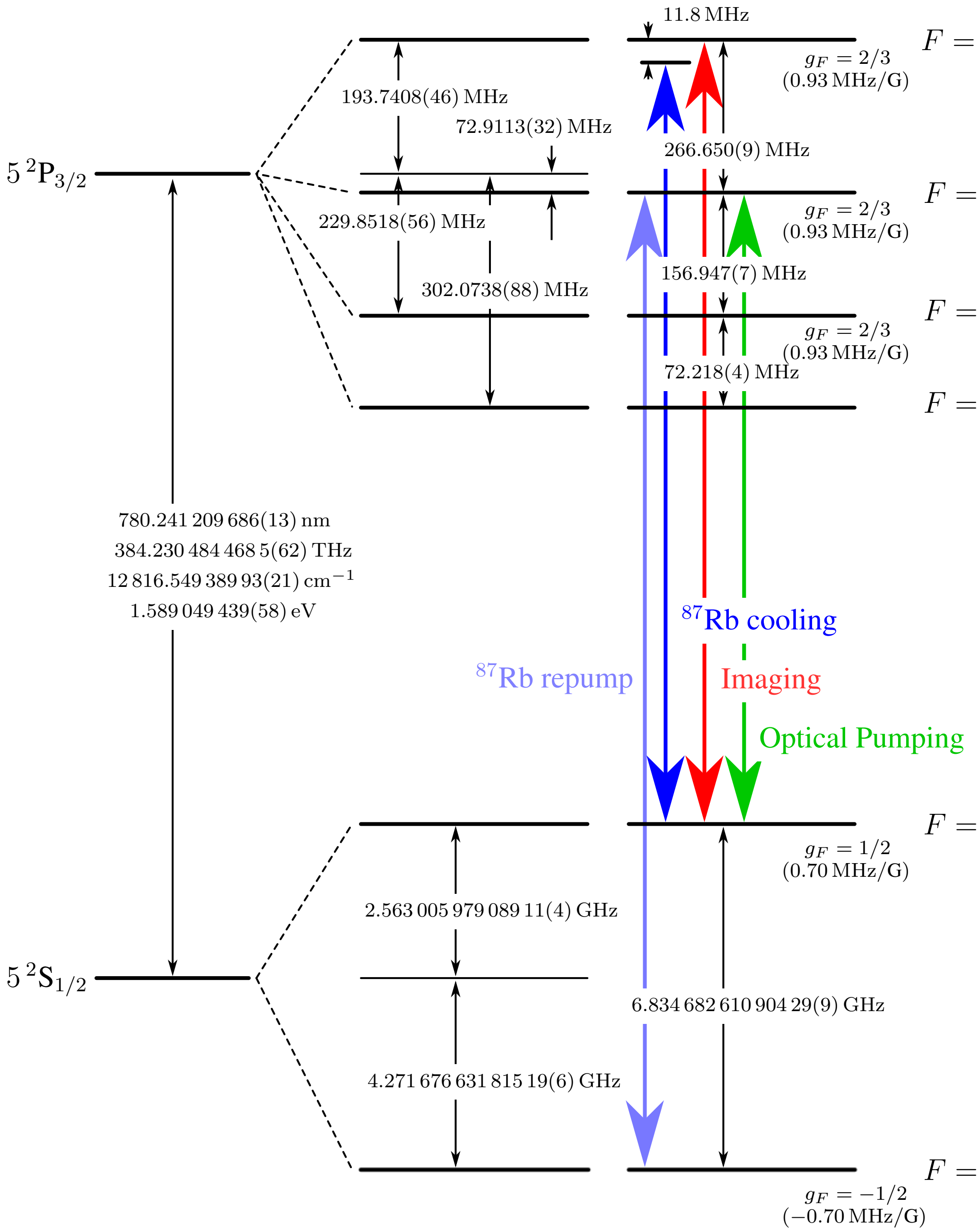

Figure 2.2: An overview of the atomic transitions used in the experiment which are used to lock our laser. We use the hyperfine states of the ^{87}Rb D_2 line transition as the base for laser cooling and trapping. Figure adapted from [104], and from [98].

The ^{87}Rb D_2 line offers convenient transitions for cooling and trapping, in that laser diodes of approximately correct frequency are cheap and readily available, and the precise lasing frequency can be controlled with use of an Extended-Cavity Diode Laser and associated controller [99]. On this line the hyperfine $F = 2 \leftrightarrow F' = 3$ transition offers a closed cycling transition commonly used for laser cooling of ^{87}Rb ensembles. Lasers tuned to this $F = 2 \leftrightarrow F' = 3$ transition have some small probability of instead exciting the $F = 2 \leftrightarrow F' = 2$ transition, from which atoms can fall into the $F = 1$ state. We therefore use a second laser tuned to the $F = 1 \leftrightarrow F' = 2$ to 'repump' atoms back into the cycling transition. These two transitions are shown in Figure 2.2.

2.2.2 Laser preparation optics

Figure 2.3 shows an overview of our laser preparation layout. Our laser beams are generated by a pair of ECDL, colloquially named 'Cooling' and 'Repump'. Each laser is frequency locked using Doppler-free saturated spectroscopy in a rubidium vapour cell, using a MOGLabs MOGBOX laser controller.

Contrary to the naming convention, the 'Cooling' laser actually supplies light for several experimental functions: the beam is fed into several pickoffs which are then frequency locked with AOMs for laser cooling, absorption imaging, optical pumping, and the contrast interferometer probe beam (see chapter 5).

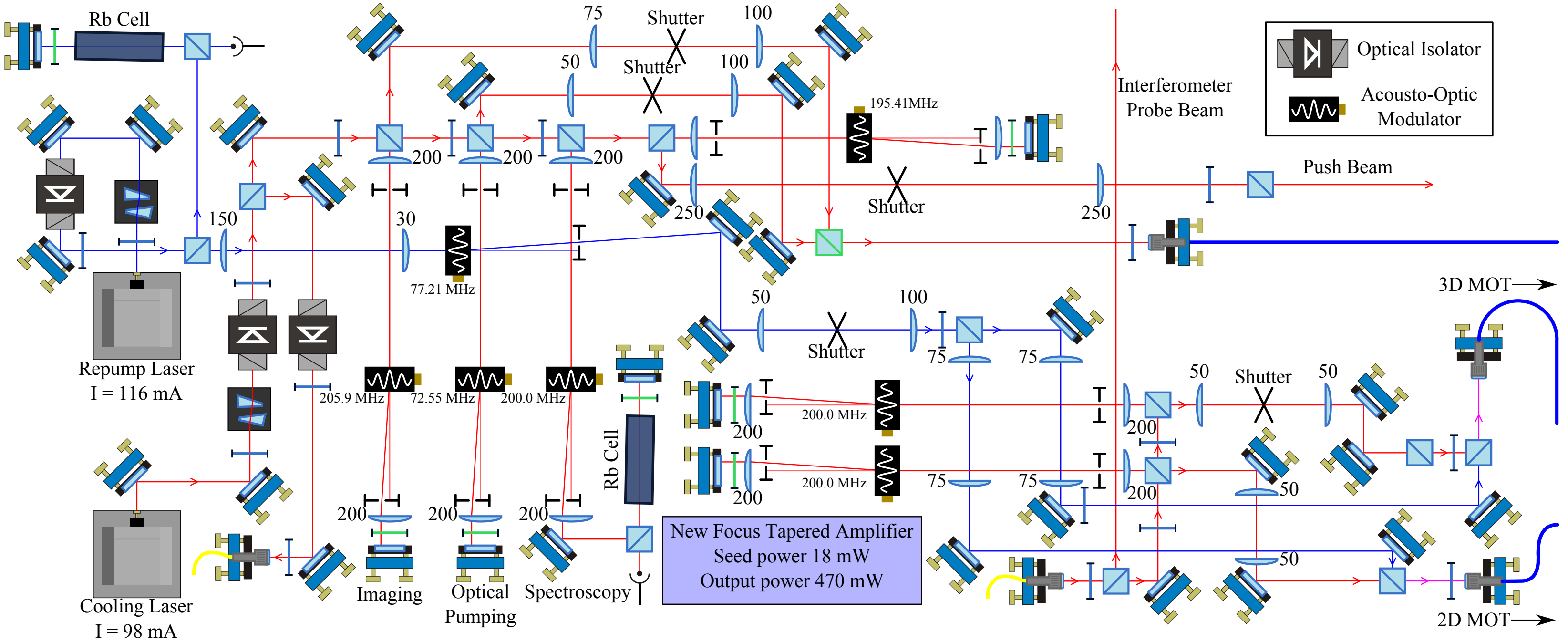

Figure 2.3: Overview of the optics table where cooling and trapping lasers are prepared. Two External-Cavity Diode Lasers are used to generate the beams for cooling, repumping, imaging, and optical pumping. The ‘cooling laser’ is fed into several pickoffs, which are then modulated with AOM to the required frequencies. Figure taken from [99].

2.2.3 Laser frequency locking

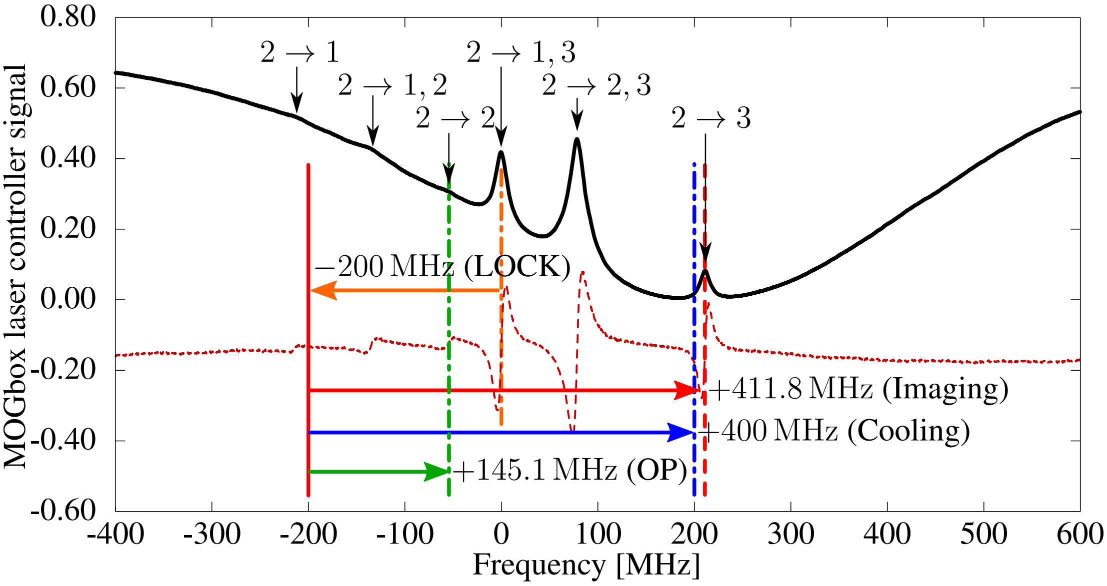

Figure 2.4: Saturated spectroscopy (Black) of a ^{87}Rb vapour cell around the cooling transition. Light transmitted through the vapour cell is drawn with a solid black line, with the MOGBox error signal drawn as dashed-red. We lock our laser to the $F = 2 \to F = 1, 3$ crossover feature (Orange dot-dashed line) shown at $0\,\mathrm{MHz}$. The spectroscopy is performed after the first pass of a double-passed AOM (Figure 2.1), and so the actual laser frequency is $200\,\mathrm{MHz}$ below this lock point (red solid line), from where we take various pick-offs for the Optical pumping (Green dot-dashed), Cooling (Blue dot-dashed), and Imaging (Red dot-dashed) beams. The various frequencies of these pick-offs are adjusted with individual AOMs. Figure adapted from [98].

We frequency-lock each ECDL to a target frequency using the doppler-free saturated spectroscopy features in a rubidium vapour cell. Since the absorption spectra are dominated by crossover features [105], we instead lock not to the desired transitions themselves, but rather to some ‘nearby’ crossover feature, and use Acousto-Optical Modulators (AOM) to shift the light to the desired frequency.

Figure 2.4 shows the spectrum used to lock our ‘Cooling’ laser to the $F = 2 \to F' = 1, 3$ crossover feature. This spectrum is sampled after the *first* pass of a double-passed AOM which modifies the laser frequency by $+200\,\mathrm{MHz}$, so the frequency at the laser output is actually $-200\,\mathrm{MHz}$ *below* the $F = 2 \to F' = 1, 3$ crossover (red, solid line). From this point, we can then map the frequencies of each pickoff forwards.

Cooling light is sourced from the largest fraction of the laser, picked off into a Tapered-Amplifier (TA), amplified to roughly 600 mW, and then double-passed through a +200 MHz AOM up to $\Delta = -11.8\,\mathrm{MHz}$ below the $F = 2 \to F' = 3$ cooling transition.

The imaging pick-off is double-passed through a +205.9 MHz AOM to push it up to resonance with the the $F = 2 \rightarrow F' = 3$ transition.

The optical pumping pick-off is double-passed through a +72.55 MHz AOM up to -266.7 MHz below the $F = 2 \rightarrow F' = 3$ transition, which is resonant with the the $F = 2 \rightarrow F' = 2$ transition.

The 'repump' laser is used only to source a single function, and as a result has a rather simpler setup. Here we lock to the $F = 1 \rightarrow F' = 1, 2$ crossover feature, and use a single-passed AOM to increase the light frequency by +77.21 MHz to the $F = 1 \rightarrow F' = 2$ repump transition frequency.

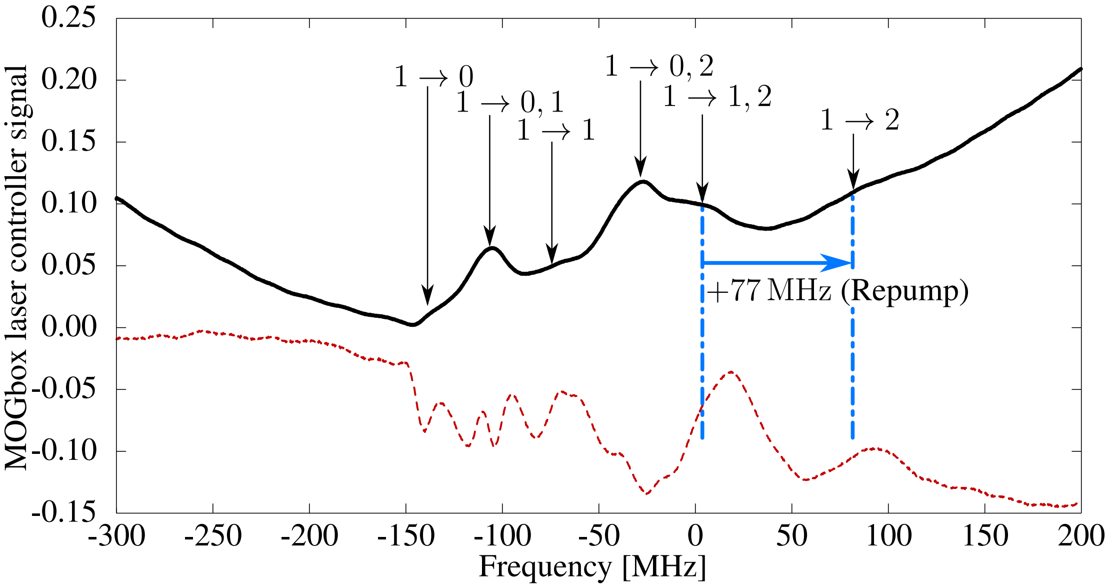

Figure 2.5: Saturated spectroscopy of a ^{87}Rb vapour cell around the repump transition. We lock our repump laser to the $F = 1 \rightarrow F' = 1, 2$ crossover feature, with an AOM further down the optical path pushing the beam up by 77 MHz to the $F = 1 \rightarrow F' = 2$ repump transition frequency.

2.3 Atomic manipulation

2.3.1 Overview

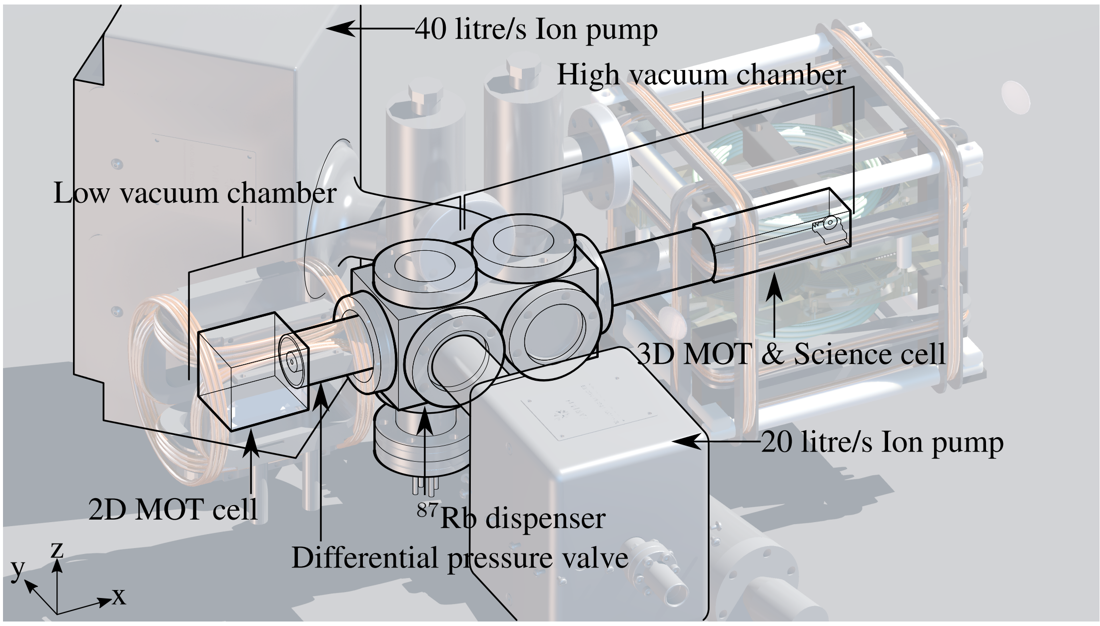

Figure 2.6: The atom chamber is split into two sections. Located in the low vacuum chamber (left), we use a 2D Magneto-Optical Trap (left) as a bright atom source to feed a 3D MOT located in the high vacuum chamber (right). A differential pumping valve is located between these sections.

We split the chamber into two sections, shown in Figure 2.6. The 'low vacuum' chamber is pumped with a $20\,\mathrm{l\,s^{-1}}$ ion pump (Agilent Varian VacIon Plus 20 StarCell Ion Pump) down to a pressure of $\approx 10^{-7}$ Torr. Atoms are loaded into this chamber from an Alvatec enhanced abundance ^{87}Rb dispenser run with a current typically around 2.6 A. The chamber is homebuilt with anti-reflection coated glass from SLS Optics, and measures approximately 5 cm across in the X,Y,Z directions [99]. This glass cell is home to a 2D MOT, which we use as a bright atom source to feed a 3D MOT.

Separating the two chambers is a differential pumping tube. We use a single resonant 'push' beam to kick atoms from the 2D MOT through this pumping tube to the capture volume of our 3D MOT, located in the 'high-vacuum' chamber. This chamber is pumped down to $\approx 10^{-11}$ Torr with a $40\,\mathrm{l\,s^{-1}}$ ion pump (Agilent Varian VacIon Plus 40 StarCell Ion Pump).

2.3.2 2D MOT

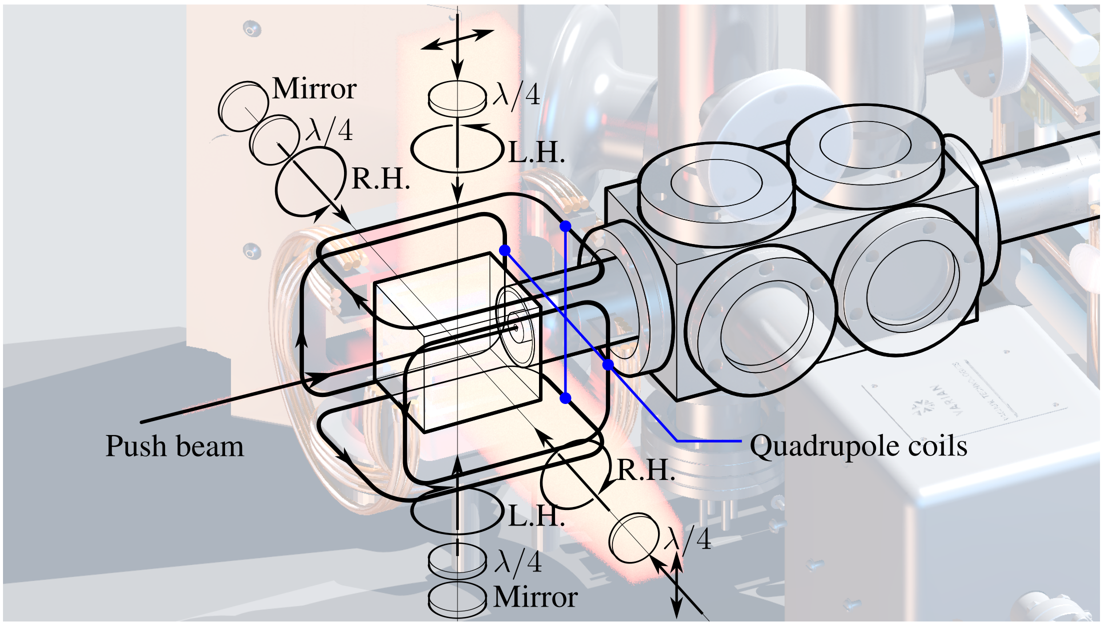

Figure 2.7: Schematic of the 2D MOT. We use two pairs of anti-Helmholtz coils to generate a field that is spatially flat along X, but increases linearly with displacement in the Y,Z directions. Both cooling and repump beams are retro-reflected to form a 4-beam 2D MOT.

The magnetic component of the 2D MOT is generated by two pairs of anti-Helmholtz coils. The overlapping quadrupole field gradients ‘add up’ in the Y and Z directions, and cancel in the X direction. The resulting field increases linearly with some small displacement from the X-axis, and is spatially flat along the X-axis. The position of the QP magnetic zero is tuned using two pairs of ‘shim’ coils in Helmholtz configuration, allowing maximum overlap with the Push beam (bottom left), which kicks atoms through the differential pumping tube.

Our dual cooling and repump lasers are spatially overlapped exiting the optical fibre from the laser preparation table, and split into two beams which approach the 2D cell from the -Y and +Z directions. These beams are converted to a circular polarisation with quarter-wave plates (QWP), and expanded with cylindrical lenses. The beams pass through the cell orthogonally, and then through a second QWP which converts to a linear polarisation. They are then retro-reflected, with the QWP converting the beams to a circular polarisation. These then pass back through the cell. Together, these form the four cooling and repump beams of a MOT.

A single laser (‘push beam’) resonant with the $F = 2 \rightarrow F' = 3$ transition kicks atoms from this 2D MOT through the differential pumping tube to the 3D MOT in the high-vacuum chamber.

2.3.3 3D MOT

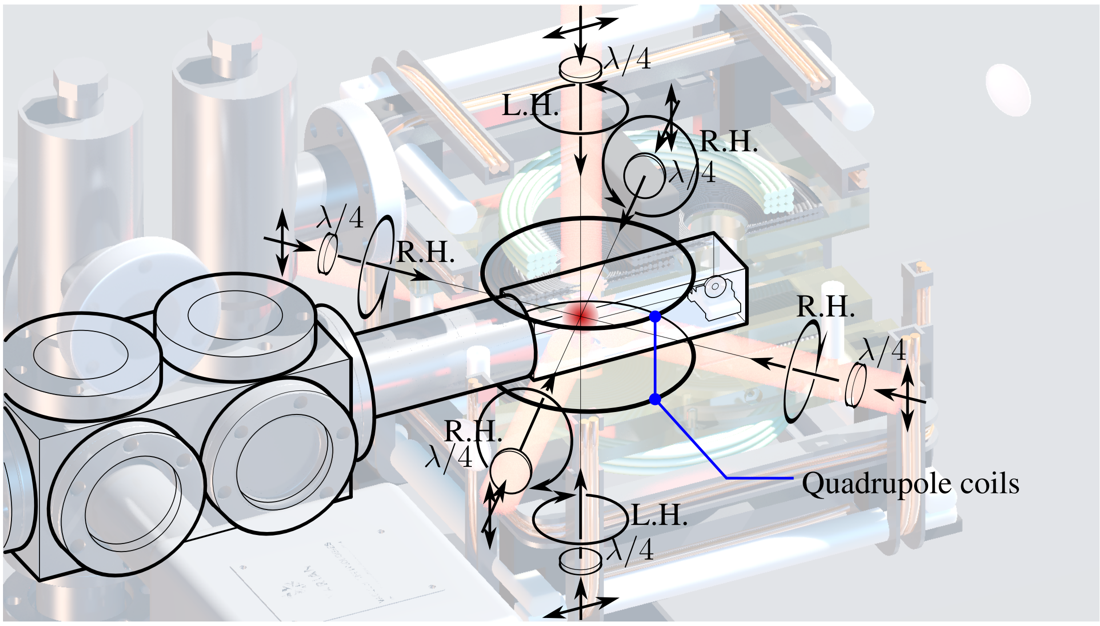

Figure 2.8: To the right is our 3D MOT, which is fed with the same overlapped cooling and repump lasers as the 2D MOT, albeit in a six-beam configuration. A single pair of anti-Helmholtz coils generate a quadrupole trap.

Our 3D MOT is constructed with the standard ‘6-beam’ geometry, where each beam contains frequencies for both cooling and repumping, and is converted to circular polarisation with a quarter-wave plate before the science chamber.

A single pair of anti-Helmholtz coils generates a quadrupole magnetic field and 3 pairs of Helmholtz coils generate spatially-flat ‘shim’ fields that we use to move the position of the quadrupole minimum [106]. Around this magnetic minimum we have a ‘capture volume’ where the magnetic field strength is sufficient to Zeeman-shift the magnetic sublevels of the ^{87}Rb atoms into resonance with the red-detuned ‘cooling’ beams. This gives us a finite ‘capture’ volume where the combined slowing (optical molasses) and trapping (magnetic trap) are sufficient to overcome the atoms’ incoming velocity. In this capture volume we grow a cloud of cooled atoms for a duration typically around 15 s until approximately 10^9 atoms are trapped. For the duration the cooling light is held at -14 MHz, with a 3d MOT quadrupole coil held at $11\,\mathrm{G\,cm^{-1}}$.

We then compress the MOT for $\sim 5\,\mathrm{ms}$ by increasing the 3D MOT quadrupole field to $16\,\mathrm{G\,cm^{-1}}$ and detuning the cooling light from -14 MHz to -25 MHz. We then perform a ‘molasses’ stage by releasing the quadrupole trap for 4 ms.

2.3.4 Optical pumping

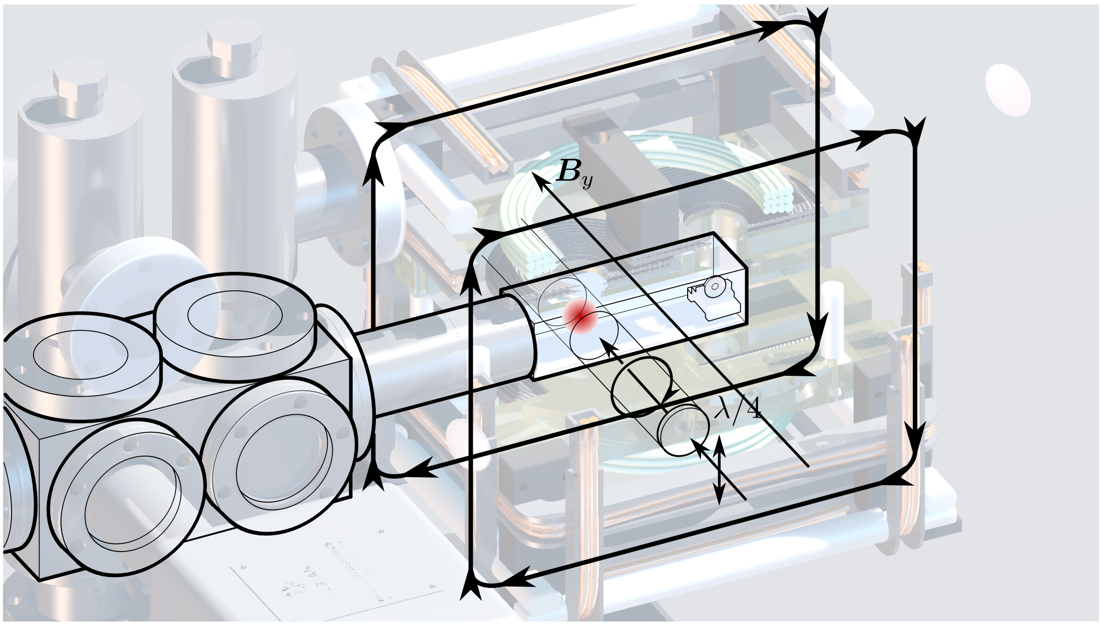

Figure 2.9: We optically pump atoms into the $|F = 2, m_F = +2\rangle$ state with a circularly polarised resonant beam overlapping the 3D MOT position. The bias coils are set to orient the atomic spins in the $+Y$ direction.

Our MOT lasers cool our atoms, but also introduce a secondary heating mechanism which limits further cooling to the recoil temperature [103]. To reach colder temperatures, we need to make our atoms trappable with purely magnetic traps. We can do this by optically pumping the atoms into a weak-magnetic-field-seeking state. We firstly orient the atoms' spin into the $+Y$ direction with a $1.6\,\mathrm{G}$ spatially flat magnetic field from the Y-shim Helmholtz coils. We then impart a right-handed circularly polarised laser beam tuned to the $F = 2 \rightarrow F' = 2$ transition for a duration of 1.2 ms, pumping our atoms into the $|F = 2, m_F = 2\rangle$ state.

We then reload the atoms pumped into the $|F = 2, m_F = 2\rangle$ state in the quadrupole trap with a field gradient of $63\,\mathrm{G\,cm^{-1}}$ over a period of 5 ms, before ramping the trap field gradient linearly to $100\,\mathrm{G\,cm^{-1}}$, compressing the atomic cloud.

2.3.5 Magnetic transport

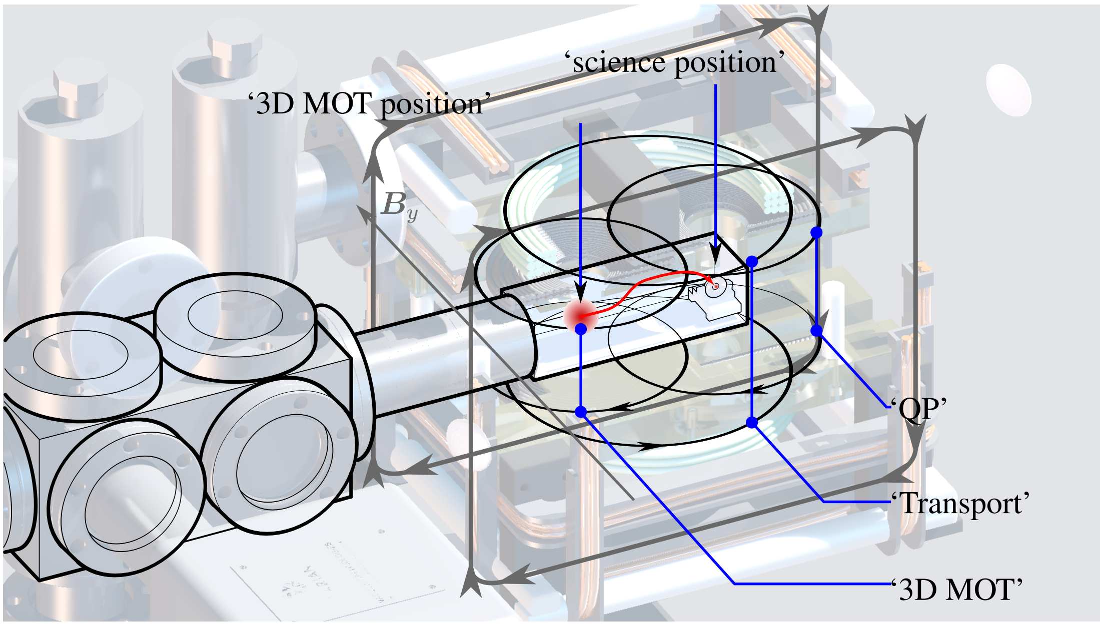

Figure 2.10: After optically pumping atoms into the magnetically trappable $|F = 2, m_F = +2\rangle$ state, we ramp the currents through the three quadrupole coil pairs to compress the trap, then smoothly move the magnetic minimum over to the optical dipole trap.

The experiment contains an AC coupled ring-trap, which has not been used in the work described in this thesis. More information can be found in the PhD Theses of Dr Aline Dinkelaker [98] and Dr Billy Robertson [99]. The ring trap is designed to load atoms from the hybrid optical trap and is therefore necessarily located around the crossed optical dipole trap. The ring trap is also physically too small to surround the 3D MOT. As a result, the optical dipole trap is spatially separated from the 3D MOT by approximately 10 cm. To cool the atoms further, we need to move them over to the location of the optical dipole trap, henceforth referred to as the 'science position'.

The science chamber has three pairs of anti-Helmholtz coils, used to magnetically transport atoms from the 3D MOT to the location of the optical dipole trap (Section 2.3.7) and atom-optics (Section 2.3.8). By ramping the current through these coils in tandem, we smoothly move the magnetic field minimum to the science position, carrying our cloud of cooled atoms. A small Y-shim bias field of a few Gauss (≈ 5 G) guides the field minimum around the ring trap.

2.3.6 Forced RF evaporation

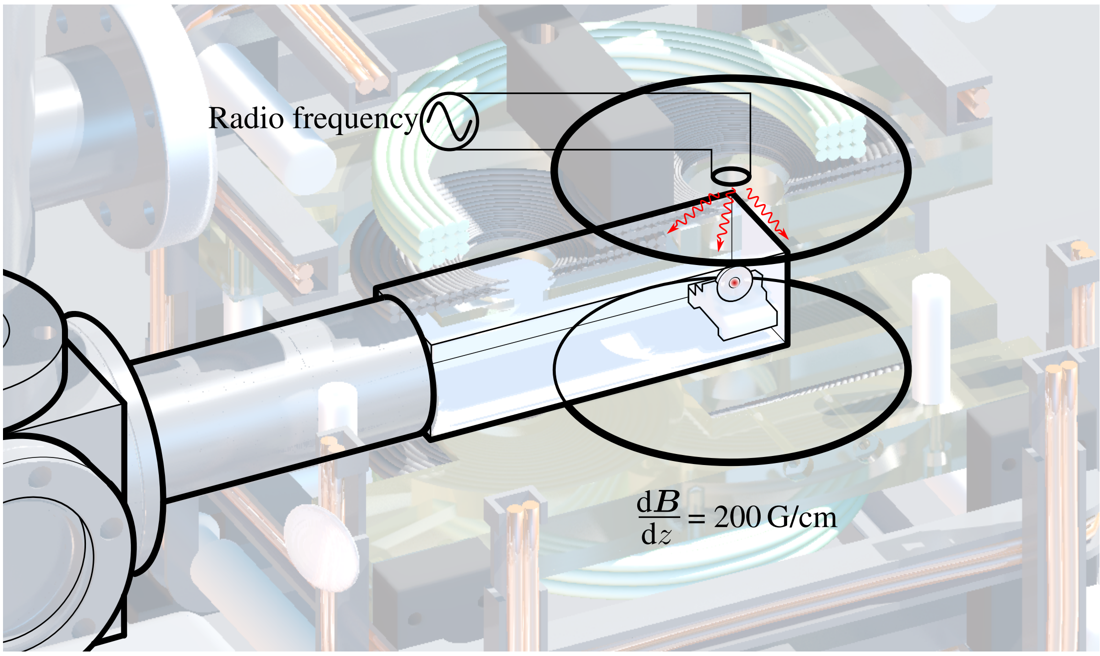

Figure 2.11: We use forced Radio-frequency evaporation to cool our surviving atomic ensemble down to approximately 30 µK before loading into our hybrid optical trap.

We need to further cool atoms before we can load them into the hybrid optical trap. With atoms in the science position, we ramp the nearest quadrupole trap current to around 170 A, where the field gradient $\mathrm{d}B/\mathrm{d}z$ is at 200 G cm^{-1}. The magnetic sublevels in the quadrupole trap are Zeeman-shifted with displacement from the trap centre, such that greater displacement from the trap centre requires greater energy (and therefore temperature). This position-dependent Zeeman shift split the degeneracy in the trapped $|F = 2, m_F = +2\rangle$ state and the anti-trapped $|F = 2, m_F = -2\rangle$ state [103].

We then ramp a Radio-Frequency (RF) current through a small coil over the science position. These RF photons couple the trapped $|F = 2, m_F = +2\rangle$ state with the anti-trapped $|F = 2, m_F = -2\rangle$, but only at a given ellipsoid around the quadrupole trap where the RF photons are resonant. As such, the RF field spin-flips atoms which reach this height in the trap into the untrapped state, removing them (and the energy they carry) [103].

We ramp this radio-frequency from 16 MHz initially down to 3.75 MHz over 3 s, reducing the temperature of our RF knife. In doing so we cut into the temperature distribution of the atomic ensemble in the trap, removing atoms which contain more than the average atomic energy, reducing the average energy (and therefore temperature) of the remaining atoms [103].

This ‘forced RF evaporation’ cools our atomic ensemble at the cost of cloud population, until we have around 5×10^7 atoms at a temperature of ~ 30 µK [99].

2.3.7 Hybrid optical trap

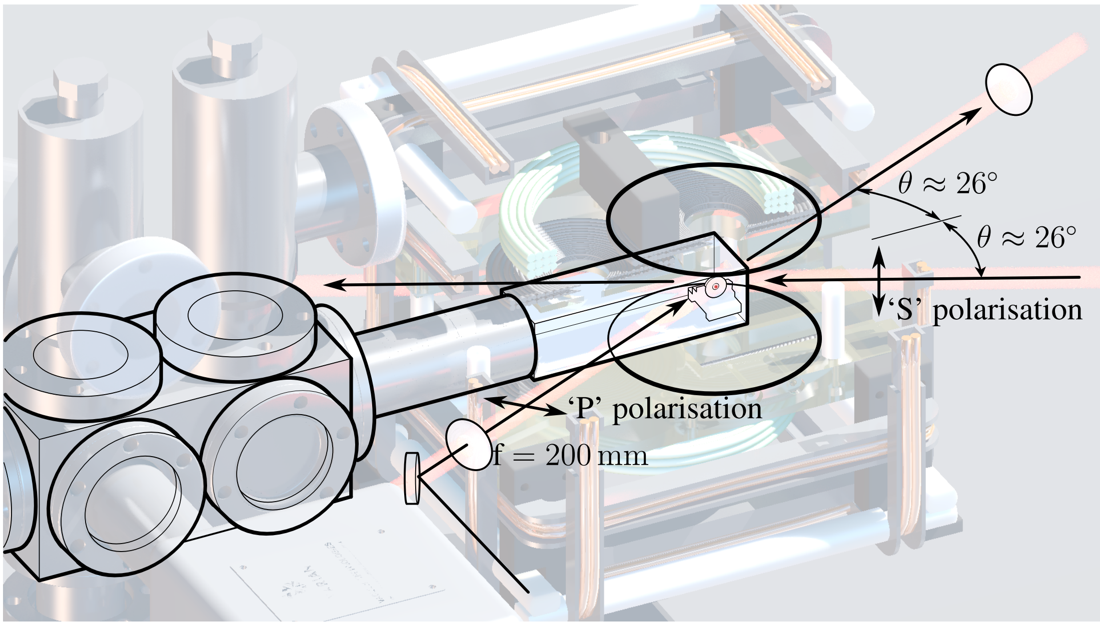

Figure 2.12: We further cool the atoms using a hybrid magneto-optical dipole trap [107], relaxing our RF-cooled atoms into the combined magnetic-optical potential. We generate Bose-Einstein Condensates typically of 1×10^5 at $80\,\%$ purity with a thermal-fraction temperature of $50 - 100\,$nK.

To cool to Bose-Einstein Condensation we use a hybrid optical trap, comprising a crossed dipole trap and magnetic quadrupole trap [107]. Forced RF evaporation cools the atoms to $T \approx 30\,\mu\mathrm{K}$, and then the quadrupole trap relaxed and the optical trap activated.

We use an IPG Ytterbium Fibre laser (YLM-20-LP-SC) as the generator of our optical dipole trap. The 10 W beam is split with a non-polarising beam cube (NPBS) into two beams of approximately 3 W, which approach the atoms from an angle of $\pm 26°$ relative to the X-axis. These beams are cross polarised so that they don't generate a optical grating. Each beam is then focussed with a $f = 20\,\mathrm{mm}$ lens such that their waists are $\approx 86\,\mu\mathrm{m}$ at their foci. These foci are positioned such that they overlap at the position of our RF-cooled atoms, creating an optical crossed dipole trap [99].

The total trap potential at this time is a combination of the optically-induced Gaussian potential and a magnetic-gradient potentials (in the Z-direction), which leads to a Gaussian shaped 'notch' potential with a lowered edge on the lower side. The hottest atoms leak from this lower edge, cooling the ensemble [107].

The optical power is then reduced in an exponential ramp over a period of $4\,\mathrm{s}$ from the initial power of $3\,\mathrm{W}$ to approximately $0.3\,\mathrm{W}$, forcibly evaporating the hottest atoms. The trap frequencies at this low power range are on the order of $\omega_{X,Y,Z} =$

$30\,\mathrm{Hz}, 70\,\mathrm{Hz}, 70\,\mathrm{Hz}$, and we expect a Bose-Einstein Condensation transition temperature of $T_{\text{critical}} \approx 100\,\mathrm{nK}$ [99].

Our hybrid cooling typically generates a ellipsoidal atom ensemble with approximately 1×10^5 atoms in the Bose-Einstein Condensate at around $80\,\%$ purity, and a thermal-fraction component temperature of $\sim\ 50\,\mathrm{nK}$. The BEC Thomas-Fermi radii are on the order of $7\,\mathrm{\mu m}$ in the Z,Y directions and $16\,\mathrm{\mu m}$ in the X direction [99].

2.3.8 Interferometry beams

Overview

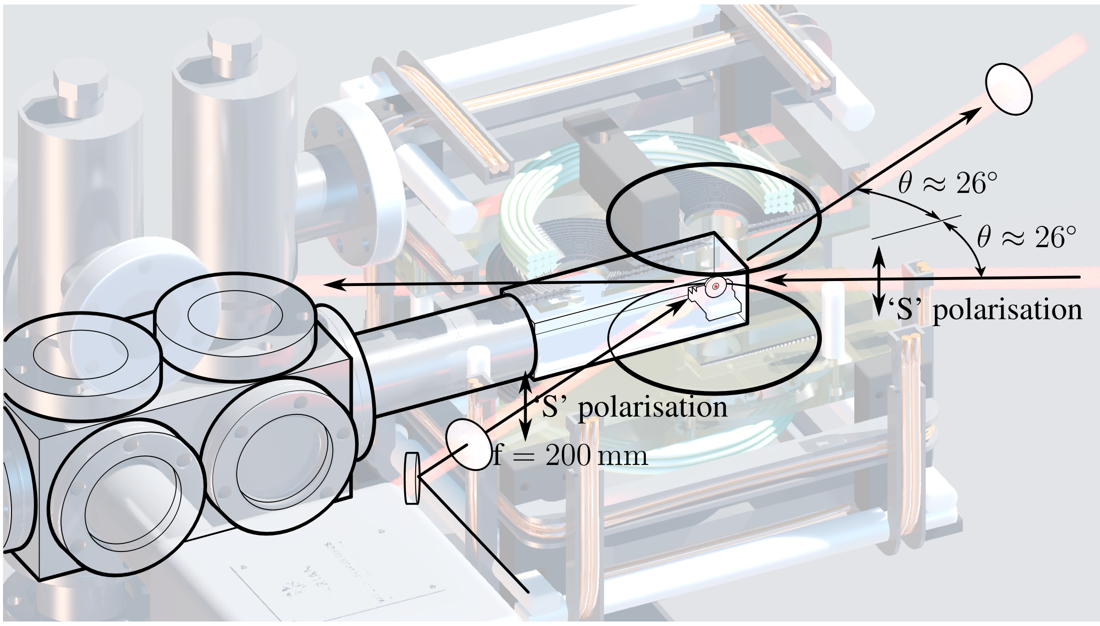

Figure 2.13: We perform our atom-optic operations by modulating an optical grating which is spatially overlapped with the BEC atoms. We initially align this grossly with the dipole trap beams, and then use Kapitza-Dirac pulses to fine-tune the alignment of the beams with the atoms.

Our atom-optics are generated by an optical grating located at the position where the BEC is formed (i.e. in the crossed dipole trap). To generate this optical grating both optical grating beams share a common polarisation (linear in the $\pm Y$ direction).

There are three major considerations when preparing the optical grating.

(1) Frequency locking: The wavelength of our optical grating is a key parameter in modelling the atom-optics. As such, we need to prepare the laser frequency used carefully.

(2) Longitudinal alignment: The off-resonant scattering used by our atom-optics (see Chapter 3) requires that the phase-fronts be as flat as possible at the atoms' position. This creates an optical grating with the least curvature possible. As such, we

need to optimise the longitudinal position of the beam foci so they overlap with each other and the atoms.

(3) Transverse alignment: The depth of our optical grating is maximised when the intensity of both beams overlap at the same position. These beams have a Gaussian profile, so we can maintain the greatest coupling consistency across our atomic ensemble by using the ‘flattest’ part of our beams’ intensity profile; the centre. As such, we need to optimise both the transverse alignment of the two beams with the atoms.

Frequency locking

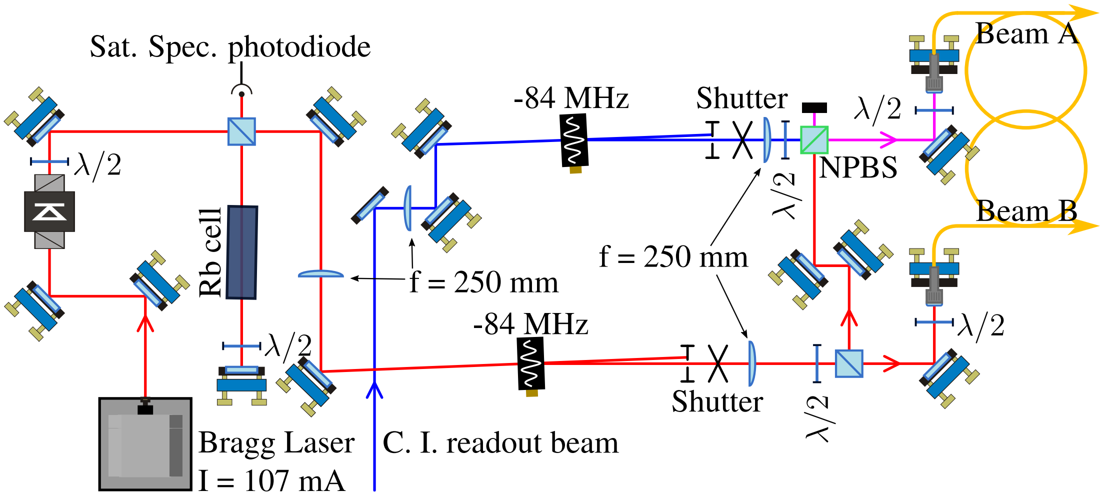

Figure 2.14: Figure adapted from [99]. Optics table layout of interferometry beam preparation. (a) We generate the atom-optics beams (Red lines) with an ECDL locked to the ^{85}Rb repump transition approximately $-4\,\mathrm{GHz}$ red detuned from the ^{87}Rb cooling transition. This AOM is used as an intensity control, allowing us to time-modulate the lattice depth at the atoms. The beam is split into two and fed into two single-mode optical fibres to clean up the spatial mode. A pickoff of the locked ‘Cooling’ laser light is used as a probe for the contrast interferometer. This is spatially overlapped with the ‘A’ atom-optic beam with an NPBS, and fibre coupled into interferometry fibre A.

Figure 2.14 shows a schematic of the optics used to control the interferometry beams. Our atom-optics are sourced from an ECDL locked to the ^{85}Rb repump transition, approximately $-4.5\,\mathrm{GHz}$ red-detuned from the ^{87}Rb $F = 2 \rightarrow F' = 3$ cooling transition (see Figure 2.15). This light is so far detuned from our ^{87}Rb transitions that the exact frequency used is not as important as knowing what that frequency is. We choose this frequency because it represents a convenient feature visible in the vapour cell used to frequency-lock the laser and is sufficiently detuned to suppress incoherent scattering.

The intensity control of the interferometry beams is done with an Acousto-Optical Modulator (AOM). Our AOM driver circuit accepts an input RF source (Keysight

N5138B) at $84\,\mathrm{MHz}$ and a DC input 'control' voltage. An RF mixer (Minicircuits ZP-3LH-S+) generates an output signal at the frequency of the RF source and the amplitude of the DC input voltage. This output signal is amplified, and used to power the AOM. We then control the frequency shift of the AOM by choosing the diffraction order we sample as our output, and the coupling efficiency into that mode by altering the DC input voltage.

Our output pickoff is taken from the '-1' scattered order, where we find that transfer function of input light to the -1 order is well approximated by a quadratic function [99]. We therefore see a frequency shift in the interferometer beams of $-84\,\mathrm{MHz}$. We modulate the optical lattice depth by altering the DC input voltage. This is done using the programmed output of an (Standford Research Systems SRS DS345) arbitrary function generator (see chapter 3 for more details).

The intensity modulated atom-optics beam is then split with a Non-Polarising Beam-Splitter (NPBS) and coupled into two single-mode optical fibres. These optical fibres are used as spatial filters to clean up the interferometry beams transverse profile.

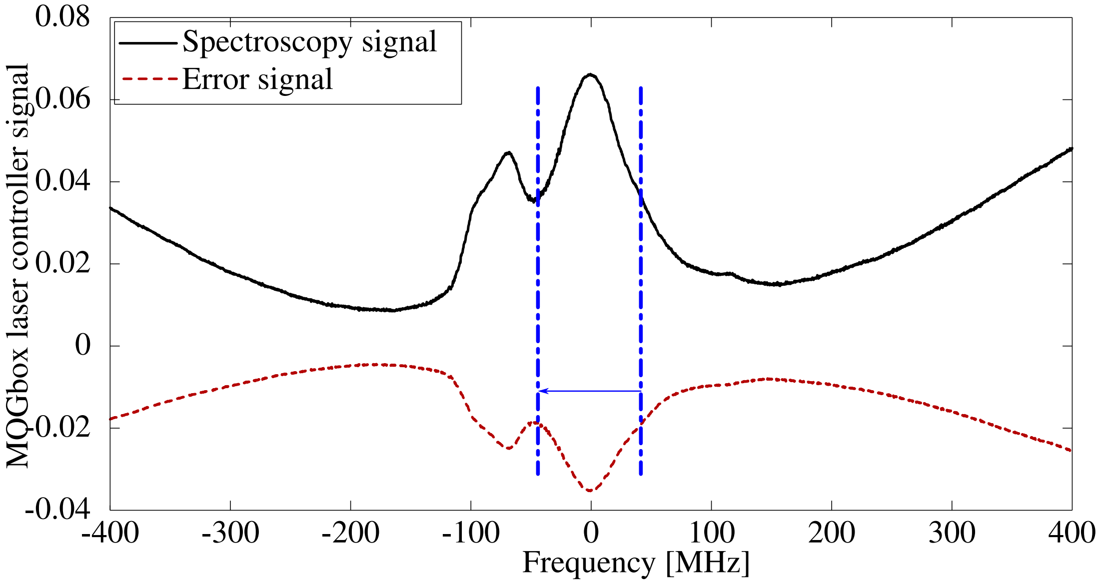

Figure 2.15: Saturated spectroscopy of a ^{87}Rb vapour cell around the ^{85}Rb repump transition. We lock our atom-optics laser near the ^{85}Rb $F = 2 \rightarrow F' = 2$ repump transition, with an AOM further down the optical path pushing the beam down by $84\,\mathrm{MHz}$. This light is so far detuned from transitions in ^{87}Rb that we could choose to lock at any nearby frequency.

The contrast interferometry probe laser (see chapter 5 for more details) is sourced from a pickoff of the cooling laser light. This is then intensity-controlled with an AOM and frequency shifted a further $-84\,\mathrm{MHz}$ to approximately $-296\,\mathrm{MHz}$ below the $F = 2 \rightarrow F' = 3$ transition.

As with the atom-optics beams, we filter the spatial profile of the probe beam by coupling it into a single-mode optical fibre. This has the secondary benefit of simplifying later alignment to the two interferometer arms, instead of three interferometer beams.

Focal position

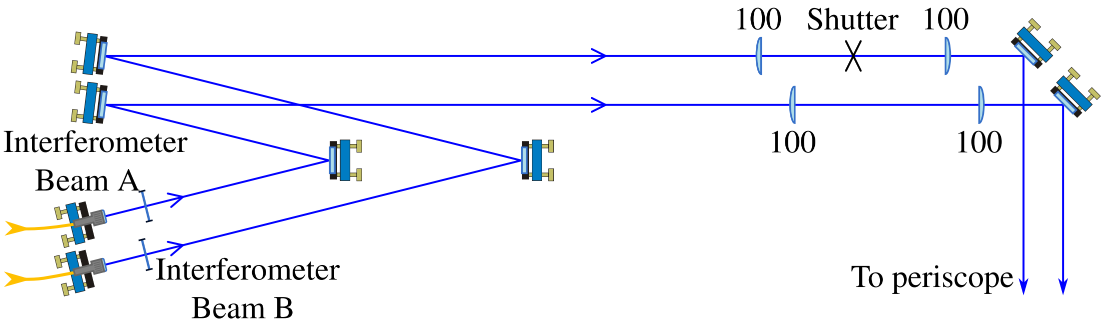

Figure 2.16: We allow the interferometry beams to propagate for some distance to filter out higher spatial frequencies in the beam profile before they enter the alignment telescopes. These telescopes project the beam foci into the science chamber at an adjustable position. Note that this schematic is not drawn to scale.

After the interferometry beam fibre output we have approximately 1.7 m propagation before the beams enter the alignment telescopes. We use this extended path primarily to filter out high spatial frequencies from our beam shape, so that they're closer to a Gaussian profile by the time they enter the telescope.

The telescopes are used to project the interferometry beam foci into the chamber at the appropriate position. We first performed knife-edge measurements on both beams to determine the q-parameter of the beams before and inside the telescope, and then projected these forwards using the software 'Gaussianbeam' [108] (shown in Figure 2.17). We can then adjust the telescope lenses (which are mounted on translation stages) to position the beam focus at the atoms' position.

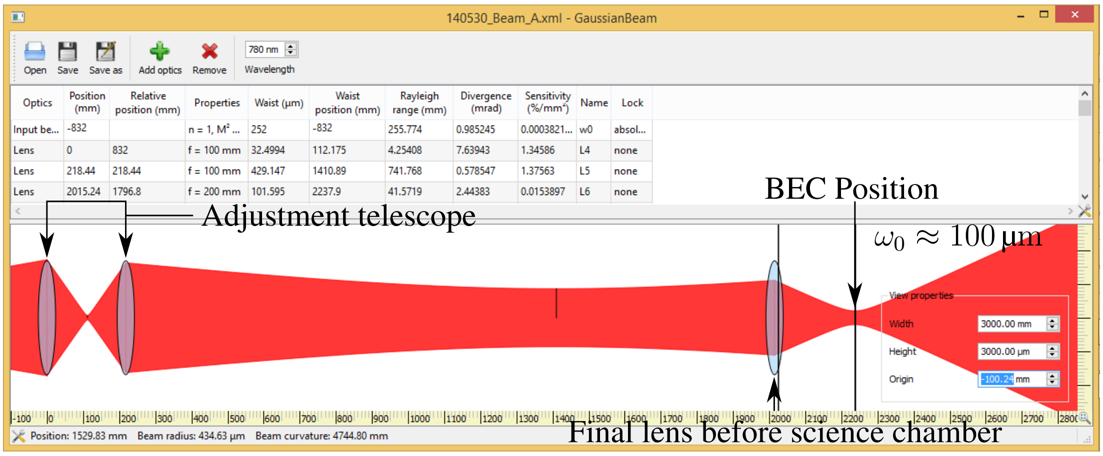

140530_Beam_A.xml - GaussianBeam

780 nm Wavelength

Optics	Position (mm)	Relative position (mm)	Properties	Waist (µm)	Waist position (mm)	Rayleigh range (mm)	Divergence (mrad)	Sensitivity (%/mm²)	Name	Lock
Input be...	-832		n = 1, M² ...	252	-832	255.774	0.985245	0.0003821...	w0	absol...
Lens	0	832	f = 100 mm	32.4994	112.175	4.25408	7.63943	1.34586	L4	none
Lens	218.44	218.44	f = 100 mm	429.147	1410.89	741.768	0.578547	1.37563	L5	none
Lens	2015.24	1796.8	f = 200 mm	101.595	2237.9	41.5719	2.44383	0.0153897	L6	none

View properties
Width 3000.00 mm
Height 3000.00 µm
Origin -100.24 mm

Position: 1529.83 mm Beam radius: 434.63 µm Beam curvature: 4744.80 mm

Figure 2.17: A *GaussianBeam* simulation of our interferometry beam A from the interferometry telescope (Figure 2.16) to the BEC position in the science chamber. Light propagates from left to right. We can fine-tune the waist size and focal position at the atoms by adjusting the positions of the second telescope lens and final focussing lens.

Transverse alignment

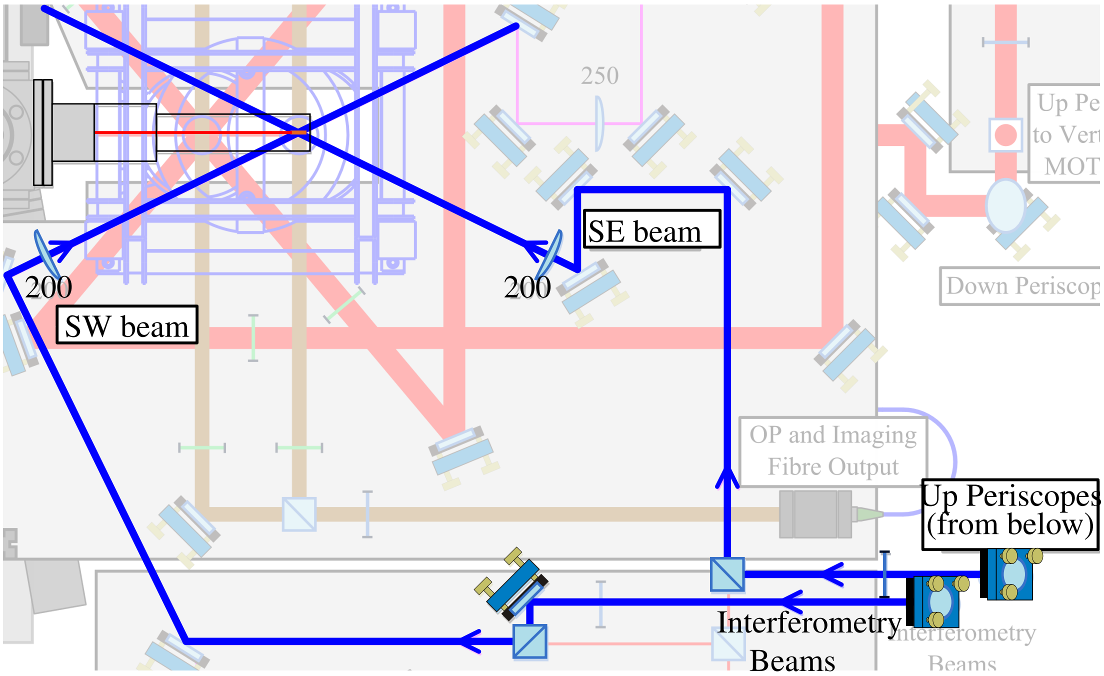

Figure 2.18: The interferometry beams are overlapped with the optical dipole trap beams with beamcubes. We align the interferometry beams with the final mirrors before these beamcubes.

We align the transverse positioning of the atom-optics initially using a beam-profiler, after the dipole laser has been aligned sufficiently well to create a BEC. We position the camera at two positions, and alternatively adjust the atom-optic periscope mirror screws to adjust the beam overlap at both camera positions. By alternating positions, we asymptotically approach co-propagation with the dipole beams.

At this point the atom-optics are sufficiently aligned to allow for off-resonant scattering (see chapter 3 for more details). We then configure a splitting pulse with parameters typically on the order of 30 µs duration and 20 $\mathrm{E_r}$ lattice depth (see Section 3), which transfers some small fraction (for example 10 %) of the $|p{=}0\hbar k\rangle$ atoms into the $[|p{=}{+}2\hbar k\rangle{+}|p{=}{-}2\hbar k\rangle]$ superposition state. If we then adjust the atom-optic lasers, an improvement in the split fraction implies an increase in optical grating contrast. We then optimise, reducing the optical lattice laser power as required to maintain a split fraction under 30 %. This is an important step, since an increase in lattice contrast can actually *reduce* the split fraction at higher 'split power' (See Figure 3.2).

2.4 Signal detection

2.4.1 Overview

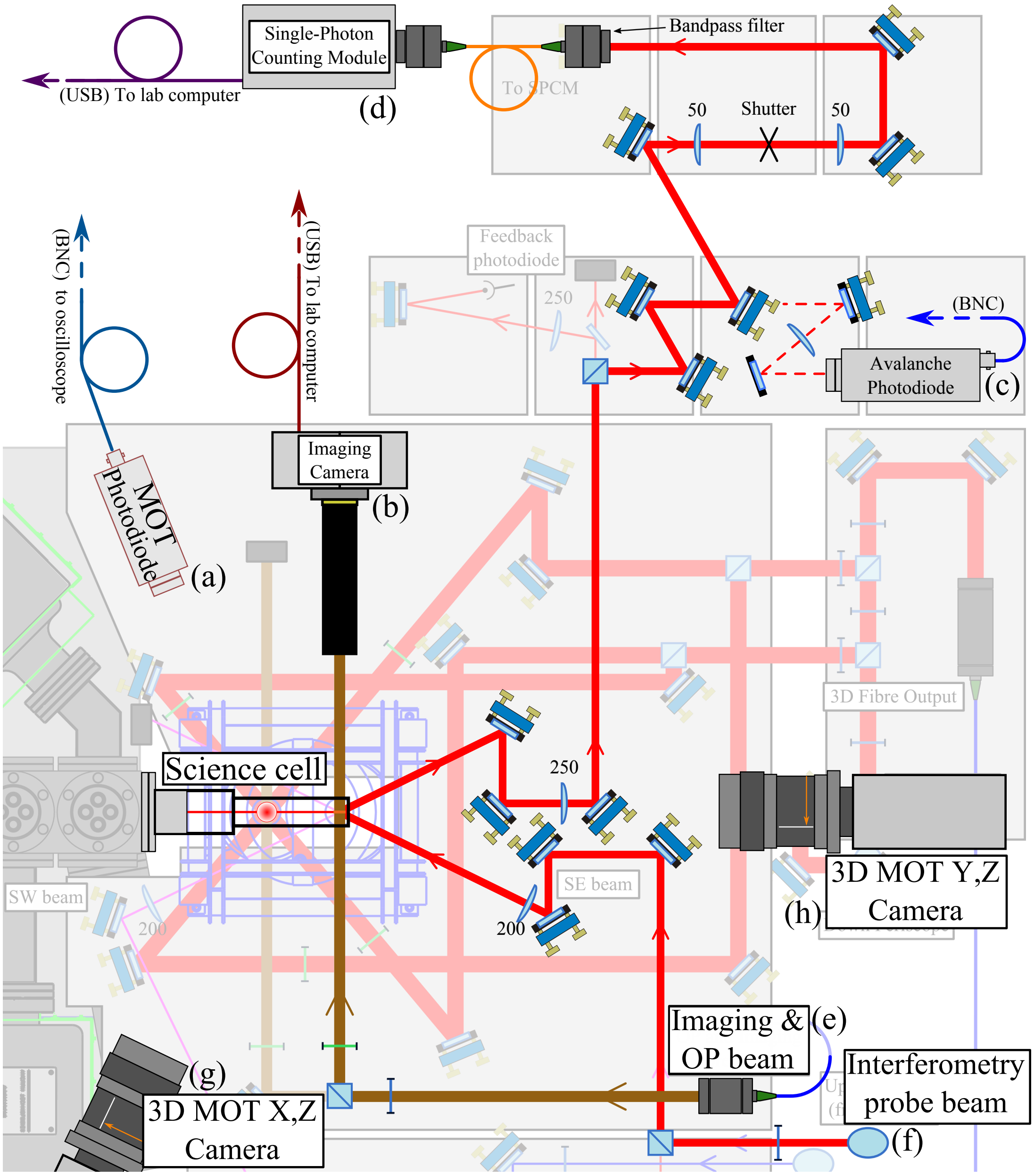

Figure 2.19: Overview of signal detection apparatus. Shown here is the 3D MOT photodiode (a), Cooled CCD Camera for absorption imaging (b), Avalanche photodiode for Contrast interferometry (c), the Single-Photon Counting-Module used in Contrast interferometry (d), the fibre output for absorption imaging light (e) and the periscope output for the contrast interferometer probe light (f). Figure adapted from [99].

2.4.2 3D MOT Fluorescence

Our 3D MOT continuously fluoresces: the incoming cooling light causes atoms to transfer from the $|F = 2\rangle$ to $|F' = 3\rangle$ state, and as atoms fall back into the $|F = 2\rangle$ state a corresponding $780\,\mathrm{nm}$ photon is emitted in a random direction. This scattering rate can be calculated with the transition linewidth Γ, light intensity I, and light detuning Δ [103].

$$\gamma_{\text{scatter}} = \frac{\Gamma}{2}\frac{\frac{I}{I_{sat}}}{1 + \frac{I}{I_{sat}} + 4\frac{\Delta^2}{\Gamma^2}} \tag{2.1}$$

Figure 2.19a shows a photodiode aimed at the 3D MOT atoms. A lens is positioned in front of this photodiode to focus light from the MOT, increasing the 'capture area' of the photodiode. Since we know the solid angle of the photodiode capture lens, we can calculate a transfer function between the number of fluorescence photons captured by the photodiode and the number of atoms captured by the 3D MOT. We use this fluorescence signal to tune our 2D and 3D MOT [99].

The 2D MOT acts as a bright collimated source of atoms for the 3D MOT, so the optimum tuning for the 2D MOT is whatever gives us the greatest load rate in the 3D MOT. We optimise the 2D MOT by setting the experiment to cycle a 1 s MOT load, followed by a 1 s 'blow-away' stage. The blow-away stage turns off the quadrupole magnetic field and shifts the 'cooling' laser frequency upwards until it is blue detuned from the $F = 2 \rightarrow F' = 3$ transition, anti-trapping atoms. This blow-away empties the MOT so that we can repeatedly perform 1 s MOT loads for load-rate optimisation. These two stages together form a cycling sequence where the 3D MOT loads atoms for 1 s, and anti-traps for 1 s. We then adjust the 2D MOT optics alignment and magnetic shim coil current to maximise the 3D MOT load rate. We typically achieve a 3D MOT load rate of $\sim$4$\times$10^7 atoms s^{-1}.

Whilst the 3D MOT load *rate* is generally a function of the 2D MOT alignment, the 3D MOT load *saturation* is mostly a function of the 3D MOT beam alignment. We optimise this by loading the 3D MOT continuously until saturation. This saturation level is typically on the order of 1×10^9 atoms, occurring some 60 s into MOT loading. A quicker saturation at a lower atom count is indicative of a reduce capture volume, usually from a misalignment between the MOT beams and quadrupole trap centre. We find that approximately 4$\times$10^8 atoms in the 3D MOT are required to successfully proceed through the remaining cooling stages to Bose-Einstein condensation.

The 3D MOT shim coils are tuned with a cycling MOT load $\leftrightarrow$ Molasses cycle. The molasses phase ramps the magnetic quadrupole trap off, and detunes the cooling frequency further into the red from the $F = 2 \leftrightarrow F' = 3$ cooling transition. This causes the atomic cloud to expand slowly (approximately doubling its size in each direction in approximately 0.2 s). Two video cameras are aimed at the 3D MOT from the South (Figure 2.19g), and from the East (Figure 2.19h), which track motion in the X,Z and Y,Z planes, respectively. Here we can track the centre of mass of the cloud, adjusting the shim currents until the cloud is stationary during the molasses phase.

2.4.3 Absorption imaging

Absorption imaging [109] is performed in three stages. Light resonant with the $F = 2 \leftrightarrow F' = 3$ transition (shown in Figure 2.19e) is collimated into a beam with waist $\omega \approx 1.25\,\mathrm{cm}$ and shone across the region of our 'science position'. This light is absorbed by the atoms, causing a shadow in the transmitted intensity. The light is then focussed with a $f = 10\,\mathrm{cm}$ lens in a '$2f$' configuration onto a cooled CCD camera (Andor LUCA, Figure 2.19b), imaging the atoms' shadow.

The dip in transmitted intensity is proportional to the optical density of the atomic cloud. We take a 'probe' (P) image with the atoms present, a 'bright field' (B) image after the atoms have been scattered by the imaging light, and a 'dark field' (D) image with the imaging light turned off. The optical density (O.D.) is calculated as

$$\text{O.D.} = \log\left(\frac{P-D}{B-D}\right). \tag{2.2}$$

From this optical density we can calculate the number of atoms per image pixel, giving us a 'column density' [109]. From this we can construct a 2D image of the atom count per pixel column [98,99,109] using the equation

$$N_{\text{atoms}} = \frac{\text{Area under absorption curve}}{\sigma_{0\,(|F=2,m_F=2\rangle\rightarrow|F=3,m_F=3\rangle)}}, \tag{2.3}$$

where $\sigma_0 = 6\pi\lambda\!\!\!^{-}{}^2$ is the resonant cross-section, which is approximately $2.9 \times 10^{-13}\,\mathrm{m}^2$ for the $|F = 2, m_F = 2\rangle \rightarrow |F = 3, m_F = 3\rangle$ transition.

We can use the atomic distribution to infer information about the atomic momentum by projecting atomic motion into a position shift by allowing some time-of-flight before image capture. This allows us to make determinations of the ensemble's temperature to optimise the RF evaporation and hybrid optical dipole trap trajectories. It also allows us to separate the interferometer arms and output ports of a our atomic 'momentum interferometer' (see chapter 4).

2.4.4 Contrast interferometry

Contrast interferometry [49,110] shines a probe beam (shown in Figure 2.19f) onto the interference fringes of a BEC, reflecting a time-oscillating signal into a high-sensitivity photo-detector (for more details, chapter 5 is dedicated to this phenomenon). We attempted to detect this signal using three different photo-detector methods; (1) an amplified silicon photodiode, (2) an Avalanche Photodiode (APD), and (3) a Single Photon Counting Module (SPCM). The first attempt with an amplified silicon photodiode was unsuccessful because (a) the detector gain was too low, (b) our atomic reflectivity was lower at the probe detuning used, and (c) our signal collection optics did not sufficiently filter out background light, but we did observe phase-contrast signals with both the APD and SPCM setups. More information on the contrast interferometer can be found in Section 5.

Avalanche Photodiode

Our first successful phase contrast signal detection occured with a C12703-1 Series Hamamatsu Avalanche Photodiode Module (Figure 2.19c). We aligned the APD by triggering only the 'B' interferometer atom-optic beam, maximising the APD output signal with the final two mirrors before the APD module, then repeating with ever-lower beam powers.

We then triggered only the 'A' interferometer beam, and closed an adjustable aperture enough to remove the APD response to just the light reflected from the glass cell, whilst allowing the transmitted light from the 'B' arm to pass.

The output signal was transmitted via BNC cable to a Tektronix DPO3034 oscillisscope, which sent saved signal traces via USB to our lab computer. Our APD detection showed a contrast signal dominated by an exponential decay envelope. We discovered a strong relationship between the power of the probe laser beam and the decay constant of this envelope. To further extend our signal duration, we needed to reduce the power of the probe, but that required a more sensitive detector. For this reason we replaced the APD with a Single-Photon Counting-Module.

Single Photon Counting Module

We used an Excelitas SPCM-AQRH-14-FC Single-Photon Counting-Module (SPCM) as our photodetector. This module features a dark count rate of $\sim 250\,\mathrm{s}^{-1}$, a maximum stated count rate of $40 \times 10^{6}\,\mathrm{s}^{-1}$ and a detection efficiency of $\sim 70\,\%$ at $780\,\mathrm{nm}$, giving us a power sensitivity ceiling of 10 pW with an expected noise floor at 70 aW.

To protect the module's internal amplifier we installed protection shutters (Uniblitz LS2T2) into the interferometer arm 'B' in the focal-positioning telescope (Figure 2.17), and shortly before the SPCM fibre input coupling (Figure 2.19d) [99]. These shutters are controlled with a single digital line; the default position has the interferometer arm open and the SPCM protection shutter closed. Both shutters are flipped over a 120 µs window after the atom-optics are triggered and before the interferometer probe is triggered.

The SPCM output is a continuous count of photon detections sent via BNC. This 'click signal' is recorded via a National Instrument PCI-6713 interface card, then time-binned and processed using LabVIEW. Typical bin-widths used in this thesis are 4 µs.

Chapter 3

Atom-Optics

3.1 Introduction

In analogy with the optical elements of optical interferometers, the construction of an atom interferometer requires atom-optics to generate interferometer arms (typically, but not exclusively) by coherently manipulating the momentum of a cloud of ultracold atoms. Most interferometers accomplish this using resonant Raman transitions which effectively 'Bragg-reflect' the atomic wavefunction from a travelling wave of light [15, 111]. Since the velocity of this travelling wave is a free parameter, momentum kicks can be repeatedly imparted to a cloud of atoms by altering the relative detuning between the laser beams generating the lattice. This technique has been used to successfully impart several hundred recoils, generating interferometers with an extremely wide momentum separation [53, 112].

These advantages do come with a cost. The use of repeated pulses to impart many recoils places stringent requirements on pulse operation fidelity; a 99 % efficient operation performed a hundred times has a combined fidelity of only 37 %. Many experiments utilise 'blow away' pulses to remove these spurious atoms, reducing the particle counts. Given that the shot noise limited error in phase ($\Delta\Phi$) scales as $\frac{1}{\sqrt{N}}$ [113, 114], this is a problem. In order to avoid disturbing the 'other' interferometer arm, atoms must change internal state before the atom-optics can be applied. This opens the interferometer up to additional sources of phase-noise, such as Zeeman shifts due to local spatially-flat magnetic fields. Some experiments compensate with magnetic shielding [115] at the cost of experimental 'bulk', and Complex pulse sequences have successfully reduced this influence [116] at the cost of reduced interferometer contrast.

Off-resonant scattering is an alternative mechanism [117–119] which has been successfully used as a basis for atom-optics [49, 110, 120–123]. Here atoms do not change internal state, so Zeeman-induced shifts from spatially-flat magnetic fields induce no differential phase across interferometer modes. The scattering mechanism couples to multiple momentum states (compared to Bragg's single mode coupling), offering the potential for more complex optical elements such as multiport beam splitters [124, 125] within single complex pulse sequences, without the need for beam detuning ramps.

This comes at the cost of a more complicated system evolution between more momentum states. It is, for example, impossible to perform a perfect transfer to another momentum state with a single simple lattice pulse. Nevertheless, some work has successfully demonstrated that complex pulse sequences can generate high-efficiency atom beam splitters [121,123,126], and theory has been developed to very successfully describe the system evolution numerically [119, 121, 123]. In an attempt to generate atom-optics for contrast interferometry, we have combined these tools to generate a toolbox for high-fidelity arbitrary-state-targeting atom-optics.

3.2 Experimental setup

A 2D magneto-optical trap (MOT) is used to load a 3D MOT of $\sim 10^9$ ^{87}Rb atoms. The atoms are then transferred to a quadrupole magnetic trap and radio-frequency evaporative cooling is performed resulting in 4×10^7 atoms at a temperature of 30 μK [98,127]. The quadrupole trap is then relaxed from 200 G/cm to 15 G/cm, and the atoms loaded into a hybrid crossed optical dipole trap [107, 128] generated by a 1069 nm Ytterbium fibre laser with approximately 3 W per beam (Figure 3.1, wide blue beams.). Following 4 s of optical evaporative cooling during which the optical power in each beam is ramped exponentially to 0.25 W, we obtain a BEC of $\sim 10^5$ atoms with $>80\,\%$ purity and a thermal-fraction temperature of $\sim$100 nK [99].

The optical diffraction grating used in the construction of out atom-optics is generated using light from a single External-Cavity Diode Laser (ECDL), running approximately 4.5 GHz red detuned from the 780.24 nm F=2 $\rightarrow$ F'=3 transition on the ^{87}Rb D$_2$ $\left(5^2S_{1/2} \rightarrow 5^2P_{3/2}\right)$ line. This interferometry laser first passes through an acousto-optic modulator (AOM) which allows for the control of the optical power, and therefore intensity, at the BEC position. It is then split and mode-matched with the optical dipole trapping beams such that their foci overlap at the position of the BEC. This generates an optical lattice of spatially varying intensity along the X direction as indicated in Figure 3.1. The ground state energy level of the atoms is reduced in proportion to the light intensity due to the AC Stark shift, and so they experience a sinusoidal spatially varying potential landscape. Fine alignment is achieved by steering the interferometry beams to maximise the splitting of the BEC when a weak lattice is applied.

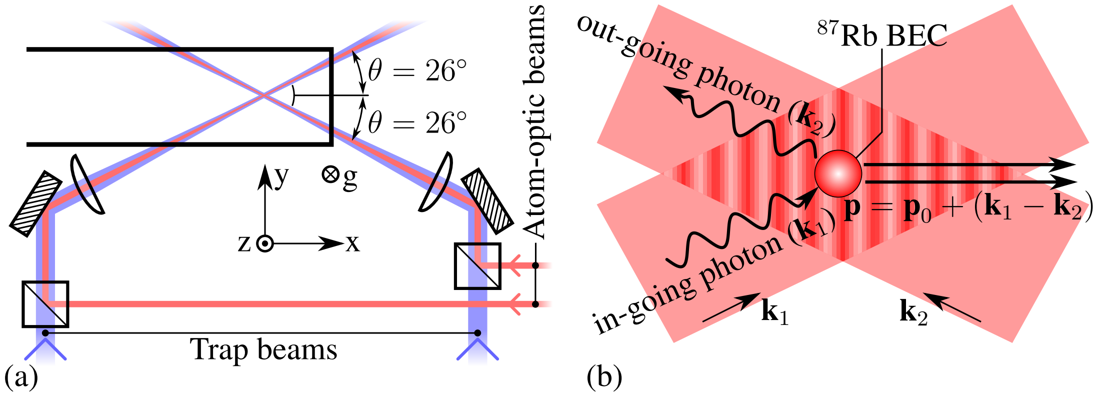

Figure 3.1: Experimental setup (a). A BEC of ^{87}Rb is formed using a crossed dipole laser trap at 1069 nm (blue). Mode-matched with the trap beams are two more beams at 780 nm, vertically polarised. These generate an optical lattice with an effective wavevector $\boldsymbol{k} = (\boldsymbol{k}_1 - \boldsymbol{k}_2)/2$ (b). Atoms can receive $2\hbar k_x$ momentum kicks by transferring photons from the $\boldsymbol{k}_1$ to $\boldsymbol{k}_2$ beams (or vice-versa) by absorption and stimulated emission.

3.3 Theory and system modelling

Our atom-optics are constructed using a standing wave of laser light, linearly polarised vertically. The AC Stark effect induces a periodic energy shift in the ground state of our atom cloud. Our model of this energy landscape follows that of Gadway *et al.* [119], with the Hamiltonian

$$\hat{H} = i\hbar\frac{\partial}{\partial t} = -\frac{\hbar^2}{2m}\frac{\partial^2}{\partial x^2} + V_0(t)\cos^2(k_x x)\,, \tag{3.1}$$

where k_x is the effective wave-vector of our optical lattice, and $V_0(t)$ the lattice depth at time t. The total wave function is considered a superposition of plane matter-waves with momenta $p = 2n\hbar k$

$$\psi(t) = \sum_n C_n(t)\, e^{i2nk_x x}. \tag{3.2}$$

If we include (3.1) and (3.2), our solution to the Schrödinger equation becomes an infinite set of coupled equations which describe the time evolution of the complex amplitude of each mode

$$\dot{C}_n(t) = -i\left[\frac{E_r^{(2)}n^2}{\hbar}C_n(t) + \frac{V_0(t)}{4\hbar}\Big(C_{n-1}(t) + 2C_n(t) + C_{n+1}(t)\Big)\right], \tag{3.3}$$

where $Er^{(2)} = 4\hbar^2k^2/2m_{87\mathrm{Rb}}$ is the two-photon recoil energy, and the complex amplitude $C_n = A_n\exp(i\Phi_n)$ describes the population $(P_n = A_n^2)$ and phase (Φ_n) of the n^{th} state with momentum $p = 2n\hbar k$. A derivation of this expression is shown in Appendix A.2.

Equation 3.3 shows an interaction between neighbouring modes which scales with lattice depth. Since the mode amplitudes C_n are complex, the nature of this interaction is *phase*-dependent. Together, these two properties of phase-sensitivity and tunable interaction strength allow for the creation of specific operations which coherently transform some input superposition of atomic momentum states into some other superposition of momentum states. These operations include our required atomic beam-splitters ($|p{=}0\hbar k\rangle \rightarrow [|p{=}{+}2n\hbar k\rangle + |p{=}{-}2n\hbar k\rangle]$), and atomic mirrors ($|{+}2n\hbar k\rangle \leftrightarrow |{-}2n\hbar k\rangle$). The phase-sensitivity alters the behaviour of each operation dependent on the relative phase between neighbouring modes which spatially overlap during the operation. In this way our atomic momentum splitters also behave as interferometric 'closing' pulses. A numerical simulation of equation (3.3) allows us to predict the behaviour of the system *without* losing the complex multi-level dynamics which appear with higher laser intensities.

We model our atom-optic operations numerically. We represent our stationary BEC atoms with the complex amplitude array $C_{n\neq 0,t=0} = 0, C_{n=0,t=0} = 1$. We model a specific pulse sequence using a 'pulse shape' function, modifying the time-dependent lattice depth $V_0\left(t\right)$ in response to a set of input pulse parameters. We then numerically integrate equation (3.3) with the initial state $C_{n,t=0}$, generating a series of new state vectors at required times $C_{n,t=t_1\ldots t_f}$. From these we can extract the relative mode populations ($P_n(t) = |C_n(t)|^2$) and phases ($\Phi_n(t) = \arg(C_n(t))$). Figure 3.2 shows the simulated variation in output population as the lattice depth of a 20 µs pulse is varied, alongside experimental measurements of the same.

Since the splitting mechanism has mirror-symmetrical along the x-direction, all atom-optic operations are also symmetrical in the absence of symmetry-breaking influences such as initial atomic velocities or accelerating gradient fields. An operation which performs the operation $|p{=}0\hbar k\rangle {\rightarrow} [|p{=}{+}2n\hbar k\rangle + |p{=}{-}2n\hbar k\rangle]$ will output a superposition of states with momentum $p = \pm 2n\hbar k$ and a common phase. And for ease of reading this output state is often referred to as $|\pm 2n\hbar k\rangle$ in the literature.

3.4 Model testing

3.4.1 Optical lattice calibration

Our laser pulses are controlled by an Acousto-Optical Modulator (AOM), with laser intensity in the first diffracted order proportional to the square of the input voltage to the AOM driver circuit. To reliably recreate pulse sequences we need a calibration method to relate the input voltage to lattice depth at the atoms. The sensitivity of the system's evolution to lattice depth makes this possible; a lattice 'pulse' of fixed duration traces out an evolution unique to that lattice depth.

If we measure the system evolution by recording mode population for pulses of various AOM voltages and fixed duration, we can overlay the simulated evolution and linearly scale the x-axes until we find the appropriate calibration factor (S) between AOM voltage squared (V^2) and lattice depth (L), shown in Figure 3.2. In this way, we use the atoms to construct a calibration $V = \sqrt{L/S}$, which directly maps our lab controls to the lattice depth at the atoms.

The BEC was scattered by our optical lattice with pulses of duration 20 µs with various AOM voltages. At each voltage the experimental sequence was run multiple times, with one absorption image per run. These absorption images were binned in the vertical direction to generate multiple integrated line profiles for each AOM voltage. These were then combined to generate a single integrated line profile at each AOM voltage with a mean line profile and error band. Thomas-Fermi profiles (equation 3.4) were fitted to the features in each profile and used to determine atom numbers in each momentum mode, and a Gaussian fit (equation 3.5), to the remaining pedestal of non-BEC thermal atoms. The use of a fit function allowed us to link the widths of the BEC features, so we could extract the unsplit BEC fraction from the surrounding thermal atoms.

$$n_{TF}(x) = n_{background} + n_0 \max\left(0, \left[1 - (\frac{x - x_0}{r_{TF}})^2\right]^2\right), \tag{3.4}$$

$$n_{Thermal}(x) = n_{background} + n_0 \exp\left(-\frac{-(x - x_0)^2}{2\sigma^2_{thermal}}\right), \tag{3.5}$$

The relative populations of each mode were then plotted, and the numerical simulation fitted to the populations by way of a scaling factor between the two x-axes. In this way, we calibrate our 'scale rule' which translates AOM voltage to lattice depth. (Figure 3.2)

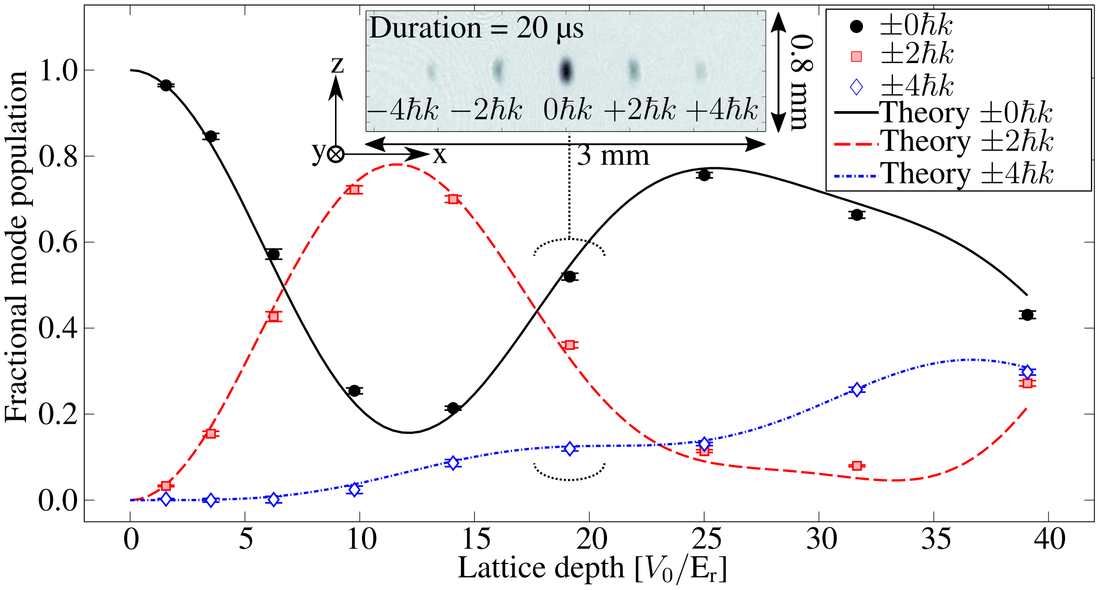

Figure 3.2: An example fitting of our numerical simulation (curves) to experimental data (points). Each vertical stack of data points corresponds to the relative mode populations after switching on an optical lattice for a duration of 20 µs at a given control voltage into an AOM driver circuit. Multiple absorption images are sampled at each voltage, with error bars derived from the spread in each population across the sample. A numerical simulation of equation (3.3) is fitted to this data, and from this we determine a linear 'scale rule' which relates our control voltage to lattice depth at the atoms. Inset is a sample absorption image obtained when the lattice AOM driver is set to 1.75 V, corresponding to a $\sim$ 20 $\mathrm{E_r}$ Lattice depth.

3.5 Optimising a high-fidelity atom-optic

3.5.1 Designing a first-order beam splitter pulse sequence

We aimed to construct a first-order beam splitter operation to transfer atoms from the $|p{=}0\hbar k\rangle$ to $|p{=}{+}2\hbar k\rangle{+}|p{=}{-}2\hbar k\rangle$ superposition state with high-efficiency. Spurious momentum states generate additional interferometer 'arms', confusing the interferometer fringes with more frequencies and phases. It is therefore important to ensure that only the interferometer arms required are actually populated. This is commonly achieved with blow-away pulses in interferometers with different internal states, but is not easily accomplished here. High-efficiency transfer operations are therefore extremely useful to Kapitza-Dirac based interferometers.

A 'perfect' $|0\hbar k\rangle \rightarrow [|{+}2\hbar k\rangle{+}|{-}2\hbar k\rangle]$ split operation requires that the Rabi oscillations of the $|0\hbar k\rangle$ and $[|{+}4\hbar k\rangle{+}|{-}4\hbar k\rangle]$ modes minimise when the $|{+}2\hbar k\rangle{+}|{-}2\hbar k\rangle$ oscillation maximises. In the simpler 'Bessel' models [111, 117, 119], there is no solution which exactly satisfies these conditions, and so no single constant intensity pulse can perform a complete population inversion [119, 121].

In previous work, Wu *et al.* developed a pulse sequence of two symmetric pulses of equal and constant lattice depth for identical durations separated by a 'wait' period of zero lattice depth. [121]. Hughes *et al.* later realised this experimentally with a peak efficiency of 99.5 % [123], and subsequently enhanced the pulse by filling the central wait period with a low level light field to force a subtle re-phasing of adjacent modes [126] (This pulse shape is shown in the inset of Figure 3.3). The low level field of the 'triple' pulse maintains coupling between modes, slightly shifting the Rabi oscillations until all three modes' oscillations coincide. This 'triple pulse' had a predicted efficiency of 99.9933 % [126]. Our optical lattice wavelength differs from that of the Sackett group [126], so the specific energies and time-scales in equation 3.3 also differ. This makes it impossible to simply reuse the optimised pulse-parameters.

Our numerical simulation can simulate the outcome of non-trivial pulse sequences, and so we set out to theoretically construct a pulse of the same shape and parameter space. The symmetrical pulse has two amplitudes and two durations, resulting in a four-dimensional parameter space. A brute force sweep through this space is computationally expensive and scales badly as pulse sequences increase in complexity. Instead, our simulation can be used as the core 'function' of an optimisation algorithm, iterating towards the highest fidelity transfers. We determined optimal mode transfer with the parameters $A_1 = 6.07\ E_r$, $T_1 = 26.6\ \mu s$, $A_2 = 0.52\ E_r$, $T_2 = 45.6\ \mu s$, where E_r is the effective recoil energy of our optical lattice, $\sim 2.02 \times 10^{-30}$ J. A sweep through the perpendicular planes which intersect at our optimised parameters is shown in Figure 3.3, where the A_1, A_2 plane is shown in (a), the T_1, T_2 plane shown in (b), and an example pulse shape shown in (c).

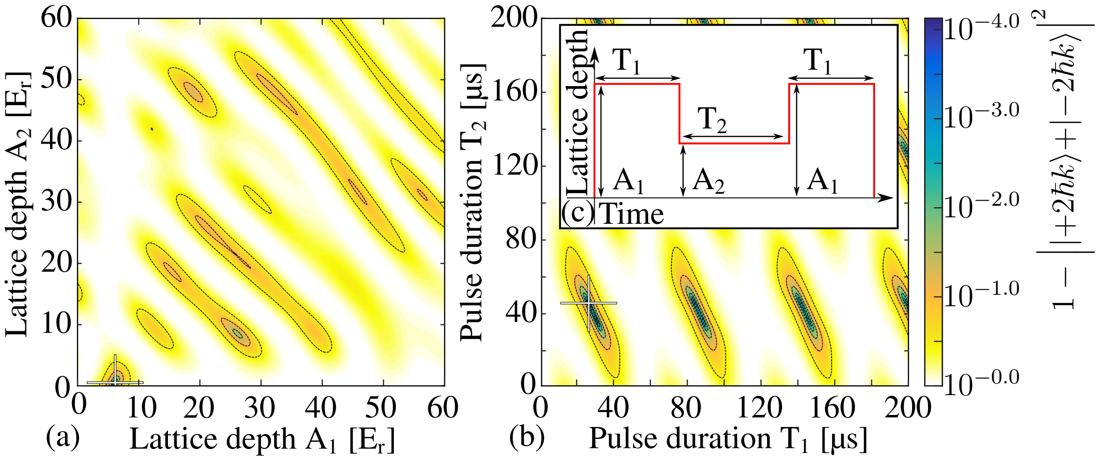

Figure 3.3: Numerical integration of equations to predict population transfer during an optical pulse sequence into the first order $\pm 2\hbar k$ momentum states. We found a maximum transfer at pulse parameters $A_1 = 6.07\ E_r$, $T_1 = 26.6\ \mu s$, $A_2 = 0.52\ E_r$, $T_2 = 45.6\ \mu s$. These plots represent the two perpendicular planes which cross at this point in the four dimensional parameter space. Inset: The 'triple-pulse' [126], simulated in the main figures. This pulse is similar to that described by Wu *et al.* [121] in that two symmetrical pulses of amplitude A1 and duration T1 and separation T2 are fired, except that the T2 time is 'filled' with a low-level light field.

3.5.2 Testing first-order splitting efficiency

The high-efficiency pulse sequence was tested with a Bose-Einstein condensate (BEC) of $\sim 10^5$ atoms. The system was calibrated as described in section 3.4.1, and the lattice controls set to our numerically optimised $|p{=}0\hbar k\rangle \rightarrow [|p{=}+2\hbar k\rangle + |p{=}-2\hbar k\rangle]$ sequence; a 'triple-square pulse' with parameters $A_1 = 6.07\ E_r$, $T_1 = 26.6\ \mu s$, $A_2 = 0.52\ E_r$, $T_2 = 45.6\ \mu s$.

The same absorption imaging process was then used to measure the relative populations in each momentum state. An example 50-shot average of the optimised beam splitter pulse is shown in Figure 3.4, which shows the transfer of atoms from the BEC to the $|+2\hbar k\rangle + |-2\hbar k\rangle$ state with a fidelity of $99.97\ \pm\ 0.03\ \%$ (that is, with an average $99.97\ \pm\ 0.03\ \%$ of our atoms in the desired momentum state). Because the scattering mechanism imparts a quantised momentum shift, the BEC clouds with $|p| = 2\hbar k$ retain their spatial shape and expansion rates as they propagate. If we fit the BEC components with a common Thomas-Fermi width and independent amplitudes, we can therefore computationally extract the population of atoms in the $p = 0\hbar k$ state from the thermal pedestal. Our example shown in Figure 3.4 fits an unsplit $p = 0\hbar k$ BEC remnant at $(2.29 \pm 18.46) \times 10^1$ atoms, and the combined split $|p = +2\hbar k\rangle + |p = -2\hbar k\rangle$ populations with $(8.70 \pm 0.44) \times 10^4$ atoms, giving a transfer efficiency from the initial BEC at $(99.97 \pm 0.03)\%$.

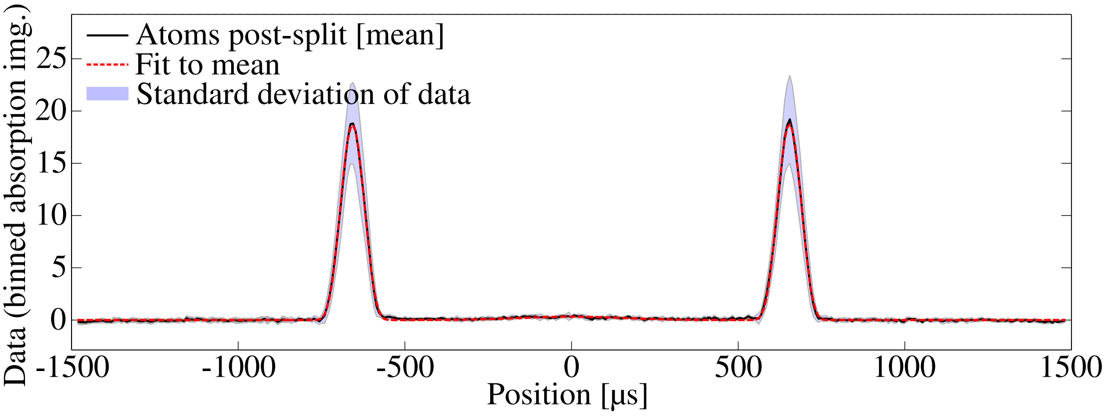

Figure 3.4: Experimental results of an optimised $|p{=}0\hbar k\rangle \rightarrow [|p{=}{+}2\hbar k\rangle{+}|p{=}{-}2\hbar k\rangle]$ pulse sequence. 50 absorption images were taken, then integrated in the vertical direction to create 50 integrated line profiles. These line profiles were used to generate a mean line profile with associated standard deviation at each horizontal position. A fit to this 'mean±error' profile allows the digital separation of the thermal background and BEC. Transfer efficiency is taken as the fraction of atoms in the central narrow BEC peak transferred to the outer moving modes. We fit a total atom number of $(9.04 \pm 0.44) \times 10^4$, a thermal background of $(3.37 \pm 0.40) \times 10^3$ $[3.73\ \%]$, a remaining $p = 0\hbar k$ BEC fraction of $(2.29 \pm 18.46) \times 10^1$ $[0.03\ \%]$, and a transferred $|p{=}{+}2\hbar k\rangle{+}|p{=}{-}2\hbar k\rangle$ fraction of $(8.70 \pm 0.44) \times 10^4$ $[96.24\ \%]$. If we assume that only the BEC atoms have sufficiently narrow momentum width to effectively transfer, we have a $|p{=}0\hbar k\rangle \rightarrow [|p{=}{+}2\hbar k\rangle{+}|p{=}{-}2\hbar k\rangle]$ transfer efficiency of $(99.97{\pm}0.03)\ \%$.

Correlation with theory was examined by performing the optimised pulse sequence, truncated at some time. This was done at numerous points throughout the duration of the pulse, and the relative populations compared with theory predictions at each time. Errors were calculated using shot-to-shot variation in the absorption images, specifically variation in atom number and cloud width returned by our fitting algorithm. If the relative population numbers are labelled $P_{-4}, P_{-2}, P_0, P_{+2}, P_{+4}, P_{thermal}$, then the fractional mode populations are calculated like

$$F_{\pm 2} = \frac{(P_{-2} + P_{+2})}{(P_{-4} + P_{-2} + P_0 + P_{+2} + P_{+4})}, \tag{3.6}$$

and the fractional uncertainty of the mth mode $\delta F_{\pm 2m}$ calculated by taking partial derivatives of this equation, like

$$(\delta F_{\pm 2})^2 = \sum_n \left(\frac{\partial F_{\pm 2}}{\partial P_{2n}} \delta P_{2n} \right)^2, \tag{3.7}$$

where n corresponds to the 'order' of the scattered mode with momentum $p = 2n\hbar k$. Figure 3.5 shows this comparison, with excellent agreement between theory and experiment, where the theoretical curves shown are a numerical simulation using the optimised pulse sequence and zero free parameters. The data shown in Figure 3.4 are represented here by the final data point occurring at time $t = 98.8$ µs.

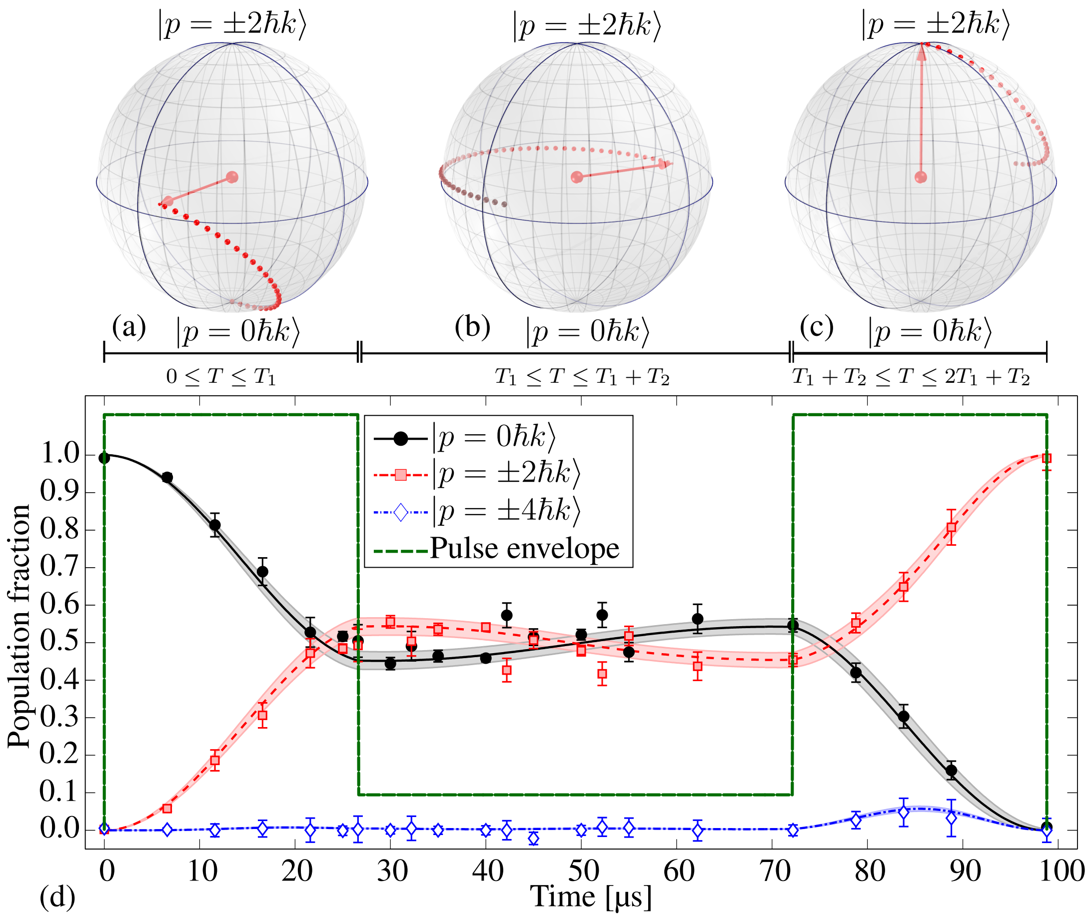

Figure 3.5: A schematic of the optimised pulse sequence is shown (a,b,c). By extracting the population and phase from the numerical simulation, the state evolution during each subsection of the pulse sequence can be calculated. Below this (d) is a comparison of theoretical and experimental results of the optimised beam splitter pulse. Solid (dashed, dash-dotted) lines show the optimised evolution of the $|0\hbar k\rangle$ ($[|+2\hbar k\rangle + |-2\hbar k\rangle]$,$[|+4\hbar k\rangle + |-4\hbar k\rangle]$) populations through the pulse sequence. The bands surrounding each theory line show the spread in population evolution when subjected to a $\pm 4\%$ variation in laser intensity. Circles (squares, rhombi) show the experimentally measured populations at each time.

3.6 Reflection pulse efficiency

If the aforementioned Kapitza-Dirac pulse which transfers atoms from the $|0\hbar k\rangle$ to the $|{+2\hbar k}\rangle{+}|{-2\hbar k}\rangle$ state is an 'atomic beam-splitter', then the remaining atom-optical element required for an atom interferometer is the 'atomic mirror'. In contrast to the off-resonant splitter pulses, we accomplish reflection with the use of Blackman pulses [129]. These possess a far wider frequency width, and therefore couple off-resonant states less efficiently. Our numerical optimisation predicts a theoretical maximum $|{-2\hbar k}\rangle{\leftrightarrow}|{+2\hbar k}\rangle$ transfer efficiency of $\sim\ 99.9\,\%$ with a Blackman pulse of duration 164 µs and maximum lattice depth 12.2 $\mathrm{E_r}$, shown in Figure 3.6.

There are some caveats. It is important to note that our simulation predicts that a fraction of the $|0\hbar k\rangle$ mode population is temporarily transferred to the $|{+2\hbar k}\rangle{+}|{-2\hbar k}\rangle$ mode during the pulse. This means that we should expect the $|+2\hbar k\rangle{\leftrightarrow}|-2\hbar k\rangle$ reflection pulse to impart a phase shift on any $|0\hbar k\rangle$ atoms, but not to beam-split them. We should expect to see intensity-dependent phase shifts which are *not* cancelled between the stationary $|0\hbar k\rangle$ and moving $[|{+2\hbar k}\rangle{+}|{-2\hbar k}\rangle]$ interferometer arms.

Additionally, we refer to this Blackman pulse as a mirror here, though it is important to note that the operation is actually a $\delta p = \pm 4\hbar k$ momentum shift, and only transfers atoms between resonant states if the initial momentum $\delta p \approx 0$. In the case that some momentum δp is present, we instead perform a $|{-4\hbar k} + \delta p\rangle{\leftrightarrow}|{+4\hbar k} + \delta p\rangle$ operation.

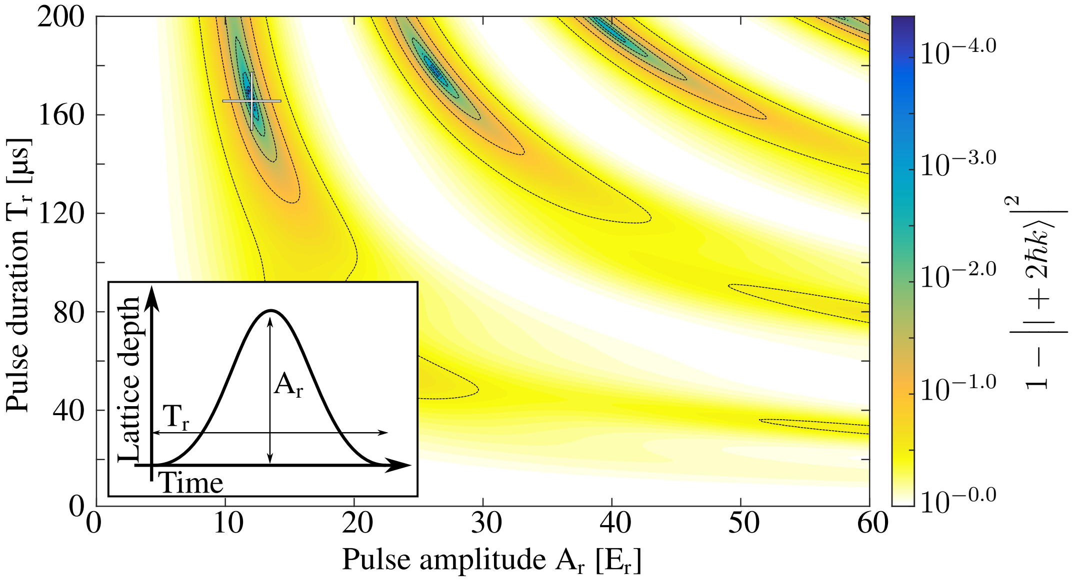

Figure 3.6: Theoretical simulation of the parameter space of our Blackman pulse. Mapped is the efficiency of the $|{-2\hbar k}\rangle \to |{+2\hbar k}\rangle$ transfer. Our optimisation algorithm finds a maximum transfer efficiency of $99.9\ \%$ at pulse duration 164 µs, lattice depth 12.2 Er. Higher transfer efficiencies are located at longer pulse durations, as might be expected with a resonant transition.

An atom interferometer can be constructed with only two splitter pulses. The first pulse creates the interferometer arms, and the second interferes the phase accumulated between the separating (but still partially overlapping) arms. The contrast of this interferometer drops rapidly as the arms separate. By extending the arm 'length' to a millisecond or so, the contrast is negligible. In this configuration, interference fringes are dependent almost entirely on a reflection pulse fired in the centre of the interferometer, and so we can use the fringe contrast to estimate the reflection pulse efficiency.

The efficiency of our reflection was tested by performing an interferometer sequence: Atoms were split with a single pulse of constant lattice depth ~ 12 E$_\mathrm{r}$ and duration ~ 10 µs into a superposition of approximately $\sqrt{\frac{1}{4}}|-2\hbar k\rangle + \sqrt{\frac{1}{2}}|0\hbar k\rangle + \sqrt{\frac{1}{4}}|+2\hbar k\rangle$. These atoms were allowed to propagate for 700 µs, and a Blackman mirror pulse fired. A closing 'splitter' pulse was then fired after some time, and the system was again allowed to evolve. After 60 ms, the relative mode populations were measured via absorption imaging. The interferometer 'closing time' was varied, and the evolution of the modes' relative populations plotted. Figure 3.7 shows these interferometer fringes with a peak contrast of 86 %, placing a lower bound on the mirror pulse efficiency of 86 %, with similar efficiencies detected with increased time of flight to separate the reflected and un-reflected modes [99].

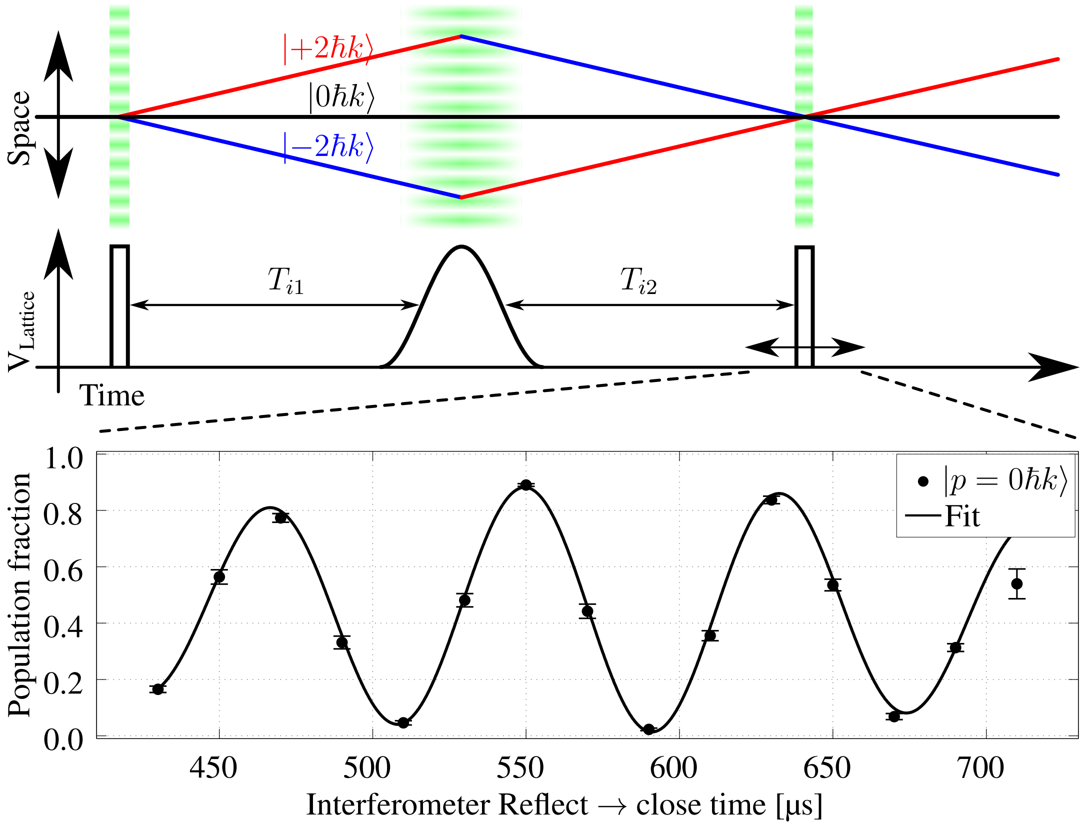

Figure 3.7: Experimental three-arm momentum interferometer. A splitter pulse is configured to push the atoms into a superposition $|\psi\rangle \approx \sqrt{1/4}|{-2\hbar k}\rangle + \sqrt{1/2}|0\hbar k\rangle + \sqrt{1/4}|{+2\hbar k}\rangle$. After 700 µs a Blackman reflection pulse is fired. Some time T_{i2} is allowed to pass, and an identical splitter pulse fired to close the interferometer. Five shots were recorded at each time T_{i2}, and the fractional population of the $|0\hbar k\rangle$ mode determined. The phase accumulation during the T_{i2} period originates in the kinetic energy of the moving atoms, building up a phase shift of $4\omega_{\text{recoil}}t$. We sample this phase by firing a second beam splitter pulse, ‘closing’ the interferometer and projecting the phase into an oscillation of mode population between the $|p{=}0\hbar k\rangle$ and $[|p{=}{+2\hbar k}\rangle + |p{=}{-2\hbar k}\rangle]$ modes. The frequency of these fringes is therefore four times the effective lattice recoil frequency, and can be used to determine the fine structure constant. Here, the contrast of 86 % implies that our reflection pulse has an efficiency of at least 86 %.

3.7 Second order atom-optics

3.7.1 Second order atom beam-splitting

A significant advantage of entirely-Bragg based systems (such as the Biraben atom interferometer, which imparts thousands of recoil kicks [50]) is that it is relatively simple to induce a larger recoil momentum, because the asymmetry of the interferometer allows detuning between the atom-optic beams as a free parameter. This means that the optical lattice can be swept at any desired speed. The system can then be repeatedly given $2\hbar k$ momentum kicks as desired. This in turn leads to a much faster phase accumulation. A significant drawback here is the requirement that the atom-optics target only one 'arm' of the interferometer, since this is typically done with an RF pulse to transfer a fraction of the atoms into a different internal state. Zeeman shifts from local spatially-constant magnetic fields introduce additional sources of phase noise, mandating the use of considerable magnetic shielding [115]. Whilst some procedures have been demonstrated to reduce the duration of these magnetically-sensitive periods, they do not entirely eliminate the susceptibility and reduce signal-to-noise. [116]

Our system has the advantage that the internal state of our atoms is never changed, removing sensitivity to such magnetic field 'offsets' entirely. Conversely, we lose the ability to impart repeated momentum kicks by simply sweeping our atom-optic beam detuning, instead performing transfers in a single operation. Nevertheless, we need to increase the momentum width of our interferometer arms to make competitive measurements.

An increase of even a single recoil ($n = 2$) offers a number of advantages: Firstly, the increased kinetic energy in the interferometer arms increases the rate of phase accumulation, giving us four times the phase for a given interrogation time. Secondly, the phase-contrast interferometer uses an evolving cloud of BEC atoms as a mirror for a readout beam. Since every reflected photon imparts a momentum kick onto an atom in this cloud, every successful photon 'bounce' reduces the reflectivity of the cloud, so the readout signal decays over time, effectively limiting our readout to a finite number of photons. A four-fold increase in fringe frequency will give us four times as many fringes in our signal. Thirdly, we then also have four times as many zero crossings in our fringe signal for our fitting algorithm.

The first-order splitter pulse uses the differing phase oscillation rates of our different modes to simultaneously suppress the population in the $|0\hbar k\rangle$ and $|\pm 4\hbar k\rangle$ modes, forcing all atoms into the $|\pm 2\hbar k\rangle$ mode. If we can accomplish the same feat by suppressing the population of the $|0\hbar k\rangle$, $|\pm 2\hbar k\rangle$ and $|\pm 6\hbar k\rangle$ modes, we will have created a second-order atomic beam splitter, with twice the momentum shift at $|\pm 4\hbar k\rangle$.

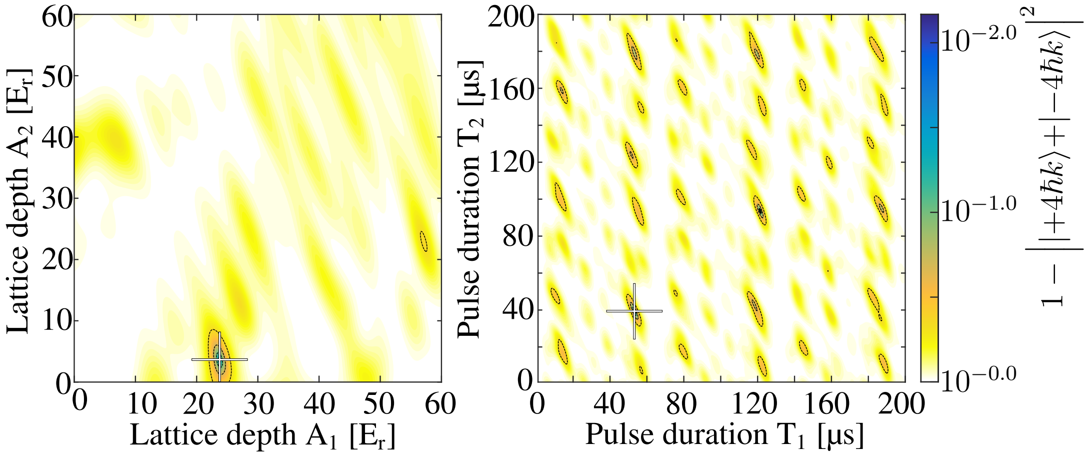

Figure 3.8: Numerical simulation of an optimised $|0\hbar k\rangle \rightarrow [|+4\hbar k\rangle + |-4\hbar k\rangle]$ beam splitter pulse sequence. The colour scale represents relative fraction of atoms which end up in the target $[|+4\hbar k\rangle + |-4\hbar k\rangle]$ state. These two plots represent the perpendicular 2D sweeps in parameter space, crossing at the optimal point located at A$_1$ = 23.7 E$_r$, T$_1$ = 53.3 µs, A$_2$ = 3.59 E$_r$, T$_2$ = 39.0 µs.

Figure 3.8 shows a scan of the $|0\hbar k\rangle \rightarrow [|+4\hbar k\rangle + |-4\hbar k\rangle]$ parameter space surrounding a point of high transfer efficiency. The transfer of atoms to the $[|+4\hbar k\rangle + |-4\hbar k\rangle]$ state requires that atoms are ‘funnelled’ through the intermediate $[|+2\hbar k\rangle + |-2\hbar k\rangle]$ state. The increased path increases the system dynamics’ complexity considerably (Figure 3.9). The difficulty here comes from the relative phase velocities of the different modes; whilst the $[+2\hbar k\rangle + |-2\hbar k\rangle]$ splitter pulse uses the phases of each mode to suppress two modes, here we suppress three. Instead of a direct transfer, we must allow atoms to ‘slosh’ back and forth between modes, until the phases align such that a minimum in the $|0\hbar k\rangle$ and $[|+2\hbar k\rangle + |-2\hbar k\rangle]$ occurs simultaneously.

A secondary result of the more complex dynamics is that the ‘islands’ of high transfer efficiency are smaller in parameter space, so the tolerance for error in laser intensity and pulse timing / shape is significantly smaller. We found that whilst a shot-to-shot laser intensity variation of $< \pm 10\%$ is sufficient to maintain a $> 98\%$ transfer to $[|+2\hbar k\rangle + |-2\hbar k\rangle]$ efficiency, that tolerance drops to $< 1\%$ when transferring to $[|+4\hbar k\rangle + |-4\hbar k\rangle]$.

Additionally, it can be seen that whilst the use of a mid-pulse low level light field is not strictly necessary in the $[|+2\hbar k\rangle + |-2\hbar k\rangle]$ case, it is essential to reach a high-efficiency transfer to $[|+4\hbar k\rangle + |-4\hbar k\rangle]$.

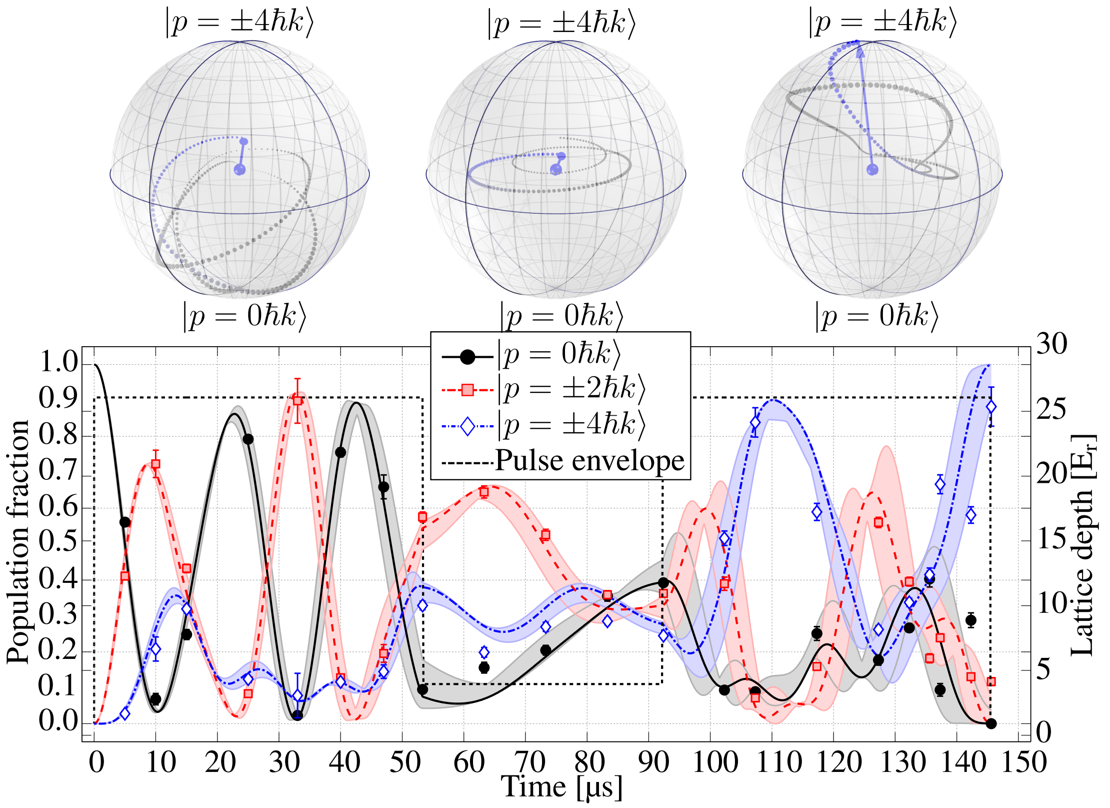

Figure 3.9: The testing of a second-order beam splitter pulse. Here we attempt to push atoms entirely into the $[|+4\hbar k\rangle+|-4\hbar k\rangle]$ superposition state, using destructive interference to suppress the population in other modes. We compare the theoretical prediction of our numerically optimised pulse with experimental data. Theory curves for the $|0\hbar k\rangle$ ($|+2\hbar k\rangle+|-2\hbar k\rangle$,$[|+4\hbar k\rangle+|-4\hbar k\rangle]$) modes are depicted by the solid (dashed, dash-dotted) lines, with surrounding bands representing the variation in population due to a ±4 % range in laser intensity. Experimental data for the $|0\hbar k\rangle$ ($[|+2\hbar k\rangle+|-2\hbar k\rangle]$,$[|+4\hbar k\rangle+|-4\hbar k\rangle]$) modes are shown as circles (squares, rhombi). Each data point represents the mean relative population across ten experimental runs. The standard deviation of each individual mode's population (calculated by considering the uncertainty in the height and width of fit as shown in Figure 3.4) is propagated through the calculations used to determine relative populations to set error bars.

3.7.2 Second order atom mirrors

As with the first-order case, we need mirrors capable of reflecting atomic wave-packets with high efficiency so that we can maintain interference contrast when our interferometer 'arm length' is greater than a few hundred microseconds. The optimal $|-4\hbar k\rangle \rightarrow |+4\hbar k\rangle$ transfer with a Blackman pulse is found with an amplitude of A_1 = 43.2 Er and duration T_1 = 131.6 µs.

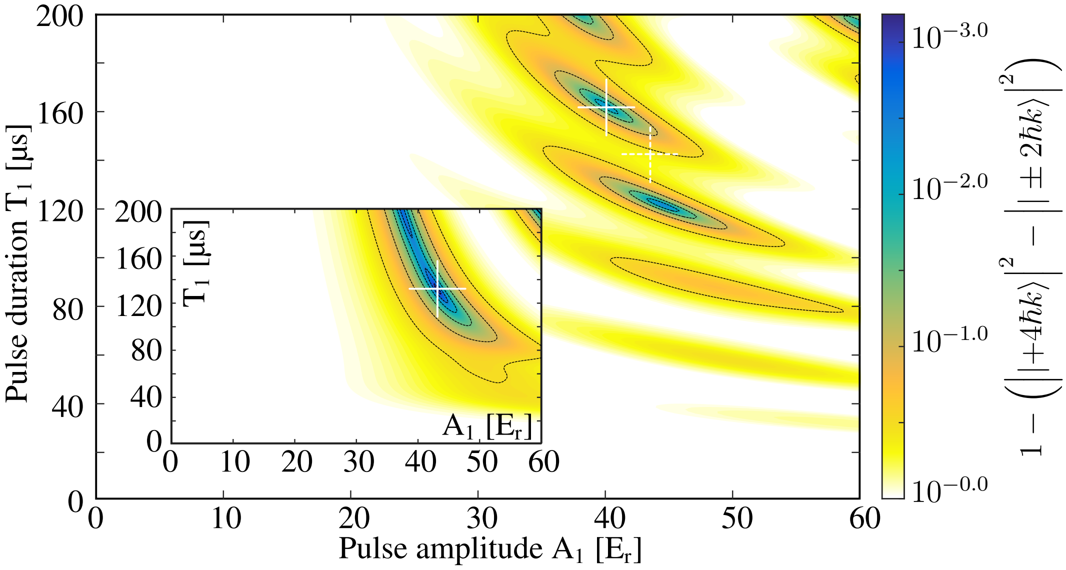

Figure 3.10: Numerical simulation of the parameter space of a Blackman pulse, this time targeting a $|-4\hbar k\rangle \rightarrow |+4\hbar k\rangle$ momentum transfer. Inset here is the fraction of atoms in the $|+4\hbar k\rangle$ momentum state after the pulse, without consideration for the influence of the pulse on stationary atoms. We generate a 'fitness' score for each parameter set by numerically simulating the pulse sequence's $|0\hbar k\rangle \rightarrow [|+2\hbar k\rangle + |-2\hbar k\rangle]$ fidelity, and subtracting it from the $[|-4\hbar k\rangle \leftrightarrow |+4\hbar k\rangle]$ operation efficiency. In this way we generate a pulse which offers the optimum *interferometry* reflection pulse. Whilst the point of maximum reflection occurs at A_1 = 43.2 E_r, T_1 = 131.6 µs, the marginally less efficient point at A_1 = 40.1 E_r, T_1 = 162 µs results in negligible disturbance of the stationary atoms, and so was chosen over the other.

Unlike the first order case, where the optimal $[|-2\hbar k\rangle \rightarrow |+2\hbar k\rangle]$ pulse also happens to not alter the momentum of the $|0\hbar k\rangle$ packet, the second order reflection requires that we find a compromise. To find a pulse which optimises the reflection efficiency of the $[|-4\hbar k\rangle + |+4\hbar k\rangle]$ atoms (Figure 3.10, inset) whilst minimising the influence on $|0\hbar k\rangle$ atoms, the numerical simulation was expanded to simulate the pulse effect on both the $[|-4\hbar k\rangle + |+4\hbar k\rangle]$ and $|0\hbar k\rangle$ states, and a fitness function created which included both output states in a new 'goodness' metric (Figure 3.10, main). This enhanced optimisation generated a 'compromise' pulse with parameters A_1 = 40.1 E_r, T_1 = 162 µs. This new pulse has a theoretical $[|-4\hbar k\rangle \rightarrow |+4\hbar k\rangle]$ transfer efficiency of 99.6 %, whilst transferring only 0.3 % of the $|0\hbar k\rangle$ atoms to other states.

3.8 Targeted operations

3.8.1 Four-port quatter

A major advantage of this mechanism is the ability to target arbitrary population states, creating the atom-optical analogues of multi-port beam splitters (1 beam into 2 out), tritters (1 beam into 3 out), quatters (1 beam into 4 out), etc. In Section 6.3 we discuss our desire for an atom-optic beam-quatter that performs the operation $|0\hbar k\rangle \rightarrow \frac{1}{2}\left(|-4\hbar k\rangle + |-2\hbar k\rangle + |+2\hbar k\rangle + |+4\hbar k\rangle\right)$. We numerically found a candidate triple-rectangular pulse with parameters A_1 = 17.5 E_r, T_1 = 15.3 μs, A_2 = 8.2 E_r, T_2 = 20.0 μs. An example binned absorption image of this pulse sequence captured experimentally is shown in Figure 3.11, where we find a population transfer efficiency of $P(0\hbar k) = 3.4 \pm 0.7\,\%$, $P(\pm 2\hbar k) = 54.2 \pm 1.6\,\%$, $P(\pm 4\hbar k) = 42.4 \pm 1.5\,\%$.

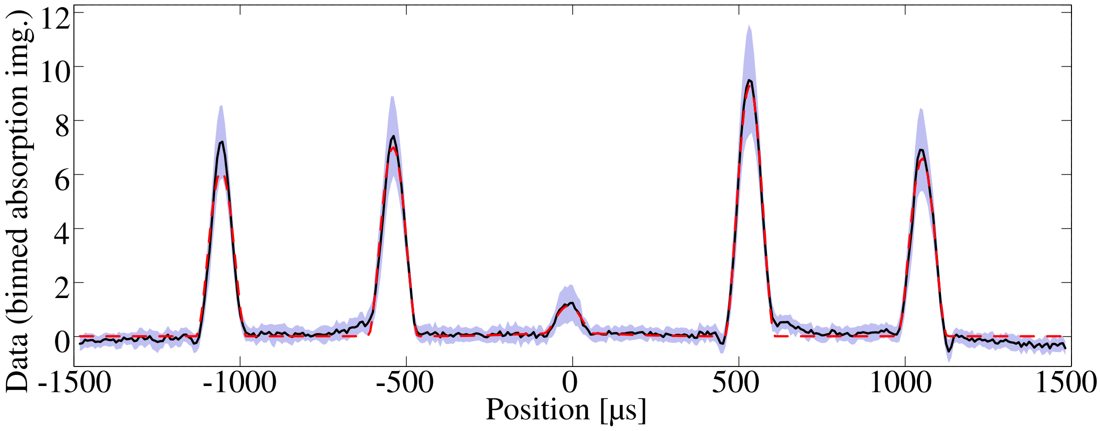

Figure 3.11: A binned absorption image of an experimental four-port beam-quatter operation that splits an incoming $|0\hbar k\rangle$ packet into a superposition $\frac{1}{2}\left(|-4\hbar k\rangle + |-2\hbar k\rangle + |+2\hbar k\rangle + |+4\hbar k\rangle\right)$. The experimental sequence was performed ten times, capturing ten absorption images. Some time of flight has been allowed to project the different momentum states within the atomic wavefunction into spatially-separated clouds. The solid black line represents the mean binned atomic density, and the surrounding shaded area represents the density encapsulated by ± one standard deviation. The dashed red line corresponds to a fit of five Thomas-Fermi profiles, used to extract atomic population within each momentum state.

Chapter 4

Atom Interferometry

4.1 Introduction

Atom interferometry exploits the wave-nature of atoms to perform precision measurement by mapping something difficult to measure (atomic phase) to something relatively easy to measure (like the number of atoms in a cloud). As an interfering medium, atoms exhibit some significant differences to photons, such as sensitivity to AC and DC electric and magnetic fields, gravitational fields, and strong sensitivity to inertial forces [15]. In addition, the low velocity of ultra-cold atoms in the laboratory frame of reference increases interaction times in a small volume. A classic example of this enhanced interaction duration is in Sagnac interferometry, where the reduced particle velocity increases the angle of rotation the interferometer undergoes whilst each particle is within the system, increasing sensitivity-per-particle [33, 99].

It is for these reasons that atom interferometry has been proposed as a tool for applied physics such as gravitational sensing [41], prospecting [37], gravitational wave astronomy [130], rotational sensing [33, 115], and for inertial navigation [42]. The mechanism, however, also offers a window into fundamental physics, such as measurement of Newton's gravitational constant G [47], the equivalence principle [48], and the fine-structure constant α [50–53].

Our ability to generate atom-optical elements with arbitrary output states allows for the construction of multiple interferometer geometries with various numbers of arms. Broadly speaking, we can build interferometers to perform homodyne measurements, in which two arms of initially-equal momenta have their phase differentially shifted by some field, such that information about that field is encoded in the resulting interferometer phase shift. Alternatively, we can perform a heterodyne measurement by building an interferometer with arms of different momenta, where the difference in energy between arms leads to a measurement of interferometer recoil frequency [49, 110].

4.2 Optical interferometry

4.2.1 Optical phase

The key principle in all interferometry is that of phase. Figure 4.1 shows a beam of light incident on an optical interferometer. Here the wave has been drawn frozen in time, where the waveform represents the cosine of the light phase at each position in space.

The light wave undergoes reflection when it encounters a sudden shift in refractive index at the boundary of each optic it encounters. It is important to note that this reflection obtains a π phase shift *only if* the refractive index transitions from a low-to-high value. Layered dielectric optical elements rely on this principle to enhance their reflectivity: each low-to-high refractive index boundary is separated by a $\lambda/2$ optical path length difference, and halfway (in terms of optical path length; the difference in refractive index ensures that this point is *not* spatially halfway) between these interfaces occurs the high-to-low interface. Whilst the reflections from the low-to-high interfaces all acquire a π phase shift and therefore constructively interfere, the reflections from the high-to-low interfaces do not, and so their spatially-dislocated wavefronts *also* interfere constructively with those from the other interfaces.

If such a dielectric element is illuminated from the reverse side, the low-to-high and high-to-low boundaries exchange places in the optical path length, and the phase of the reflection is altered by π. Beam cubes are commonly constructed of two right-angled glass prisms, where one of the joined faces has been coated in some dielectric coating [131], and so exhibit the same 'face-selectivity' in terms of reflection phase.

For our hypothetical interferometer in Figure 4.1, this means the light obtains a π phase shift when it encounters each mirror, but only obtains a π phase shift if it is reflected after entering the 'front' face of a beam-cube (marked with a dot).

Counting up the phase shifts along all arms, we see that the upper (red) arm gains π phase during reflection from the first beam cube (a), π phase from reflection from the mirror (c), and 0 phase as it reflects to both outputs (A) and (B) from the last beam cube (d). Likewise, the lower (blue) arm gains 0 phase as it passes through the first beam cube, π phase as it reflects from the first mirror (b), and 0 phase as it passes through the last beam cube (d) to output (B), but gains π phase as it reflects from the last beam cube (d) to output (A).

Suppose that we have some input light wave of intensity $I_{\text{in}} = |E_{\text{in}}(t)|^2$, with frequency $\omega = 2\pi f$, and a well-defined phase $\phi = \omega t$ into our interferometer. This wave is split by the first beam splitter (a) into two arms (upper 'u', and lower 'l'), one of which acquires some additional phase $\Delta\phi$. A second beam splitter (d) is encountered by both arms, each of which is again split into two output ports (A and B), giving us four output terms,

$$\begin{aligned} E_{\text{Au}}(t) =&\ E_{\text{in}}(t)\tfrac{1}{\sqrt{4}}e^{i\omega t+\Delta\phi+\pi+\pi}\ , \\ E_{\text{Al}}(t) =&\ E_{\text{in}}(t)\tfrac{1}{\sqrt{4}}e^{i\omega t+\pi+\pi}\ , \\ E_{\text{Bu}}(t) =&\ E_{\text{in}}(t)\tfrac{1}{\sqrt{4}}e^{i\omega t+\Delta\phi+\pi+\pi}\ , \\ E_{\text{Bl}}(t) =&\ E_{\text{in}}(t)\tfrac{1}{\sqrt{4}}e^{i\omega t+\pi}\ , \end{aligned} \tag{4.1}$$

where the light intensity output at the ports A and B are the squares of the superpositions of the respective E-fields, so at port A we have the light intensity

$$\begin{aligned} I_{\text{A}}(t) =&\ \left|E_{\text{Au}}(t) + E_{\text{Al}}(t)\right|^2 \\ \dots =&\ \left|E_{\text{in}}\tfrac{1}{\sqrt{4}}\left(e^{i\omega t} + e^{i(\omega t+\Delta\phi)}\right)\right|^2 \\ \dots =&\ E_{\text{in}}(t)^2\tfrac{1}{4}\left(e^{i(\omega t-\omega t)} + e^{i(\omega t-\omega t-\Delta\phi)} + e^{i(\omega t-\omega t+\Delta\phi)} + e^{i(\omega t+\Delta\phi-\omega t-\Delta\phi)}\right) \\ \dots =&\ E_{\text{in}}(t)^2\tfrac{1}{2}\left(1 + \tfrac{e^{i\Delta\phi}+e^{-i\Delta\phi}}{2}\right) \\ \dots =&\ E_{\text{in}}(t)^2\tfrac{1}{2}\Big(1 + \cos\left(\Delta\phi\right)\Big) \\ \dots =&\ E_{\text{in}}(t)^2\cos^2\left(\tfrac{\Delta\phi}{2}\right) \end{aligned}\ , \tag{4.2}$$

and likewise at port B our output looks like

$$\begin{aligned} I_{\text{B}}(t) =&\ \left|E_{\text{Bu}}(t) + E_{\text{Bl}}(t)\right|^2 \\ \dots =&\ \left|E_{\text{in}}(t)\tfrac{1}{\sqrt{4}}\left(e^{i\omega t} + e^{i(\omega t+\Delta\phi+\pi)}\right)\right|^2 \\ \dots =&\ E_{\text{in}}(t)^2\tfrac{1}{4}\left(e^{i0} + e^{i(\omega t-\omega t-\Delta\phi-\pi)} + e^{i(\omega t-\omega t+\Delta\phi+\pi)} + e^{i0}\right) \\ \dots =&\ E_{\text{in}}(t)^2\tfrac{1}{2}\left(1 + \tfrac{e^{i\Delta\phi}e^{i\pi}+e^{-i\Delta\phi}e^{-i\pi}}{2}\right) \\ \dots =&\ E_{\text{in}}(t)^2\tfrac{1}{2}\Big(1 - \cos\left(\Delta\phi\right)\Big) \\ \dots =&\ E_{\text{in}}(t)^2\sin^2\left(\tfrac{\Delta\phi}{2}\right) \end{aligned}\ , \tag{4.3}$$

where the total output intensity $I_{\text{total}}(t) = I_{\text{A}}(t) + I_{\text{B}}(t) = I_{\text{in}}(t)$. We can therefore model the output probabilities per photon of the interferometer with a pair of waves $P(\text{A}) = \cos^2(\Delta\phi/2)$, $P(\text{B}) = \sin^2(\Delta\phi/2)$, again with $P(\text{total}) = P(\text{A}) + P(\text{B}) = P(\text{in}) = 1$. With no interferometer bias, this reduces to $P(\text{A}) = 1$, $P(\text{B}) = 0$, and all light leaves the interferometer via the right-side port.

Measurements are performed by introducing a differential phase shift $\Delta\phi$ between the two interferometer arms. This could be a small shift in the optical path length of the upper arm, or some material of a different refractive index, for example. This phase shift alters the interference at the output ports, mapping the phase shift to a shift in the balance of light intensity at the output ports.

The sensitivity of a measurement therefore depends on the ability to resolve changes in the light intensity at the output, which is greatest where some shift in interferometer phase maps to the largest change in output population, i.e. when $\mathrm{d}P(\text{A})/\mathrm{d}\phi$ is maximised. The gradient is maximised when the output at both ports is equal, corresponding to a differential phase of $\pi/2$. For this reason interferometers are often biased with a $\pi/2$ phase shift, such that any perturbation due to measurement $\Delta\phi$ results in the greatest shift in light intensity at the output ports.

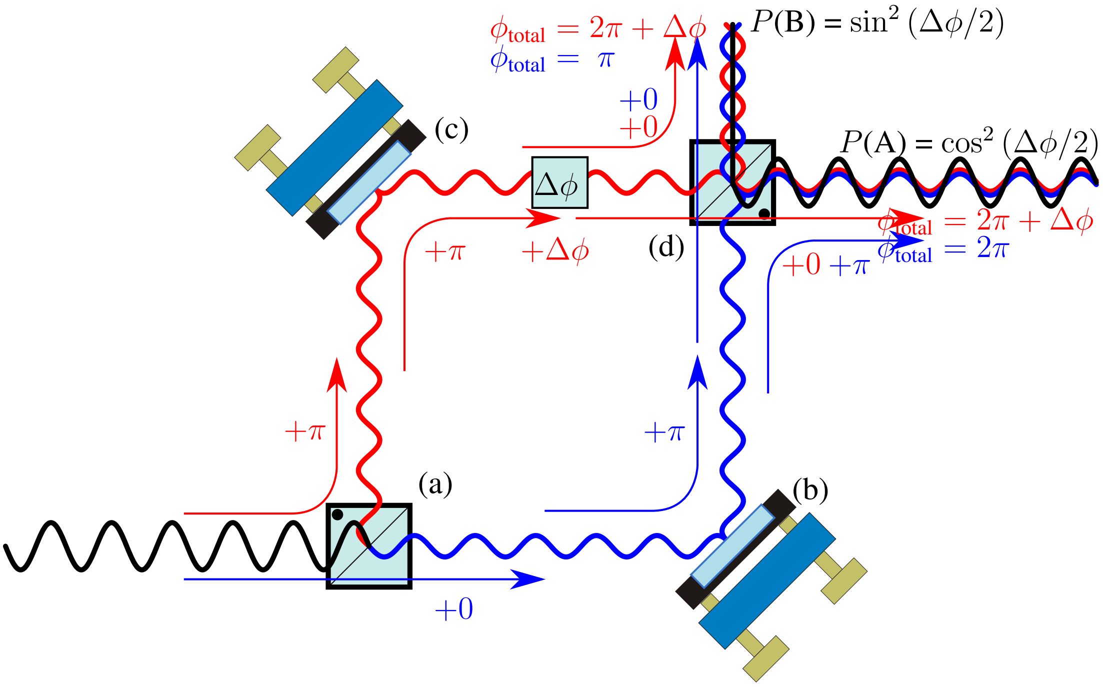

Figure 4.1: An example light-based Mach-Zehnder interferometer. An incoming wave is coherently split into two beams by a non-polarising beamsplitter (NPBS) (a), opening the interferometer into two spatially separated arms. This first partial reflection occurs when the refractive index along the beam path rises from a low to a higher value, resulting in a π phase shift in the reflected arm. Both arms accumulate another π phase shift when reflected by mirrors (b) and (c). A second NPBS closes the interferometer, crucially imparting a π phase shift *only* to the lower arm's reflection which enters the 'front' face of the beam-cube, leading to an overall 'phase-slip' between the interferometer arms of π. This induces a complementarity between the output ports A and B, where completely constructive interference at port A necessarily implies completely destructive interference at port B. Small differential phase shifts in the interferometer arms are then mapped to the output populations $P(\text{A})$ and $P(\text{B})$, mapping the light's phase information to output intensity.

4.2.2 Sagnac interferometry

Figure 4.2 shows an optical Mach-Zehnder interferometer used as a rotation sensor. This implementation is known as a Sagnac interferometer [132]. Here, the finite speed of light allows the orientation of the interferometer to change between the moment that light encounters the first beam-splitter and the moment that it hits the second. This change in orientation acts as an effective differential shift in the optical path length of each interferometer arm. If the arc that the beam-splitters circumscribe during a rotation is plotted as a circle, the speed of their motion is given by $v_{\text{rot}} = \boldsymbol{\Omega}_{rot} r$, where r is the radius of the interferometer ring and $\boldsymbol{\Omega}_{rot}$ the rotation rate of the interferometer in radians per second.

The phase shift of the Sagnac interferometer is determined by the projection of the rotation rate into a displacement of the closing beam-splitter when the light reaches that point in the interferometer. The phase shift is therefore determined by the path that the light takes in the interferometer. If the light is guided along a circular path (for example, by an optical fibre as is the case in optical ring-gyroscopes) the time delay between light hitting the first and second beam splitter is determined by the half-circumference of this circle, $t = \pi r/c$, where c is the speed of light.

The effective shift in the path length of one arm is then given by the position shift of the closing beam-splitter during this time delay, $\delta x = v_{rot} t = \boldsymbol{\Omega}_{rot} \pi r^2/c$. The phase shift in one arm is just this spatial shift in units of the light wavelength,

$$\delta\phi = 2\pi\frac{\delta x}{\lambda} = 2\pi\frac{\boldsymbol{\Omega}_{\text{rot}} \cdot (\pi r^2)}{\lambda c} = \frac{2\pi}{\lambda c}\boldsymbol{A} \cdot \boldsymbol{\Omega}_{\text{rot}}, \tag{4.4}$$

where $\boldsymbol{A}$ is the area enclosed by the circle circumscribed by the interferometer's optical path.

If we instead consider the 'square' optical path geometry shown in Figure 4.2, we need to address some subtleties. In the limit $\Omega_{\text{rot}} \to 0\,\text{rad}\,\text{s}^{-1}$, the path length from the first beam-splitter to the first mirror is $\sqrt{2}r$, and from there to the closing beam-splitter also $\sqrt{2}r$, giving us a delay time along the optical path of $t = 2\sqrt{2}r/c$. The subtlety here is that the motion of the beam-splitters and mirrors during a rotation is *not* co-linear with the direction of the light propagation, but at an angle of $45°$. We therefore see a change in path length as the *projection of the movement of each element along the optical path*, such that $\delta x = v_{\text{rot}} t/\sqrt{2} = 2\Omega_{\text{rot}} r^2/c$. As with the circular optical geometry above, our phase shift in one interferometer arm is therefore

$$\delta\phi = 2\pi\frac{\delta x}{\lambda} = 2\pi\frac{\boldsymbol{\Omega}_{\text{rot}} \cdot (2r^2)}{\lambda c} = \frac{2\pi}{\lambda c}\boldsymbol{A} \cdot \boldsymbol{\Omega}_{\text{rot}}, \tag{4.5}$$

where $\boldsymbol{A}$ is now the area of the *square* enclosed by the optical path, $|\boldsymbol{A}| = 2r^2$.

Since any rotation causes an equal and opposite spatial-shift in the interferometer arms, any such $+\delta\phi$ shift in one arm necessarily induces a $-\delta\phi$ shift in the other. With a total phase shift of $\Delta\phi = +\delta\phi - -\delta\phi = 2\delta\phi$, our rotation-induced phase shift is therefore

$$\Delta\phi = \frac{4\pi}{\lambda c}\boldsymbol{A} \cdot \boldsymbol{\Omega}_{\text{rot}}, \tag{4.6}$$

known as the Sagnac phase [15, 132]. This configuration gives us a rotation sensitivity

$$\frac{\partial \phi}{\partial \boldsymbol{\Omega}_{\text{rot}}} = \frac{4\pi \boldsymbol{A}}{\lambda c} , \tag{4.7}$$

which offers two simple methods by which the phase shift from a given rotation rate can be enhanced by modifying the $\boldsymbol{A}$ term. This $|\boldsymbol{A}| = \pi r^2$ term is derived from the optical path difference in the interferometer, which can be increased either by (1) increasing the number of times each particle passes around the loop so that $|\boldsymbol{A}| = N\pi r^2$ for a linear scaling $\phi \sim N$ [133], and (2) increasing the radius of the interferometer so that $|\boldsymbol{A}| = \pi(r = r_{\text{old}} + \delta r)^2$ for a quadratic scaling $\phi \sim r^2$.

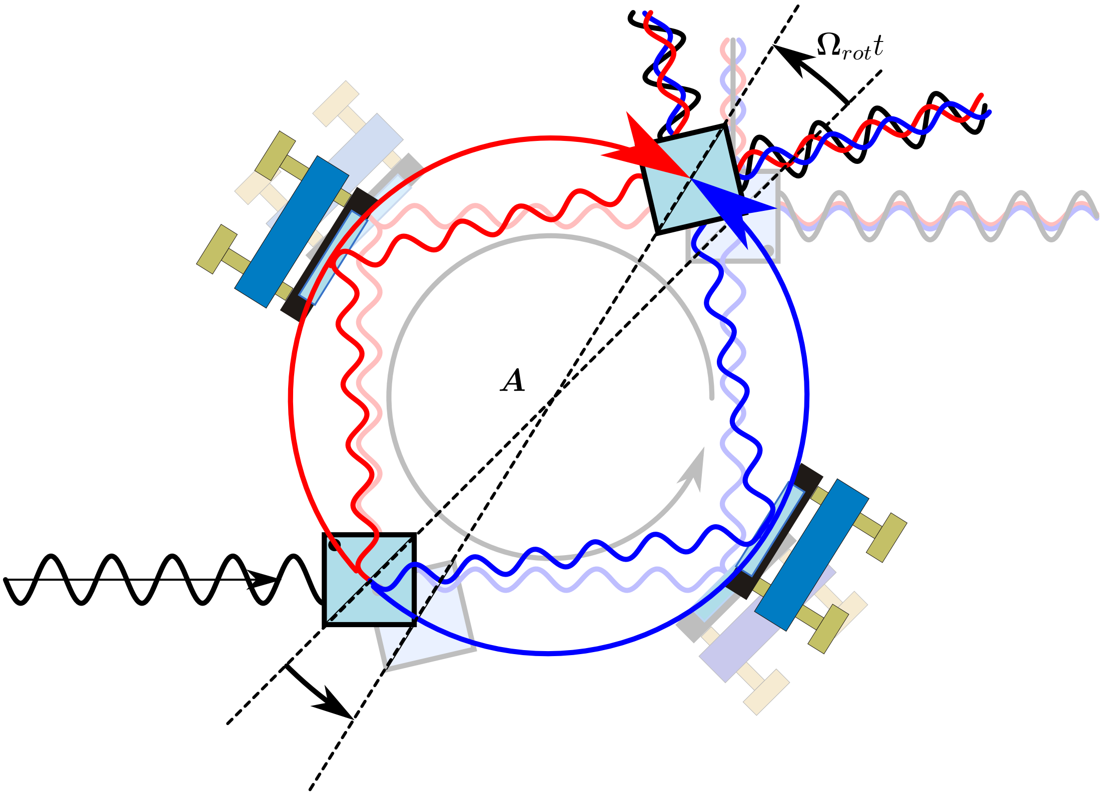

Figure 4.2: The Sagnac interferometer uses the finite travel-time of the interfering medium in its arms to generate a rotation-dependent phase-shift at the output ports. An incoming coherent light beam is split into two interferometer arms. Whilst the light travels along paths towards outputs A and B, the interferometer rotates, slightly shortening the arm A and lengthening arm B, generating a differential phase shift at the closing beam cube. The compact geometry allows for the interferometer arms to ‘wrap’ around the paths many times, increasing the enclosed area and the resulting rotation-induced phase-shift.

4.3 Atom interferometers

4.3.1 Enhanced sensitivity

The enhanced interaction mentioned in Section 4.1 is derived from this sensitivity Sagnac interferometers have to particle wavelength [33, 99, 134]. A more general expression for the Sagnac phase is in terms of particle energy E

$$\phi_{\text{Sagnac}} = \frac{4\pi}{hc^2} E \boldsymbol{A} \cdot \boldsymbol{\Omega}_{\text{rot}} \,, \tag{4.8}$$

which we can use to determine a phase shift for a Sagnac atom interferometer

$$\phi_{\text{atom}} = \frac{2m_{\text{atom}}}{\hbar} \boldsymbol{A} \cdot \boldsymbol{\Omega}_{rot} \,. \tag{4.9}$$

Our experimental apparatus uses ^{87}Rb atoms with a velocity on the order of 10 mm/s and a mass of 1.4×10^{-25} kg [104], giving us an energy-per-atom of 8.0×10^{-30} J, with cooling lasers targetting the D_2 line at 780 nm. If we somewhat arbitrarily use these values to compare Sagnac phase sensitivity with equations 4.4 and 4.9, we can estimate an enhancement factor

$$\frac{\Delta\phi_{\text{atom}}}{\Delta\phi_{\text{photon}}} = \frac{2m_{\text{atom}}}{\hbar}\frac{\lambda_{\text{photon}}c}{4\pi} = 5.1 \times 10^{10} \,, \tag{4.10}$$

when using an atom Sagnac interferometer over an optical Sagnac interferometer. It is important to note that this enhancement is per particle, and that it is typically far easier to increase photon flux than it is atom flux [99]. Our experiment typically generates a Bose-Einstein condensate of 2.0×10^5 atoms with an experimental cycle time of 30 s, giving a particle flux of 17×10^3 atoms s^{-1} [98, 99]. A corresponding photon flux at 780 nm is obtained with only 4.2 aW of laser power. For comparison, the sensitivity of the Sagnac interferometer with respect to particle number scales as

$$\frac{\partial\phi}{\partial N} \propto \sqrt{N} \,. \tag{4.11}$$

To generate a comparable interferometer sensitivity, we require something on the order of $2.0 \times 10^5 \times (5.1 \times 10^{10})^2 = 1.0 \times 10^{32}$ photons over each 30 s cycle, for a photon rate of $3.3 \times 10^{30}\,\text{s}^{-1}$. With a wavelength of $780\,\text{nm}$, each photon has an energy of

$$E_{\text{phot}} = hc/\lambda = 6.63 \times 10^{-34}\,\text{J}\,\text{s} \times 3.00 \times 10^8\,\text{m}\,\text{s}^{-1}/780\,\text{nm} = 2.55 \times 10^{-19}\,\text{J} \,. \tag{4.12}$$

This implies a required laser power of $0.85\,\text{TW}$ to match the sensitivity of our BEC cycle through photon number alone. A real experiment would more likely make up only part of the sensitivity with particle number, and rely on increasing the enclosed interferometer area by increasing the radius r ($\delta\phi \propto r^2$) and by guiding the photons around the interferometer path N times before recombining ($\delta\phi \propto N$).

4.3.2 Phase shifts

Whilst the first atom interferometers used material gratings as diffractive optics [15] and some recent experiments rely on matter-matter boundary effects [135], most modern atom interferometers make use of optical gratings [15]. As with optical interferometers, these atom-optics impart phase shifts in the atoms they interact with. In the case of Bragg interferometers the atom-optic lasers are detuned such that they are two-photon resonant between a state with zero momentum $|1, p = 0\hbar k\rangle$ of an atom, and a second state with momentum $|2, p = +2\hbar k\rangle$ of the same atom.

The transfer of the atomic wavefunction between the two states using a pulsed optical grating is controlled with two parameters; the pulse duration t, and the two-photon Rabi frequency Ω. The analysis of [136] shows that the complex amplitudes of the two modes are well approximated by a two level system, given by

$$\begin{bmatrix} c_1(p = 0\hbar k, t) \\ c_2(p = 2\hbar k, t) \end{bmatrix} = \begin{bmatrix} \Lambda_c & -i\Lambda_s e^{-i\phi_L} \\ -i\Lambda_s^* e^{i\phi_L} & \Lambda_c \end{bmatrix} \begin{bmatrix} c_1(p = 0\hbar k, t_0) \\ c_2(p = 2\hbar k, t_0) \end{bmatrix}, \tag{4.13}$$

where $\Lambda_c = \cos(|\Omega| t/2)$ and $\Lambda_s = (\Omega/|\Omega|)\sin(|\Omega| t/2)$. The value of $|\Omega| t$ determines the phase of our Rabi oscillation between the two states,

$$\Lambda_{\pi/2} = \frac{1}{\sqrt{2}} \begin{bmatrix} 1 & -ie^{-i\phi_L} \\ -ie^{i\phi_L} & 1 \end{bmatrix}, \; \Lambda_\pi = \begin{bmatrix} 0 & -ie^{-i\phi_L} \\ -ie^{i\phi_L} & 0 \end{bmatrix}. \tag{4.14}$$

It is from this that the 'π' and '$\pi/2$' pulse derive their name, with the $\pi/2$ pulse being a 'beam-splitter' Rabi oscillation that performs the transition

$$\begin{aligned} |1, p = 0\hbar k\rangle &\rightarrow \frac{1}{\sqrt{2}}\Big(|1, p = 0\hbar k\rangle + e^{-i\pi/2}e^{-i\phi_L}|2, p = 2\hbar k\rangle\Big), \\ |2, p = 2\hbar k\rangle &\rightarrow \frac{1}{\sqrt{2}}\Big(e^{-i\pi/2}e^{+i\phi_L}|1, p = 0\hbar k\rangle + |2, p = 2\hbar k\rangle\Big), \end{aligned} \tag{4.15}$$

and the π pulse acting as a mirror that performs the transitions

$$\begin{aligned} |1, p\rangle &\rightarrow e^{-i\pi/2}e^{-i\phi_L}|2, p + 2\hbar k\rangle, \\ |2, p + 2\hbar k\rangle &\rightarrow e^{-i\pi/2}e^{+i\phi_L}|1, p\rangle\ . \end{aligned} \tag{4.16}$$

It can be seen from these equations that each interaction imparts a $\pi/2$ phase shift to the interacting atomic mode.

Figure 4.3 shows a Mach-Zehnder atom interferometer constructed from three optical grating pulses in a $\pi/2$, π, $\pi/2$ configuration. Drawn alongside each interferometer arm (red upper u and blue lower d) are the contributions to the phase as the atoms travel to the output ports (upper 2, and lower 1). If we sum these phase contributions along the four possible paths the atoms can travel, we obtain the phases

$$\begin{aligned}
\phi_{2u} =&\ +\phi_A - \pi/2 - \phi_B - \pi/2 + \phi_C - \pi/2 + 4\omega_\mathrm{r} T_1 \\
=&\ +\phi_A - \phi_B + \phi_C - 3\pi/2 + 4\omega_\mathrm{r} T_1 \\
\phi_{2l} =&\ 0 + \phi_B - \pi/2 + 0 + 4\omega_\mathrm{r} T_2 \\
=&\ +\phi_B - \pi/2 + 4\omega_\mathrm{r} T_2 \\
\phi_{1u} =&\ +\phi_A - \pi/2 - \phi_B - \pi/2 + 0 + 4\omega_\mathrm{r} T_1 \\
=&\ +\phi_A - \phi_B - \pi + 4\omega_\mathrm{r} T_1 \\
\phi_{1l} =&\ 0 + \phi_B - \pi/2 - \phi_C - \pi/2 + 4\omega_\mathrm{r} T_2 \\
=&\ +\phi_B - \phi_C - \pi + 4\omega_\mathrm{r} T_2\ ,
\end{aligned} \tag{4.17}$$

where the phase ϕ_{ij} is the phase accumulated by an atom that followed arm j and output port i. These phases are analogous to those of the optical interferometer we considered in equation 4.1. As in that example, the probability of a particle (in this case an atom) exiting the interferometer at a given port is determined by the interference of these phase terms at each output,

$$\begin{aligned}
\phi_2 = \phi_{2u} - \phi_{2l} =&\ (\phi_A - \phi_B + \phi_C - 3\pi/2 + 4\omega_\mathrm{r} T_1) - (\phi_B - \pi/2 + 4\omega_\mathrm{r} T_2) \\
=&\ (\phi_A - 2\phi_B + \phi_C + 4\omega_\mathrm{r}(T_1 - T_2) - \pi) \\
\phi_1 = \phi_{1u} - \phi_{1l} =&\ (\phi_A - \phi_B - \pi + 4\omega_\mathrm{r} T_1) - (\phi_B - \phi_C - \pi + 4\omega_\mathrm{r} T_2) \\
=&\ (\phi_A - 2\phi_B + \phi_C + 4\omega_\mathrm{r}(T_1 - T_2))\ .
\end{aligned} \tag{4.18}$$

If the interferometer timings T_1 and T_2 are equal the $4\omega_\mathrm{r} T$ terms cancel, and the output port probabilities go to

$$\begin{aligned}
P(1) =&\cos^2\Big(\phi_A - 2\phi_B + \phi_C\Big), \\
P(2) =&\cos^2\Big(\phi_A - 2\phi_B + \phi_C - \pi\Big) = \sin^2\Big(\phi_A - 2\phi_B + \phi_C\Big),
\end{aligned} \tag{4.19}$$

resulting in a pair of conjugate output ports where the output population depends on the phase of the optical grating during pulses A, B and C.

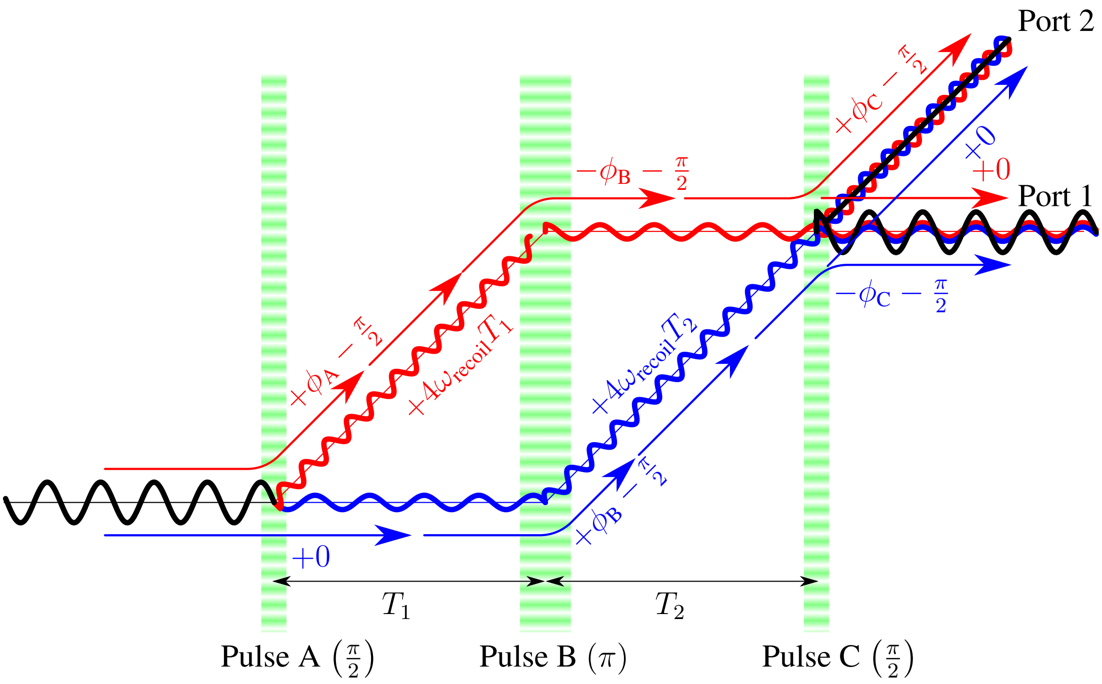

Figure 4.3: An example Mach-Zehnder atom interferometer. Here the interfering medium is an atomic ensemble, and the interferometer 'arms' are comprised of the states $|1, p = 0\hbar k\rangle$ and $|2, p = +2\hbar k\rangle$ in a two-level atomic system. The 'beam-splitter' and 'mirror' optics are formed from optical gratings, where the counter-propagating lasers are detuned such that the optical lattice moves at a velocity $v = \hbar k/m$, causing atoms to Bragg diffract between the $|1, p = 0\hbar k\rangle$ and $|2, p = +2\hbar k\rangle$ states.

We could then rotate the interferometer during an experimental sequence to perform a Sagnac rotation measurement where the inertia of the atoms causes their position in the final optical pulse to change, altering the output interferometer phase. The slower motion of the atoms allows the interferometer to rotate more during the sequence, increasing the shift in optical path length and therefore accumulated phase.

4.4 Interferometer geometry

The tunable off-resonant atom-optics described in Chapter 3 allows for the creation of interferometers with various geometries. Our interferometers have been symmetrical in momentum around the laboratory frame of reference, because our atom-optic beams share a common frequency, but a detuning of the atom-optic lasers would allow for asymmetrical momentum distributions.

4.4.1 Two-arm interferometry

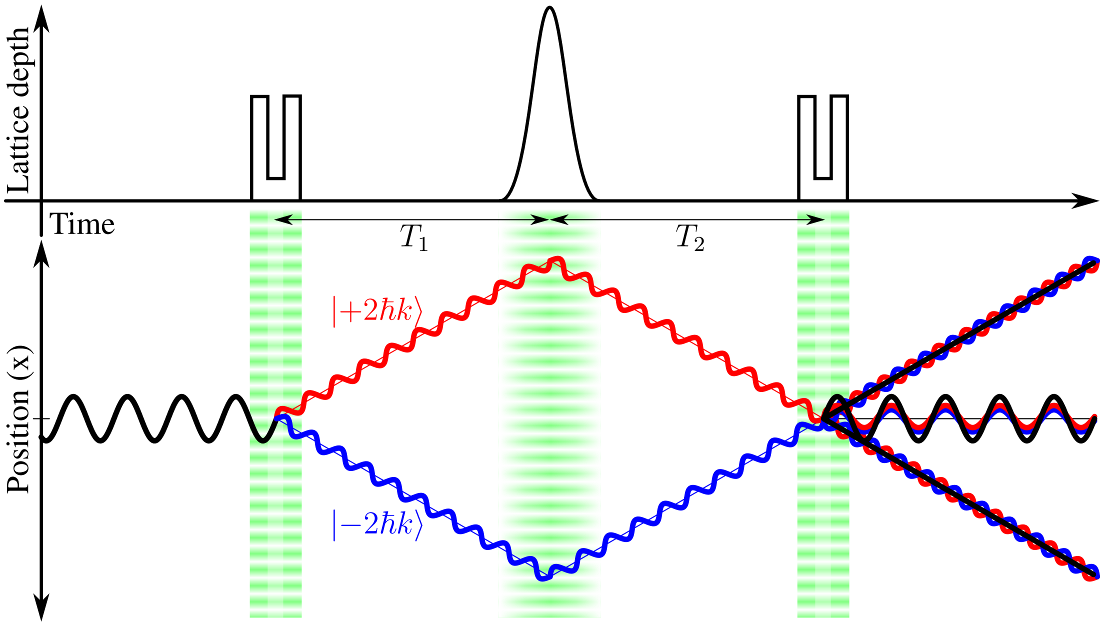

Figure 4.4: The use of off-resonant composite pulses described in Section 3.5 allows us to generate a ‘two-arm’ atom interferometer like that shown in Figure 4.3, but with no change in internal state. Here both arms spend equal times moving, so the output is independent of recoil phase regardless of interferometer timings.

We can approximate the interferometer described in Figure 4.3 using the beam-splitter $|0\hbar k\rangle \rightarrow [|{+2\hbar k}\rangle + |{-2\hbar k}\rangle]$ atom-optics described in Figure 3.5. Figure 4.4 shows this ‘two-arm’ geometry. Here both interferometer arms are travelling during times T_1 and T_2, so the accumulating $\int 4\omega_{\mathrm{recoil}}\,\mathrm{d}t$ phase is common to all arms and rejected at the interferometer output.

We use a Blackman pulse [129] to perform a reflection of the $[|{+2\hbar k}\rangle + |{-2\hbar k}\rangle]$ momentum states to re-overlap the atomic packets at time $T = T_1 + T_2$. This interferometer configuration has the advantage that there is no change in the internal state of the atoms, so Zeeman-induced phase shifts from homogenous magnetic fields are subject to common-mode rejection at the output. We therefore have less need of magnetic shielding, which has been crucial in Bragg-based experiments [33, 115].

Without an applied phase-shift, we naively calculate a complete return of atoms to the $|0\hbar k\rangle$ mode after the third interferometer pulse. Figure 4.5 shows the experimental output of an unbiased interferometer, where we instead observe a slow decay from a $P(0\hbar k) \approx 1$ result at short durations to $P(0\hbar k) \approx 0.3$ after 3 ms. With a Thomas-Fermi radius in the X-direction $r_{\mathrm{TF}_X} \approx 15\,\mu\mathrm{m}$ and a wavepacket velocity of $v_X \approx 10\,\mathrm{mm\,s^{-1}}$, we expect the $[|{+2\hbar k}\rangle + |{-2\hbar k}\rangle]$ clouds to spatially separate after a time $t \approx 1.5\,\mathrm{ms}$.

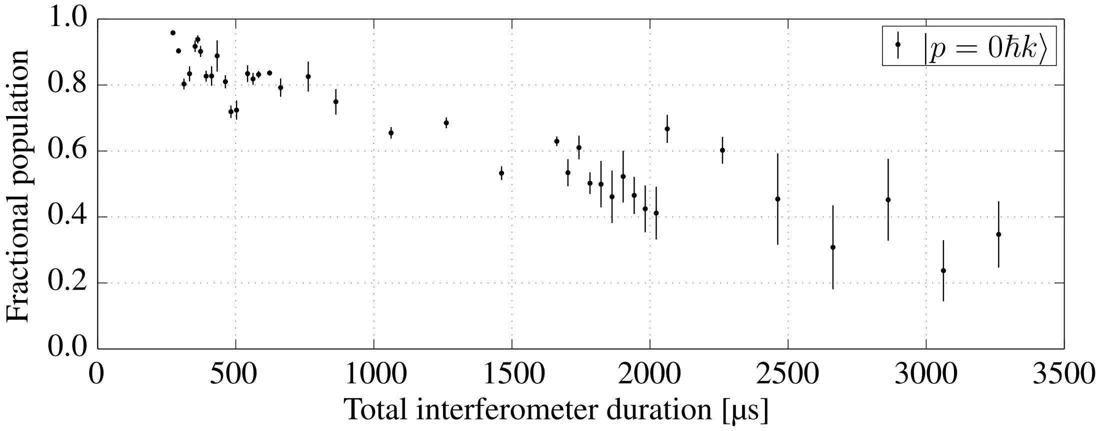

Figure 4.5: Experimental off-resonant two-arm Mach-Zehnder interferometer with no external fields applied. Each point represents at fractional population of the $|0\hbar k\rangle$ momentum state after a two-arm interferometer with no applied gradient field, for a given total interferometer duration (from the beginning of the first pulse to the end of the last). The error bars around each point are the standard deviation of five experimental runs. In principle this interferometer configuration should return a fractional population P$(0\hbar k) = 1$ at all times.

4.4.2 Three-arm interferometry

If we define the 'geometry' of our interferometer to mean the composition of momentum states included in it, i.e. 'a two-arm interferometer with states $[|{+2\hbar k}\rangle + |{-2\hbar k}\rangle]$', then we can alter this geometry by changing the pulse sequence we use to open and close the interferometer. This change in geometry might be as simple as switching to an increased momentum separation using a $|0\hbar k\rangle \to [|{+4\hbar k}\rangle + |{-4\hbar k}\rangle]$ pulse as described in Section 3.7, or might involve changing the number of momentum components we include in the interferometer.

For our atom-optics, the experimentally-simplest such geometry involves using a single, short pulse to split our atoms in a $|0\hbar k\rangle \to C_{\pm}|{+2\hbar k}\rangle + C_0|0\hbar k\rangle + C_{\pm}|{-2\hbar k}\rangle$ 'beam-tritter' [125, 137] operation. Again, there is no change in the internal state of the atoms, and therefore common-mode rejection of Zeeman phase shifts induced by spatially flat magnetic fields. Here the outer arms' velocity causes them to accumulate a $4\omega_{\text{recoil}}t$ phase, but the central $|0\hbar k\rangle$ arm does not.

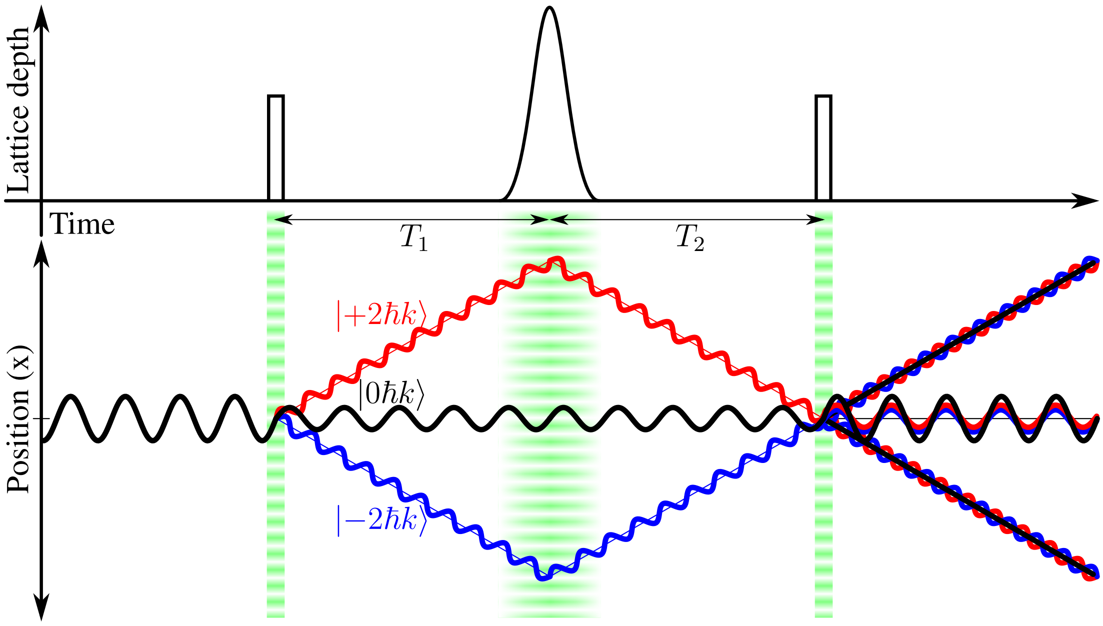

Figure 4.6: We generate a 'three-arm' off-resonant interferometer geometry using a simpler pulse sequence. The first pulse (shown in Figure 4.12) will act as a 'beam-tritter' [125], pushing the atoms into a superposition $|\psi\rangle = C_\pm|+2\hbar k\rangle + C_0|0\hbar k\rangle + C_\pm|-2\hbar k\rangle$. Here, only the moving $|+2\hbar k\rangle + |-2\hbar k\rangle$ arms experience a recoil phase, and so the interferometer phase (in the absence of gradient fields) becomes a heterodyne frequency measurement.

4.5 Homodyne interferometry

4.5.1 Background

The optical interferometer shown in Figure 4.1 is an example of *homodyne* interferometry. Here we take a single laser beam at a reference frequency, and split it along the two arms of the interferometer. Measurement is performed by encoding information in one arm of the interferometer, whilst the other arm represents a reference oscillation with no encoded information. The measurement is taken by interfering this 'null' arm with that containing phase information. In this instance *homodyne* refers to the fact that the 'detection' and 'reference' beams share a common frequency.

In contrast, a *heterodyne* interferometer intentionally alters the frequency between the detection and reference arms, f_{det} and f_{ref}, projecting the measurement into new frequencies $f_{\text{det}} + f_{\text{ref}}$ and $f_{\text{det}} - f_{\text{ref}}$, known as heterodynes.

The interferometer described in Section 4.4.1 splits an initially stationary cloud of atoms into two counter-propagating momentum states with equal speed, and therefore equal kinetic energy. As a result, the phases of these modes evolve at an equal rate in the absence of other influences.

This measurement with different modes of identical frequency is an example of homodyne (same frequency) detection. Since the output of the interferometer is determine by the *relative* phase of these modes, our interferometer has common mode rejection of the 'kinetic' frequency. Measurements *not* rejected are those which perturb the relative phase of the modes, such as the phase shifts induced by gravitational fields, magnetic fields, or van der Waals interactions [135].

Since our interferometer uses ^{87}Rb atoms in the $|F = 2, m_F = 2\rangle$ state, a brief magnetic gradient of duration Δt will cause a shift in the potential at the atoms proportional to their displacement,

$$U_B(x) = -m_F g_F \mu_B \frac{\mathrm{d}B}{\mathrm{d}x} x \, . \tag{4.20}$$

Each arm therefore obtains a proportional phase shift

$$\Delta\phi_{\text{potential}} = m_F g_F \mu_B \frac{\mathrm{d}B}{\mathrm{d}x} x \frac{\Delta t}{\hbar}, \tag{4.21}$$

and the interferometer output can be used as a measurement of the magnetic gradient of the pulse.

Importantly, the application of a potential gradient will necessarily induce an acceleration into the interferometer atoms,

$$a_B = F/m = -\frac{\mathrm{d}U_B}{\mathrm{d}x}/m = -m_F g_F \mu_B \frac{\mathrm{d}B}{\mathrm{d}x}/m \, . \tag{4.22}$$

This shift in velocity alters the balance of the arms' $4\omega_{\text{recoil}}t$ terms, introducing a persistent frequency component to the interferometer phase, $\phi_{\text{kinetic}}(t)$. In addition, the induced motion of the atoms causes the location where they overlap as the interferometer close to shift. This shift in position is accompanied by a shift in the phase of the optical grating, introducing an additional 'laser phase' shift, ϕ_{laser}.

4.5.2 Gradiometry

In the special case where the interferometer is time-symmetrical ($T_1 = T_2$) and a time-uniform potential gradient (such as a magnetic or gravitational field) is applied across the interferometer splitting axis, the kinetic and potential phases are exactly equal and opposite, $\phi_{\text{kinetic}}(T_1 + T_2) + \phi_{\text{potential}}(T_1 + T_2) = 0$ [138].

The remaining laser phase ϕ_{laser} is linearly proportional to the spatial shift in the centre-of-mass of the atoms as a result of the applied gradient [138]. If the gradient is constant in time, the laser phase can be calculated with Newtonian equations of motion, where the acceleration a_B (equation 4.22) is applied for the total interferometer duration $T = T_1 + T_2$,

$$\Delta x = \frac{1}{2} a_B T^2, \tag{4.23}$$

and the laser phase is just the spatial shift in units of the optical grating period λ_{grating},

$$\Delta\phi_{\text{laser}} = 2\pi\frac{\Delta x}{\lambda_{\text{grating}}} = \frac{1}{2}k_{\text{grating}}a_B T^2. \tag{4.24}$$

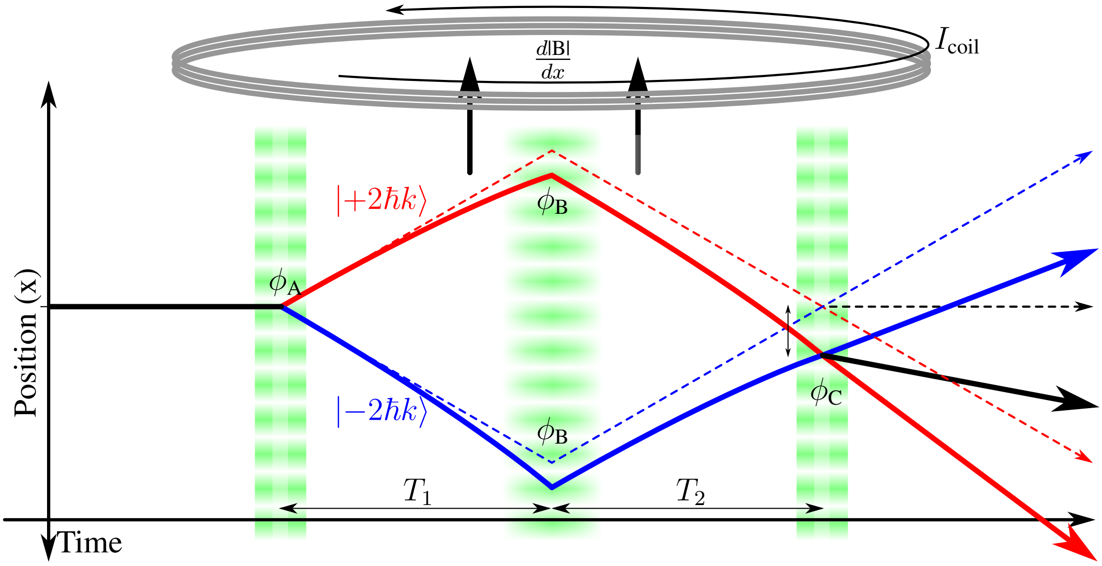

Figure 4.7: A current-carrying coil induces a magnetic gradient field $\mathrm{d}|\boldsymbol{B}|/\mathrm{d}x$ that accelerates atoms in our interferometer. This acceleration over the period $T_1 + T_2$ curves the atomic trajectories (red and blue traces) changing the local laser phase when they recombine in the closing interferometer pulse.

Figure 4.7 shows a schematic of the interferometer, where an initial beam-splitter pulse A splits the atoms into the $|+2\hbar k\rangle+|-2\hbar k\rangle$ momentum states, a Blackman pulse B performs a $|-(2+\delta)\hbar k\rangle\leftrightarrow|+(2-\delta)\hbar k\rangle$ reflection, and a second beam-splitter pulse C closes the interferometer. With no applied accelerating fields, this recombination occurs when the atoms are in the same position where the initial split occurred. These atomic trajectories are drawn in dashed lines.

The phase of the optical grating is determined by the relative positions of the optical elements in the atom-optic laser path, and so the spatial-phase of the optical grating (i.e. where the nodes and anti-nodes are located spatially) should be the same for all interferometer pulses. In practice these optical elements may move (due to acoustic noise, for example) during the pulse sequence, altering the optical phase between the first and last pulses.

We can apply a magnetic gradient field by passing an electric current through a coil located near the interferometer atoms. When this magnetic gradient is applied across the interferometer axis the interferometer atoms experience a potential $U(x)$ and corresponding acceleration $a(x)$, which alters the velocity of the atoms during the interferometer, altering the accumulating recoil phase. Appendix A.3 shows that these phase contributions exactly cancel when the interferometer timing is symmetrical ($T_1 = T_2$). The *remaining* phase contribution is that of the laser phase; the induced velocity moves the interferometer closing position by Δx, which introduces a phase shift in the optical grating of $\phi_{\text{laser}} = \phi_C - \phi_A = (2\pi\Delta x)/(\lambda_{\text{grating}})$ (see equation 4.24). Here we are using the optical lattice which closed the interferometer to measure how far the field gradient has moved the atoms' centre of mass during the interferometer duration.

4.5.3 Experimental gradiometer

Gradient coil calibration

The source of our magnetic gradient field is a single copper coil of four turns with radius 12.7 mm located such that the atoms are approximately 15 mm axially from the centre of the coil. We induce a gradient field by sending an electric current through the coil. To confirm that our gradiometer works correctly, we need an independent way of calibrating our gradient field $\frac{\mathrm{d}\boldsymbol{B}}{\mathrm{d}x}$ as a function of coil current I.

Since the gradient field exerts a force on our atoms, we can image the atoms' position when we apply some current through the coil, and calculate the acceleration required to achieve that displacement. We allow the atoms with initial velocity $v_a = 0$ to fall freely while we send some current I through the gradient coil for a time T_1. This gradient potential causes the atoms to accelerate until a velocity $v_b = a_{B(x)}T_1$. We then switch off the gradient coil, and allow the accumulated velocity to project into a larger spatial separation $\Delta x = x_C - x_A$ for a time T_2, when we perform absorption imaging. A schematic of this trajectory is shown in Figure 4.8.

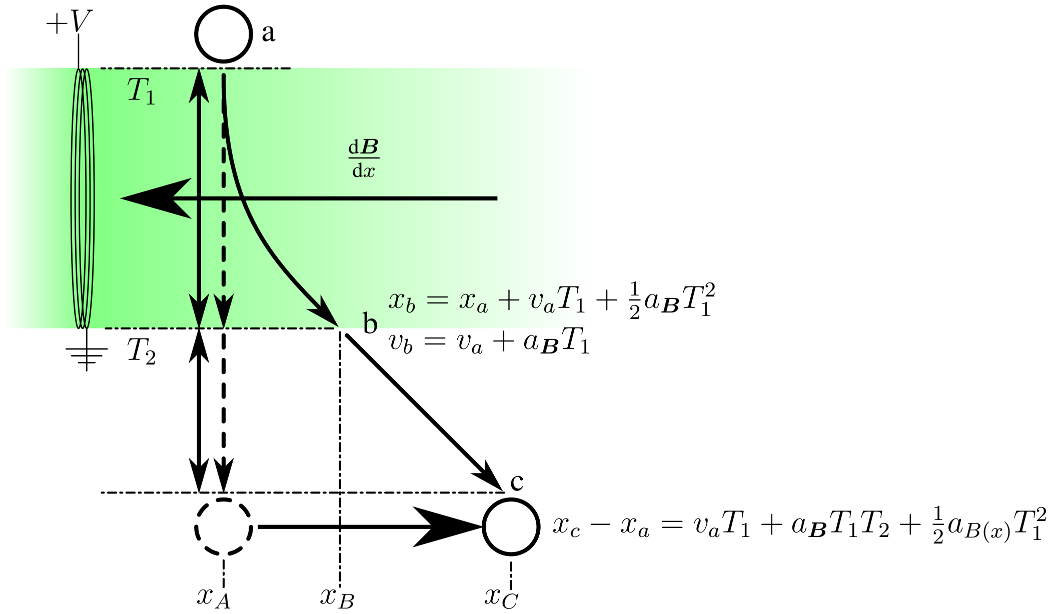

Figure 4.8: Classical method of calibration of our magnetic gradient coil. We position a copper coil with 4 turns and a radius of 12.7 mm approximately 15 mm from the atoms. When then allow the atoms to freely fall whilst sending some electric current I the coil for a time T_1, inducing a gradient potential across the atoms. We then turn the current off, and allow the accumulated velocity to project into a larger spatial shift. We can then calculate the acceleration required to generate that spatial shift, and extract the magnetic gradient applied at that current.

We begin by re-arranging the spatial shift of the atoms due to our applied gradient to make the acceleration the subject,

$$a_{B(x)} = \frac{\Delta x}{\left(\frac{1}{2} T_1^2 + T_1 T_2\right)}, \tag{4.25}$$

and from here convert this acceleration into a magnetic gradient in the x direction using equation 4.22,

$$\frac{\mathrm{d}\boldsymbol{B}}{\mathrm{d}x} = -\frac{m_{87\mathrm{Rb}}}{m_F g_F \mu_B} \frac{\Delta x}{\left(\frac{1}{2} T_1^2 + T_1 T_2\right)}. \tag{4.26}$$

Equation 4.26 therefore gives us a way of relating the shift in position of atoms to some applied magnetic gradient in the x direction.

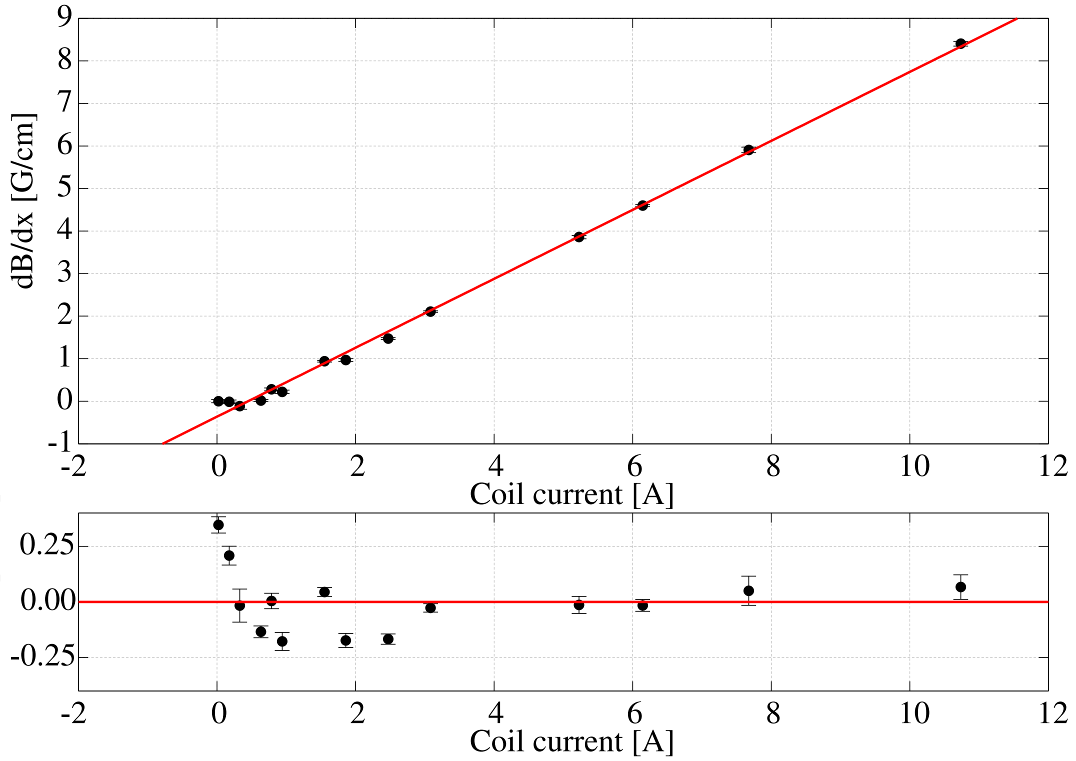

Figure 4.9: Calibration of our magnetic gradient coil. Here we send various currents through our gradient coil for a time T_1 during free fall, and then turn the coil off for a further time of flight T_2. We then perform absorption imaging, and fit the falling atomic cloud, obtaining a spatial position at the end of each time of flight. Using equation 4.26 we convert the spatial displacement of the atomic cloud into the magnetic gradient required to perform the observed atomic shift in position. This gives us a calibration curve between the coil current and resulting magnetic gradient.

We build our calibration curve by allowing a BEC to fall under gravity whilst sending some current through our gradient coil, taking an absorption image after the time of flight $T_1 + T_2$. Using equation 4.26 we calculate the magnetic field gradient required to generate the shift in the atoms position, and plot this against the coil current applied in each instance in Figure 4.9. A linear fit returns a gradient of

$$\frac{\mathrm{d}B_x}{\mathrm{d}x}/I = 0.88\,\mathrm{G\,cm^{-1}\,A^{-1}}\,. \tag{4.27}$$

Interestingly, whilst we see a strong linear relationship between atomic acceleration and applied coil current from $\sim 1\,\mathrm{A}$ and above, this linear fit crosses $0\,\mathrm{G\,cm^{-1}}$ at $0.42\,\mathrm{A}$. The mapping we have performed to extract a field gradient assumes that all positional shift is linearly proportional to an applied magnetic field (because time is fixed for all samples in equation 4.25). As a result we can also view the $\mathrm{d}B/\mathrm{d}x$ y-axis in Figure 4.9 as a measure of position. The atoms have a position of $x \approx 0 \pm 1\,\mu\mathrm{m}$ at

$I = 0\,\mathrm{A}$ and $I = 0.6\,\mathrm{A}$, and a position $x \approx -4 \pm 2\,\mu\mathrm{m}$ at $I = 0.3\,\mathrm{A}$. This is consistent with a small ambient magnetic gradient field with a gradient pointing towards our gradient coil.

There is a very subtle point to be made here; when we send a current through our gradient coil the weak-field seeking $|F = 2, m_F = 2\rangle$ atoms move *away* from our coil because the centre of the coil is where the strongest magnetic field is located. If we reverse the polarity of the current through that coil, the atoms *still move in the same direction, away from the coil centre*. The atoms re-orientate their spins with the magnetic field, such that away from the coil is always lower potential. With this in mind, the behaviour of our motion in Figure 4.9 makes sense; a small magnetic field with a gradient opposing that generated our coil will still push atoms away from our coil, except when the gradient field from the coil cancels to generate a spatially-uniform magnetic field. We would then naively expect to find an ambient magnetic field gradient of magnitude $\mathrm{d}B/\mathrm{d}x \approx 0.37\,\mathrm{G\,cm^{-1}}$. An additional complication is the addition of our magnetic 'shim' coils, used to compensate for the Earth's magnetic pull on our quadrupole trap minima and to provide a quantisation axis for our atomic spin. These concepts have been examined more thoroughly in our previous work, where we did indeed find a combination of stray magnetic and non-magnetic accelerating forces in our interferometer [139].

The interferometer

The above calibration method took the acceleration imparted by a magnetic gradient, and projected this acceleration into a shift in position. Interferometers can perform the same task by using their optical gratings as a ruler against which they measure this gradient-induced-acceleration.

Figure 4.10a shows a simplified schematic of the operation of an optical lattice on the phase of a BEC during an atom interferometer sequence, drawn at various times. For simplicity this schematic uses a simplified splitter pulse, and *not* the tuned $|0\hbar k\rangle \leftrightarrow [|{+2\hbar k}\rangle + |{-2\hbar k}\rangle]$ pulse our experimental gradiometer does.

In Figure 4.10(b) we see the initial conditions of the system at $T = t_0$. Our optical lattice has a phase locked with the x_0 position, and our BEC has a uniform phase. We then apply our optical lattice for some time until $T = t_1$, in Figure 4.10(c). The presence of a spatially-modulated light field has induced an AC Stark shift in the atomic states of our BEC atoms. This AC Stark shift is proportional to the intensity of the light, and so the energy shift is greater where the light field is more intense. Our BEC which had a uniform phase (dashed line) has therefore accumulated more phase in the high-intensity locations than the low intensity locations (solid black line). In reality the density of our BEC is also modulated during our atom-optic pulses, but for simplicity this is not shown here.

After the first splitter pulse we have some free evolution during which a magnetic field gradient can induce an acceleration in the atoms until the second closing pulse at time $T = t_2$. Let's examine the cases where the atoms remain in place without moving $\Delta x = 0$, and where the atoms move exactly one half optical grating period $\Delta x = \lambda_{\text{grating}}/2$.

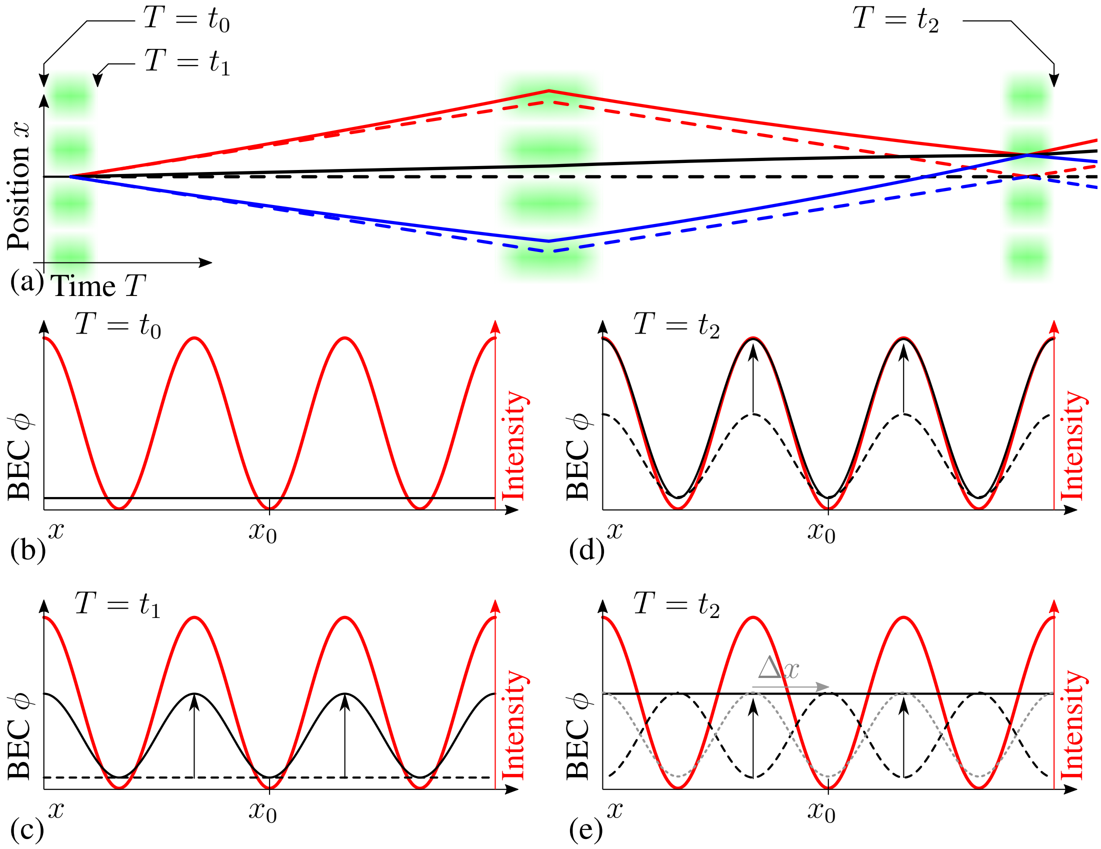

Figure 4.10: A simplified schematic of the AC Stark shifts in an atom interferometer used as a gradiometer. An overview of the interferometer through time is displayed on top, with a gradient field applied (solid lines) and with no field applied (dashed lines) (a). The optical grating light intensity is drawn in red, phase locked to the x_0 position. Figures are drawn for times (b) before the first splitter pulse, (c) during the first splitter pulse, (d) during the closing pulse with no position shift, and (e) during the closing pulse with a $\Delta x = \lambda_{\text{grating}}/2$ position shift. The arrows indicate the maximum shift in BEC phase during each optical grating pulse, with dashed black lines showing the BEC phase at the beginning of each pulse, and solid black lines the phase at the end of each pulse.

If the atoms remain in place, as shown in Figure 4.10(d), the optical grating remains in phase with the previous atomic phase shift. As such the AC Stark shift from this second pulse is spatially in phase with the previous one. The regions of our BEC which previously accumulated most phase accumulate more, and the regions which previously accumulated no additional phase again accumulate none. This second pulse has essentially increased the effect of the opening splitter pulse.

If the atoms obtain a $\Delta x = \lambda_{\text{grating}}/2$ positional shift, shown in Figure 4.10(e), there is now a π mis-match between the spatial phases of the optical grating and previously-induced BEC phase. The closing splitter pulse which now advance the phase most in positions where the previous was previously untouched, and will least adjust the phase in regions where it was previously advanced most. The end-result of the pulse is to regain our original uniform BEC phase.

The superposition of momentum states after the closing pulse is determined by the phase (and density) distribution across the BEC. The uniform phase BEC in Figure 4.10(e) corresponds to a condensate with all its amplitude in the $|0\hbar k\rangle$ state. Conversely, the corrugated phase BEC in Figure 4.10(d) corresponds to some superposition of the $[|{+2\hbar k}\rangle + |{-2\hbar k}\rangle]$ and $|0\hbar k\rangle$ states. Again, it is important to remember that the optical grating similarly modulates the density distribution of the BEC.

The interferometer here has effectively used the optical grating as a ruler, first imprinting the optical grating's 'reference' phase and density modulation onto our BEC, and then after some time has compared this imprinted BEC phase with the optical reference phase. The resulting output phase (and density) distribution determines the relative fractions of each momentum state in the superposition, which we then measure by way of absorption imaging after some evolution time to spatially separate the momentum states.

Our experimental gradiometer functions by the same principle, albeit with more complex pulse splitter pulse sequences. The experimental results of our magnetic gradiometer is shown in Figure 4.11. Here the interferometer was configured with two arms in the $[|{+2\hbar k}\rangle + |{-2\hbar k}\rangle]$ states, with an evolution time $T_1 = T_2 = 100\,\mu\text{s}$ on either side of a central reflection pulse. The magnetic gradient was applied 40 ms before the opening splitter pulse, and remained on until after the closing splitter pulse. This gives a total interferometer duration of $98.8\,\mu\text{s} + 100.0\,\mu\text{s} + 164.0\,\mu\text{s} + 100.0\,\mu\text{s} + 98.8\,\mu\text{s} = 561.6\,\mu\text{s}$.

As with our gradient coil calibration, we are measuring the spatial shift of the atoms induced by some accelerating force, except that instead of projecting the acceleration onto a displacement several hundred micrometres in size, we are using the optical grating to measure displacements on the scale of tens to hundreds of nanometers.

We observe a population change in the interferometer $|0\hbar k\rangle$ output port which is modulated with the applied gradient field. To this data we fit a cosine with an exponential decay (Red, solid line). For comparison, alongside this is the cosine of optical grating phase at the position we expect the atoms to be (blue dash-dotted line), given the calibration curve shown in Figure 4.9. The same optical phase curve is drawn again (green dashed line) with the envelope parameters extracted from the fit.

We see a modulation of the population in our $P(p = 0\hbar k)$ output port with a rate similar to our prediction from the coil calibration. We also see a phase shift $\delta\phi \approx 0.18\,\pi\,\text{rad}$. If the 0.37 G cm^{-1} stray field we mentioned in the coil calibration is real, we would expect this to generate an acceleration of 0.24 m s^{-1}, projected over our $\sim 550\,\mu\text{s}$ interferometer duration into a spatial shift of $\delta x \approx 36\,\text{nm}$, corresponding to an optical grating phase shift of $\delta\phi \approx 0.17\,\pi\,\mathrm{rad}$, which is consistent between both measurements.

We also observe a decay in the interferometer contrast as the field gradient is increased. Since the applied gradient accelerates the atoms, the position of the atoms during the closing pulse is not fixed, but rather changes over the $\sim 100\,\mu\mathrm{s}$ closing pulse. Since the closing pulse compares the optical reference phase against the BEC phase, this swept phase ‘washes out’ the phase during the closing pulse as the current coil is increased.

The coil calibration suggests that our gradient field is around $9\,\mathrm{G\,cm^{-1}}$ when our coil current is at $I \approx 11\,\mathrm{A}$ (at the upper end of our interferometer data where the contrast has reduced significantly). This gradient field generates an acceleration of approximately $5.5\,\mathrm{m\,s^{-1}}$, such that during the closing pulse at $T \approx 500\,\mu\mathrm{s}$, our atoms are moving at around $2.5\,\mathrm{mm\,s^{-1}}$. During our $\sim 100\,\mu\mathrm{s}$ closing pulse our atoms therefore move $250\,\mathrm{nm}$, causing a phase slip between the BEC and optical reference phase of approximately $1.1\,\pi\,\mathrm{rad}$. We interpret the reduction in contrast of the gradiometer here as being most likely caused by this phase-slip.

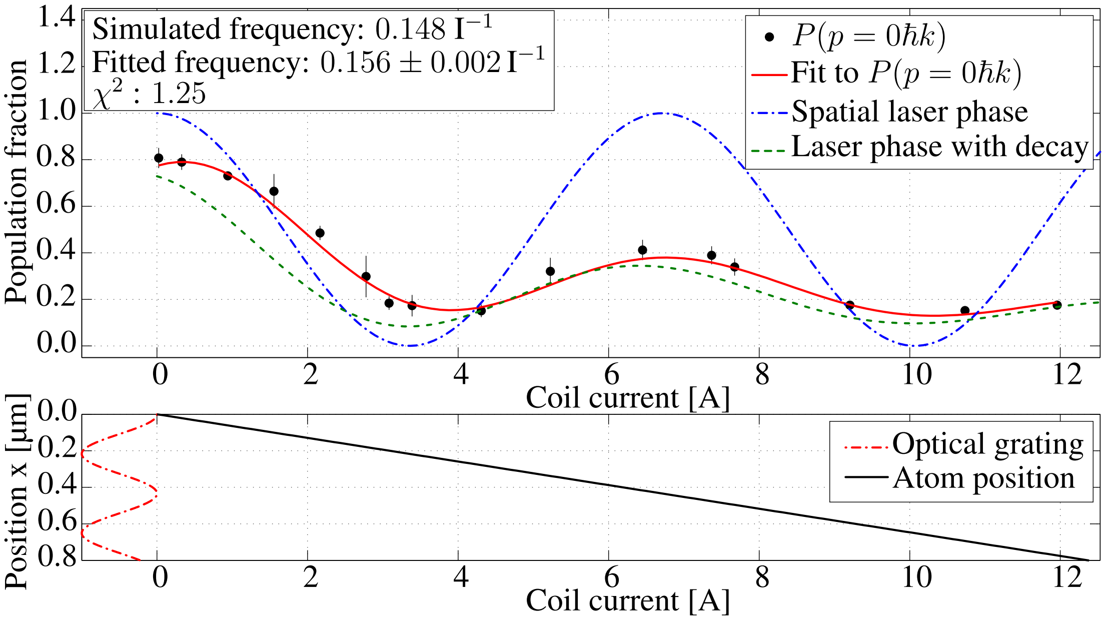

Figure 4.11: Experimental output of the first-order two-arm magnetic gradiometer. The interferometer is in a two-arm $[|{+2\hbar k}\rangle + |{-2\hbar k}\rangle]$ configuration, and the interferometer output recorded for various gradient coil currents (black filled circles represent the mean fractional $P(0\hbar k)$ population, where errorbars are the standard deviation of the sampled values). To this we fit a cosine wave with an exponential decay. The blue sine wave is a representation of the interferometer phase we should expect given our coil calibration (Figure 4.9). The green decaying sine is the same expected phase with an envelope matching the red fit.

4.6 Heterodyne interferometry

4.6.1 Theory & Background

The simplest interferometer we can create is that of a square beam-splitter pulse which ‘opens’ the interferometer, followed after some time T by a second beam-splitter pulse which ‘closes’ the interferometer. This is essentially a ‘two-pulse’ atom-optic beam-splitter [121], except that the wait time between pulses is swept in duration.

The evolution of this short interferometer is visualised on the Bloch sphere in Figure 4.12, with an example pulse sequence shown in Figure 4.12a, and the numerically simulated output of that example sequence shown in Figure 4.12b. The first pulse (1) causes the Bloch vector (red arrow) to rotate around the axis of the Rabi vector (blue arrow), pushing the atoms into a superposition $|\psi\rangle = \frac{1}{\sqrt{2}}\left(|0\hbar k\rangle + e^{i\phi}[|+2\hbar k\rangle + |-2\hbar k\rangle]\right)$, when the optical grating is switched off. Since the different momentum states have different energies, the relative phase between them oscillates in time, causing a precession of the Bloch vector around the equator of the sphere for some ‘wait’ time T (2). The third pulse (3) then applies the same Rabi vector again, mapping the accumulated phase to some final population.

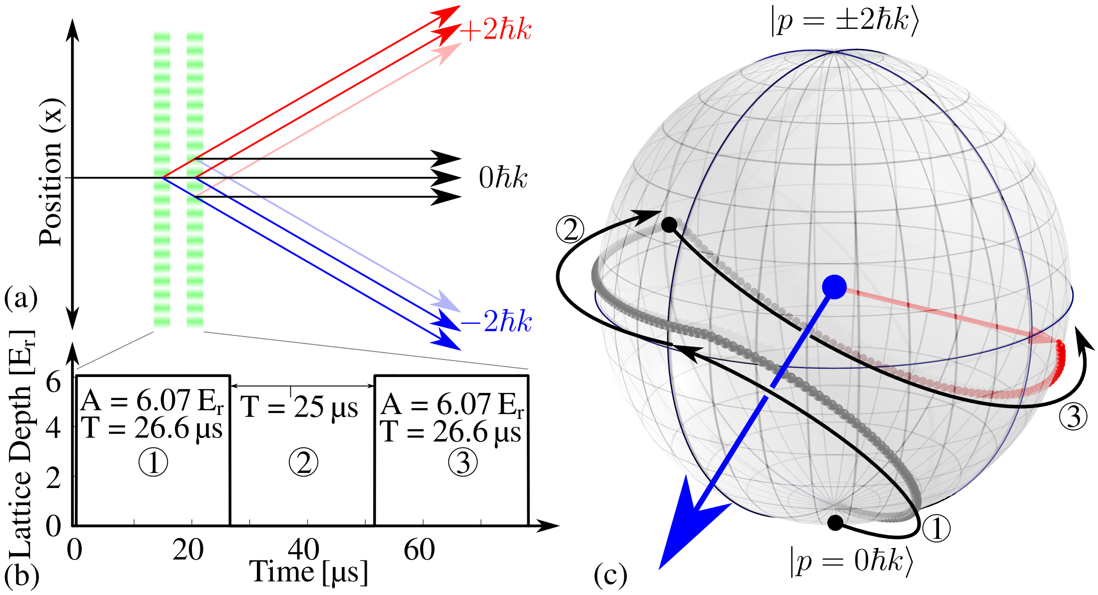

Figure 4.12: An example three-arm first-order momentum interferometer shot for a given time T. The first interferometer pulse (1) rotates the state vector (red) around the Rabi (blue) vector from an initial $|0\hbar k\rangle$ state to a superposition $|\psi\rangle = \frac{1}{\sqrt{2}}\left(|0\hbar k\rangle + e^{i\phi}[|+2\hbar k\rangle + |-2\hbar k\rangle]\right)$. The different energies of these modes then cause a phase-rotation to occur during a wait time (drawn here at $T = 25\,\mu\text{s}$, as an example), generating a phase slip $\phi \approx \pi/2$. A final ‘closing’ pulse performs another rotation, mapping this $\pi/2$ phase to a fractional population $P_{p=0\hbar k} \approx 0.5$.

Since the interferometer sequence maps the phase accumulation to a population, we can measure the evolution of this phase by repeating the interferometer measurement with varying T times. We should then see a periodic modulation in the output fractional population of the $|0\hbar k\rangle$ and $[|{+2\hbar k}\rangle + |{-2\hbar k}\rangle]$ modes. The phase of the interferometer evolves in proportion to the difference in kinetic energy of the momentum states involved, so we can calculate the interference frequency we should expect to see,

$$\omega = \frac{p^2}{2m_{87\mathrm{Rb}}\hbar} = \frac{(2\hbar k)^2}{2m_{87\mathrm{Rb}}\hbar} = \frac{4\hbar\,(7.24\times10^{6}\,\mathrm{m}^{-1})^2}{2\times 86.9\times 1.66\times 10^{-27}\,\mathrm{kg}} = 2\pi\times 12.2\,\mathrm{kHz}. \quad (4.28)$$

A simulated interferometer fringe is shown in Figure 4.13, where the 82 μs period corresponds to a frequency of 12.2 kHz, and the fringe contrast is predicted at approximately 100 %. The simulation includes all momentum states between $|{-12\hbar k}\rangle$ and $|{+12\hbar k}\rangle$, and small populations within these states slightly reduce the population in the $|0\hbar k\rangle$ state. A second initially-confusing result is that the zero-momentum population at $T = 0$ is *not* $P(0\hbar k) = 1$. This is because $T = 0$ does not correlate to an initial state, but rather zero separation time between the two beam-splitter pulses. Each beam-splitter pulse has a duration of 26.6 μs, over which time some phase accumulates. This is analogous to the deviation from 'thin' lens approximations in optics.

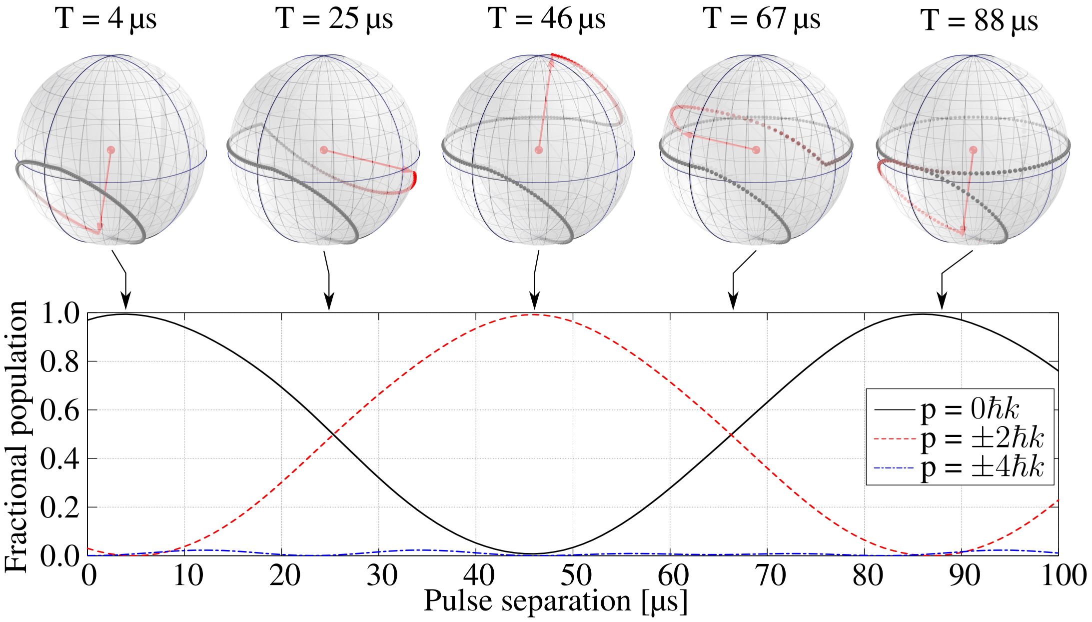

Figure 4.13: Numerical simulated interference fringes of the three-arm momentum interferometer. Here, the wait time T is swept from 0 μs to 100 μs, and the fractional populations $P(0\hbar k)$ (solid black line) and the $P(|{+2\hbar k}\rangle + |{-2\hbar k}\rangle)$ (dashed red line) plotted as a function of the interferometer delay time T. We see an oscillation with nearly 100 % contrast and a period of approximately 82 μs.

4.6.2 Experimental realisation

We configured our interferometer with the same parameters as those used in our simulation. The optical grating was pulsed with a depth of 6.07 E$_\mathrm{r}$ and duration 26.6 µs to open the interferometer, a pulse separation time T where the optical grating is switched off, and a second identical pulse fired to close the interferometer.

The atoms were then allowed a period of free flight, mapping the momenta to spatial positions, before an absorption image is taken. Five shots are recorded at each evolution time, and the resulting atomic distributions fitted with Thomas-Fermi profiles to extract the atomic population of each mode. These are converted to fractional populations, and a mean and estimate of standard deviation of measurement taken at each time. The resulting data are shown in Figure 4.14

The interferometer fringes were fit with a model comprising a cosine with decaying envelope,

$$P = \Big(A\cos(2\pi f_{\text{fringes}}x + \phi) - y_d\Big)\exp\left(-\frac{(x-t_0)^2}{(2\sigma^2)}\right) + y_o + y_d\ , \qquad (4.29)$$

where A is the cosine amplitude, f the cosine frequency, ϕ the cosine phase offset, y_d the envelope decay ‘zero’ level, t_0 the central time of the envelope, σ the envelope width, and y_0 the signal’s overall vertical offset. The interferometer contrast at T = 0 µs is $98 \pm 1.6\,\%$, before the different momentum modes significantly spatially separate, and before mean field effects induce phase-shifts which ‘wash-out’ the contrast fringes [140].

The Levernberg-Marquardt fit returns the parameters A = 0.490 ± 0.008, f_{fringes} = $12295 \pm 30\,\mathrm{Hz}$, ϕ = $0.094 \pm 0.014\,\mathrm{rad}$. This frequency results in a signal period of $\frac{1}{12300\,\mathrm{Hz}} = 81.3\,\mathrm{µs}$. This phase offset leads to first maximum at $\frac{0.094\,\mathrm{rad}}{2\pi\,\mathrm{rad}} \times \frac{1}{12230\,\mathrm{Hz}} = 1.22 \pm 0.18\,\mathrm{µs}$. Since our interferometer arms use *two* photon recoils per arm, the kinetic energy of these moving atoms is four times that of a single recoil. Our single-photon-recoil frequency is therefore $\omega_{\text{recoil}} = 2\pi f_{\text{fringes}}/4 = 2\pi \times 3.058\,\mathrm{kHz}$.

This experimental sequence is based on the same parameters that generated the simulation shown in Figure 4.13. Our fitted experimental frequency of $12300 \pm 30\,\mathrm{Hz}$ gives us a period of $81.3 \pm 0.2\,\mathrm{µs}$, inconsistent with the simulated $82.0\,\mathrm{µs}$ signal. The fitted time offset to the first maximum of $1.22 \pm 0.18\,\mathrm{µs}$ is also inconsistent with the simulated time offset of $4\,\mathrm{µs}$. These discrepancies can both be most simply explained by our poor knowledge of our interferometer beam angle; a small shift in the optical lattice wavelength will change the momentum imparted per photon recoil, altering the energy transferred per interaction and therefore the interferometer frequency. If the relative energies between neighbouring momentum states changes, the speed at which their relative interactions occur also changes.

In addition to the timing, we observe a decaying envelope in our interferometer contrast. Our short interferometer has no reflection pulse, and so the atoms do separate spatially as the pulse separation time increases. With fewer atoms spatially overlapping

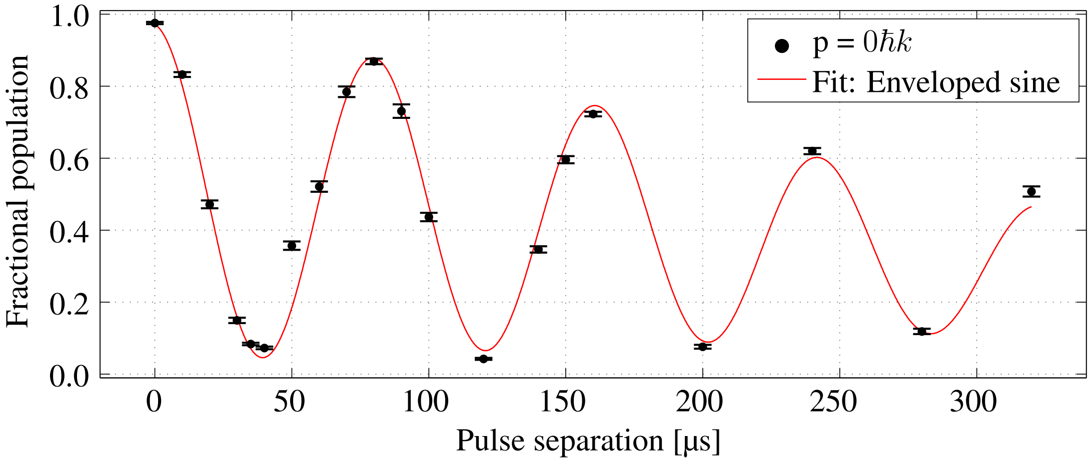

Figure 4.14: Experimental interferometer fringes from the ‘split → wait → split’ interferometer sequence described in Figure 4.13. Five measurements were taken at each time index, with mean counts plotted as black circles above, and the standard deviation as error bars. A Levenberg-Marquardt algorithm is used to fit a model to the data, with a cosine modulated by an exponential decay.

4.6.3 Fine structure constant

Having measured the recoil frequency ω_{recoil}, we can make a determination of the fine-structure constant using our atom-optics beam parameters for wavelength $\lambda_{\text{eff}} = 2\lambda_{\text{grating}}$ and wave-vector $k_{\text{eff}} = k_{\text{grating}}/2$, where the ‘eff’ subscript implies that we mean the projection of either atom-optic beam along the interferometer x-axis. Since our interferometer frequency comes from the energy differential in the moving and non-moving arms, we have

$$\omega_{\text{recoil}} = E/\hbar = \frac{1}{\hbar}\frac{\hbar^2 k_{\text{eff}}^2}{2m} = \frac{\pi h}{m\lambda_{\text{eff}}^2} \, . \tag{4.30}$$

We can re-arrange this equation so:

$$\frac{h}{m} = \omega_{\text{recoil}}\frac{4\pi}{k_{\text{eff}}^2} = \omega_{\text{recoil}}\frac{\lambda_{\text{eff}}^2}{\pi} \, , \tag{4.31}$$

thus placing our interferometer fringe into the class of ‘h/m’ measurements [50, 110]. These measurements of h/m can be used to evaluate α [50],

$$\alpha^2 = \frac{2R_\infty}{c}\frac{m_{87\text{Rb}}}{m_{\text{e}}}\frac{h}{m_{87\text{Rb}}} \, . \tag{4.32}$$

Combining equations 4.30, 4.31, and 4.32 and using the known constants listed in Appendix A.1, we obtain expressions for the fine-structure constant as a function of recoil frequency and atom-optic beam parameters,

$$\alpha^2 = \frac{2R_\infty}{c}\frac{m_{87\mathrm{Rb}}}{m_\mathrm{e}}\frac{4\pi\omega_\mathrm{recoil}}{k^2} = \frac{2R_\infty}{c}\frac{m_{87\mathrm{Rb}}}{m_\mathrm{e}}\frac{\omega_\mathrm{recoil}\lambda_\mathrm{eff}^2}{\pi} \,. \tag{4.33}$$

Our optical grating is formed from lasers 4.5 GHz red detuned from the 780 nm $F = 2 \rightarrow F' = 3$ transition on the ^{87}Rb D$_2$ $(5^2S_{1/2} \rightarrow 5^2P_{3/2})$ line at an angle of $26.0\pm0.5°$ (see Section 2.3.8), so we have an optical grating wavelength of $\lambda_\mathrm{grating} = \frac{780\,\mathrm{nm}}{2\cos(26°)} = 434\,\mathrm{nm}$. Likewise, the projection of our laser light along the interferometer x-axis is increased by a factor of $\cos(26°)$ such that $\lambda_\mathrm{eff} = 868\,\mathrm{nm}$, and the wavevector of that light reduce by the same $\cos(26°)$,

$$k_\mathrm{eff} = \frac{2\pi}{\lambda_\mathrm{eff}} = \frac{2\pi}{868\,\mathrm{nm}} = 7.24\times10^{-7}\,\mathrm{m}^{-1} \,. \tag{4.34}$$

If we assume that the only significant uncertainties are in our measured frequency ω_recoil and the interferometer beam angle θ, the uncertainty in our α^2 measurement is

$$\left(\delta\alpha^2\right)^2 = \left(\frac{\partial\alpha^2}{\partial\theta}\delta\theta\right)^2 + \left(\frac{\partial\alpha^2}{\partial\omega_\mathrm{recoil}}\delta\omega_\mathrm{recoil}\right)^2 , \tag{4.35}$$

where the partial derivatives are

$$\frac{\partial\alpha^2}{\partial\omega_\mathrm{recoil}} = \frac{2R_\infty}{\pi c}\frac{m_{^{87}\mathrm{Rb}}}{m_\mathrm{e}}\frac{\lambda_\mathrm{laser}^2}{\cos^2(\theta)} , \tag{4.36}$$

$$\frac{\partial\alpha^2}{\partial\theta} = \frac{4R_\infty}{\pi c}\frac{m_{^{87}\mathrm{Rb}}}{m_\mathrm{e}}\lambda_\mathrm{laser}^2\,\omega_\mathrm{recoil}\frac{\tan(\theta)}{\cos^2(\theta)} \,. \tag{4.37}$$

With an measured interferometer beam angle $\theta \approx 26° \pm 0.5°$, our example fringes generate a value $\alpha^{-1} = 136.74 \pm 0.86$ (6300 ppm). Whilst this value is consistent with the current best measurement of α from CODATA [71] ($\alpha^{-1} = 137.035999139$), the uncertainty is significantly larger. The dominant contribution to our uncertainty in equation 4.35 is the interferometer beam angle.

Clearly, we can't use the interferometer as an α measurement until the interferometer beam angle θ is not the most poorly-defined variable in the system. The conceptually simplest and most 'correct' solution to this problem is to reduce the angle itself to zero. As θ approaches zero, so does the gradient $\mathrm{d}\cos(\theta)/\mathrm{d}\theta$ and therefore also the sensitivity of α to the interferometer beam angle. If we were to suppose for the moment that the interferometer angle $\theta = 0 \pm 0.5°$, our error falls to $\delta\alpha^{-1} = 0.24$ (1700 ppm).

One major advantage of a $\theta = 0°$ configuration is that beam angle gets easier to measure. Currently we measure the beam angle by trilaterating the positions that the interferometry beams hit the mirrors on each side of the science chamber. A pair of counter-propagating beams could instead by defined by a pair of apertures centred on one beam, where any deviation of the ‘other’ beam can be directly measured in the surface of the apertures. Such an experimental setup with beam paths defined by apertures mounted in translation stages has been successfully used to measure and implement interferometer beam angles [141]. In our case, a simpler method would be to spatially-mode match counter-propagating beams into optical fibres mounted on either side of our science chamber. For more details on how we measured θ see Section 4.7.

It is also important to note that the frequency uncertainty is determined by the Levenberg-Marquardt fitting algorithm. This algorithm numerically calculates uncertainties using the input errors, but does so assuming that the fitted model and parameters are correct. From our measurement shown in Figure 4.14, the fitted model only passes through 5 out of 20 points, indicating that the model chosen is under-fitting the data. Here each time index is calculated with the mean and standard deviation of 5 experimental cycles (there is nothing special about our choice of 5 cycles here, other than that the uncertainty in atom counting over 5 cycles has previously shown to be consistent with more cycles and takes less time).

The data at each time interval was captured sequentially, taking approximately 5 minutes for acquisition at each interferometer time. The most likely explanation for the seeming underestimation of the error bars is an additional source of phase noise which occurs at a frequency too low to be detected in a single data run at a given interferometer time, but which does alter the recorded phase over the ~ 2 hours that the overall fringe is recorded. The correct way to fix this would be to ‘shuffle’ the order in which we take data, such that slow drifts over time would be as equally present within the measurements at a single time index as they were over the whole run. Nevertheless, the fit algorithm is most likely underestimating the uncertainty in the fitted frequency.

4.7 Interferometer beam angle

4.7.1 How do we measure the beam angle?

We determined the interferometer beam angle by firstly locating points of intersection between each beam and the nearest optical element before and after the science chamber. Each of these four positions were measured relative to a set of three markers screwed into the optical table in a common base-line. We then determined the position of these four points using the principle of trilateration, shown in Figure 4.15.

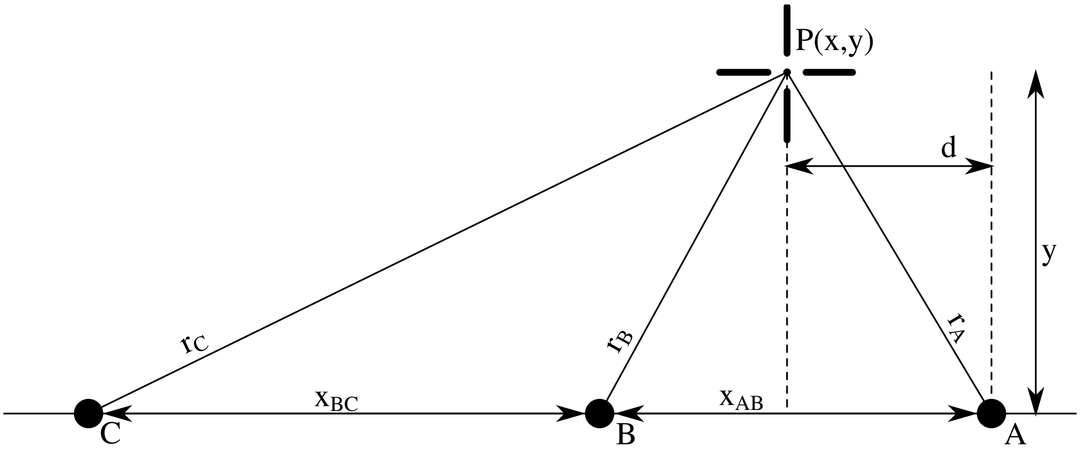

Figure 4.15: We can trilaterate the position of any point relative to three co-linear markers by measuring the distance from each of those markers to that point.

With the three markers (A,B,C) positions being co-linear, we can determine the position of any point (P(x,y)) using the distances to the three markers, where

$$d = \frac{r_A^2 - r_C^2 + 2x_{BC}x_{AB} + x_{AB}^2 + x_{BC}^2}{2x_{BC} + 2x_{AB}} \,, \tag{4.38}$$

and

$$y = \sqrt{r_A^2 - d^2} \,. \tag{4.39}$$

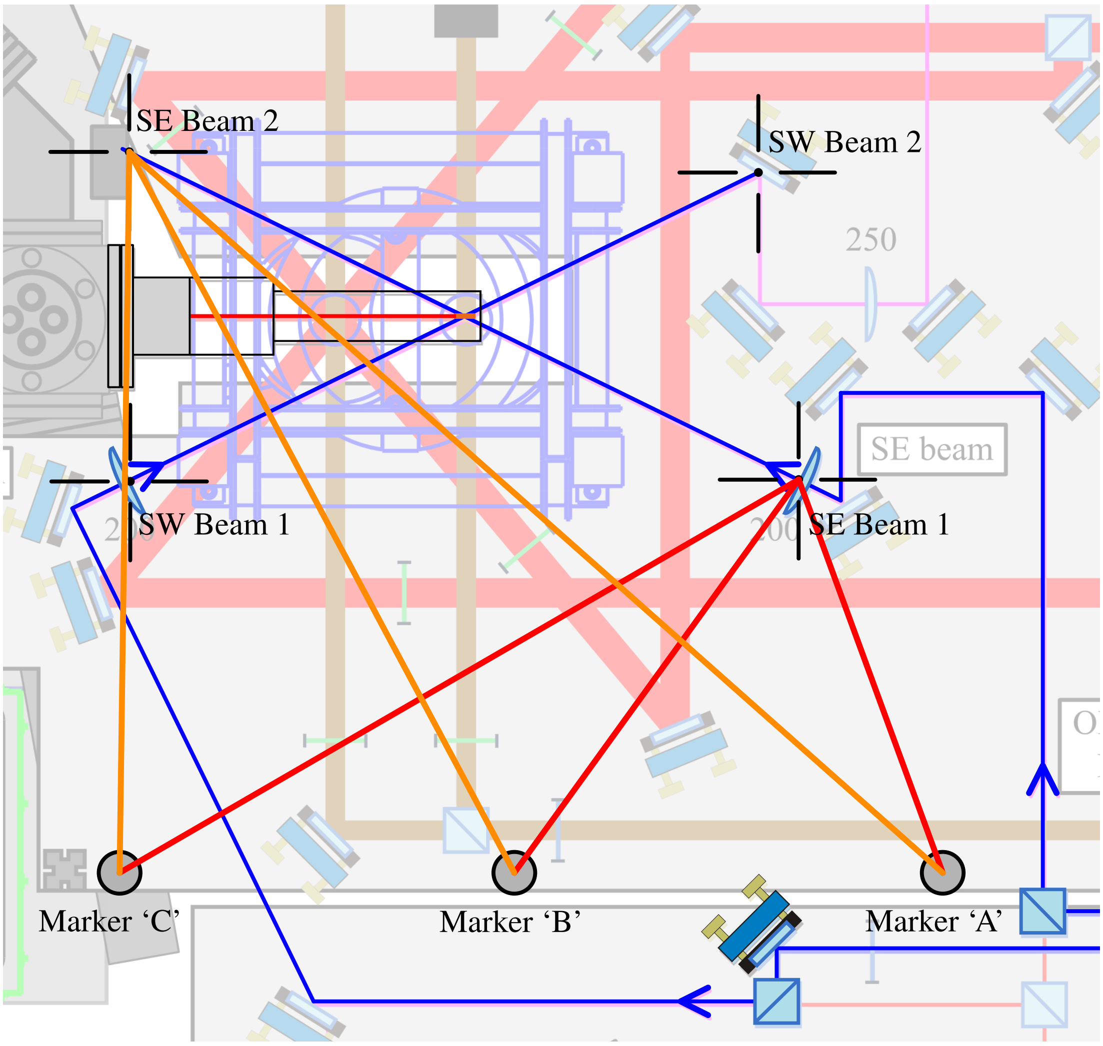

Figure 4.16: We calculated our interferometer beam angle by trilaterating the position that each beam intersects with the nearest optical elements to the science chamber. The interferometer beams are drawn in blue. Shown in red and orange are the measurements required to obtain the trajectory of the South-East interferometer beam, which we then use to determine the relative angle to the marker baseline in the X, Y plane. We then performed a similar second set of six measurements to determine the South-West beam parameters.

Figure 4.16 shows the beam interesction points chosen, which were the final lenses before the science chamber, and the first mirror after the chamber for the South-West beam and the beam-dump for the South-East beam. The markers were screwed into the optics table near the interferometer setup, to ensure that they were very closely co-linear in position.

The actual position of the beam intersection was determined using an IR-sensitive laser viewing card and an IR-sensitive night-vision camera. The distance of these position to each marker was then measure with a measuring tape to the nearest millimetre. Uncertainty in this process were mainly derived from (1) the finite thickness of the marker posts: measurements were taken from the point of laser intersection with a metal tape ruler to the tangent on either side of each marker rod, and (2) the laser intersection points existing on the surface of optical elements: we could not physically push the tape onto the optical elements for fear of damage, and so would align vertically above the point of intersection. We would then attempt to hold the tape ruler horizontally (using a liquid-bubble spirit level), and read off the distance to the marker's tangent surfaces.

We then trilatered co-ordinates for each intersection point, and used the tangent of the X, Y separation between each pair to infer an angle in the X, Y plane relative to our marker baseline. Uncertainties were calculated by performing each distance measurement and calculating mean with standard deviation of the measurements, and propagating these through equations 4.38 and 4.39 as the upper and lower bounds. It is from this calculation that we derive the $\theta = 26^\circ \pm 0.5^\circ$ beam angle listed in Section 4.6.3.

4.7.2 How do we fix it?

Experiments with non-colinear optical grating beams have been performed, using various techniques to determine the beam angle [141]. Here the optical path is determined using adjustable apertures mounted to translation stages. In this way the position of each intersection point can be (a) arbitrarily determined by re-locating the mount to some other location along the beam path and (b) the positions of each intersection can be measured to far greater precision than our ± 1 mm.

A conceptually simpler (but more time-consuming) solution is to alter the interferometer beam angle to 0°, as suggested in Section 4.6.3. The cosine sensitivity to small perturbations around $\theta = 0$ is zero, and so we can dramatically reduce uncertainties from θ by altering our interferometer geometry to some counter-propagating lattice. This change in the effective laser wavevector $k_{\text{eff}} = \frac{2\pi \cos(\theta)}{780\,\text{nm}}$ *would* alter the frequency we detect, raising it from approximately 24.6 kHz to roughly 30 kHz, increasing our phase gradient $\mathrm{d}\phi/\mathrm{d}t$ and inducing a secondary reduction in uncertainty.

Chapter 5

Contrast Interferometry

5.1 Background and Theory

5.1.1 Motivation

The Contrast Interferometer was first demonstrated by Gupta *et al.* in 2002 [111]. Here, off-resonant scattering splits a BEC of sodium atoms into a superposition of three momentum states: $|\psi\rangle = \left(\frac{1}{\sqrt{2}}|0\hbar k\rangle + \frac{1}{\sqrt{4}}e^{i\phi}[|+2\hbar k\rangle + |-2\hbar k\rangle]\right)$. The moving states are reflected after some time T, and the wave packets allowed to evolve until they overlap at time $2T$. Rather than closing the interferometer with a second 'beam-splitter' pulse, the evolving recoil phase is encoded in the contrast of the matter-wave fringes [111], and these fringes are read by shining a single laser along one of the beam-splitting laser's wavevector, with the reflected signal modulated in time with the recoil phase. This allows for pseudo-non-destructive measurements that persist for many oscillations, allowing for single-shot measurements of the fine-structure constant.

This offers us some significant benefits. Firstly, our interferometer technique listed in the previous chapter uses a 'closing' interferometer pulse to project the interferometer phase into a modulation of momentum states, where data is then captured using absorption imaging (henceforth referred to as a 'momentum interferometer'). This is a time-consuming process. A typical momentum interferometer fringe in our lab might consist of 50 data points, each of which has been generated from 5 (for example) measurements. Since our existing momentum interferometer has an experimental cycle time of around 30 s, a single fringe measurement lasts at least 2 hours of continuous measurement time. To perform a precision measurement, we want to increase the available statistics on the measurement by performing that measurement repeatedly [113]. Single-shot measurements would allow our experiment a vastly reduced data acquisition time, whilst increasing the number of times the interference phase is sampled per measurement. A corresponding measurement with our contrast interferometer typically samples the interferometer phase at 150 evolution times in a single experimental run, generating an entire interferometer fringe in around 30 seconds; a speed-up of around 700 times.

Secondly, an experimental run of several hours creates a tremendous bandwidth range over which our experiment is sensitive to noise. If the total measurement time across a fringe is reduced from several hours to a few hundred microseconds many of these noise sources are frozen out, effectively giving the experiment frequency-dependent rejection to noise sources like temperature variation, laser intensity noise, vibrations in optical elements at acoustic frequencies. These single-shot measurements could be thought of as the correlated measurement of many phases, each of which offers additional information on the others.

Thirdly, the nature of the measurement is different. Typical interferometers don't measure phase at various evolution times, but will instead repeatedly measure phase at a single time chosen to maximise the gradient of phase with respect to the measurement parameter in question. In this way the maximum information is taken in each experimental run. This only works, if the 'correct' phase is already approximately known. In such a scheme small drifts in amplitude, background level, frequency and phase *all* appear as shifts in the output interferometer population. A measurement like contrast interferometry which samples interferometer phase many times in a single experimental run separates all of these effects out, allowing measurement of phase to be unambiguous.

5.1.2 Theory and concepts

The key concept involved in the contrast interferometer is that of holography. A hologram is created by shining a coherent light source through a beam splitter, generating two phase-matched beams. One of these beams is used as an unperturbed phase-reference, and other 'measurement beam' allowed to interact with some target. The influence that the target has on a flat-phase beam is light is now imprinted in the difference in phase between the measurement and reference laser beams. If the measurement and reference beams are then recombined, interference fringes are generated according to the mixing phases of the reference and measurement. If the fringes are generated in some photo-reactive substance, these fringes can be 'fixed' in the medium, encoding the target's phase information [2]. These embedded interference fringes are a hologram.

If we then illuminate the hologram with light that has the reference beam's unperturbed phase, the hologram diffracts part of that incoming beam into the now-missing measurement beam, recreating the phase of the light that *had* interacted with the now-absent target. Looking into this medium, we can see the target in the diffracted light as though it were still present, because the hologram has effectively remodulated the light as though it had reflected from the target [2].

In the case of a contrast interferometer, the target we measure against the reference beam is not an object we reflect light from, but rather another laser beam - in this case one of the lasers used in our atom-optics.

Atom-optics work because the optical grating used to manipulate the atoms imprints a spatial and phase grating into the atomic cloud [142]. Particular states can be targeted by recreating the atomic fringe pattern that you would see if those target momentum states were overlapping. This process is made more complicated by the fact that the atomic ensemble evolves whilst our atom-optics are being applied; in our $\sim$100 µs long '$|0\hbar k\rangle \rightarrow [|+2\hbar k\rangle + |-2\hbar k\rangle]$' beam-splitter operation, the phase, energy and position of the atoms alter significantly. We rely on our numerical simulation to plot an evolution trajectory that results in the state we desire.

Since those fringe patterns have been created by interfering the wavefronts from a coherent light source, the atomic cloud's fringe pattern can acts a a hologram. Light sent along one of the wavevectors used to make the hologram ($\boldsymbol{k}_1$) will be diffracted into the 'missing' wavevector ($\boldsymbol{k}_2$) [2]. Unlike the hologram fixed into a medium that is held at a fixed phase, the hologram in our BEC is continuously evolving in time according to the energies of the encoded momentum states.

The interference fringes in our hologram naturally only appear when the modes in the hologram are spatially overlapping. Since the atoms in the hologram are free to move and have been encoded with various momenta, our hologram only exists at certain times during an interferometer sequence. Figure 5.1 shows a schematic of the spatial extent of our BEC atoms during an interferometer sequence. Our BEC is split into multiple momenta with a beam-splitter pulse, and the atoms are allowed to spatially separate for a time T_{sep}, when a reflection pulse is triggered. The atoms then converge, re-overlapping at a time $2T_{\text{sep}}$. This gives us two periods in time in which the atoms are overlapping, and therefore two periods in time during which our BEC hologram exists. If required, we could generate additional re-imaging of our hologram by adding more reflection pulses at multiples of T_{sep}.

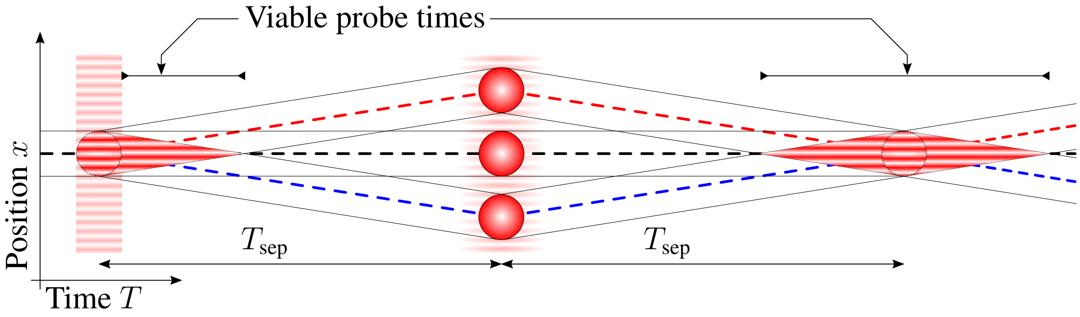

Figure 5.1: A schematic of the contrast interferometer. Shown are the trajectories of our BEC atoms during the interferometer, in the momentum states $|0\hbar k\rangle$ (black dashed), $|+2\hbar k\rangle$ (red dashed), $|-2\hbar k\rangle$ (blue dashed). Also drawn are the physical extents of the BEC in each mode, where interference fringes are present when all three modes spatially overlap. Our atoms overlap spatially only around the time of the beam-splitter pulse, spatially separating until a reflection pulse are a time T_{sep}, before converging at a time $2T_{\text{sep}}$.

In Figure 5.1 we have two periods at which we could successfully probe our contrast interferometer. These are immediately after the beam-splitter pulse (henceforth referred to as a 'short' contrast interferometer), and during the re-imaging of the hologram after a reflection pulse at $2T_{\text{sep}}$ (a 'long' contrast interferometer). There are advantages and disadvantages to both short and long contrast interferometers.

The long interferometer has the advantage that all atom-optics pulses have already been applied before the time of maximum overlap, so there is no issue of shutter-switching time that limits when we can begin probing. The total duration of the hologram is also longer, since we can access the times before and after the maximum spatial overlap of the different BEC modes. The longer duration between the initial beam-splitter pulse and readout of the hologram also allows a greater accumulation of phase, in principle increasing sensitivity to effects which scale with T. In comparison the short interferometer forbids us access to times before the maximum overlap, times during the beam-splitter pulse, and for a $\sim 120\,\mu\text{s}$ period after the beams-splitter pulse while our SPCM protection shutter system is switching. If our aim is only to measure the recoil frequency, the short interferometer offers less time for interactions to distort the hologram.

Figure 5.2a shows a schematic of the short contrast interferometer. An initially stationary BEC is illuminated by two lasers beams with wave-vectors $\boldsymbol{k}_1$ and $\boldsymbol{k}_2$. This coherently splits the condensate into a superposition of three momentum states, $|\psi\rangle = \Big(C_0|p = 0\hbar k\rangle + e^{iE/\hbar}C_{\pm 2}\Big[\frac{1}{\sqrt{2}}\big(|p = +2\hbar k\rangle + |p = -2\hbar k\rangle\big)\Big]\Big)$, that form a matter-wave interference fringe.

Our BEC hologram could be considered as an example of a distributed Bragg-reflector, where periodic modulation of the condensate's refractive index generates multiple reflective surfaces that coherently amplify the reflected light wave, where the reflective surfaces are separated by half the probe light's wavelength. The refractive index of the BEC η scales with its density n ($\eta - 1 \propto n$),

$$\eta = 1 + \frac{\sigma_0 n \lambda}{4\pi}\left[\frac{i}{1+\delta^2} - \frac{\delta}{1+\delta^2}\right] , \tag{5.1}$$

where $\sigma_0 = 6\pi\lambda^2$ is the resonant cross section of a two-level atom, n is the density of the BEC, λ the wavelength of the probe light, and $\delta \equiv (\omega - \omega_0)/(\Gamma/2)$ is the detuning of the probe light in half linewidths [109]. We should therefore expect to see Bragg-scattering from the hologram when the condensate has a modulation in its density with a spatial period of half the probe laser's wavelength. Our probe laser is projected along the X-axis at an angle of approximately 26°, giving us an effective probe wavelength of $\lambda_{\text{eff}} = 780.24\,\text{nm}/\cos(26°) = 868\,\text{nm}$, and an optical grating wavelength of $\lambda_{\text{lattice}} = 780.24\,\text{nm}/2\cos(26°) = 434\,\text{nm}$.

Figure 5.2b shows the interference fringe, frozen at a time of maximum contrast. The incoming probe laser wavefronts (along $\boldsymbol{k}_2$) coincide with the spatial periodicity of the condensate's density, generating a Bragg reflection along the wave-vector $\boldsymbol{k}_1$.

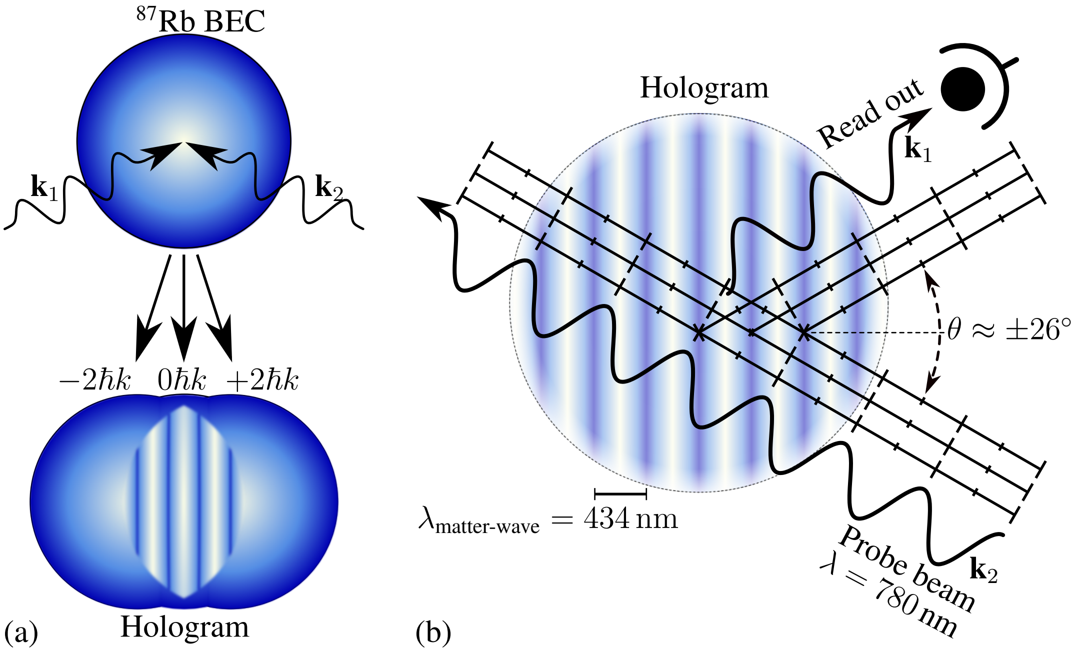

Figure 5.2: Generation of the contrast interferometer signal in the short contrast interferometer configuration. (a) If a beam-splitter pulse is used to coherently split a stationary BEC into a superposition $|\psi\rangle = \left(\sqrt{1/2}|0\hbar k\rangle + e^{iE/\hbar}\sqrt{1/4}|{+2\hbar k}\rangle + e^{iE/\hbar}\sqrt{1/4}|{-2\hbar k}\rangle\right)$, the evolving interference fringes are necessarily also a hologram which encodes the wavevectors $\boldsymbol{k}_1$ and $\boldsymbol{k}_2$. (b) The contrast signal is the outgoing diffraction of a single incoming laser along one of these wavevectors. The recoil phase of the hologram's interference fringe is encoded in the intensity of this diffracted beam. A photon counting device placed in the path of this wavevector can then measure the interferometer phase continuously.

As mentioned above, the BEC atoms are not fixed in position and have an evolving phase, so the matter-wave interference fringes in the condensate evolve over time, altering the spatial density distribution of the condensate. The nature of the interference fringes are determined by the momenta (and relative phase) of the atoms comprising the condensate. If the atoms are in a superposition state $(C_0|p = 0\hbar k\rangle + e^{i\phi}C_{\pm 2}[\frac{1}{\sqrt{2}}(|p = \pm 2\hbar k\rangle + |p = \pm 2\hbar k\rangle)])$, then the hologram evolves according to the difference in energy between the states. Since this energy difference is due to the recoil momentum from a photon-atom interaction, this is known as a recoil frequency; $\omega_{\text{recoil}} = p^2/2m\hbar = 4\hbar k^2/2m$. For our ^{87}Rb atom and $434\,\text{nm}$ optical grating, this recoil frequency is approximately 12.3 kHz.

Since the interference of these different momentum states is phase-dependent, and the phase of the moving $p = \pm 2\hbar k$ modes evolve at the rate $\frac{d\phi}{dt} = \frac{E}{\hbar}$, the hologram generated also evolves cyclically with frequency $\frac{E}{\hbar}$, which is for us $\omega = (2\hbar k)^2/2m \approx 2\pi \cdot 12.3\,\text{kHz}$. The resulting interference pattern evolving through time appears like a Talbot carpet [143] with a finite number of input wave-vectors. A two-dimensional

Gross-Pitaevskii equation (GPE) simulation of this evolution is shown in Figure 5.3a. Here, $T = 0\,\mu\text{s}$ corresponds to the moment at which the beam-splitter pulse ends and free evolution begins. The first $26.5\,\mu\text{s}$ of evolution from $T = -26.5\,\mu\text{s} \rightarrow T = 0\,\mu\text{s}$ show the imprinting of a density grating into the condensate.

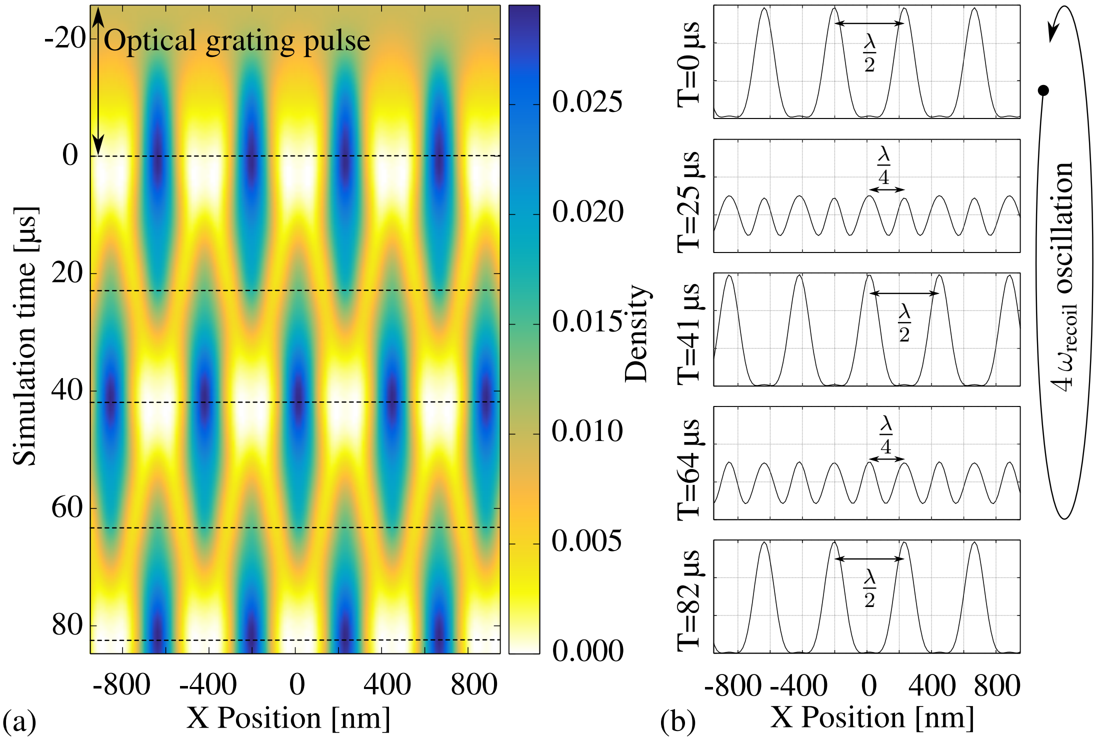

Figure 5.3: A 2D GPE simulation of the BEC during the opening of a contrast interferometer. (a) An optical grating pulse acts as a beamsplitter, pushing the atoms into a superposition of the $|p{=}0\hbar k\rangle$ and $[|p{=}{+}2\hbar k\rangle{+}p{=}{-}2\hbar k\rangle]$ states with approximately equal population. The kinetic energy of the $[|p{=}{+}2\hbar k\rangle{+}p{=}{-}2\hbar k\rangle]$ states cause an oscillation in the relative phase between the moving and stationary modes, generating a time-oscillation in the interference fringe which appears as a Talbot carpet which images the optical diffraction grating periodically in time. Since the atomic momentum distribution has only three modes, we only see the matter-wave re-image the optical grating at both the Talbot period and at half the Talbot period.

The atomic cloud contains only the ground ($|p = 0\hbar k\rangle$) and first excited state ($|p{=}{+}2\hbar k\rangle{+}|p{=}{-}2\hbar k\rangle$), so the Talbot carpet contains only the first and second wavevectors, such that the matter-wave re-images the optical grating at both the Tablot period and half this distance [143]. With our experimental parameters we have a Talbot period of

$$T = \frac{1}{f} = \frac{h}{E} = h\frac{2m}{(2\hbar k)^2} \approx 81\,\mu\text{s}, \tag{5.2}$$

over which we complete a cycle where the atomic grating re-images the optical grating with spatial wavelength $\lambda_{\text{effective}}/2 = 434\,\mathrm{nm}$. At half this time, we have a density grating with identical spatial wavelength, but a phase shift of π. At each $\frac{1}{4}T$ and $\frac{3}{4}T$ time, we have a frequency-doubled density grating with spatial period $\lambda_{\text{effective}}/4 = 217\,\mathrm{nm}$. This oscillation sequence is shown in Figure 5.3b.

In terms of our atomic hologram, this means that whilst our hologram oscillates at a frequency of $\omega_{\text{hologram}} \approx 12.3\,\mathrm{kHz}$ and period 81.3 µs, the reflectivity of our hologram undergoes *two* oscillations. We should therefore expect to see a contrast signal with frequency $\omega_{\text{contrast}} \approx 24.6\,\mathrm{kHz}$ and period 40.7 µs.

5.2 Experimental realisation

5.2.1 First detection and confirmation of a contrast signal

The development of our contrast interferometer was not a quick or easy process; around a year passed between our first observation of momentum interferometer fringes and the appearance of a contrast interferometer signal. In retrospect I think this is mainly because we had preconceptions about what the signal would look like when we found it. We had anticipated a reflected beam with an obvious sinusoidal modulation, because that is how the data has been presented in previous literature. In fact the probe and detection method we were using did not return such an obvious contrast signal until we addressed weaknesses in the techniques used.

For example, our initial attempts used one of our atom-optic lasers as the probe beam, with a simple Silicon BPX65 photodiode circuit as a photon-detector. We thought this was sensible, since our atom-optics were already necessarily aligned with the BEC atoms. However, our atom-optic lasers are tuned with an intensity and frequency detuning appropriate to *that* task. The refractive index of a BEC is sensitive to the detuning of the incident light (see equation 5.1) [109], but our atom-optics are detuned approximately $4.5\,\mathrm{GHz}$ from the D_2 line (around 800 linewidths). The probe frequency we eventually settled on had a detuning at around $295\,\mathrm{MHz}$ (around 50 linewidths). Comparing these two detunings using equation 5.1, we see that the refractive index modulation ($\eta - 1$) of the condensate at our atom-optics frequency is some 50 million times smaller than at our current probe frequency. The reflected intensity was, to put it mildly, significantly lower the sensitivity of our BPX65 photodiode.

We realised this sensitivity of the refractive index to light frequency when performing some reflectivity calculations. Our first adjustment was a modification to our optics setup, pulling a new probe laser from the ‘cooling’ MOT laser (see Section 2.3 and Figure 2.2.2). This new probe was controlled with an AOM, and mode matched with the atom-optics beam (see Section 2.3.8). The second adjustment was the replacement of our silicon BPX65 photodiode with a C12703-1 Series Hamamatsu Avalanche Photodiode Module (APD).

It was with these adjustments in place that we saw the first signal from our contrast interferometer. At this time the interferometer was in the ‘long’ configuration, with the contrast interferometer probe taking the place of the usual closing beam-splitter pulse. The signal we observed was *not* the 24.6 kHz sinusoidal modulation we were expecting. Instead, we saw a brief ‘bump’ in light captured by our APD when the contrast sequence was triggered, shown in Figure 5.4a.

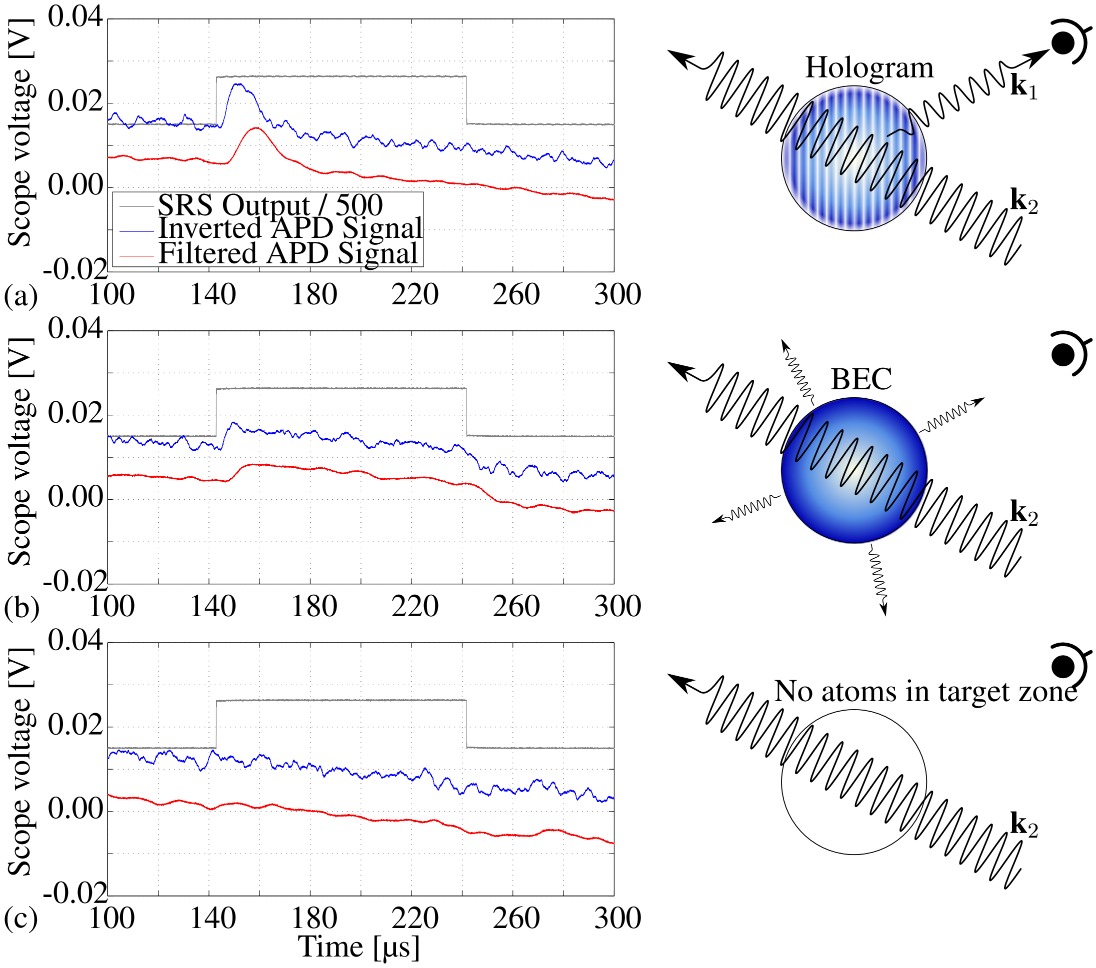

Figure 5.4: The first confirmation of a contrast interferometer signal. Drawn here is the probe control signal (grey lines), raw APD voltage (blue lines), and low-pass filtered APD voltage (red lines). (a) When the complete interferometer sequence has been fired and a set of matter-wave fringes generated, we observe a distinct increase in reflected light. (b) The absence of the same feature when a BEC alone is present suggests that the signal observed in (a) is *not* fluorescence. (c) Likewise, the absence of light in the absence of atoms indicates that the signal observed in (a) is also not a stray reflection of the probe beam from some optical element of the science chamber.

To determine whether the bump shown in Figure 5.4a was indeed a contrast signal and not fluorescence or leakage light, the sequence was run with some modifications to compare. Figure 5.4b shows the captured light without any atom-optics applied, such that a BEC is created and the readout probe fired, but there is no interference fringe present (i.e. A BEC with no interference fringes). We see a low level light value above the background over the whole duration of the probe, but no spike in output as shown when fringes are present. Figure 5.4c shows the captured light when the MOT beams are blocked (i.e. when no atoms are present). Here we see no obvious extra light due to the pulse. From this we infer that reflections from the science chamber and optics are *not* the source of the detected signal in Figure 5.4a.

Figure 5.5 shows an absorption image captured at the end of this interferometer sequence, with the contrast probe active (red dashed line) and disabled (black solid line). A time of flight has projected the different momenta into spatially separated clouds. To this data we have fitted Gaussian envelopes to extract the relative atomic populations of each momentum state.

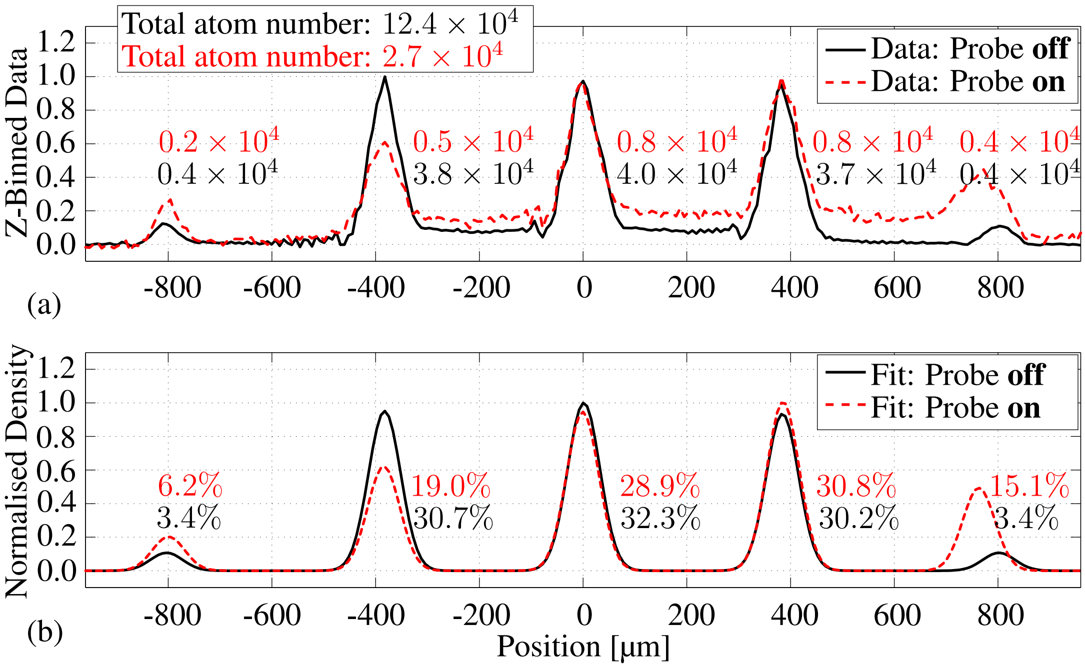

Figure 5.5: (a) An absorption image captured at the end of the experimental sequence, with the contrast probe laser (red dashed line) and without (black solid line). Time of flight has projected the various momentum states into spatially separated clouds. (b) We extract the population in each momentum state by fitting Gaussian envelopes to each cloud. That we see a population transfer between the momentum states implies the presence of discrete $\delta p = +2\hbar k$ momentum kicks, confirming the existence of coherent scattering of the probe beam.

Incoherent scattering here induces two momentum kicks per scattering event; one in the direction of the probe beam along $\boldsymbol{k}_2$ from the absorption of a photon, and one from the *spontaneous* re-emission of a photon in a random direction. The presence of significant incoherent scattering should 'wash out' the discrete spatial localisation of the atomic clouds, generating a raised pedestal of atoms in the absorption image.

Coherent scattering of the probe laser also imparts two momentum kicks per scattering event; one in the direction of the probe beam along $\boldsymbol{k}_2$ from the absorption of a photon, and one opposite the wave-vector $\boldsymbol{k}_1$ from the *stimulated* re-emission of a photon into the Bragg-reflected mode. The presence of significant coherent scattering should induce discrete $\delta p = 2\hbar k$ momentum kicks, transferring atomic population between the atomic clouds whilst retaining the localisation of atoms in those discrete clouds.

The expected magnitude of the incoherent scattering component can be calculated. The intensity of our readout beam is given by

$$I_{\text{probe}} = \frac{13.5 \times 10^{-6} W}{\pi (100 \times 10^{-6})^2} = 42.9\,\text{mW}/\text{cm}^2, \tag{5.3}$$

and the incoherent scattering [103] given by

$$\gamma_{sc} = 2\pi \times 6.06 \times 10^6\,\text{Hz} \times \frac{42.9/2.5}{1 + 42.9/2.5 + 4(46)^2} = 38.5 \times 10^3\,\text{s}^{-1}, \tag{5.4}$$

so for our 20 μs probe pulse each atom scatters 0.77 photons, and we should therefore expect our initial atom count of 12.4 × 10^4 atoms to fall to 2.7 × 10^4, which is what we find experimentally.

The pedestal shown in Figure 5.5 is approximately 1600 μm wide (and vertically binned), and is approximately triangle shaped with a with a binned-column-density of approximately 0 at $x = -800\,\mu\text{m}$ and approximately 0.2 at $x = +800\,\mu\text{m}$. From this we can naively calculate the number of atoms in the pedestal at

$$N_{\text{pedestal}} = \frac{\text{Area under absorption curve}}{\sigma_{0\,(|F=2,m_F=2\rangle \to |F=3,m_F=3\rangle)}} \approx \frac{1600 \times 10^{-6}\,\text{m}^2 \times 0.5 \times 0.2}{2.9 \times 10^{-13}\,\text{m}^{-2}} = 8.8 \times 10^4\,, \tag{5.5}$$

for a population in the pedestal of approximately 9×10^4 atoms. From this we infer that the atoms 'missing' from our discrete momentum clouds are those which have been incoherently scattered into the atomic pedestal.

Our contrast interferometer relies on the coherent scattering of our probe beam from the BEC, so what we want to see in our absorption data is this discrete transfer of atoms between the spatially localised clouds, ideally with no pedestal of atoms between those discrete modes. In reality we see both of these effects, but most importantly the discrete population transfer is clearly visible in the $P(-2\hbar k)$ mode at -400 μs. The three $P([-2, 0, +2]\hbar k)$ peaks have been generated with nearly equal probability, but the $P(-2\hbar k)$ peak has lost around a third of its fractional population after the probe.

Taken together with the detected photon signal in Figure 5.4, we felt confident that we had indeed observed a contrast interferometer signal. However, we expected some periodic oscillation with a period of $\sim 40\,\mu\mathrm{s}$. Averaging of the filtered APD signal revealed something consistent with a very small second hump around $\sim 40\,\mu\mathrm{s}$ after the first obvious hump. The key to this behaviour was the realisation that the scattering process we were using to extract the contrast signal was also destroying the hologram as we were probing it.

5.2.2 Contrast signal decay and probe intensity

Our hologram is generated when the three momentum states $|-2\hbar k\rangle, |0\hbar k\rangle, |+2\hbar k\rangle$ spatially overlap. If we were to remove atoms from one of these modes, the interference fringes we read lose contrast, which in turn reduces the reflectivity of the hologram. Since the reflection of probe photons reduces the population in the $P(-2\hbar k)$ mode, as is shown in Figure 5.5, we should expect an exponential decay of the contrast signal as this mode is depleted, with a time constant inversely proportional to the power of the probe laser. Our first adjustment at this time was a reduction in the intensity of our probe light (to around $1.5\,\mu\mathrm{W}$, from $\sim 10\,\mu\mathrm{W}$), which yielded data such as that shown in Figure 5.6a, containing four clear oscillations at a frequency of $\sim 24\,\mathrm{kHz}$, modulated by an exponential decay with a time constant on the order of $100\,\mu\mathrm{s}$.

We reasoned that if our probe light was destroying the hologram, we should be able to influence the rate of the exponential decay in our contrast signal by altering the probe's duty cycle. In this way we could perhaps extend the useful duration of the signal whilst retaining its amplitude. Figure 5.6 shows an examination of this effect. Our signal decay constant with a full duty cycle is $66\,\mu\mathrm{s}$. When we halved the duty cycle we observed a two-fold increase in decay constant to $132\,\mu\mathrm{s}$, shown in Figure 5.6b. The strength of this correlation implied that the probe-induced reduction in hologram contrast was the dominant loss mechanism in the contrast signal.

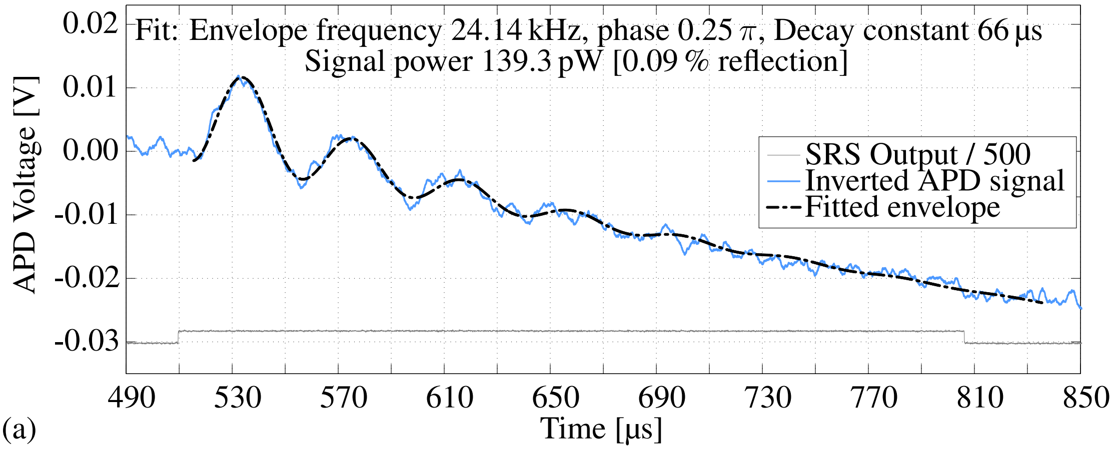

(a)

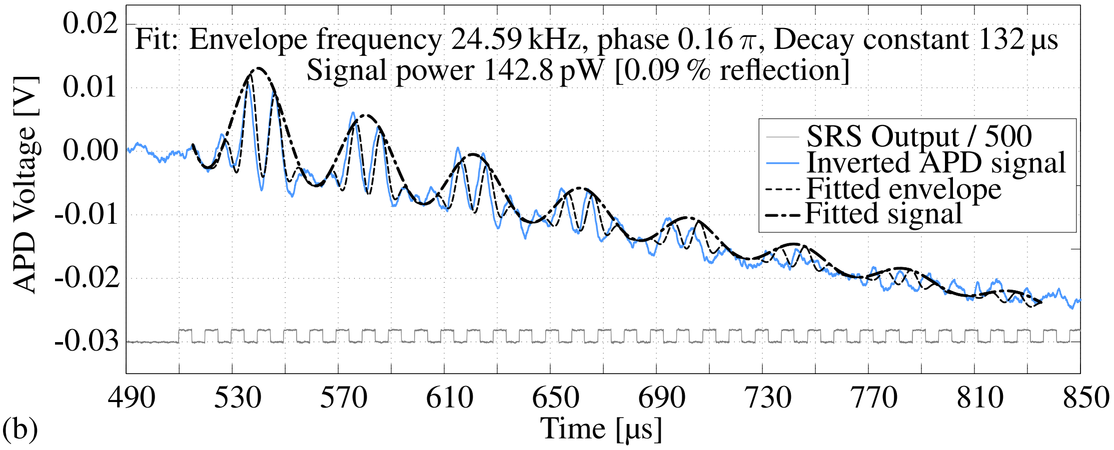

(b)

Figure 5.6: A comparison of contrast interferometer decay constants with the probe intensity set to a (a) 100 % and (b) 50 % duty cycle. The probe control is drawn in grey, the raw APD voltage in blue, and the fitted contrast envelope in dot-dashed black lines. We observe a decay constant of 66 µs with the 100 % duty cycle, and 132 µs with the 50 % duty cycle. The maximum bandwidth of the APD was $\sim$ 100 kHz, which is why the light-modulations within the half-duty-cycle signal appears as a sine-wave. A relatively large background light level ($\sim$ 3 nW) has been subtracted in processing.

5.2.3 Detection with a Single-Photon Counting Module

Whilst we now had access to around six usable periods from our contrast interferometer, we were still relying on the averaging of data from the APD. Since part of the attraction of contrast interferometry is the enhanced data acquisition rate, we wanted to be able to detect weaker reflection signals. This would allow us to (1) further reduce the probe intensity to extend the duration of the contrast signal further, and (2) to enable access to single-shot measurements. To this end we installed an Excelitas SPCM-AQRH-14-FC fibre-coupled Single-Photon Counting Module (SPCM), which is described in Section 2.4.

Using the SPCM we were able to reduce our probe intensity by around a hundred times to $\sim 15\,\mathrm{nW}$ (this was done by placing an ND filter into the probe optical path). An example of the data captured from a long contrast interferometer is shown in Figure 5.7.

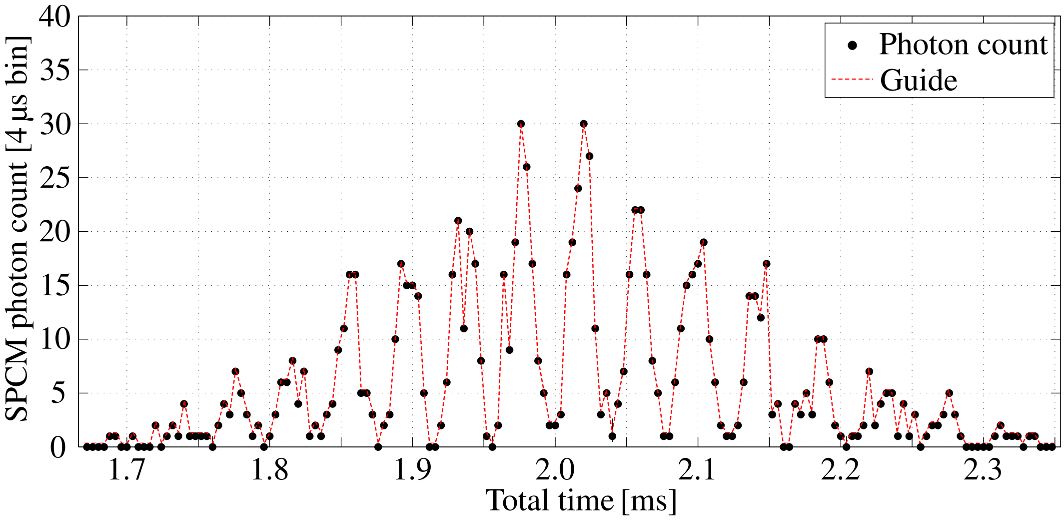

Figure 5.7: A Single-Photon Counting Module (SPCM) was used to reduce the required probe intensity, dramatically increasing signal quality. The recoil-induced atom loss no longer dominates, and we observe an envelope function. This interferometer was configured with a split → reflect time $T_1 = 1000\,\mu\mathrm{s}$, and reflect → probe time $T_2 = 400\,\mu\mathrm{s}$. A peak photon count of 30 photons in a 4 µs bin, gives us an approximate peak signal of 2 pW.

Figure 5.7 shows a contrast signal with a peak photon count of 30. Given that the energy of a photon at our 780 nm probe wavelength is given by

$$E_{\text{photon}} = hf = h\frac{c}{\lambda} = 6.63 \times 10^{-34}\,\mathrm{J\,s} \times \frac{3.00 \times 10^{8}\,\mathrm{m\,s}}{780\,\mathrm{nm}} = 2.55 \times 10^{-19}\,\mathrm{J}, \tag{5.6}$$

we can determine the peak power of our typical contrast signal as

$$P_{\text{contrast}} = 30\,\text{photons} \times 2.55 \times 10^{-19}\,\mathrm{J} \times \text{photon} \div 4\,\mu\mathrm{s} = 1.91\,\mathrm{pW}. \tag{5.7}$$

Assuming equal hologram reflectivity as that shown in Figure 5.6, this reduction in probe intensity of $\sim 100\times$ should increase photon-recoil-induced decay constant to several milliseconds, effectively removing the photon-recoil associated signal decay as a dominant factor in the measured signal. This allows us to see the underlying envelope of the contrast signal without our probe light destroying the hologram as we probe it. In addition, we now had the photo-sensitivity to perform single-shot measurements.

5.3 Extracting information from single-shot data

5.3.1 Numerical Model Fitting

A typical method of extracting information about a parameter from some set of data is model fitting. Here we generate some mathematical model that takes a series of input parameters (including the one we want information about) that aims to match the data we see. We construct some sort of metric that quantifies how well the model matches the data (a goodness-of-fit) parameter, and we try to minimise this goodness-of-fit parameter numerically by altering the model's input parameters. When the fitting algorithm finds a minimum of the goodness-of-fit, the corresponding model parameters are considered to be the best estimate of those parameters in the data. Typically the error bars accompanying the data are then processed numerically to estimate the uncertainty in those fitted parameters.

A very common goodness-of-fit parameter is the χ^2 [144], which takes the form

$$\chi^2 = \frac{1}{n}\sum_{i=1}^{n}\frac{(y_i - u(x_i))^2}{\alpha_i^2}\ , \tag{5.8}$$

where in a set of discrete data n samples long, y_i is the observed data value at the ith index, and $u(x_i)$ is the value our model returns at the ith index, and α_i is the uncertainty associated with the ith measurement.

A fitting algorithm will typically require a set of initial 'guess' parameters $\boldsymbol{p}_0$ from which the algorithm starts. The algorithm then calculates the χ^2 and attempts to numerically determine how to alter these parameters in order to reduce χ^2. It then repeatedly performs the same calculations over N iterations. A very naive way to accomplish this χ^2 minimisation is to reduce the derivatives $\mathrm{d}\chi^2/\mathrm{d}\boldsymbol{p}$ to zero. One of the simplest numerical methods for this is the Newton-Raphson method (see equation 5.17) [144]. If we numerically calculate the derivative of our model with respect to our input parameters, we can then use this Newton method to reduce those derivatives to zero. When the derivatives have fallen below some acceptable tolerance, we say that the algorithm has converged on a fit. We then have a set of fit parameters, a numerically calculated set of uncertainties on each parameter, and the χ^2 value of this converged fit.

Given that we expect uncertainties in our measured data, we should also expect that the model will not exactly touch all of our measured data points. If the error bars we have measured are the $1\,\sigma$ confidence intervals for each data point, we should expect that $\sim 68\,\%$ of the error bars cross the fitted model (because in the other $32\,\%$ of instances, the 'true' data value lies outside the error bars). The χ^2 goodness-of-fit quantifies this aspect of our fit; if the $\chi^2 \gg 1$, it implies that the model does not follow our data closely enough, because the model implies that too many of the 'true' values of our data lie outwith our measured error bars. Conversely, if the $\chi^2 < 1$, it implies that our model is following our data *more* closely than we should expect statistically, because too few of the 'true' data values lie outside our measured error bars. A χ^2

of 1 corresponds to a balance between these scenarios, where the distribution of data around the fitted model satisfies the statistics of our randomly sample noise in the data.

5.3.2 Data dominated by Poisson noise

Our data presents us with a pair of problems that we must address before we can use a fitting algorithm to extract information from our contrast interferometer signal. Firstly, our data is an array of single shot measurements. This means that we have no measured statistics with which we can estimate the uncertainties in each photon count. Related to this is our second problem; that our contrast signal typically contains counts ranging from zero to a few tens of photons. In this regime Poisson statistics dominate the counting of photons from a given ‘true’ number.

The above statements may initially appear to be contradictory. If we know that the counting of photons is dominated by Poisson statistics, how can we not know the uncertainties on our measurements? The distinction is this: if λ photons are incident on our photodetector, the Poisson distribution tells us the probabilities of measuring k photons in that photo-detector. Our contrast signal is not an array of photon numbers, but an array of photon *measurements*. That is, we have the k, but not the λ. There is a subtle point to be made here; if I measure 0 photons in some experiment, there is a non-zero probability that there was actually 1 photon present. If I instead measure 1 photon, there *cannot* have been 0 photons present. At these low counts the Poisson distribution is *significantly* different from the uncertainties we should expect in our data.

What we need to do is use the Poisson distribution to generate a new distribution that does tell us the probability of the photon number λ, given that we have measured k. Essentially this is a Bayes’ Theorem problem [144], where the Poisson distribution gives us $P(k|\lambda)$ (The probability of measuring k, given that λ has occurred), and we want to use this to ‘invert’ the Poisson distribution into the new distribution $P(\lambda|k)$ (The probability that λ occurred, given that we measured k),

$$P(\lambda|k) = \frac{P(k|\lambda)P(\lambda)}{P(k)} \,. \tag{5.9}$$

The second problem we have is in finding a goodness-of-fit parameter for our fitting algorithm. The χ^2 definition in equation 5.8 has a term of the form $(y_i - u(x_i))^2$. This means that the χ^2 makes no distinction between a data-point being above or below the fitted model curve. Given that the Poisson distribution is asymmetrical, it is reasonable to assume that the ‘Bayesian inverted’ distribution that describes the uncertainties around our contrast signal photon counts is also asymmetrical. The symmetrical nature of the χ^2 renders it incapable of respecting the asymmetry of uncertainties of our photon counts, and thus an inappropriate goodness-of-fit parameter in this instance [145].

We then need to find an appropriate goodness-of-fit parameter, and a fitting algorithm compatible with our data. For this we can use a ‘log likelihood’ estimator [146], to which we can apply a Newton method.

5.3.3 Inferring error bars from single-shot photon-counts

What we want to do is infer confidence bands on what the true photon count probably is, given that we have a single measurement of it. A similar problem is examined in [147] using a binomial distribution. The argument here is that the since the probability of a given measurement x of some quality given a 'true' distribution with parameters n, p is

$$P(x|n,p) = \binom{n}{x} p^{x} \left(1-p\right)^{n-x} \ , \tag{5.10}$$

we can build up a graph of the confidence bounds for obtaining a measurement x from the distribution over n measurements, shown in Figure 5.8. Since all possible outcomes are contained in this space, the entire system is normalised. We can then flip the axes, and read the confidence bounds for the 'true' parameter p given the measurement x.

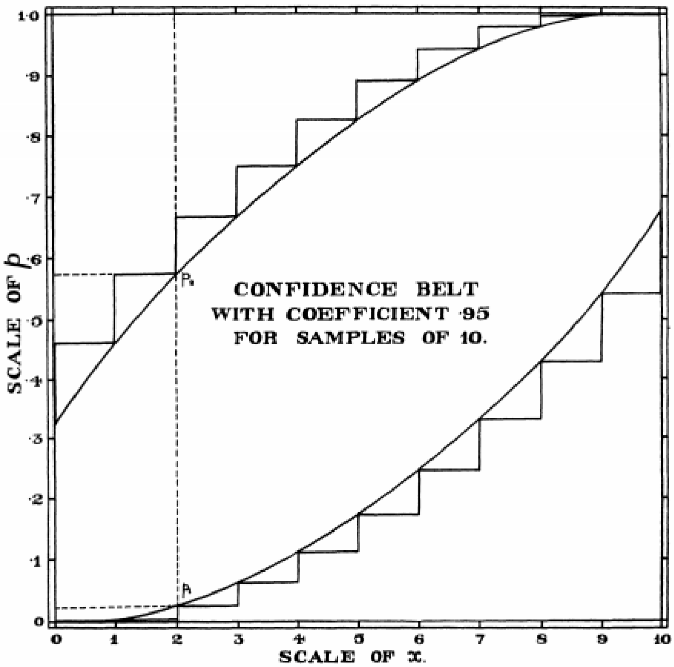

FIG. 1

* In the charts described below the coefficients ·95 and ·99 were chosen as giving two useful pairs of limits. It is not essential that the intervals chosen should be "central," but for many purposes this appears to be the most convenient arrangement.

Figure 5.8: Taken from [147]. Here p is the fractional probability of some property like a coin being marked 'heads', where we observe x heads in our sample of ten coins. The figure is 'constructed' sideways, generating the confidence bounds for measuring a *sample* x of the true distribution p, mapping the entire probability space to the interior of the square bounds.

If we have a sample of ten coins which can either be marked 'heads' or 'tails', then x is the fraction of our sampled coins which are heads (for example). We can use this sample x to predict the fraction of *all* coins that are heads p. This process is known as fiducial confidence estimation.

If our contrast signal is dominated by photon shot noise, the statistics we need to consider are Poisson,

$$P(k|\lambda) = \frac{\exp(-\lambda)\,\lambda^k}{k!}\ , \tag{5.11}$$

where $P(k|\lambda)$ is the probability of measuring k photons if λ photons are present. We can accomplish the same 'probability inversion' for the Poisson distribution by generating confidence bounds for every possible photon number λ up to some arbitrary value above our measurement maximum of 100 photons.

For each possible photon mean number, we generate a Poisson distribution with the mean as parameter λ , and generate a cumulative probability distribution for measuring k photons. We then interpolate this cumulative distribution to find where the required confidence intervals lie, as shown in Figure 5.9a. These are plotted horizontally for each mean in Figure 5.9b (open circles). We read the figure by interpolating each bounded region to find the points directly above and below our measurement (respectively closed circles, and black squares). These represent the confidence bands that our mean lies within, given a photon measurement.

We can see in Figure 5.9 that unlike the binomial case, our Poisson mapping has no upper bound: it doesn't include every possible outcome. It is nevertheless still valid because it *is* lower bounded; we can generate the distributions up beyond some arbitrary cut-off, and have all the *relevant* cumulative probability be mapped out. That is, we know our distribution, so we know that the bulk of probability density is clustered around the mean, and the unmapped 'high' end is left outside our region of interest. If we require some specific confidence bound, for example 99 %, we can extend our probability map until that confidence level is within the map boundaries. The unmapped region is then outwidth the confidence interval of interest. This is only valid because we assert that the distribution is known.

Usefully, our data tells us what this maximum count is likely to be. For example, the data shown in Figure 5.10 has a maximum photon count of $k = 30$. If we generate Poisson distributions with every λ up to 50, we have mapped out $99.5\ \%$ of the possible true photon counts that result in a measurement of $k = 30$. If our maximum photon count was $k = 2$, we can see from Figure 5.9 that we would need to calculate up to $\lambda = 11$ to incorporate the $3\,\sigma$ cumulative probability bounds.

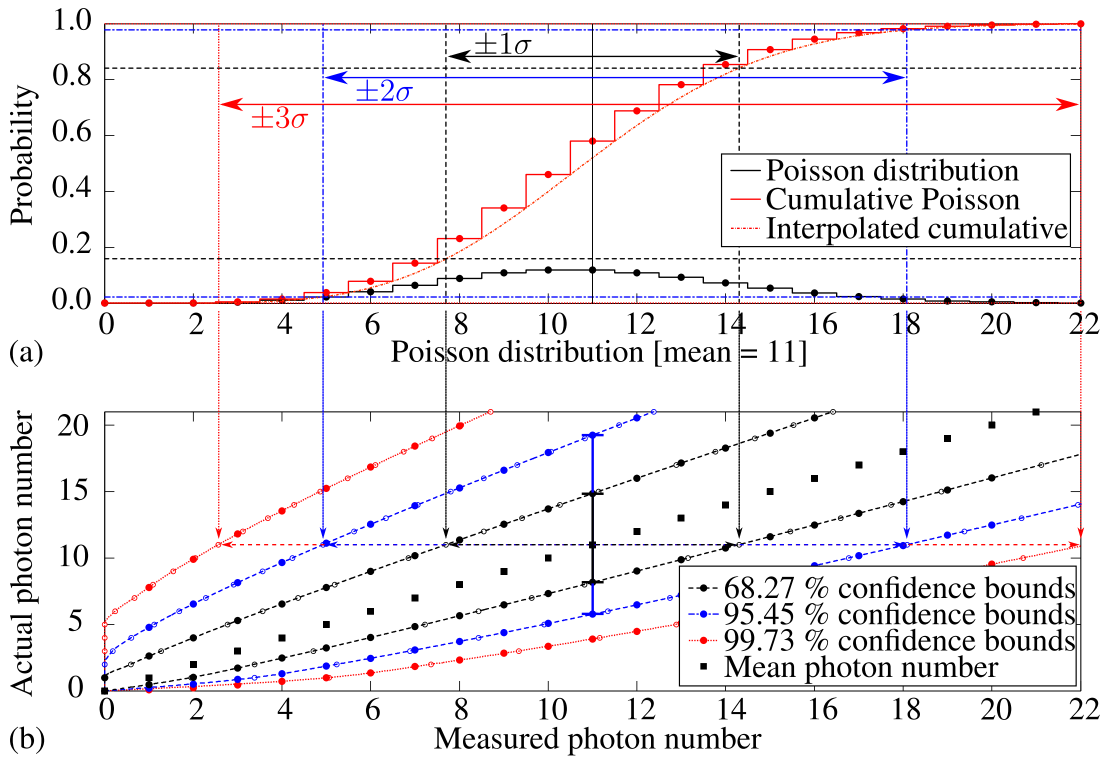

Figure 5.9: Top: Confidence bands for a Poisson distribution with mean number of 11 photons. We generate a cumulative probability distribution, and read off measured photon values where the cumulative probability reaches a given tolerance. Bottom: These values are plotted horizontally, generating an envelope in which we are confidence that one (black), two (blue), or three (red) sigma of measurements will lie. We then read the confidence bands for a given measurement by interpolating these bounds to a given measured sample number and reading vertically.

Figure 5.9 shows an example of the distribution inversion algorithm centred on the value $\lambda = 11$. Figure 5.9a shows the Poisson distribution for this λ as the black stepped line. The corresponding cumulative Poisson distribution is shown as the red stepped line. The red interpolated line under this is the interpolated cumulative Poisson distribution. We generate confidence bounds on measuring k photons by checking the photon counts where the interpolated cumulative distribution crosses various probability levels. The mean k always lies where the cumulative distribution crosses $P = 0.5$. Likewise, the $\pm 1\sigma$ intervals lie where the cumulative distribution crosses $P = 0.5 \pm 0.341$.

These confidence bounds are plotted in Figure 5.9b, horizontally. That is, for a given λ we calculate the corresponding mean k with confidence intervals σ. We then plot that $k \pm \sigma$ along the x-axis at a position λ up the y-axis. We continue this process for increasing λ values, until the left-most confidence interval crosses the maximum photon count we measure.

At this point we have mapped out all of the possible λ and k combinations relevant to our data set up to the confidence interval we earlier selected (as in Figure 5.9b). In this map of probability space, the distribution $P(k|\lambda)$ (the Poisson distribution) represents the sub-space horizontally where $y = \lambda$. The distribution that we want ($P(\lambda|k)$) is the subspace *vertically* where $x = k$.

We then write the total probability map to a look-up-table for later processing. Since this algorithm takes only a few minutes to run, and we need only do it once, the actual look up table was written to a maximum of $\lambda = 250$, which turned out to be several times higher than any of our contrast data required.

Figure 5.10 shows the SPCM data from Figure 5.7 with error bars generated with the above method. Each error bar represents the $1\,\sigma$ confidence interval for the 'true' photon number in each bin, given the measured count. We can see that the uncertainties are distinctly asymmetrical at low photon counts, but tend towards symmetrical distributions as the count increases.

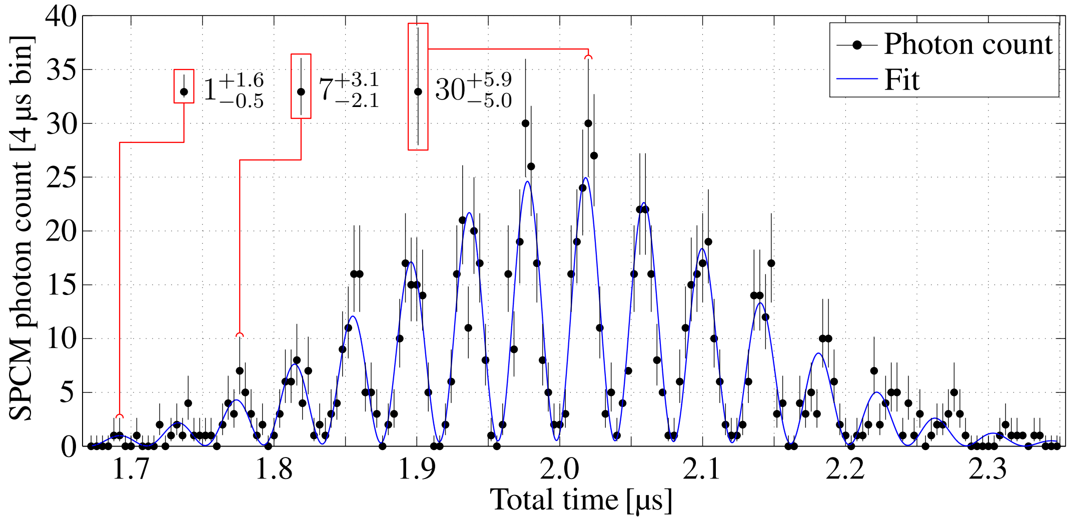

Figure 5.10: A single-shot SPCM contrast signal with errors. The 'inverted' uncertainty distribution shown in Figure 5.9 has been used to generate $1\,\sigma$ confidence intervals for the value of the true photon count given the measured count. The fit is the result of a χ^2 minimisation routine, and is included as a guide to the eye (discussed in Section 5.3.1). Inset are some example errors, which are highly asymmetrical at low photon counts.

5.3.4 Maximum Likelihood fitting for data dominated by Poisson noise

The definition of the χ^2 includes a term of the form $\frac{1}{n}\sum_i^n (y_i - u(x_i))^2$ (see equation 5.8), where y_i is the ith data point and $u(x_i)$ is the value of a model at the ith data point. This definition is symmetrical; it returns an identical value regardless of whether the data point in question is above or below the model. An alternative metric which can respect asymmetrical uncertainty distributions is the ‘likelihood estimate’, in an optimisation process that is generally referred to as ‘Maximum Likelihood Estimation’ (MLE) [146].

One such analysis designed specifically for handling Poisson uncertainties is described in [146], where the authors fit a Gaussian model to data of the wavelength of photons Thomson scattered from a plasma to obtain information about the plasma’s temperature. We can apply the same approach to our data. We have a model of the ‘true’ photon number $u(\boldsymbol{x}, a_1, \ldots, a_M)$ that we want to fit to our data points $y_i(x_i)$, where x_i are our times at each index i, $a_1 \ldots a_M$ are our M parameters, and y_i the values of our data points. The Poisson distribution is given by

$$P_i = \frac{\exp[-u(x_i)]u(x_i)^{y_i(x_i)}}{y_i(x_i)!} \;, \tag{5.12}$$

so the probability of a specific measurement of N samples is given by

$$P = \prod_{i=1}^{N} \frac{\exp[-u(x_i)]u(x_i)^{y_i(x_i)}}{y_i(x_i)!} \;. \tag{5.13}$$

The point of maximum likelihood corresponds to a set of parameters that generate a mean which is most likely to result in our measurement. This occurs when the partial derivatives of equation 5.13 are zero. The calculation of the partial derivatives of the product in equation 5.13 are numerically expensive, so we can instead take the log of equation 5.13 to convert the product into a sum, and instead take the derivative of that function. We can then attempt to set the ‘log likelihood’ to zero:

$$L_j = \frac{\partial}{\partial a_j}(\ln P) = \sum_{i=1}^{N} \frac{\partial u(x_i)}{\partial a_j}\left(1 - \frac{y_i}{u(x_i)}\right) = 0 \;, \tag{5.14}$$

where this minimisation method is known as Maximum Likelihood Estimation (MLE).

In our case we model our data with a cosine wave with a Gaussian envelope

$$u(\boldsymbol{x}) = a_1 \exp\left(-\frac{(\boldsymbol{x} - a_3)}{(2a_2^2)}\right)\frac{\Delta x}{2}\left[\cos\left(2\pi a_4 \boldsymbol{x} + a_5\right) + 1\right], \tag{5.15}$$

where the parameters are envelope amplitude (a_1), envelope width (a_2), envelope centre (a_3), cosine frequency (a_4), and cosine phase offset (a_5), and Δx is our measurement bin width.

We obtain our likelihood functions by passing equation 5.15 through equation 5.14, obtaining

$$\begin{aligned}
L_1 &= \sum_{\mathrm{i}=1}^{\mathrm{N}} \left(u(x_\mathrm{i}) - y_\mathrm{i}\right) \\
L_2 &= \sum_{\mathrm{i}=1}^{\mathrm{N}} \left(u(x_\mathrm{i}) - y_\mathrm{i}\right) \frac{(x_i - a_3)^2}{a_2^3} \\
L_3 &= \sum_{\mathrm{i}=1}^{\mathrm{N}} \left(u(x_\mathrm{i}) - y_\mathrm{i}\right) \frac{(x_i - a_3)}{a_2^2} \\
L_4 &= -\sum_{\mathrm{i}=1}^{\mathrm{N}} \left(u(x_\mathrm{i}) - y_\mathrm{i}\right) \sin\left(2\pi a_4 x_\mathrm{i} + a_5\right) 2\pi x_\mathrm{i} \\
L_5 &= -\sum_{\mathrm{i}=1}^{\mathrm{N}} \left(u(x_\mathrm{i}) - y_\mathrm{i}\right) \sin\left(2\pi a_4 x_\mathrm{i} + a_5\right) \ .
\end{aligned} \tag{5.16}$$

We then use a Raphson-Newton secant-method (see Equation 5.19) to find the roots of Equations 5.16 by starting from set of initial guess parameters $\boldsymbol{a}_0$, then calculating the gradient of $\boldsymbol{L} = (L_{j=1} \ldots L_{j=M})$, and following the gradient descent to a local minimum.

In one dimension, we can find the root of a function $f(x)$ by iterating from an initial x_0 using the Newton-Raphson method [144], by iterating

$$x_{n+1} = x_n - f(x) / \frac{\mathrm{d}f(x)}{\mathrm{d}x} \ . \tag{5.17}$$

We generalise this to our M-equation, M-parameter system using the Jacobian

$$\boldsymbol{J}[\boldsymbol{L}(\boldsymbol{a})] = \left[\frac{\partial \boldsymbol{L}}{\partial a_1} \cdots \frac{\partial \boldsymbol{L}}{\partial a_M}\right] = \begin{bmatrix} \frac{\partial L_1}{\partial a_1} & \cdots & \frac{\partial L_1}{\partial a_M} \\ \vdots & \ddots & \vdots \\ \frac{\partial L_M}{\partial a_1} & \cdots & \frac{\partial L_M}{\partial a_M} \end{bmatrix} , \tag{5.18}$$

which we estimate numerically [148]. This results in an M dimensional Raphson-Newton algorithm like

$$\boldsymbol{a}_{n+1} = \boldsymbol{a}_n - \alpha \boldsymbol{J}[\boldsymbol{L}(\boldsymbol{a}_n)]^{-1} \boldsymbol{L}(\boldsymbol{a}_n) \ . \tag{5.19}$$

By iterating this process from a suitable initial guess $\boldsymbol{a}_0$, we converge on a solution $\boldsymbol{a}_n$ which represents the parameters of the model which is the most likely to have generated our measurements y_i.

In practice, the gradient descent is less efficient and less stable than more eloquent 'derivative-based' algorithms like the Gauss-Newton or Levenberg-Marquardt, but many of these alternatives require a scalar 'goodness-of-fit' parameter. We could recreate this, but in doing so we would have to combine the M number of L_M terms in some arbitrary fashion, most likely shifting the 'optimal' fit point. Instead, we stabilise the gradient descent with a damping parameter α (see equation 5.19). This damping parameter is set to some constant base value (50 is typical for real data), and divided by the χ^2 at each fit iteration,

$$\boldsymbol{a}_{n+1} = \boldsymbol{a}_n - \left(\frac{\alpha}{\chi_n^2}\right) \boldsymbol{J}[\boldsymbol{L}(\boldsymbol{a}_n)]^{-1} \boldsymbol{L}(\boldsymbol{a}_n) \ , \tag{5.20}$$

where the χ^2 has been defined as

$$\chi^2 = \sum_i^N \left(\frac{y_i - u_i}{\sigma_i(+) + \sigma_i(-)} \right)^2 \ , \tag{5.21}$$

and $\sigma_i(+)$ and $\sigma_i(-)$ are confidence bounds upwards and downwards respectively for the ith data point.

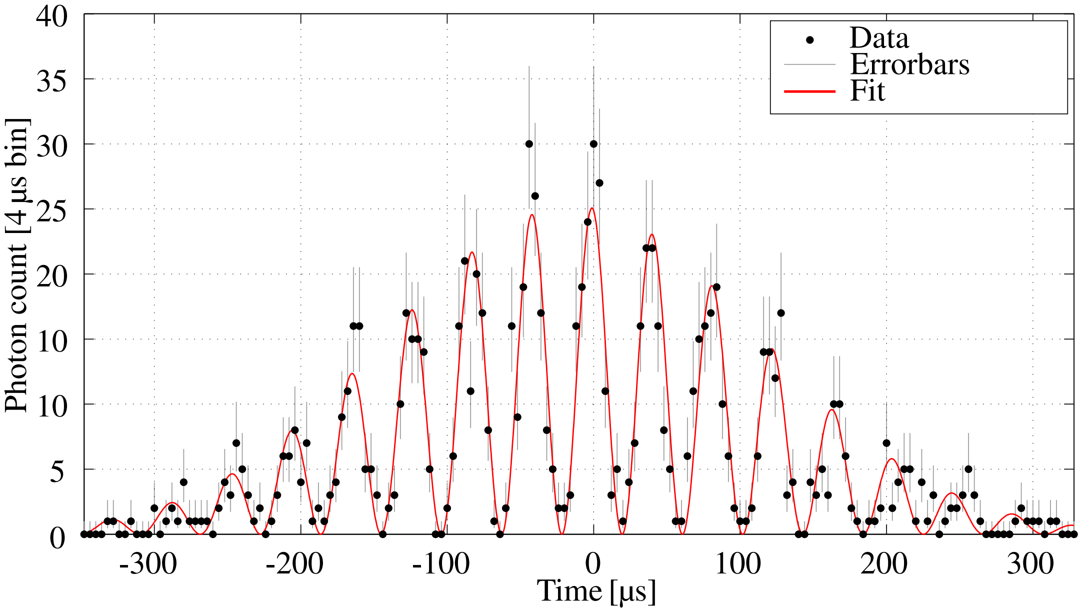

Figure 5.11: Output of the MLE fit algorithm when applied to the data shown in Figure 5.10. The calculation of the uncertainty in fitted parameters is performed by shifting each data-point up and downwards slightly, and refitting to determine $\partial \boldsymbol{a}/\partial y_{\mathrm{i}}$, and combining as shown in equation(5.22). The red trace marks the best fit, i.e. the one that minimises $\boldsymbol{L}$ in equation 5.14.

Once an optimal fit is found, we calculate errors by numerically calculating the gradient $\mathrm{d}a_j/\mathrm{d}y_i$ for every data point y_i, by shifting each y_i slightly and refitting $\boldsymbol{a}$ for each shift. The shift in each case is one photon upwards and downwards, except when the measurement is zero. For zero counts we take the gradient of the secant between the 'zero' and 'one' photon calculations. We then combine these to calculate the total estimated variance in each parameter, $\sigma_{\boldsymbol{a}}^2$

$$\sigma_{\boldsymbol{a}}^2 = \sum_{\mathrm{i}=1}^{\mathrm{N}} \sigma_{y_{\mathrm{i}}}^2 \left(\frac{\partial \boldsymbol{a}}{\partial y_{\mathrm{i}}} \right)^2 , \tag{5.22}$$

where $\sigma_{y_{\mathrm{i}}}^2$ is the uncertainty around the value of our fitted model at each time index. Since the uncertainty distribution of the model *is* given by the Poisson distribution, $\sigma_{y_{\mathrm{i}}}^2 = y_{\mathrm{i}}$. This procedure returns the fit parameters for our SPCM data set as

$$\begin{aligned}
a_1(\text{Amplitude}) &= 6.300,\ (\sigma_1 = 0.251)\ [\text{Photons}/\mu\text{s}] \\
a_2(\text{Envelope Width}) &= 127.063,\ (\sigma_2 = 3.242)\ [\mu\text{s}] \\
a_3(\text{Envelope Centre}) &= -13.652,\ (\sigma_3 = 4.163)\ [\mu\text{s}] \\
a_4(\text{Frequency}) &= 24.295,\ (\sigma_4 = 0.083)\ [\text{kHz}] \\
a_5(\text{Phase offset}) &= 0.171,\ (\sigma_5 = 0.005)\ [\text{rad}]\ .
\end{aligned}$$

With the fit algorithm returning fit parameters with associated uncertainties, we wanted to test the fitting with a range of data. In principle we could have taken a range of data experimentally with various parameter settings, such as temporal bin size and probe intensities, but this would have been time-consuming. Instead we could test the algorithm by simulating the output of our contrast interferometer. This has some significant benefits: (1) Because we were generating the data, we *knew* the 'true' photon counts in our data before shot noise was added, (2) we could generate simulated data much more quickly than we could capture it experimentally, and (3) we could alter the parameters of the simulated data much more easily than we could experimentally.

We generated data first by deciding on a set of model parameters consistent with our experimental contrast signal. We would modify these parameters slightly with some random factor, and from these perturbed parameters we would generate an array of photon counts, like our contrast signal but with no photon shot noise. From this array we would generate a set of simulated contrast signals with random shot noise derived from the Poisson distribution. These sets of data would then be fitted one by one, and the resulting fit parameters, uncertainties, and uncertainties collated.

We had two simulated controls for altering the simulated data. Once was a pre-multiplier on the intensity of the contrast signal (before shot noise was added), and one was the temporal bin width. Using these controls we generated two different sets of fit results.

Figure 5.12a shows the first simulated data fitting run, where the total intensity of the contrast signal remained the same, but we altered the bin-width of the signal. Here the total number of photons in each contrast signal remained nearly constant across all simulated data.

Figure 5.12b shows the second simulated data run, where the total intensity of the contrast signal was scaled inversely to the temporal bin-width, such that the number of bins changed, but the photon count per bin remained nearly constant. In this configuration the number of photons increased with the number of bins across the sample.

We should expect that our fit uncertainties should scale with the total photon count n as $1/\sqrt{n}$. Our fit algorithm recreates this behaviour in both cases.

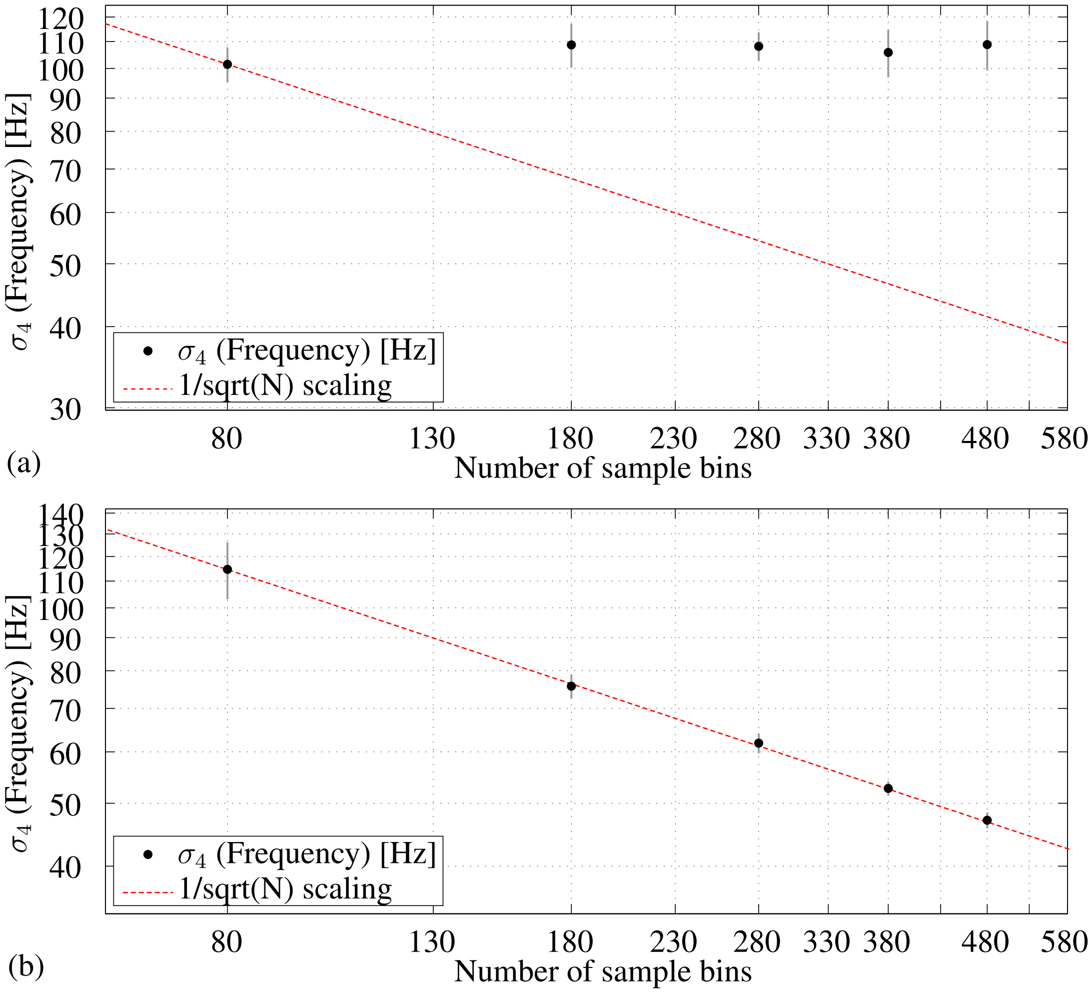

Figure 5.12: Variation in fit error estimation as a function of bin width and total photon count. Multiple data sets were created, and the fit algorithm run on each to return a set of fit parameters, and associated fit uncertainties. (a) The total photon count during each data set is held constant, but the bin width is varied, such that the total photon count across the entire measurement is constant. (b) The total photon count was modified so that the photon count per bin was constant. This caused an increase in photon count linear with the number of bins in the signal.

5.4 Contrast measurement of α

5.4.1 Interferometer configuration

We performed a measurement of the fine structure constant α in Section 4.6.3, where we used a 'short' three-arm interferometer geometry. To recap, the short geometry omits the reflection pulse, instead opening and closing the interferometer with identical splitter pulses separated by a delay time T_{delay}, shown in Figure 5.13. We observe the evolving phase as this delay time varies, where the frequency of the oscillation is tied to the fine structure constant. We can perform the same α measurement with the contrast interferometer in the same 'short' configuration. Figure 5.13 shows a comparison in the pulse sequences between the short momentum interferometer and short contrast interferometer.

Common to both techniques is an opening (1) pulse of 26.6 µs duration and 6.07 $\mathrm{E_r}$ lattice depth, drawn in black. The pulse corresponds to a laser power of approximately 20 µW per beam, and an intensity at the atoms of ~180 mW cm^{-2} per beam. This pulse splits the initially stationary cloud of BEC atoms into a superposition of the $|-2\hbar k\rangle, |0\hbar k\rangle, |+2\hbar k\rangle$ momentum states with respective probabilities $P_p \approx (\frac{1}{4}, \frac{1}{2}, \frac{1}{4})$.

Whilst the momentum interferometer uses a delayed closing pulse (2, red), the contrast interferometer instead uses a single, sustained, probe pulse (drawn in blue (3)) on the order of 10 nW and intensity 0.088 mW cm^{-2} at the atoms. Whilst the splitter pulses are comprised of two beams which form an optical grating, this probe consists of a single laser beam. The use of shutters to change this configuration requires a 120 µs delay after the splitter pulse before the probe can be triggered.

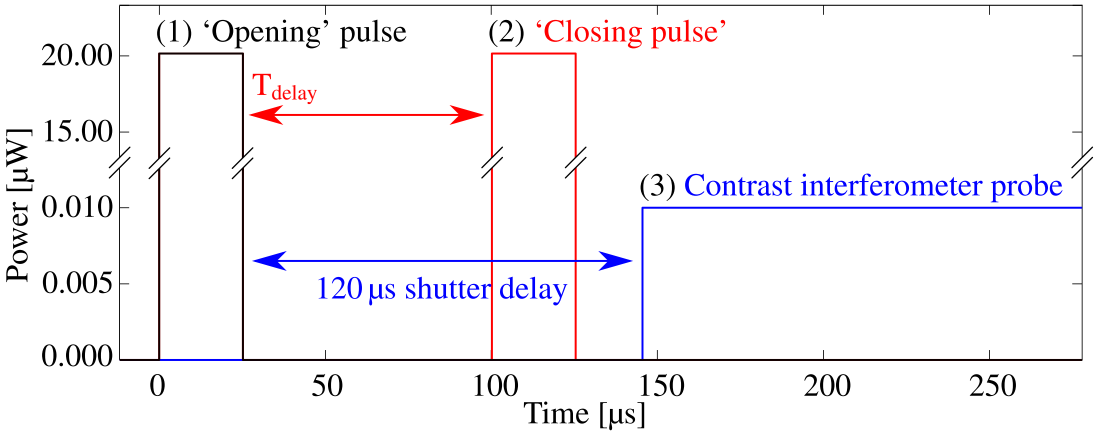

Figure 5.13: Comparison of the interferometer sequences for the momentum and phase-contrast interferometers. Whilst the opening splitter pulse (1) is common to both techniques, the contrast interferometer uses a continuous weak probe beam (3) to probe the evolving matter-wave.

5.4.2 Extracting α information from contrast interferometer data

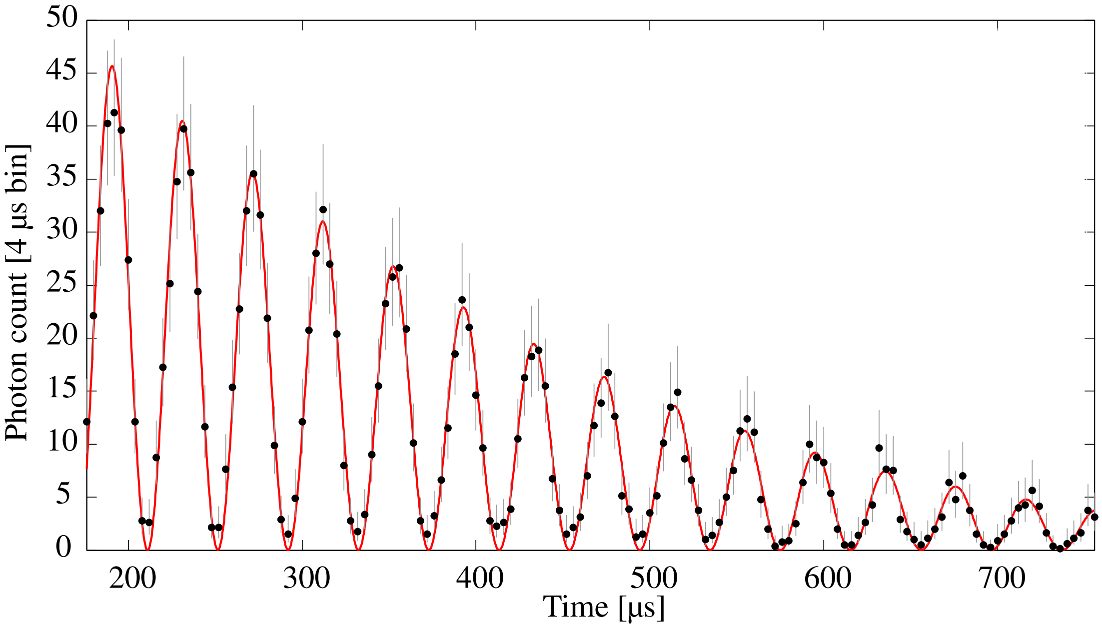

Figure 5.14: An example of single-shot data from the short contrast interferometer. Here photons from a probe laser are reflected from the evolving matter-wave into a Single Photon Counting Module (SPCM), with the detected photon counts shown here as black points. Error bars are calculated as described in Section 5.3.3. The data is fit with our Poisson-sensitive algorithm, where the fit model is a cosine with a Gaussian envelope.

While the contrast interferometer probe is active, photons are Bragg-scattered into our SPCM, shown above in Figure 5.14 as black points. The error bars have been calculated as the fiducial confidence bounds described in Section 5.3.3.

To this data we fit the model,

$$u(\boldsymbol{x}) = a_1 \exp\left(-\frac{(\boldsymbol{x} - a_3)}{(2a_2^2)}\right) \frac{\Delta x}{2} \left[\cos\left(2\pi a_4 \boldsymbol{x} + 2\pi a_6 \boldsymbol{x}^2 + a_5\right) + 1\right] , \quad (5.23)$$

where a sixth parameter a_6 has been added to the model. This parameter is the coefficient for a linear frequency chirp, which will be discussed in Section 6.2. From this fit we extract the parameter values,

$$\begin{aligned}
a_1(\text{Amplitude}) &= +24.21,\ (\sigma_1 = 1.93)\ [\text{Photons/µs}]\\
a_2(\text{Envelope Width}) &= +428.7,\ (\sigma_2 = 10.2)\ [\text{µs}]\\
a_3(\text{Envelope Centre}) &= -523.0,\ (\sigma_3 = 21.7)\ [\text{µs}]\\
a_4(\text{Frequency}) &= +24730,\ (\sigma_4 = 80)\ [\text{Hz}]\\
a_5(\text{Phase offset}) &= -0.450,\ (\sigma_5 = 0.068)\ [\text{rad}]\\
a_6(\text{Frequency chirp}) &= -0.031,\ (\sigma_6 = 0.12)\ [\text{Hz/ µs}]\ .
\end{aligned}$$

We use the same method as shown in Section 4.6.3, using the fitted frequency to obtain an α measurement for this single experimental run, with the exception that our CI returns frequencies twice that of the MI. Here we obtain α^{-1} = 136.74 ± 0.88 (6500 ppm). Once again the majority of this error comes from the uncertainty $\delta\theta \approx 0.5°$. If we assume that the angle uncertainty is zero, we obtain an uncertainty $\delta\alpha^{-1}$ = 0.32 (2300 ppm).

Comparing the contrast interferometer (CI) measurement here to the momentum interferometer (MI) measurement in Section 4.6.3, we can see that the experimental uncertainties are of the same order of magnitude. Despite this, the CI retains a few advantages: most obviously, the above measurement uses 146 data points to measure the fine structure constant in a 30 second acquisition period. If we attempt the same measurement with the MI, we accomplish the same in a $\sim$ 6 hour period (146 data points $\times$ 5 experimental runs per data point $\times$ 30 seconds per experimental run = 6 hours 5 minutes). The CI measurement is approximately 720 times faster in this instance, so we should expect a $\sqrt{720} \approx 27$-fold reduction in uncertainties from contrast interferometry over the MI over an equal time-period, bringing our CI uncertainty down to $\delta\alpha^{-1}$ = 0.011 (85 ppm). At this level of precision and with a 30 s experimental cycle time, we could expect to reduce our uncertainty to 11 ppm within a month of integration (assuming a data acquisition duration of 12 uninterrupted hour per day).

Additionally, the fact that our CI performs single-shot measurements renders the technique insensitive to sources of phase noise operating at a frequency lower than our data acquisition rate. If a single measurement occurs over a time period of approximately 500µs, then noise of a frequency of 2 kHz will appear as a single oscillation across our fringes. Lower frequency noise would appear as common vertical offset across all data points. In comparison, to appropriately understand the noise distribution in our MI measurement requires an increase in the number of samples taken (from 5 currently), further increasing data acquisition time.

Chapter 6

Advanced techniques

6.1 Introduction

We described in Chapter 5 the principle of operation of a single-shot atom interferometer with a holographic readout technique, that we then used to perform a measurement of the fine structure constant. The description glossed over some caveats when extracting information from the data. such as the aforementioned frequency chirps. This chapter aims to elaborate on these, and investigate some methods of improving our interferometer.

6.2 Mean field effects

6.2.1 Introduction and background

The ^{87}Rb atoms we use have a positive scattering length [149], so in low energy collisions the atoms experience a mutually repulsive distance-dependent potential [103]. This manifests as a density-dependent energy interaction-potential within the BEC.

Our BEC is created in an optical dipole trap, which balances the interaction potential with a trapping potential. The BEC forms in the ground state and ‘fills’ the trapping potential up to the chemical potential μ, such that the interaction potential and trapping potential remain balanced. Since the BEC is in an eigenstate of the total potential, the system remains time-invariant, which leads to a uniform phase across the condensate. Figure 6.1(a,b,c,d) shows such a condensate within an optical dipole potential. The condensate has ‘filled’ the trapping potential up to the chemical potential, expanding in space up to the Thomas-Fermi radius r_{TF} (Figure 6.1a,b). Figure 6.1c shows the spatially uniform total potential $g|\psi(x,t)|^2 + u(x,t)$. Since this potential is uniform, the phase of the BEC also remains spatially-uniform throughout its extents.

Figure 6.1(e,f,g,h) shows the same condensate some time after the dipole trap has been released. Here the trapping potential and interaction potentials are no longer balanced, such that the total potential along the condensate is no longer uniform (Figure 6.1g). The non-uniform potential induces a non-uniform phase shift throughout the condensate, proportional to the atomic density (Figure 6.1h). The gradient of this phase with respect to position induces motion in the condensate. That is, whilst the density profile of the BEC determines the profile of the phase evolution, the spatial gradient of the phase profile causes the BEC to move.

The de Broglie matter wave is determined by the relation $\lambda_{\text{dB}} = h/p$, where λ_{dB} in this instance is the spatial period under which the phase of our atomic wave-function varies by 2π. We therefore have

$$p(x,t) = \frac{h}{2\pi}\frac{\mathrm{d}\phi(x,t)}{\mathrm{d}x} , \tag{6.1}$$

such that the momentum of our BEC atoms is proportional to their local phase gradient.

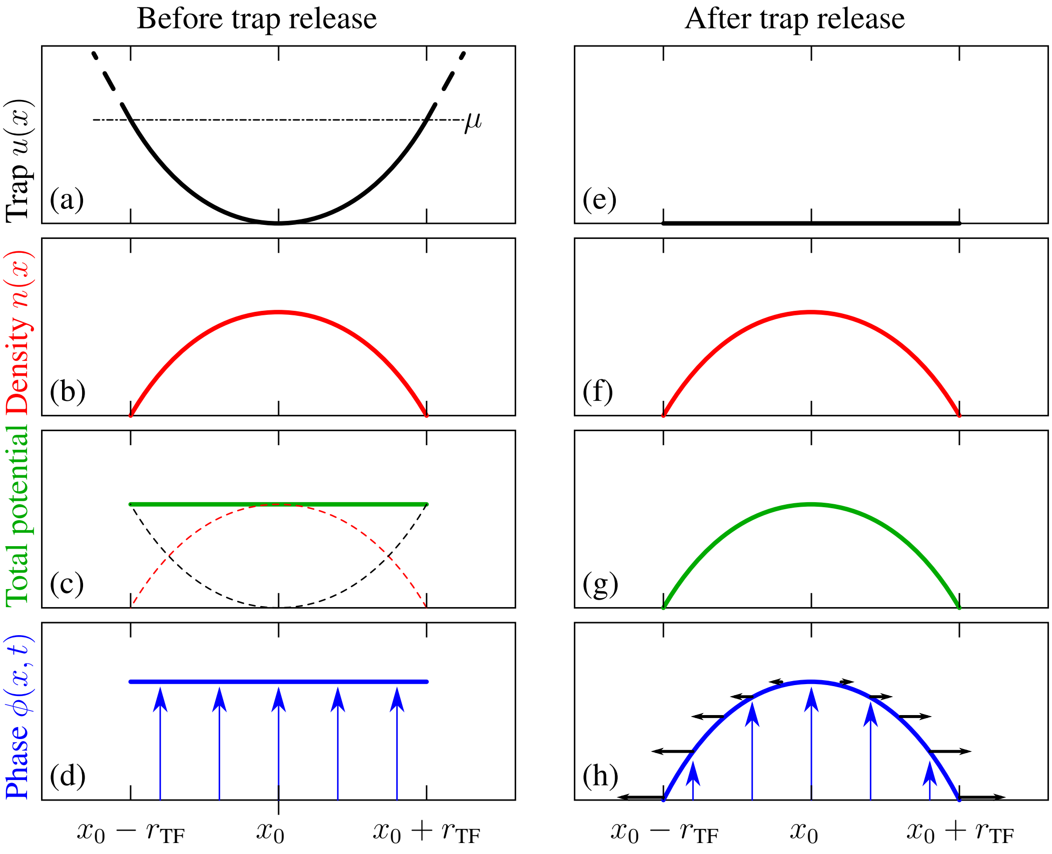

Figure 6.1: A description of our BEC before and after the dipole trap is switched off. On the left (a,b,c,d) are shown the dipole trap potential $u(x)$ (black), BEC density $n(x)$ (red), total potential $g|\psi|^2 + u(x)$ (green), and phase $\phi(x,t)$ whilst the condensate is held in the optical trap. On the right (e,f,g,h) are the same, shown some short time after the optical dipole trap has been released.

The sign of the momentum induced is dependent on the interaction potential: in our case the ^{87}Rb atoms experience a repulsive interaction potential, and so the momentum vectors point outwards, away from the highest density. If the density profile of the BEC is parabolic (assuming a Thomas-Fermi approximation), then the spatial-gradient of the density profile is linear with displacement from the BEC centre of mass (because $\frac{\mathrm{d}}{\mathrm{d}x}(1-x^2) = -2x$). The spatial gradient of the phase profile is therefore also linear, and as a result the momentum of BEC atoms is linearly proportional to their displacement from the BEC centre of mass: our BEC expands, but retains the shape of its profile.

As the BEC expands its density necessarily decreases, lowering the average density. Since the rate at which the BEC acquires phase is proportional to its density, the phase accumulation rate also decreases as the BEC expands. The consequence of the above mechanisms together (see equation 6.2) is that when our BEC is released from a trapping potential, it rapidly acquires a density-dependent phase that induces an expansion in the condensate. Together we have

$$\begin{cases} \frac{\mathrm{d}\phi(x,t)}{\mathrm{d}t} & = \frac{1}{\hbar}\Big[g|\psi(x,t)|^2 + u(x,t)\Big] \\ p(x,t) & = \frac{h}{2\pi}\frac{\mathrm{d}\phi(x,t)}{\mathrm{d}x} \end{cases}, \tag{6.2}$$

where $g = 4\pi\hbar^2 a_s/m$ and a_s is the scattering length (98 Bohr Radii, for ^{87}Rb). As the condensate expands the density lowers, and so the interaction potential weakens reducing the acceleration of the expansion.

These physics have been examined in the work of Castin *et al.* [150], where the authors model this interaction-induced BEC expansion for an ellipsoidal condensate generated in a trapping potential with trap frequencies $\omega_1 = \omega_2 \equiv \omega_\perp \gg \omega_3 \equiv \omega_z$. Their model is expressed with the equations

$$\begin{aligned} \frac{\mathrm{d}^2}{\mathrm{d}\tau^2}\lambda_\perp &= \frac{1}{\lambda_\perp^3\lambda_z} \\ \frac{\mathrm{d}^2}{\mathrm{d}\tau^2}\lambda_z &= \frac{\epsilon^2}{\lambda_\perp^2\lambda_z^2} \end{aligned}, \tag{6.3}$$

where $\tau = \omega_\perp t$ is the dimensionless scaled time, $\epsilon = \omega_z(0)/\omega_\perp(0) \ll 1$, and $\lambda_\perp(t) = R_\perp(t)/R_\perp(0)$ and $\lambda_z(t) = R_z(t)/R_z(0)$ are the dimensionless scaling parameters of the Thomas-Fermi radii in the axial (z) and radial ($\perp$) directions.

Previous work has established that the trap frequencies of our optical dipole trap when our BEC is formed are on the order of $\omega_{x,y,z} \approx (35\,\mathrm{Hz}, 74\,\mathrm{Hz}, 76\,\mathrm{Hz})$ [99]. If we approximate this with the Castin equations as a cigar-shaped BEC with trap frequencies $\omega_{\perp,x} = (75\,\mathrm{Hz}, 35\,\mathrm{Hz})$, we obtain the BEC expansion trajectories shown in Figure 6.2.

In this approximation our interferometer axis (referred to previously as the x-direction) lies along the axial direction. Looking at our predicted axial trajectory in Figure 6.2, we see that at $t = 0\,\mathrm{s}$ the expansion rate is $v_0 = 0\,\mathrm{mm\,s^{-1}}$. The curvature of the trajectory is greatest here (corresponding to the greatest acceleration), due to the relatively high density of the condensate. The acceleration is lower with increasing time due to the decreasing density, but as time increases more velocity has accumulated.

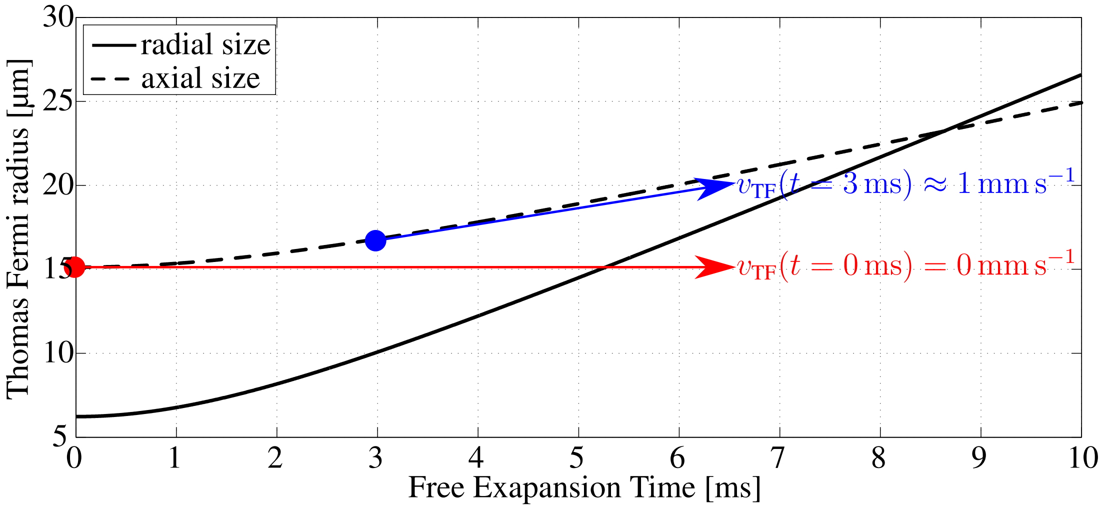

Figure 6.2: The Thomas-Fermi radii of our Bose-Einstein Condensate from the moment we release our trapping potential at $T = 0\,\mathrm{ms}$, modelled using the work of Castin *et al.* [150] using Equations 6.3. The velocity of the Thomas Fermi radius is given by the gradient with respect to time, marked at $t = 0\,\mathrm{ms}$ (red) and $t = 3\,\mathrm{ms}$ (blue).

We have two regions of interest, then. At long times the interaction-induced accelerating expansion has mostly expired, but the condensate has acquired an expansion velocity that persists forever. At short times interactions are at their strongest, accelerating the BEC expansion, but insufficient time has passed for this acceleration to project into an expansion speed. Our contrast interferometer generates a superposition of momentum states from a BEC, and maps the evolving phase of that superposition to extract information about the atom-photon recoil energy. Given that the interaction induced phase shifts alters the phase and momentum of our BEC, it is crucial that we investigate the effect interactions have on our interferometer.

Figure 6.3 shows an examination of the contrast interferometer running in both of the above regimes. The left and right sides describe the BEC density (red) and phase (blue) throughout time (shown vertically, evolving downwards). On both sides we start with a BEC held in an optical dipole trap at time T_1. Each subfigure left and right show corresponding snapshots of the BEC at times T_1, T_2, and T_3.

On the left (Figure 6.3a,b,c,d) the dipole trap is held on until the time T_2. At this ‘release time’ the condensate still has a spatially-uniform phase. Almost immediately atom-optics are applied, imprinting a phase and density modulation on the condensate. The evolution of the atomic-wavefunction is now dominated entirely by this new density and phase profile.

On the right (Figure 6.3e,f,g,h) the dipole trap is turned off at time T_1, and a period of free evolution occurs. During this time tonly the interaction potential exists, and so the BEC accumulates a phase chirp profile that matches its density profile. When the atom-optics are triggered at time T_2, some phase chirp (and therefore also a momentum distribution) has already accumulated in the BEC. This chirp is inherited by the matter-wave fringes generated by the atom-optics. As was the case with our BEC in Figure 6.1, the matter-wave fringes now have a momentum distribution that is linearly proportional to their displacement from the centre of mass.

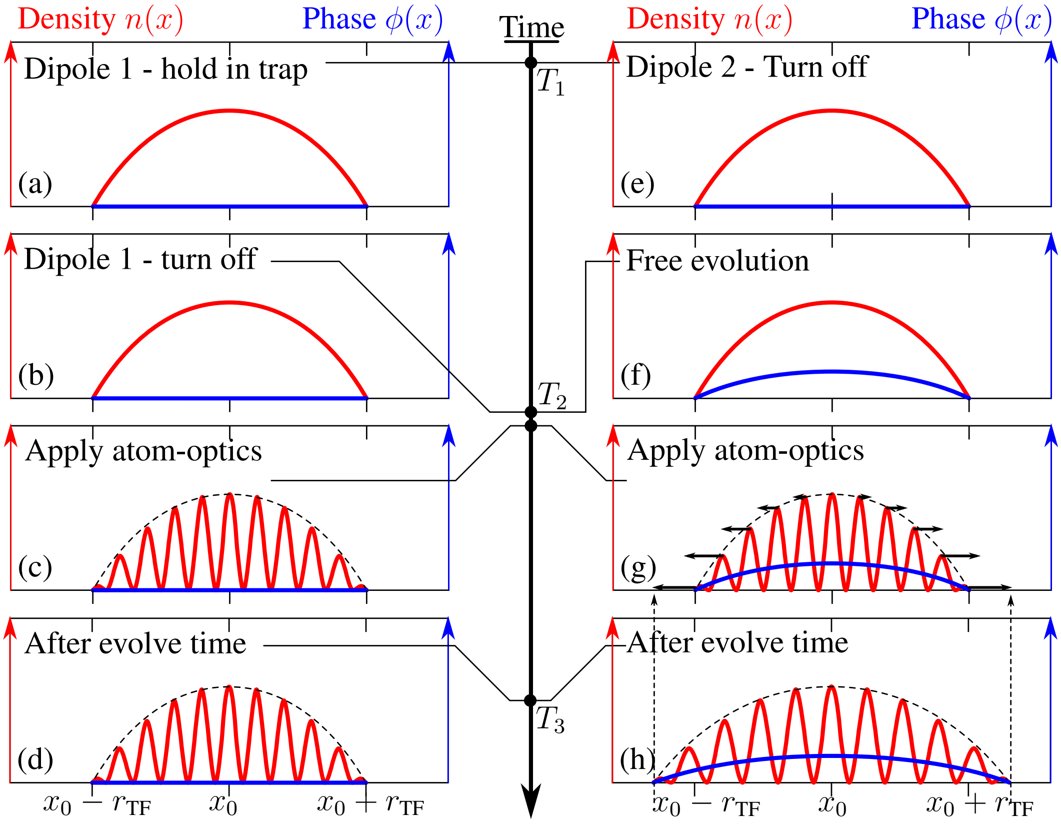

Figure 6.3: A schematic of our BEC density (red trace) and phase (blue trace) throughout the contrast interferometer. On both sides a BEC is formed in an optical dipole trap. On the left (a,b,c,d) this trap is held on until a time T_2, immediately before atom-optics are triggered. On the right (e,f,g,h) the dipole is released at T_1, allowing some evolution time before the atom-optics are triggered. The phase induced by the untrapped evolution time on the right induces a phase-chirp across the condensate, which is inherited by the matter-wave fringes through the rest of the experiment.

When we allow a phase chirp to accumulate in the BEC, the interference fringes inherit the expansion rate of the BEC at the time the atom-optics are applied. This means that the matter-wave interference pattern imprinted on the condensate also expands as time progresses.

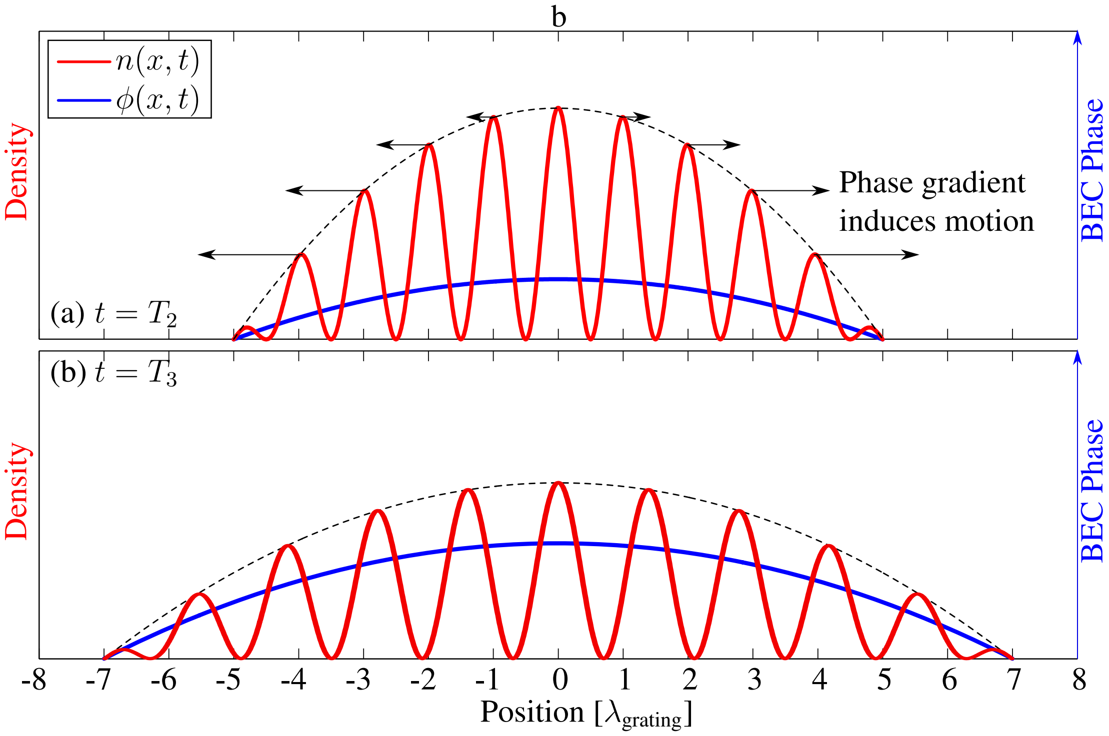

Figure 6.4: An ‘inherited’ phase chirp from the interaction potential induces motion in the matter-wave fringes during an interferometer run. (a) If we perform our beam-splitter pulse when the condensate is already expanding, the outer ‘notches’ inherit momentum from the expanding condensate in the form of a phase chirp across the notch. (b) The expansion then alters the spatial period of the matter-wave grating, altering the encoded wavevector.

This expansion of the matter-wave fringe has an important effect on the contrast interferometer: the spatial period of the matter wave $\lambda_{\text{m.w.}}$ encodes the momentum exchange Δp and corresponding 2-photon recoil energy $E^{(2)}_{\text{recoil}}$ in our atom-light interaction,

$$\begin{cases} \Delta p & = 2\hbar k = & 2\hbar \frac{2\pi}{\lambda_{\text{m.w.}}} \\ E^{(2)}_{\text{recoil}} & = \frac{(2\hbar k)^2}{2m} = & \frac{2\hbar^2}{m}\frac{4\pi^2}{\lambda^2_{\text{m.w.}}} \end{cases} . \tag{6.4}$$

If the wavelength of the matter-wave increases, the encoded momentum and energy both decrease. A zoom-in of Figure 6.3(g,h) is shown in Figure 6.4, where the BEC has been released for some time before the atom-optics have been applied at time $t = T_2$. The phase accumulated has been inherited by the matter-wave fringes, giving the fringes an expansion speed (a). After some time at $t = T_3$, the fringe period has increased to approximately 1.4 λ_{grating} (b).

An alternative picture of this mechanism might be that our atom-optics generate a superposition of three momentum states: A $|0\hbar k\rangle$ state with a spatially uniform phase, and a pair of $[|{+2\hbar k}\rangle + |{-2\hbar k}\rangle]$ states with phase chirps across each wave-packet with a linear gradient. If we add on this interaction-induced phase chirp, we cause all three clouds to expand. With each momentum wave-packet expanding, the relative velocities at the position of maximum cloud overlap changes with time. For example: at the moment of maximum overlap the centre of mass of all three clouds overlap, and so the relative velocities match our $|-2\hbar k\rangle, |0\hbar k\rangle, |+2\hbar k\rangle$ momentum states. At some later time, the trailing edges of the clouds are overlapping. Since the clouds are expanding and moving apart, the trailing edges are moving more slowly than their centres. As these trailing edges overlap, their de Broglie wavelengths are larger, and their phase rotation rate $\mathrm{d}\phi(t)/\mathrm{d}t$ is slower in comparison to their centres.

We should therefore see a gradual reduction in the oscillation rate of our hologram as the clouds separate if those clouds are expanding, and this reduction in frequency should happen at a rate proportional to their expansion. We can use the Castin [150] model of our Thomas-Fermi radius (shown in Figure 6.2) to predict the frequency chirp we should expect to see in our contrast interferometer for a given expansion time between dipole release and atom-optics.

For a given duration $T_{\text{expansion}}$ of free expansion between the dipole trap release and triggering of atom-optics, we can use Figure 6.2 data as a lookup table for the Thomas Fermi radius of our condensate in the axial (x) direction $R_{\text{TF}}(T)$. We then divide $R_{\text{TF}}(T)$ by $\lambda_{\text{grating}} = 434\,\text{nm}$ to determine how many interference fringes we generate across our condensate as we apply the splitter pulse. We then calculate the expansion rate of the condensate using the gradient $\mathrm{d}R_{\text{TF}}/\mathrm{d}t$ at the time we apply the splitter pulse. Using this gradient we expand our matter-wave fringe as time evolves, calculating the spatial wavelength of the hologram over time. From this spatial wavelength we can calculate the modification to our contrast interferometer frequency using equations 6.4.

If we perform the same calculation for a variety of expansion times $T_{\text{expansion}}$, we can map out a prediction of the frequency encoded in our contrast signal, and from this calculate the corresponding frequency chirp we expect to see. Figure 6.5 shows such a map. On the x-axis here is the delay time between the optical dipole trap release and triggering of atom-optics, and the on the y-axis is the evolution time after the triggering of atom-optics.

We can read the map by choosing a free expansion time along the x-axis, and following the evolution vertically. For example, suppose our contrast interferometer sequence switches off the optical dipole trap at $t = 0\,\text{ms}$, and atom-optics are applied at $t = 2\,\text{ms}$. We can predict the frequency of the contrast signal from Figure 6.5(a) by moving to $T_{\text{expansion}} = 2\,\text{ms}$ on the x-axis, where $y = 0\,\text{ms}$ corresponds to the instant that the atom-optics are applied. Here we see that our CI frequency begins at our expected $24.6\,\text{kHz}$, but decreases to approximately $23.2\,\text{kHz}$ after $500\,\mu\text{s}$ of contrast readout time. Figure 6.5(b) shows the corresponding frequency chirp, which begins at approximately $\mathrm{d}f/\mathrm{d}t \approx -2.25\,\text{Hz}\,\mu\text{s}^{-1}$ and decreases to approximately $\mathrm{d}f/\mathrm{d}t \approx -2.0\,\text{Hz}\,\mu\text{s}^{-1}$ after $500\,\mu\text{s}$ of contrast readout time.

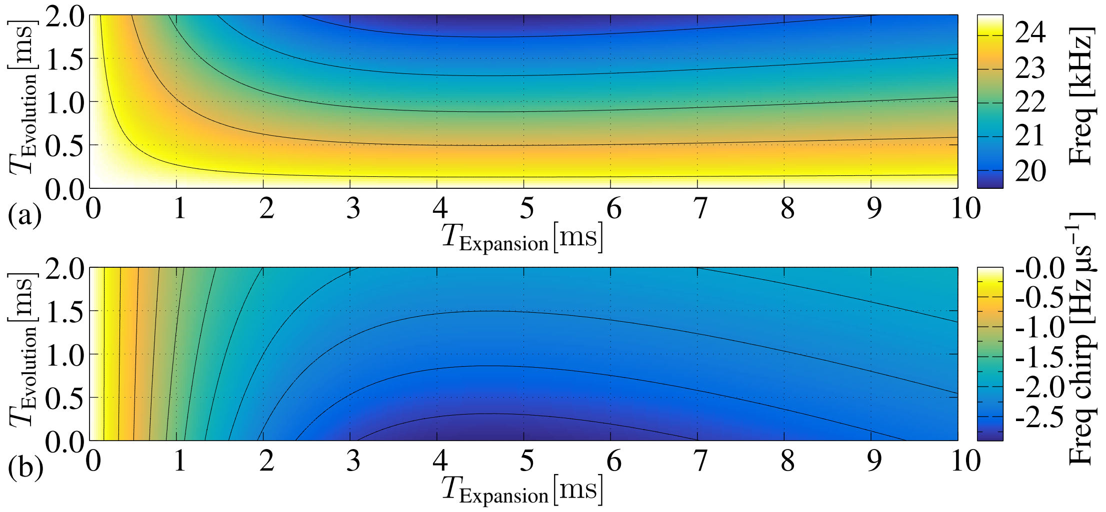

Figure 6.5: The predicted contrast signal frequency (a) and frequency chirp (b), numerically generated by the Castin BEC expansion model described in equations 6.3 [150, 151]. The x-axis represents the time delay between the release of our optical dipole potential and the activation of our atom-optics beam-splitter pulse: that is, the free flight time during which the BEC acquires a density-dependent phase profile. The y-axis represents the evolution time after the beam-splitter has been applied.

There is an important caveat here. This analysis assumes that the interaction-induced acceleration ends at the moment the beam-splitter pulse is applied. We instead calculate the velocity of the Thomas-Fermi radius at the moment of the atom-optics pulse, and project that velocity forwards in time. This drawn in Figure 6.2, where the expansion profile at $t = 3\,\mathrm{ms}$ now follows the blue ballistic trajectory, rather than the black accelerating one.

In Figure 5.3 we see that our example atom-optics pulse has a duration of approximately $26\,\mu\mathrm{s}$, and that at the end of this pulse we have altered the spatial density profile of the BEC with a spatial modulation of period λ_{grating}, where the *low* density occurs at $x = 0\,\mathrm{nm}$. We also see that this wave oscillates in time, such that a λ_{grating} matter-wave re-images at $t \approx 41\,\mu\mathrm{s}$, but with the spatial phase offset by π such that the density is then *high* at $x = 0\,\mathrm{nm}$. The interaction-induced phase shift within the BEC should then be greatest at the positions of highest density, and therefore also alternate spatially by π as the matter-wave re-images spatially in and out of phase with the optical grating.

Taken together, we see that (1) the Thomas-Fermi density distribution that generated a position-dependent phase-gradient across the BEC has been altered by the application of atom-optics, and (2) the subsequent interaction-induced phase-shift alternates in position such that it (to some extent) time-averages to a spatially-uniform phase shift. The extent to which this time-averaging occurs depends on the specific density-evolution of the BEC after the atom-optics have been applied. We should therefore expect that the linearity of the frequency chirp we see during the CI will depend on the specific beam-splitter pulse used to generate the BEC momentum states. In the limit that the phase-shift is spatially-uniform, would would indeed see a halt to the expansion acceleration.

6.2.2 Observation of frequency chirp in GPE simulation

To test the above hypothesis in a controlled environment, we configured our 2D GPE simulation [152, 153] with an interaction term tuned such that the expansion of our simulated 2D condensate was similar to that of our simulation shown in Figure 6.2. We then programmed the simulation to allow some free BEC expansion time, and then a single beam-splitter pulse to begin the contrast interferometer. The complex amplitude of the BEC was recorded at time intervals after the split, and converted into a density grid. This gave us a series of samples at regular time intervals, where each sample described the density distribution of the BEC during the contrast interferometer.

To be clear: our simulation gave us the complex amplitude of the BEC wavefunction within a two-dimensional simulation space (x, y) over a range of times t. We then calculated the density $P(x, y, t) = |\psi(x, y, t)|^2$, and binned this along the y-axis to result in a one-dimensional binned density along the x-axis for each time index, $n(x, t) = \sum_y P(x, y, t)$.

For every time sample, we calculated the spatial autocorrelation in the x-direction by multiplying the binned density with itself offset by some spatial displacement δx,

$$C(\delta x, t) = \sum_i n(x_i, t) \times n(x_i + \delta x, t) \; . \tag{6.5}$$

This outputs a one-dimensional array of values that correspond to the magnitude of our density distribution in the spatial period δx at a given time t. That is, if our spatial density has a distinct wavelength of λ_{grating}, we would expect to see a peak in $C(\delta x, t)$ around $\delta x = \lambda_{\text{grating}}$.

This autocorrelation method was chosen over a Fast Fourier Transform (FFT) algorithm because the latter attempts to decompose the signal into the relative fractions of *sine waves* in the density. For example, if our spatial density were composed of delta functions spaced λ_{grating} apart we might have a reasonable Bragg-reflector for our probe laser, but the FFT would return a multitude of frequencies. The spatial autocorrelation is a clearer metric for our purpose in this instance.

We use the autocorrelation described above at each time step in our 2D GPE simulation, to convert the simulated wavefunction $\psi(x, y, t)$ into a spatial autocorrelation $C(\delta x, t)$. We would then extract the value of $S(t) \equiv C([\delta x = \lambda_{\text{grating}}], t)$, giving us an array $S(t)$ that approximates how much of our simulated density distribution is in a λ_{grating} spatial period as a function of time. A slight complication here is that a density distribution with a spatial period of $\lambda_{\text{grating}}/2$ will also return a large value of $C([\lambda_{\text{grating}}], t)$. As a result we redefine $S(t) = C([\lambda_{\text{grating}}], t) - C([\lambda_{\text{grating}}/2], t)$. In this way we suppress the sensitivity of $S(t)$ to higher spatial frequencies.

The black line trace in Figure 6.6 shows an example of the spatial autocorrelation

$S(t)$. To this we fit (red trace) the model

$$y = \frac{A}{2}\left[1 + \cos\left(2\pi f[t - t_{\mathrm{o}}] + 2\pi c[t - t_{\mathrm{o}}]^2 + \phi_{\mathrm{o}}\right) - y_{\mathrm{o}1}\right] \times \ldots$$
$$\ldots \times \exp\left(-\frac{[t - t_{\mathrm{o}}]^2}{[2\sigma^2]}\right) + y_{\mathrm{o}1} + y_{\mathrm{o}2}\ , \quad (6.6)$$

where A is the amplitude of the signal oscillation, t_{o} is the centre of the Gaussian envelope, ϕ_{o} is the oscillation phase offset, σ the Gaussian envelope width, $y_{\mathrm{o}1}$ and $y_{\mathrm{o}2}$ vertical offsets, and most importantly f is the frequency (at $t = 0$) of the CI signal, and c is the associated linear frequency chirp.

Figure 6.6 shows an example simulation of $S(t)$ where the BEC has had a free expansion time of $5\,\mathrm{ms}$ between the optical dipole trap release and a beam-splitter pulse. The fit returns a fitted frequency chirp $c \approx 2\,\mathrm{Hz}\,\mu\mathrm{s}^{-1}$.

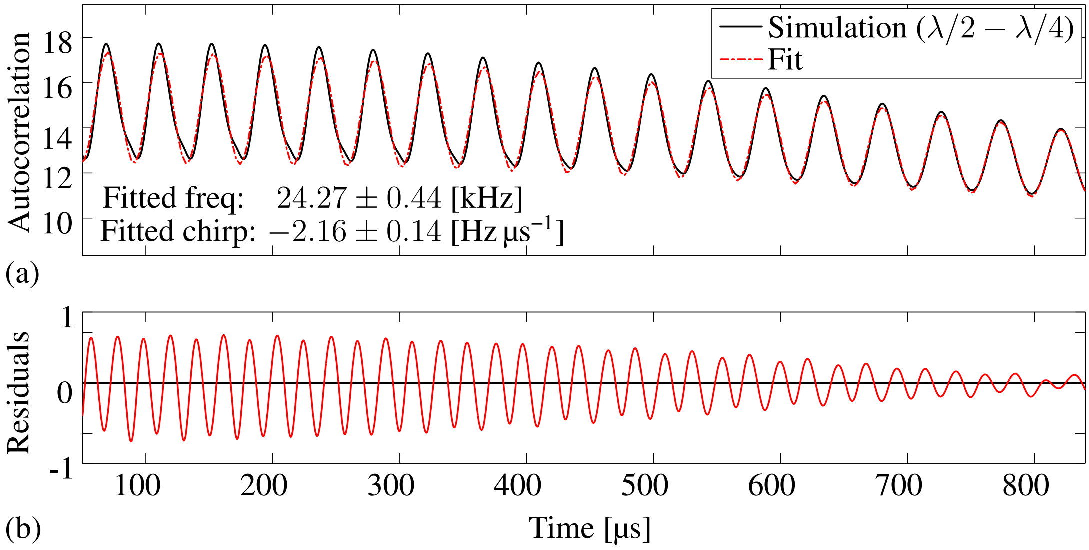

Figure 6.6: Spatial autocorrelation analysis of a 2D GPE simulation configured to resemble our BEC experiment with a 5 ms free expansion time. We see a fitted frequency chirp of $-2.16 \pm 0.14\,\mathrm{Hz}\,\mu\mathrm{s}^{-1}$.

We repeated this process for a selection of free expansion times, comparing the fitted 2D GPE frequency chirps (red points) with those we expect from equations 6.3 (black solid line) in Figure 6.7. Qualitatively we see a similar ‘scooped’ pattern emerge, with a steep increase in frequency chirp magnitude from 0 ms to around 4.5 ms followed by a slow return. The differences between the Castin expansion model and 2D GPE simulation were not entirely unexpected: firstly, the 2D GPE was tuned to give similar increases in Thomas-Fermi radius to the expansion model, but has fewer dimensions for the density to expand into, so we should expect the interaction energy to scale with density differently. Secondly, the expansion model here quotes the initial

$T_{\text{Evolution}} = 0\text{ms}$ frequency chirp, which is a good approximation for low expansion times (see the left-hand side of Figure 6.5(b)), but breaks down as $T_{\text{Expansion}}$ increases. Since our simulated contrast signals begin at 200 µs and continue for around 700 µs, a better comparison here might be to also plot the Castin model with $T_{\text{Evolution}} = 0.5\text{ms}$, and 0.5ms, performing an approximate integration to compare the two models.

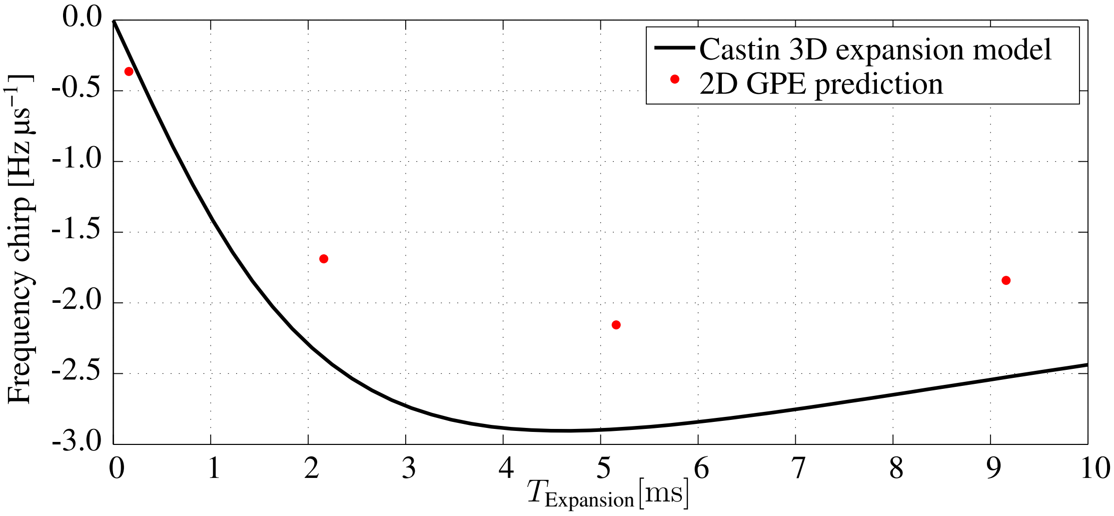

Figure 6.7: Comparison of the numerical frequency chirp calculation from the Castin BEC expansion (solid black line), and the 2D GPE simulation (red points).

6.2.3 Observation of frequency chirp in Contrast data

With our ability to detect an interaction-induced frequency chirp seeming plausible, we needed to alter our data analysis algorithm. We extended our Poisson fitting model (section 5.3.4) to include a frequency chirp by adjusting our model and likelihood functions. We can rewrite our previous model to match the frequency chirp shown in equation 6.6 by including an additional parameter a_6, corresponding to a linear change in frequency

$$u(\boldsymbol{x}) = a_1 \exp\left(-\frac{(\boldsymbol{x} - a_3)}{(2a_2^2)}\right) \frac{\Delta x}{2} \left[\cos\left(2\pi a_4 \boldsymbol{x} + 2\pi a_6 \boldsymbol{x}^2 + a_5\right) + 1\right]. \tag{6.7}$$

We pass this model through Equation 5.14 to obtain our array of probability likelihood expressions

$$\boldsymbol{L} = \begin{bmatrix} \sum_{\mathrm{i}=1}^{\mathrm{N}} \Big(u(x_{\mathrm{i}}) - y_{\mathrm{i}} \Big) \\ \sum_{\mathrm{i}=1}^{\mathrm{N}} \Big(u(x_{\mathrm{i}}) - y_{\mathrm{i}} \Big) \frac{(x_i - a_3)^2}{a_2^3} \\ \sum_{\mathrm{i}=1}^{\mathrm{N}} \Big(u(x_{\mathrm{i}}) - y_{\mathrm{i}} \Big) \frac{(x_i - a_3)}{a_2^2} \\ -\sum_{\mathrm{i}=1}^{\mathrm{N}} \Big(u(x_{\mathrm{i}}) - y_{\mathrm{i}} \Big) \sin\left(2\pi a_4 x_{\mathrm{i}} + 2\pi a_6 x_{\mathrm{i}}^2 + a_5\right) 2\pi x_{\mathrm{i}} \\ -\sum_{\mathrm{i}=1}^{\mathrm{N}} \Big(u(x_{\mathrm{i}}) - y_{\mathrm{i}} \Big) \sin\left(2\pi a_4 x_{\mathrm{i}} + 2\pi a_6 x_{\mathrm{i}}^2 + a_5\right) \\ -\sum_{\mathrm{i}=1}^{\mathrm{N}} \Big(u(x_{\mathrm{i}}) - y_{\mathrm{i}} \Big) \sin\left(2\pi a_4 x_{\mathrm{i}} + 2\pi a_6 x_{\mathrm{i}}^2 + a_5\right) 2\pi x_{\mathrm{i}}^2 \end{bmatrix} = 0\,, \tag{6.8}$$

where the sixth term a_6 corresponds to our frequency chirp parameter.

Experimentally, the contrast interferometer was set in a ‘long’ configuration (see Section 5) with typical parameters: In this instance with 2 ms free expansion time before the first split, the first wait time set to 750 µs, and the second to approximately 500 µs. The resulting photon-count data are shown in Figure 6.8. Errors were calculated using the same method as described in section 5.3.4. The fitting algorithm returns the parameters with errors,

$$\begin{aligned} &[\text{Env amp}]\ a_1 = +8.750\ (\sigma = 0.080)\ [0.91\%]\ [\text{Photons}/\mu\text{s}]\,, \\ &[\text{Env width}]\ a_2 = +135.0\ (\sigma = 0.9)\ [0.63\%]\ [\mu\text{s}]\,, \\ &[\text{Env centre}]\ a_3 = -56.46\ (\sigma = 1.01)\ [1.80\%]\ [\mu\text{s}]\,, \\ &[\text{Cosine Freq}]\ a_4 = +24570\ (\sigma = 22)\ [0.09\%]\ [\text{Hz}]\,, \\ &[\text{Phase offset}]\ a_5 = +0.429\ (\sigma = 0.015)\ [3.49\%]\ [\text{rad}]\,, \\ &[\text{Freq chirp}]\ a_6 = -2.335\ (\sigma = 0.052)\ [2.23\%]\ [\text{Hz}/\mu\text{s}]\,. \end{aligned}$$

where the uncertainty σ is the standard error, and corresponding percentage errors have been given as a more convenient fractional uncertainty.

From our Castin model (Figure 6.7) we expect a frequency chirp of approximately -2.3 Hz μs^{-1} at 2 ms expansion time, if we are correct in our assumption that at the moment of the splitter pulse we ‘freeze’ our interaction-induced accelerating expansion into a ballistic expansion.

This is a striking match, given the naivety of our expansion-chirp model. The fitted frequency chirp is 45 times larger than our estimated uncertainty $\sigma = 0.052$ Hz/µs, but lies within one σ of the predicted value. This is a strong indicator that (1) a frequency chirp exists within the contrast interferometer signal, and (2) our model is effective in predicting the magnitude of this chirp. From this we infer that our expansion-chirp model is an approach worthy of further development.

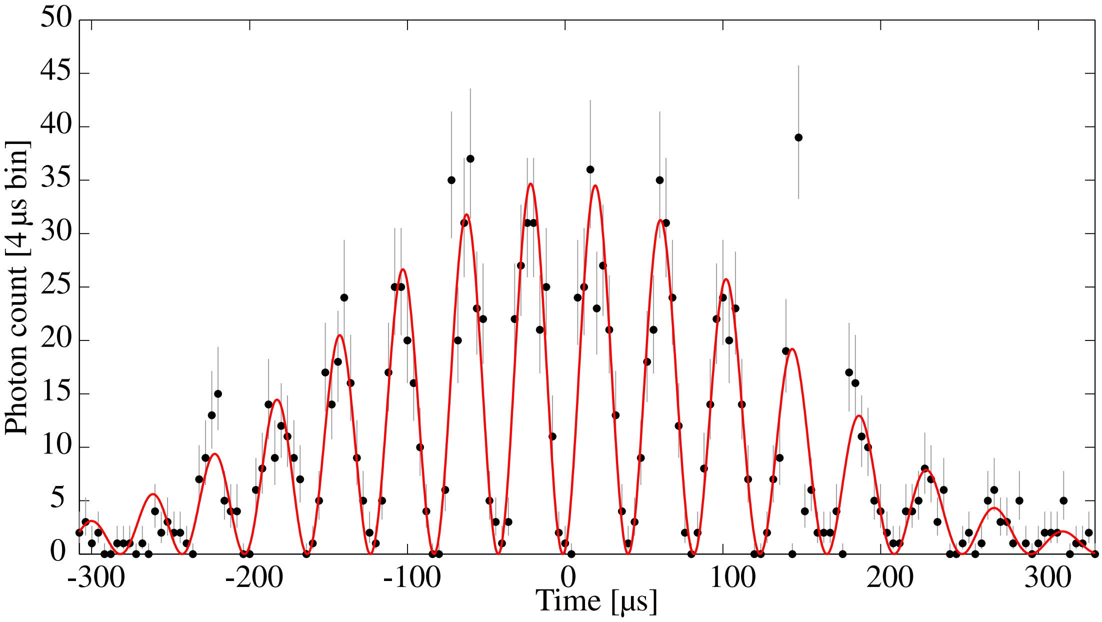

Figure 6.8: Our contrast interferometer signal with 2 ms free expansion time before the opening splitter pulse. The red line is a fit of our model described in equation 6.7, which returns a fitted frequency chirp of -2.335 ($\sigma = 0.052$) [Hz/µs] around a central frequency of $+24570$ ($\sigma = 22$) [Hz].

For comparison, we see approximately zero (-0.03 ± 0.12 Hz µs^{-1}) frequency chirp for our contrast interferometer when no expansion time is present before the first splitter pulse (Figure 5.14).

This frequency chirp is of obvious importance to our measurement of the fine structure constant; the frequency measurement that we obtain is now a function of the expansion time we allow before applying our first interferometer pulse, and the frequency that we obtain is dependent on *when* we start and end our photon measurement. Since our model of the phenomenon predicts that our interferometer frequency should be ‘correct’ at the moment of the interferometer opening, a naive compensation would be to ‘project’ the frequency back to this moment linearly using the fitted chirp.

Testing the linearity of the chirp experimentally is difficult: our short CI configuration rapidly loses contrast over a period of ~ 500 µs, and our long CI configuration introduces additional effects from the reflection pulse used. In addition, the experimental interferometer has additional delay times for shuttering of the atom-optics beams that reduces our ability to examine low evolution times. In comparison our 2D GPE simulation has fewer restrictions, and can be probed in the short and long configurations within the same simulation run.

The linearity tests were conducted with the 2D GPE, configured with $T_{\text{Expansion}} = 3\,\text{ms}$ between the optical dipole trap release and first beam-splitter pulse, and a Blackman reflection pulse centred $750\,\mu\text{s}$ after the beam-splitter pulse end. This sequence is shown in Figure 6.9.

The BEC autocorrelation was examined over the entire duration of the simulated interferometer, from $t = 0\,\text{ms}$ to $t \approx 2\,\text{ms}$. Rather than fitting the entire signal at once to determine a single frequency chirp, the autocorrelation signal $S(t)$ was sampled over a $200\,\mu\text{s}$ sub-region (approximately five periods of our contrast signal), and a frequency extracted for that sample. This $200\,\mu\text{s}$ region was then swept over the interferometer duration, sampling the simulated frequency as a function of interferometer evolution time, shown in Figure 6.9 as the black line in the lower graph.

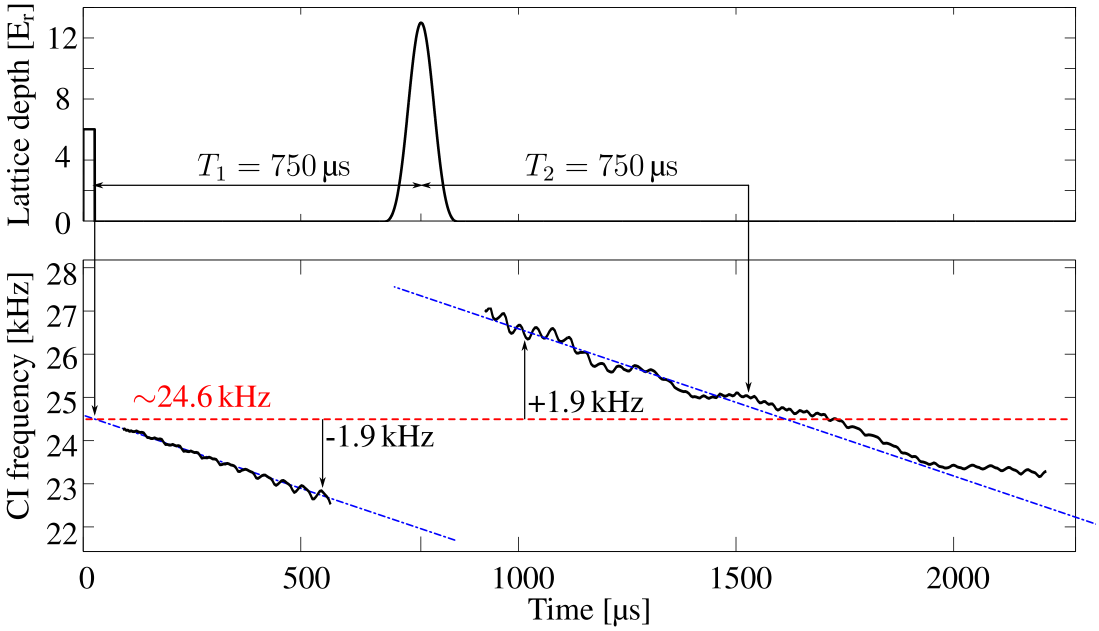

Figure 6.9: Linearity of frequency chirp in 2D GPE. Black solid lines refer to the local fitted frequency in a five-period subsample as a function of time. The blue dot-dashed lines are a linear frequency chirp fitted to the black frequency lines. Our simulation shows a linear frequency chirp of approximately -3 $\text{Hz}\,\mu\text{s}^{-1}$ following the opening splitter pulse in the contrast interferometer. After the reflection we see that the contrast frequency has been increased by the reflection, and that whilst an overall linear trend in the frequency is dominant, there are additional features.

We see a very nearly linear frequency chirp of approximately -3 $\text{Hz}\,\mu\text{s}^{-1}$ (dot-dashed blue trace) before the reflection pulse, with a similar (though less linear) frequency chirp afterwards. This linear approximation does project backwards in time to our expected $24.6\,\text{kHz}$ contrast signal at the end of the beam-splitter pulse. From this we infer that the linear approximation is probably valid for a CI in the short configuration for comparable $T_{\text{Expansion}}$ times.

Whilst this appears valid for the ‘short’ reflectionless contrast interferometer, we need to take care with the longer split → reflect → probe configuration. Our reflection is not truly a reflection of the $p = \pm 2\hbar k$ modes, but rather a $\delta p = \mp 4\hbar k$ momentum kick. If the momentum of our interferometer arms has slowed from $\pm 2\hbar k$ to $\pm(2-\epsilon)\hbar k$, we will see the momentum *after* the reflection of $\mp(2+\epsilon)\hbar k$. We see this in our 2D GPE simulation in Figure 6.9 as the ± 1.9 kHz frequency offsets in the contrast signal at equal ± 260 µs offsets on either side of the reflection pulse.

This means that whilst we expect to see a reduced interferometer frequency due to ballistic BEC expansion, this reduction in frequency should manifest as an *increase* in frequency after the reflection. Our 2D GPE simulation recreates this behaviour when we include a reflection pulse. Interestingly, since the frequency chirp before and after the reflection pulse are both approximately linear and of similar magnitude, we see the contrast frequency return to our expected 24.6 kHz at a time $2T$. From this we infer that the valid measurement times are at $t = 0$ and $t = 2T$. The previous measurements by Jamison *et al.* [54, 110] probably minimised the effect of interaction-induced expansion effects by measuring the interferometer phase at $t = 2T$.

6.3 Higher-order scattering

6.3.1 Motivation

In section 4.5.2 we used our atom interferometer to measure acceleration induced by a magnetic field gradient. Essentially we used an optical grating as a spatial ruler by converting the spatially-varying optical phase of the grating to the phase of the interferometer's output ports. The measurement precision δx is ultimately limited by the periodicity of the ruler we use; if we half our optical grating wavelength the phase gradient $\mathrm{d}\phi/\mathrm{d}x$ doubles, and our uncertainty, $\delta x = \delta\phi\ \mathrm{d}x/\mathrm{d}\phi$, halves.

Our phase-contrast measurement of the fine structure constant (section 5.4.2) uses the matter-wave's time-evolution as a 'temporal ruler' to measure the oscillation period, with the measurement uncertainty $\delta t = \delta\phi\ \mathrm{d}t/\mathrm{d}\phi$. To match the current state-of-the-art uncertainties of $\delta\alpha^{-1} \approx 1 \times 10^{-9}$, we would need to measure our ~24.6 kHz signal to a precision of 24.6 µHz.

The state of the art measurements commonly obtain their tremendous precision by increasing the frequency that they measure; the Biraben group experiment induces 900 scattering events [50] increasing the interferometer frequency by increasing the energy in the system. Such a feat with our interferometer with a $\pm 900 \times 2\hbar k$ momentum separation would yield a (0.81) million-fold increase in interferometer frequency to 20 GHz, with a significantly more feasible required measurement resolution of 20 Hz.

6.3.2 Viability of the second order Contrast signal

Since we can generate atom-optics with arbitrary output states, we can in principle generate interferometer geometries with greater momentum separation. One might then think the simplest enhancement for our contrast interferometer is to develop a beam-tritter pulse like our existing $p{=}(-2, 0, +2)\hbar k$ momenta, but with an increased momentum in the moving modes such as $p{=}(-4, 0, +4)\hbar k$.

Unfortunately, whilst such a pulse would indeed generate a matter-wave that oscillates four times faster than our first-order interferometer, the matter-wave grating does not satisfy the Bragg condition for our probe laser into our detection system.

With an interferometer beam-angle $\theta \approx 26°$, our $\lambda_{\text{laser}} = 780\,\mathrm{nm}$ generates an optical lattice of wavelength $\lambda_{\text{grating}} = \frac{780\,\mathrm{nm}}{2\cos(26°)} = 434\,\mathrm{nm}$. Our $780\,\mathrm{nm}$ projected along the optical grating axis at 26° gives us an 'effective' probe wavelength of $\lambda_{\text{eff}} = 868\,\mathrm{nm}$. Let us use this '$\lambda_{\text{eff}}$' as a standard unit of measurement for the discussion that follows.

Our first-order ($p{=}(-2, 0, +2)\hbar k$) phase-contrast interferometer generates a matter-wave grating with a periodicity of $\lambda_{\text{eff}}/2$. This $\lambda_{\text{eff}}/2$ matter-wave has a rotating phase that interferes with the flat phase of the $0\hbar k$ mode, such that the density wave oscillates between $\lambda_{\text{eff}}/2$ and $\lambda_{\text{eff}}/4$ configurations (see Figure 5.3). Whilst the $\lambda_{\text{eff}}/2$ configuration satisfies the Bragg condition for our probe laser, the $\lambda_{\text{eff}}/4$ does not [142]. This is why we see a periodic modulation in the light Bragg-scattered from our matter-wave at a frequency of 8 ω_{recoil}, as explained in Section 5.1.2.

If we simply increase the momentum in our moving interferometer arms to a $p{=}(-4, 0, +4)\hbar k$ configuration, we instead see an oscillation between $\lambda_{\text{eff}}/4$ and $\lambda_{\text{eff}}/8$ spatial periods in the matter wave, neither of which scatter into the collection mode of our detector. What we require is a combination of momenta which will periodically generate a $\lambda_{\text{eff}}/2$ spatial period in our atom condensate.

6.3.3 Holographic 'beat' measurements

Our solution to the problem was to think of the $[|{+2\hbar k}\rangle{+}|{-2\hbar k}\rangle]$ superposition state as the foundation for our Bragg-reflection. This configuration of momenta generate a continuous $\lambda_{\text{eff}}/2$ matter-wave, continuously Bragg-scattering our interferometer probe into the SPCM collection mode. Our previous CI added a $0\hbar k$ into the superposition, beating the $\omega = 2\pi \cdot 0\,\text{Hz}$ phase against the $\omega = 2\pi \cdot 12.3\,\text{Hz}$ phase of the $\pm 2\hbar k$ mode to generate a $12.3\,\text{Hz}$ modulation of the reflectivity of the matter-wave.

We can replace the $0\hbar k$ mode with some other momentum mode, altering the frequency that we beat with the $\pm 2\hbar k$ modes. For example, a four-arm interferometer with the momentum modes $p = (-4, -2, +2, +4)\hbar k$ should generate an evolving matter wave with some $\lambda_{\text{eff}}/2$ component at a higher frequency. Like the first-order contrast interferometer, the oscillation rate of this matter-wave is taken from the difference in the input modes. Since the energy of each mode is proportional to the square of the momentum and the phase-contrast interferometer has two reflective phases per cycle, the first order $|p|{=}2\hbar k$ modes oscillate with at $(2 \times 2^2 = 8)\,\omega_{\text{recoil}}$, and the second order $|p|{=}4\hbar k$ modes oscillate at $(2 \times 4^2 = 32)\,\omega_{\text{recoil}}$. A measurement which beats these two modes should generate some matter-wave that oscillates at the difference in frequencies, $24\,\omega_{\text{recoil}}$.

To test this hypothesis we configured a 2D GPE simulation which applied the $(-4, -2, +2, +4)\hbar k$ pulse sequence described in section 3.8.1 to a BEC with approximately the same spatial dimensions and interaction strength to that used in our experiment (see Section 6.2.2). We then looked at snapshots of the matter-wave's evolution through time, plotted in Figure 6.10. Here we see the matter-wave plotted as a Talbot carpet in time, showing a periodic re-imaging of the optical grating with higher frequency harmonics. As hoped, we see a $\lambda_{\text{eff}}/2$ matter-wave grating which oscillates at $24\,\omega_{\text{recoil}}$.

Comparing this second order evolution in Figure 6.10 to the first-order CI shown in Figure 5.3, we can see that both matter-waves re-image with a period of approximately $82\,\mu\text{s}$, and both have additional re-imaging in and out-of-phase periods at higher frequencies. In the case of our first-order CI this occurs an additional time once per oscillation at half the Talbot time of $82\,\mu\text{s}$, for a two-fold increase in oscillation frequency over the base $12.3\,\text{kHz}$ matter-wave frequency to $24.6\,\text{kHz}$. In the case of the second-order signal, we see an additional 5 re-imaging times, for a total six-fold increase in frequency to approximately $73.8\,\mathrm{kHz}$. We also see that the second-order interferometer generates a more complex spatial density profile across the BEC with narrower, taller density peaks, and features with a $\lambda_{\text{grating}}/4$ periodicity.

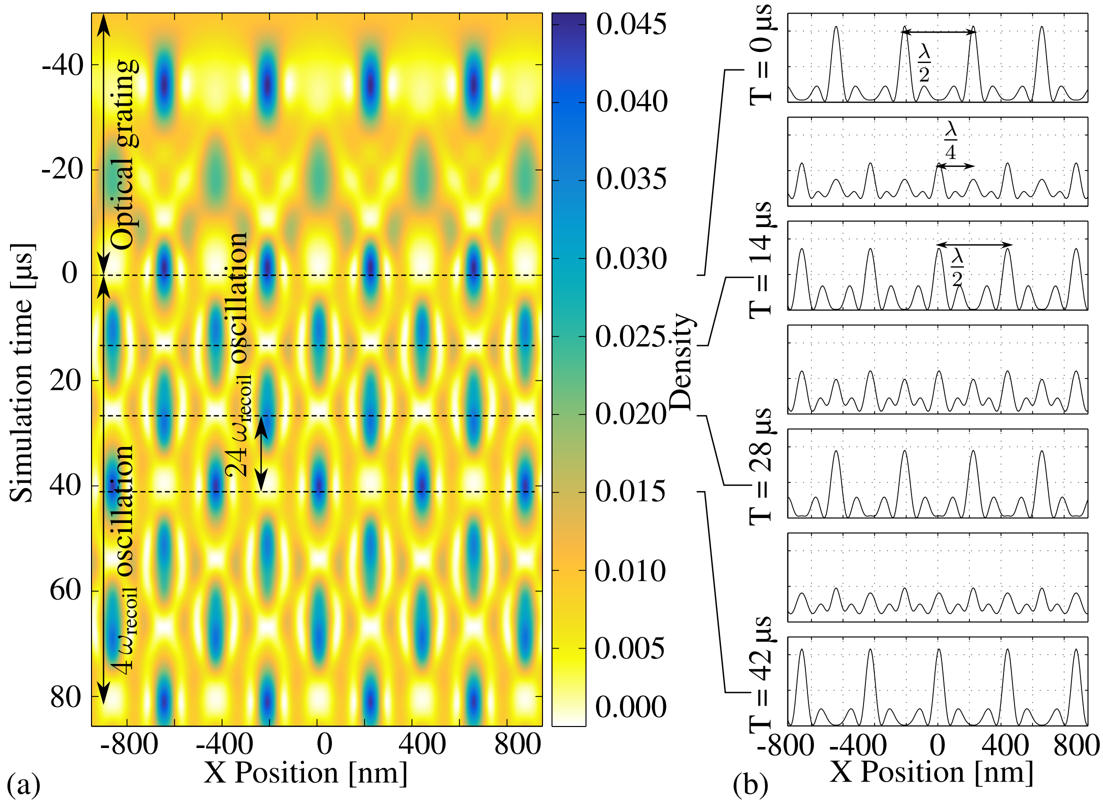

Figure 6.10: (a) The Talbot carpet of a $p{=}(+4, +2, -2, -4)\,\hbar k$ contrast interferometer. Here the $|p|{=}2\hbar k$ modes generate a continuous $\lambda/2$ grating which would continuously reflect a probe beam. The $|p|{=}4\hbar k$ modes interfere with this grating, generating a hologram which reflects at a frequency of $24\,\omega_{\text{recoil}} \approx 73\,\mathrm{kHz}$, with an oscillation period of approximately $13.7\,\mu\mathrm{s}$ (b).

In principle, this technique should be extendible to higher momentum states, if those momentum states are integer multiples of $2\hbar k$. If we are able to generate a four-port atom-optic that splits our atoms into an equal superposition of the states with momentum $|p|{=}2\hbar k$ and $|p|{=}n\hbar k$, we should expect a signal frequency of $(n^2 - 1) \times 4\,\omega_{\text{recoil}}$.

6.3.4 Experimental realisation

The pulse-optimisation method described in chapter 3 was used to generate a pulse sequence (section 3.8.1) that would output the state

$$|\psi\rangle = \frac{1}{2}|-4\hbar k\rangle + \frac{1}{2}|-2\hbar k\rangle + \frac{1}{2}|+2\hbar k\rangle + \frac{1}{2}|+4\hbar k\rangle \; , \tag{6.9}$$

using the pulse parameters A_1 = 17.5 E_r, T_1 = 15.3 µs, A_2 = 8.2 E_r, T_2 = 20.0 µs.

We then configured the experiment with a phase-contrast interferometer sequence as shown in Figure 5.13, except that that single ‘opening’ pulse was replaced with the four-port beam-quatter above. In anticipation of the increased signal frequency we raised the sample rate of our single-photon counting-module to 1 MHz.

The resulting data are shown in Figure 6.11. The experiment was run ten times, with the photon counts for each run shown as light grey crosses. The mean of each time-bin is drawn as a black dot, with error bars calculated as the standard deviation of the measurements per bin. A blue sinusoidal overlay is drawn in dashed-blue as a guide at 78 kHz.

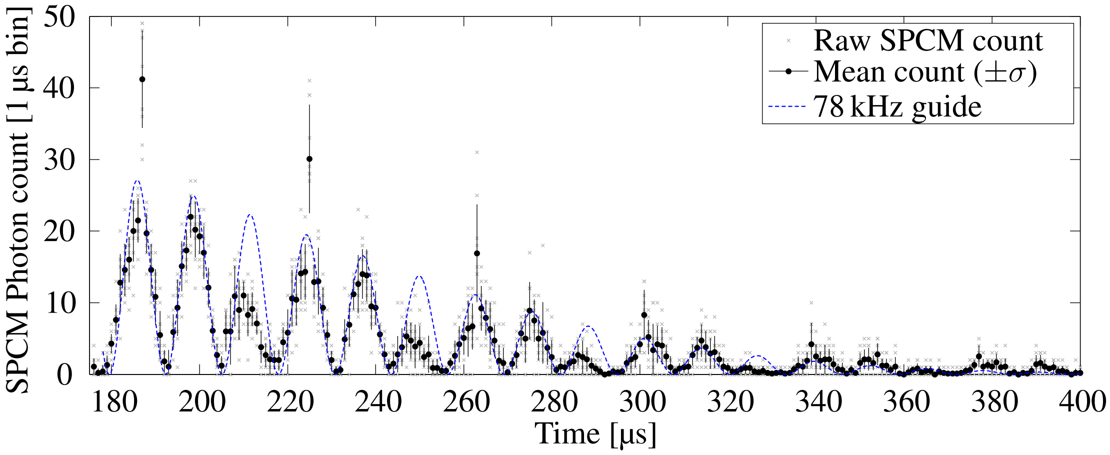

Figure 6.11: The experimental realisation of the ‘beat-note’ contrast interferometer shown in Figure 6.10. Grey crosses show the SPCM counts in each of ten separate experimental runs. The dots are the mean value in each time bin, and the error bars the standard deviation of those ten values per bin. The dashed blue line is a cosine model with an exponential decay, with parameters set by hand as a guide to the data. Here we see a reproducible periodic oscillation in every single shot with a frequency of approximately 78 kHz.

What we see in Figure 6.11 is a periodic modulation of the reflected light. This shows that we can indeed use a beat-note measurement technique to incorporate higher frequency components into our contrast signal whilst still scattering probe photons into our collection mode. This modulation does appear to predominantly contain two frequencies as we expected: we see clusters of three peaks, repeated. The first cluster can be seen with peaks at times $186\,\mu s$, $196\,\mu s$, and $206\,\mu s$, with the amplitude of the third peak significantly smaller then the previous two peaks.

Even so, there are some surprising aspects to the data collected. Firstly, the first peak within each cluster contains a single bin with a large spike in detected photons. These spikes can be observed at times $187\,\mu s$, $225\,\mu s$, $263\,\mu s$, $301\,\mu s$ and contain around twice the number of detected photons as each of their nearest neighbours do. Even the lowest individual shots show photon counts around $50\,\%$ higher than the nearest neighbour averages. The data shown in Figure 6.11 represents ten repeated shots, but the same features were visible in fifty consecutive shots over an experimental run lasting around 30 minutes. Secondly, these clusters repeat with a period of around $38\,\mu s$ corresponding to a $26.3\,\mathrm{kHz}$ frequency component, which is $6.9\,\%$ faster than our expected $24.6\,\mathrm{kHz}$ frequency component. The sub-features within each three-peak cluster appear to oscillate at approximately 78 kHz, which is $5.7\,\%$ faster than the expected $73.8\,\mathrm{kHz}$ contribution from our $24\,\omega_{\mathrm{recoil}}$ term.

Interestingly, our 2D GPE simulation recreates neither the narrow photon spikes nor the oscillation frequency we observe experimentally. Figure 6.11 shows features which oscillate with around $42\,\mu s$ and $14\,\mu s$ periodicity, corresponding to frequencies of approximately $25\,\mathrm{kHz}$ and $73\,\mathrm{kHz}$ as expected. Figure 6.13 shows a simulation of our contrast signal that shows no sign of the narrow spike features we see in Figure 6.11. One feature that *is* recreated by the 2D GPE simulation is the varying amplitudes of the sub-features within each repeated cluster. The amplitude of the second and third peaks varied noticeably during the data run, starting from the data shown in Figure 6.11, and ending with almost no photons in the third hump. Likewise, the amplitude of the second and third oscillations vary with the ratio h/m, as shown in Figure 6.13.

To compare this data, we configured our 2D GPE simulation to perform the same interferometer sequence as in Section 6.3.3. The simulation was configured to run over only the first $\sim 200\,\mu s$, generating a 2D map of complex amplitudes for the atomic ensemble at each time interval $\psi(x, y, t)$. As with the autocorrelation analysis, each of these complex amplitude maps was converted into a density $n(x, y, t)$, and used to generate a refractive index map at each time interval $\eta(x, y, t) = 1 + \alpha n(x, y, t)$ (see equation 5.1), where α is a pre-factor tweaked during testing to enable a detectable reflection amplitude. To simulate the reflection of our probe laser from this matter-wave, we used a Finite-Difference Time-Domain (FDTD) simulation [154] using Yee's method [155]. Yee's method is a technique for simulating the propagation of Electro-Magnetic (EM) fields through a medium [155]. The simulation software used generates an EM wave driver that generates a driven perturbation in the simulation space's E and H fields, updating these in a leapfrog manner [154, 155].

The refractive index maps $\eta(x, y, t)$ were used by the FDTD simulation to simulate the Bragg-reflection of our contrast probe beam from the matter-wave hologram for each time index t. For each GPE time index we simulated $300\,\mathrm{fs}$ of light-field propagation time, such that emitted light could reach the detection region of the simulation space after reflecting from the hologram. At the end of the simulation, we would sum over the magnitude of the reflected wave's |H| field to quantify the reflected light field. Figure 6.12 shows the last frame of a 300 fs FDTD simulation of our contrast interferometer.

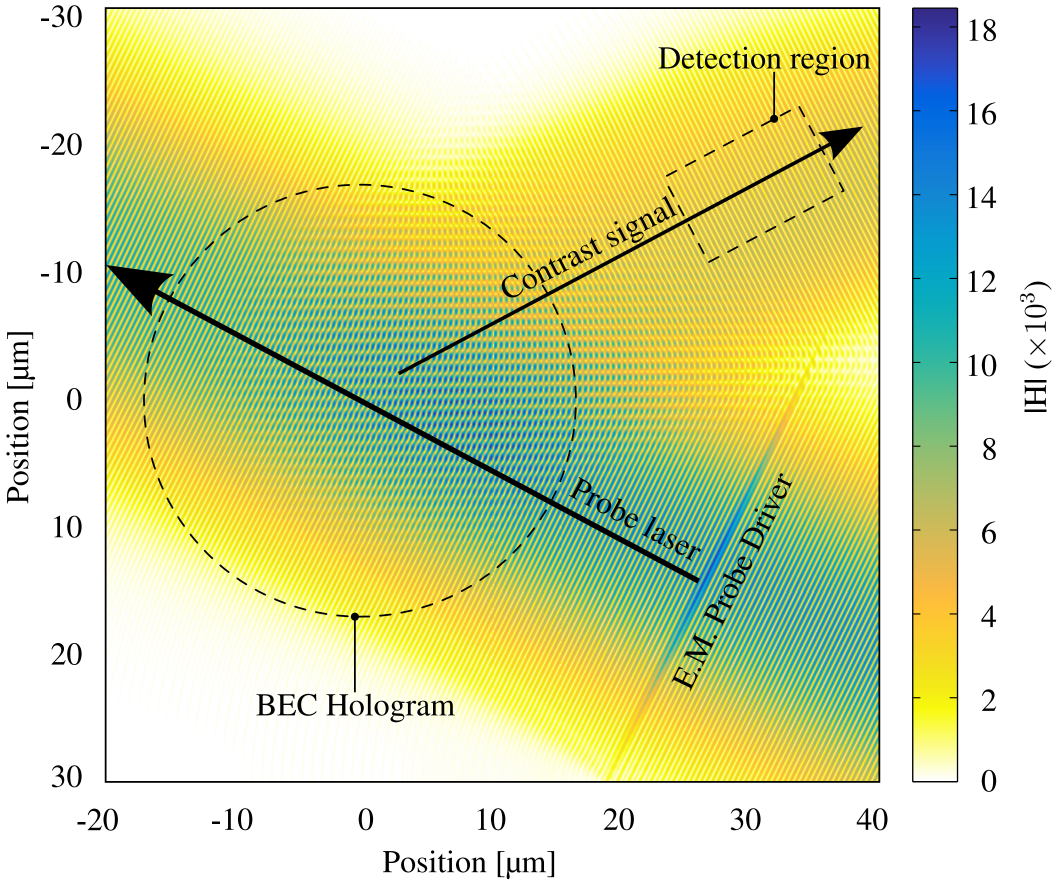

Figure 6.12: We simulate our Contrast signal by way of a Finite-Difference Time-Domain (FDTD) method, where an electromagnetic 'driver' creates EM waves that encounter a structure with modulated refractive index. This structure is determined by the density of our 2D GPE BEC simulation. We then sample the average reflected wave amplitude after 300 fs, repeating the FDTD simulatyion for each GPE evolution time-step.

We ran this simulation multiple times with slightly different values of h/m to better understand the sensitivity of the system as an α measurement. These data are plotted in Figure 6.13. What we found was that unlike our first-order interferometer, the amplitude of the 'between' peaks altered as h/m changed. This is most likely caused by the shift in effective amplitude of our atom-optics pulse as h/m changes. This is a subtle point. The phase of our momentum states changes significantly during our atom-optic pulses. We rely on this effect to perform state targeting: since the interaction terms in equation 3.3 are phase sensitive, we can use the phase-evolution of the different modes to plot a trajectory to a target state. When we alter the ratio h/m, the energies associated with each momentum state change, and as a result so do their phase oscillation rates. Essentially, when we alter h/m we 'detune' out atom-optics such that they no longer quite target the states we intended. This shift alters the output populations of our atom-optics slightly, altering the balance of $|p|{=}2\hbar k$ and $|p|{=}4\hbar k$ populations. This perturbation is sufficient to alter the time-evolution of the hologram, modifying the reflected signal. Whilst this behaviour will, at least in principle, increase the information 'about' h/m in our data, at the time of writing we do not have a model capable of extracting this information.

Whilst we hoped to obtain a signal similar to our first-order CI except faster, the second-order CI shows some interesting and unexpected behaviour. The response of the signal to variations in h/m offers the possibility of increased information content if a suitable model could be found. The experimental data shown in Figure 6.11 shows behaviour that is not explained by our current understanding of the system. The sharp peaks, aside from being as-yet unexplained, offer the potential for very sharp timing features for the extraction of a frequency from the contrast signal. A future examination of these should aim to resolve the shape and width of these features for potential use as a frequency signal.

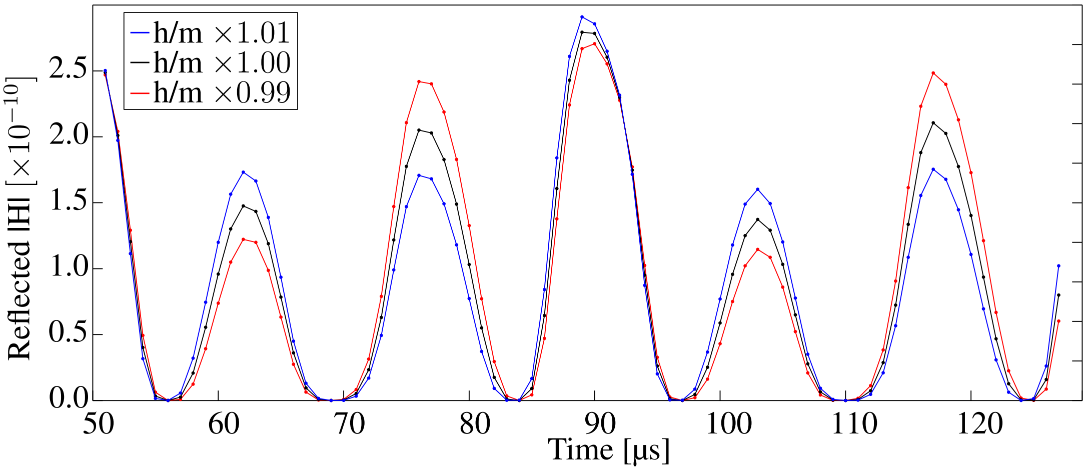

Figure 6.13: A 2D GPE simulation of the 'beat-note' contrast interferometer signal. Here we have varied the value of h/m from the expected value (black line) by $\pm 1\,\%$ (blue and red lines, respectively).

6.4 Combining multiple measurements

6.4.1 Motivation and background

Whilst our contrast interferometer is capable of performing measurements several hundred times quicker than our conventional momentum interferometer (section 5.4.2), this doesn't aid us unless we can combine multiple experimental runs to enhance our measurement.

The Contrast Interferometer (CI) by Jamison *et al.* [54] determined $\partial\phi_{\text{recoil}}/\partial t$ by performing many CI measurements at various interferometer durations, where T is the split $\rightarrow$ reflect time, then probing the atomic hologram and observing the phase at the time $t = 2T$. The recoil frequency can then be calculated trivially as $\omega_{\text{recoil}} = \frac{1}{2}\partial\phi_{\text{recoil}}/\partial T$. Unlike our α measurement detailed in section 5.4.2, the measurement here is one of a unique phase per 'shot'.

The advantage of the CI in a phase measurement remains; we do not take a single amplitude as our only data, but instead read phase from our fitted curve. By rapidly performing many measurements of phase we freeze out many sources of phase noise per shot, and because we observe our data to be well represented by the Poisson distribution [99], we can appropriately consider the noise sources we haven't frozen out.

Some precision interferometers have enhanced precision by altering the counting they do; in the work of Hume *et al.* [156], rather than count atoms N_{atom} directly the authors count the number of fluorescence photons N_{photon} scattered from the atomic cloud as the atoms are trapped. Here their measurement statistics are still limited with the phase uncertainty $\delta\phi \propto 1/\sqrt{N}$ as with many atom interferometers, but since $N_{\text{photon}} \gg N_{\text{atom}}$, they are able to bring their uncertainty $\delta N_{\text{atom}} < 1$ [156].

Typically, the data from an interferometer is two-dimensional, in so far as it returns a one-dimensional value $y(x)$ (such as atomic population or light intensity, for example) as a function of some control parameter x (such as time, or rotation rate). This $y(x)$ data generally undergoes a sinusoidal modulation as the x co-ordinate is varied. In the absence of noise each $y(x)$ value can be mapped to an infinite number of phases $\phi(x) + 2n\pi$, and $\pi - \phi(x) + 2n\pi$, where $(n \in \mathcal{Z})$. By folding this infinite range of phase into the range $0 \leq \phi(x) < 2\pi$, we can reduce this mapping such that each phase maps to one of two possible phases. We can determine which of these phases our measurement lies on by varying x slightly and determining the sign of $\mathrm{d}y(x)/\mathrm{d}x$. We could then choose whatever x gives us the greatest sensitivity (generally where $\mathrm{d}y(x)/\mathrm{d}x$ is maximised), and repeatedly record $y(x)$, for N total measurements. Here our uncertainty scales as $\delta\phi \propto 1/\sqrt{N}$.

The above procedure reduces the number of contributing parameters down to just the phase $\phi(x)$, removing the need to consider the $y(x)$ modulation amplitude, background level offsets, etc. The trouble here occurs when additional noise is present beyond our counting statistics: since noise manifests as variation in the $y(x)$ value, we inadvertently map this extra noise into phase. With all measurement of phase at a single x value, we can only assume that all $y(x)$ shifts we see are caused by some change in the phase. In practice we would observe that our repeated measurements of $y(x)$ converge on some varying range greater than we would expect from our sensitivity, and this extraneous noise would place a lower bound on our best possible measurement resolution of phase.

In comparison, the CI performs a composite measurement; each individual shot rapidly captures M sequential measurements of phase. This composite measurement helps to separate out the different contributions to phase because we measure an oscillation and not a single value. Noise sources which introduce a background level shift or an amplitude change do not hinder our ability to estimate the phase $\phi(x)$, providing those noise sources are of a sufficiently low frequency. This frequency is determined by the rate and duration of our M sequential measurements: if our signal captures photons in $4\,\mu\mathrm{s}$ bins and lasts for a total of $500\,\mu\mathrm{s}$, then a photon-count error with a maximum frequency component of $50\,\mathrm{Hz}$ would appear as a common shift to all M photon counts, and could be distinguished from the phase-induced modulation.

From Figure 5.12 we see that our uncertainty in phase scales as $\delta\phi \propto 1/\sqrt{M}$. In addition, our ability to estimate these parameters also scales with repeated N experimental runs as $\delta\phi \propto 1/\sqrt{N}$. Together, we expect our uncertainty over N repeated experimental cycles to scale as

$$\delta\phi \sim \frac{1}{\sqrt{NM}} \; . \tag{6.10}$$

An alternative phrasing of this statement is that our measurement uncertainty is still ultimately limited by the number of photons that are used in our measurement, but the nature of our measurement technique introduces correlations into the noise that allow us to distinguish some noise sources from uncertainties in our phase.

6.4.2 Fisher information

The Fisher Information is a metric used in parameter estimation to quantify how much information about some parameter is contained in some data. If we have a set of data x, which can be used to estimate the parameter θ with the estimator $f(x;\theta)$, the Fisher Information is defined as

$$\mathcal{I}(\theta) \equiv \int \left(\frac{\partial}{\partial\theta} \log f(x;\theta) \right)^2 f(x;\theta)\, dx \; . \tag{6.11}$$

The Fisher Information is then commonly used to determine the minimum possible variance in an estimate of θ obtainable from the data x, using the Cramér-Rao Lower Bound (CRLB) [157]

$$\mathrm{Var}(\theta) \geq \frac{1}{\mathcal{I}(\theta)} \; . \tag{6.12}$$

Together the Fisher Information and Cramér-Rao bound are commonly used to design or bias interferometry experiments such that they are most sensitive to a parameter that we wish to estimate [157]. Our recoil frequency CI measurement consists of discrete photon counts rather than a continuous variable, and so we can transform equation 6.11 into

$$\mathcal{I}(f_\mathrm{r}) = \sum_\mathrm{i} \left[\frac{\partial}{\partial f_\mathrm{r}} \log \Big(u(f_\mathrm{r}, t_\mathrm{i}) \Big) \Big| f_\mathrm{r} \right] = \sum_\mathrm{i} \frac{1}{u(f_\mathrm{r}, t_\mathrm{i})} \left[\frac{\partial u(f_\mathrm{r}, t_\mathrm{i})}{\partial f_\mathrm{r}} \Big| f_\mathrm{r} \right]^2 , \qquad (6.13)$$

where f_r is our measured recoil frequency, and our fitted model $u(f_\mathrm{r}, t_\mathrm{i})$ outputs a photon count for each time index t_i.

We can then use the Fisher Information of our model to determine the minimum possible uncertainty in frequency that our model (section 5.4.2) offers us. Here we fit our CI data with the model

$$u(t) = \frac{A}{2} \exp\left(-\frac{(t-t_0)^2}{2\tau^2} \right) \Delta t \Big(\cos(2\pi f_\mathrm{r} t + 2\pi c t^2 + \phi) + 1 \Big) , \qquad (6.14)$$

which describes a sinusoidal modulation with a Gaussian envelope. Here A represents our maximum signal amplitude, t_0 is the time-centre of our Gaussian envelope, τ is the time-width of the Gaussian envelope, f_r is the frequency of the sinusoidal modulation at time $t = 0$, c is the linear frequency chirp as a function of time , and ϕ is a phase of the sinusoidal modulation at time $t = 0$. Passing this through equation 6.13 we obtain an expression for the Fisher Information in our contrast signal,

$$\mathcal{I}\left(f_\mathrm{r}\right) = (2\pi t)^2 \frac{A}{2} \exp\left(-\frac{(t-t_0^2)}{2\tau^2} \right) \Delta t \sin^2 \left(\frac{1}{2} \left[2\pi f_\mathrm{r} t + 2\pi c t^2 + \phi \right] \right) . \qquad (6.15)$$

Here $u(t)$ can be thought of as the probability of measuring photons as a function of time over the duration of the contrast signal. In this respect the result in equation 6.15 is somewhat surprising: we would naively expect the sensitivity $s(t)$ of the model to be given by the square of the gradient of the probability,

$$s(t) = P^2 \Delta t^2 \sin^2 \Big(\left[2\pi f_\mathrm{r} t + 2\pi c t^2 + \phi \right] \Big) (2\pi t)^2 , \qquad (6.16)$$

with $P = \frac{A}{2} \exp\left(-\frac{(t-t_0)^2}{2\tau^2} \right)$. Instead we see that the Fisher Information modulates at half the expected frequency,

$$\mathcal{I}\left(f_\mathrm{r}\right) = P \Delta t \sin^2 \left(\frac{1}{2} \left[2\pi f_\mathrm{r} t + 2\pi c t^2 + \phi \right] \right) (2\pi t)^2 . \qquad (6.17)$$

This is caused by the nature of the Fisher Information calculation in equation 6.13: we calculate the square of the derivative of our probability, and divide by the value of our probability at each time. In this sense we can look at the Fisher Information as a measure of the *fractional* sensitivity of our probability: how much the value at a given time index changes as a fraction of its unperturbed value, summed over all time indices. For example, a shift in $u(t)$ of $+1$ photon is fractionally small when $u(t)$ is large, but tends to infinity as $u(t)$ approaches zero. As a result, our Fisher Information is highest when the contrast signal is near zero, because at these times a given change in photon count has the largest relative shift in the overall photon count.

It has been postulated that a model of our contrast signal photon count that includes a 'photon-shot-noise' term will offer a more complete modelling of the Fisher Information in the contrast interferometer signal [158]. As is, our model assumes that it can predict the photon count with sub-photon precision and no uncertainty. Figure 6.14a shows a plot of the fitted model, with parameters taken from our fitted recoil frequency measured in section 5.4.2. The corresponding Fisher Information is shown below in Figure 6.14b.

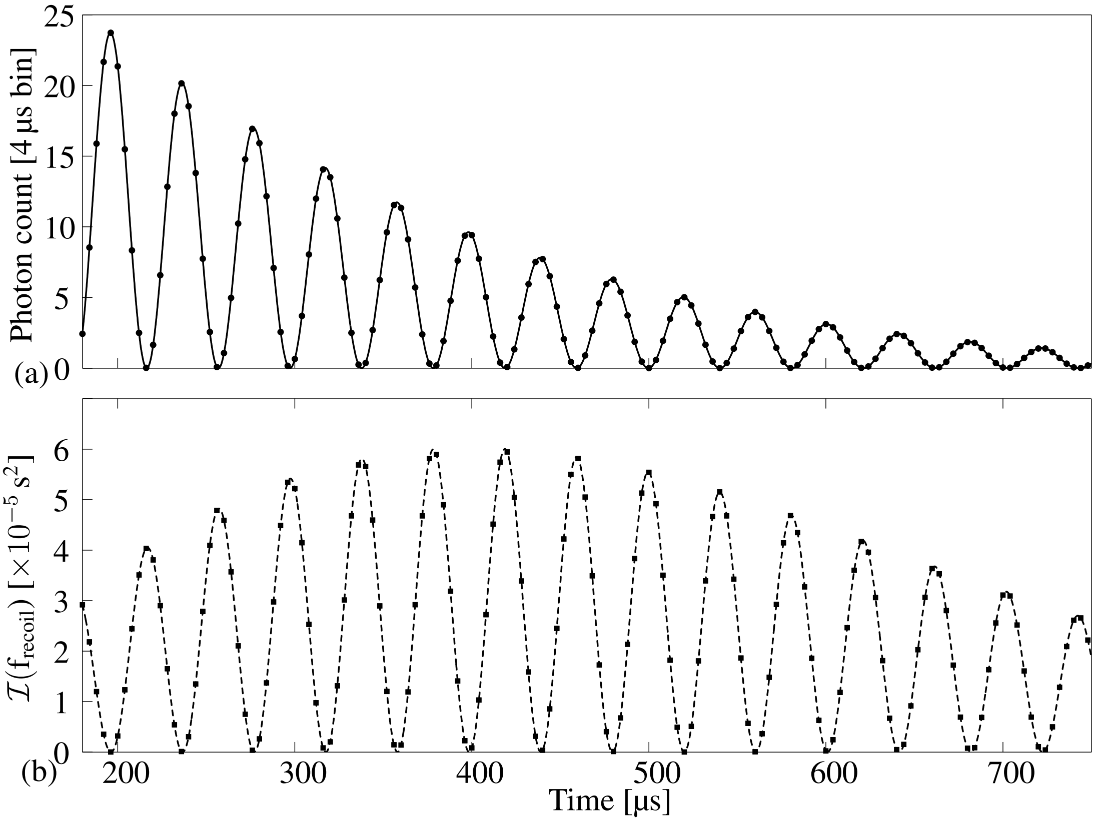

Figure 6.14: Fisher information of our contrast signal model. (a) As our input we re-use the model (equation 6.14) fitted to our CI measurement of recoil frequency from section 5.4.2, with the fitted parameters. We then pass this model through equation 6.13 to obtain the corresponding Fisher Information (b).

Despite the limitations of the analysis, we can use the Fisher Information of our model (equation 6.15) to place a lower bound on the uncertainty our fitting algorithm can obtain, as a test of the procedure. The Fisher Information of independent measurements adds linearly [157], so we can gain an estimate of our minimum uncertainty by summing $\mathcal{I}\left(f_{\text{recoil}}\right)$ and using the Cramér-Rao bound. Here we obtain a total Fisher Information of $\mathcal{I}\left(f_{\text{recoil}}\right) = 0.034\,\mathrm{Hz}^{-2}$, which implies Var$(f_{\text{recoil}}) = 291\,\mathrm{Hz}^2$ and $\sigma_{FI}(f_{\text{recoil}}) = 17.1\,\mathrm{Hz}$. From this we infer that our fitting procedure (that returns $\sigma_{\text{Measured}}(f_{\text{recoil}}) = 80\,\mathrm{Hz}$, see Section 5.3.4) is *not* claiming a precision beyond the maximum information the model offers.

Chapter 7

Conclusions and Future Work

7.1 Conclusions

The primary result of the work contained within this thesis is the construction of an atom interferometer capable of single-shot measurements of the fine-structure constant using a holographic readout technique. This method enhances our measurements of recoil frequency by rapidly performing many sequential measurements of interferometer phase, allowing the separation of frequency from other noise sources that would confuse the data from a more traditional interferometer.

We have developed an atom-optics toolbox using off-resonant two-photon scattering capable of generating arbitrary superpositions of target momentum states with high transfer efficiency: experimentally shown as $99.97 \pm 0.03\,\%$ in the case of a two-arm $|0\hbar k\rangle \rightarrow [|{+2\hbar k}\rangle + |{-2\hbar k}\rangle]$ beam-splitter pulse sequence. We have used these tunable atom-optics to generate different atom-interferometers capable of measuring gradient fields, and recoil frequency.

In Section 5.4.2 we have demonstrated a contrast-interferometer capable of measuring entire interference fringes in a single shot. This is approximately 700 times faster than the data acquisition rate of our interferometer in the standard configuration that uses a closing beam-splitter pulse to project the interferometer phase into momentum populations.

This contrast interferometer is capable of determining the fine structure constant with an uncertainty $\alpha^{-1} = 136.74 \pm 0.88$ (6500 ppm) in a single experimental cycle of $30\,\mathrm{s}$ duration, where most of this uncertainty can be attributed to uncertainty in the angles of our interferometer atom-optic beams. If we alter the geometry of our interferometry beams, we calculate that we can obtain a precision of $\delta\alpha^{-1} = 0.32$ (2300 ppm) in a single shot, and can integrate to 60 ppm over a period of around 12 hours, or to 10 ppm in around one months of continuous integration. In comparison, the previously quoted α uncertainty with this experiment is $\alpha^{-1} = 137 \pm 5$ [99].

Whilst the best feasible precision from this experiment is currently around 4 orders of magnitude below the current state-of-the-art, we can increase the precision of our measurement by increasing the momentum width that separates our interferometer arms. We have successfully demonstrated a contrast interferometer signal with a higher frequency using a beat-note measurement of the first and second $(n = 2)$ excited momentum states. This can, in principle, be extended to higher momentum states for an $n^2 - 1$ scaling of recoil frequency with scattering mode n.

We have discovered the existence of interaction-induced frequency chirps within our experimental contrast interferometer signal, and have constructed a model that predicts this frequency chirp with excellent agreement. In Section 6.2 we experimentally detect a frequency chirp of $(\mathrm{d}f/\mathrm{d}t)_{\text{experiment}} = -2.335 \pm 0.052\ \mathrm{Hz}\,\mu\mathrm{s}^{-1}$, with a predicted $(\mathrm{d}f/\mathrm{d}t)_{\text{predict}} - 2.3\,\mathrm{Hz}\,\mu\mathrm{s}^{-1}$. This behaviour may present a new method for the examination of mean-field effects in BECs.

7.2 Future Work

7.2.1 Interferometer beam angle

The single largest source of error in our measurements of the fine-structure constant is the angle θ between our atom-optic laser beams. Whilst physically time-intensive, it is conceptually simple to alter the geometry of these beams on our optics table until they are counter-propagating. We can fine-tune the alignment of these beams by fibre-coupling each interferometer arm into each other, reducing the angle to nearly zero. Since our uncertainty associated with our beam angle is proportional to $\mathrm{d}\cos(\theta)/\mathrm{d}\theta = -\sin(\theta)$, this will reduce the uncertainty from our beam angle far below that from our recoil frequency measurement, effectively removing that noise source from our uncertainty calculations, and improving our overall knowledge of the interferometer parameters

7.2.2 Data analysis

We have developed a data-analysis algorithm capable of fitting models to our data whilst respecting the asymmetrical uncertainties of our photon-counting. Whilst this algorithm returns fit parameters from single shot data, we do not yet have a good method to combine multiple measurements. Our analysis of the Fisher Information (FI) within our fitted model appears to confirm that our fitting algorithm is not claiming a precision beyond the CRLB, but our FI calculation does not yet take account of quantised photon counts in our data or the Poisson distribution around the fitted model. As such it does not consider the contribution of noise we would expect in our data. Further investigation should be taken to include this aspect of our data in a better mathematical model of our interferometer output.

A secondary investigation should compare the Quantum Fisher Information (QFI) and Classical Fisher Information (CFI) of our 2D GPE simulation with the CFI of the contrast signal, as a test of the validity of the contrast CFI calculation, and to potentially quantify advantages of the CI over the MI.

7.2.3 Beam-splitters

Our BEC hologram partially reflects an incoming laser beam, that is, it is effectively an asymmetrical beam-splitter for light. Previous work has shown that such optical elements can display unintuitive behaviour [159]. If we introduce a strong beam such that shot noise is no longer significant, we may be able to learn something about beam-splitters by examining the weakly reflected photons. The fact that we can generate BEC holograms with tunable density-distributions [142] may allow us to conduct some unique experiments investigating the behaviour of beam-splitters .

7.2.4 Higher-order scattering

Our experimental higher-frequency contrast signals display behaviour that does not agree with our 2D GPE simulations of the system, instead showing features with a temporal width of $\delta t \leq 1\,\mu\mathrm{s}$, and a photon count approximately twice neighbouring bins. Our data was captured with a $1\,\mu\mathrm{s}$ bin width, so we as-yet have no knowledge of the shape of these features. We also do not understand the processes which generate such sharp spikes in photon count.

Spikes in photon count with a very narrow time-width may represent an attractive feature for the measurement of recoil frequency. The counting frequency of our SPCM module is significantly higher than the $100\,\mathrm{kHz}$ frequency tested, and if our aim is to measure only a few tens of microseconds, we can afford to increase the intensity of our probe beam to compensate for a smaller bin-width. A more rigorous investigation of these features at a higher time-resolution should be performed.

7.2.5 Mean-field chirp

Whilst our model predicts the frequency-chirp observed in our experimentally acquired data, our data is somewhat sparse. This is in part a result of the shuttering mechanism used to protect our SPCM from our atom-optic pulses: we have a minimum $120\,\mu\mathrm{s}$ delay where we close a shutter to extinguish leakage from our atom-optics and open a shutter to expose the SPCM [99]. This renders the first $120\,\mu\mathrm{s}$ of our short contrast signal unobservable. The duration of our short contrast signal reduces with increased BEC expansion time, and so we rapidly run out of available fringes to fit our model to, which renders fitting difficult. A replacement of these shutter mechanisms would increase the time-range of our observable short interferometer. Data could then be captured to map out the frequency chirp experimentally in the short and long configurations, for a more complete comparison with our model.

Appendix A

A.1 Useful physical constants

We use equation 1.2 to determine the fine-structure constant α,

$$\alpha^2 = \frac{2R_\infty}{c}\frac{m_{87\text{Rb}}}{m_e}\frac{h}{m_{87\text{Rb}}} ,$$

where our recoil frequency measurement is used to determine h/m. The remaining physics constants are the Rydberg constant R_∞, electron mass m_e, rubidium-87 mass $m_{87\text{Rb}}$, speed of light in a vacuum c, and the unified atomic mass unit u. The values for these physical constants used in the calculations with associated uncertainties in this thesis are shown in Table A.1.

Table A.1: Physical constants

Constant	Numerical value		Fractional uncert.	Source
R_∞	$10973731.568508(65)$	m^{-1}	5.9×10^{-12}	[92,93]
m_e	$9.10938356(11) \times 10^{-31}$	kg	1.2×10^{-8}	[71]
$m_{87\text{Rb}}$	$86.909180520(15)$	u	1.7×10^{-10}	[71,94,95]
c	299792458	$\text{m}\,\text{s}^{-1}$	Exact	[71]
u	$1.44316060(11) \times 10^{-25}$	kg	1.2×10^{-8}	[71]

A.2 Analytical theory for off-resonant scattering

Start off by assuming that the Hamiltonian of our atoms in an optical lattice takes the form:

$$\hat{H} = -\frac{\hbar}{2m}\frac{\partial^2}{\partial z^2} + V_0 \cos^2(kz) \ , \tag{A.1}$$

where V_0 is the lattice potential depth, and k the effective wave vector of the lattice. If we construct our modes as a superposition of plane waves:

$$\psi\left(t\right)=\sum_n C_n\left(t\right)e^{i2nkz}\ , \tag{A.2}$$

we can substitute (1) and (2) into the time-dependent Schrödinger equation to describe the evolution of each mode through time:

$$i\hbar\frac{\partial}{\partial t}\sum_n C_n\left(t\right)e^{i2nkz}=-\frac{\hbar^2}{2m}\frac{\partial^2}{\partial z^2}\sum_n C_n\left(t\right)e^{i2nkz}+V_0\cos^2\left(kz\right)\sum_n C_n\left(t\right)e^{i2nkz} \tag{A.3}$$

We have an infinite set of coupled equations here, so let's use the orthogonality of the plane wave exponentials to extract a single mode. Multiply through by an exponential of the same form with a negative sign of a single mode 'm', and take the integral over all space,

$$\times\, e^{-i2mkz}\rightarrow\int_{-\infty}^{+\infty}dz\ , \tag{A.4}$$

$$i\hbar\frac{\partial}{\partial t}\int_{-\infty}^{+\infty}\sum_n C_n\left(t\right)e^{i2nkz}e^{-i2mkz}\mathrm{d}z=\cdots \tag{A.5}$$

$$\cdots-\frac{\hbar^2}{2m}\int_{-\infty}^{+\infty}e^{-i2mkz}\frac{\partial^2}{\partial z^2}\sum_n C_n\left(t\right)e^{i2nkz}\mathrm{d}z+\cdots$$

$$\cdots+V_0\int_{-\infty}^{+\infty}\cos^2\left(kz\right)\sum_n C_n\left(t\right)e^{i2nkz}e^{-i2mkz}\mathrm{d}z\ . \tag{A.6}$$

The derivative of a sum is the same as the sum of the derivatives, so we can take the middle term's double z derivative inside the sum over all n:

$$i\hbar\frac{\partial}{\partial t}\int_{-\infty}^{+\infty}\sum_n C_n\left(t\right)e^{i2nkz}e^{-i2mkz}\mathrm{d}z=\cdots \tag{A.7}$$

$$\cdots-\frac{\hbar^2}{2m}\int_{-\infty}^{+\infty}\sum_n C_n\left(t\right)\left(i2nk\right)^2e^{i2nkz}e^{-i2mkz}\mathrm{d}z+\cdots$$

$$\cdots+V_0\int_{-\infty}^{+\infty}\cos^2\left(kz\right)\sum_n C_n\left(t\right)e^{i2nkz}e^{-i2mkz}\mathrm{d}z\ . \tag{A.8}$$

Since $e^{iz}=\cos(z)+i\sin(z)$, the real part of the integrand is cosine-like, and the imaginary part sine-like. An integral over all space of an odd function like a sine is zero, and the integral of the cosine-like part from 0 to $+\infty$ is equal to that from $-\infty$

to 0. So to make the integrals easier, let's instead do:

$$\int_{-\infty}^{+\infty} e^{i2nkz} e^{-i2mkz} \mathrm{d}z \rightarrow 2 \int_{0}^{+\infty} e^{i2nkz} e^{-i2mkz} \mathrm{d}z \ , \tag{A.9}$$

$$i\hbar \frac{\partial}{\partial t} 2 \int_{0}^{+\infty} \sum_n C_n\left(t\right) e^{i2nkz} e^{-i2mkz} \mathrm{d}z = \cdots \tag{A.10}$$

$$\cdots - \frac{\hbar^2}{2m} 2 \int_{0}^{+\infty} \sum_n C_n\left(t\right) \left(i2nk\right)^2 e^{i2nkz} e^{-i2mkz} \mathrm{d}z + \cdots$$

$$\cdots + 2V_0 \int_{0}^{+\infty} \cos^2\left(kz\right) \sum_n C_n\left(t\right) e^{i2nkz} e^{-i2mkz} \mathrm{d}z \ . \tag{A.11}$$

We now have three integrals. From the left to the right:

$$\int_{0}^{+\infty} \sum_n C_n\left(t\right) e^{i2nkz} e^{-i2mkz} \mathrm{d}z \ . \tag{A.12}$$

The exponentials are periodic in z, so as we integrate to further towards infinity the integral is increasingly dominated by the average value of the function over each period, making our upper limit effectively an integer number of periods. If we define this upper limit as $\lim\limits_{j \rightarrow +\infty} j\lambda$ where j is an integer and λ the period, and transform to dimensionless variables to make the integral easier:

$$\bar{z} = \frac{z}{\lambda}, \mathrm{d}z = \bar{z}\lambda \ , \tag{A.13}$$

we can use the orthogonality condition on complex exponentials:

$$\int_{0}^{j} e^{i2n\bar{z}} e^{-i2m\bar{z}} \lambda \mathrm{d}\bar{z} = j\lambda\delta_{n,m} \ , \tag{A.14}$$

which sets all integrals to zero except when $n = m$. The only term that survives in our infinite series of n terms is $n = m$.

$$\int_{0}^{j} \sum_n C_n\left(t\right) e^{i2n\bar{z}} e^{-i2m\bar{z}} \lambda \mathrm{d}\bar{z} = j\lambda C_m\left(t\right) \ . \tag{A.15}$$

The integral kills off all the remaining z term, so we don't need to worry about changing variables back.

The same thing happens with the second (middle) integral, so what we get is:

$$\int_0^{+\infty} \sum_n C_n(t)\,(i2nk)^2\, e^{i2nkz} e^{-i2mkz} \mathrm{d}z = j\lambda C_m(t)\,(i2mk)^2 \ . \tag{A.16}$$

The third (right) integral is a bit more interesting because of that $\cos^2(kz)$ term, and we need to treat it slightly differently.

$$\int_0^{+\infty} \cos^2(kz) \sum_n C_n(t)\, e^{i2nkz} e^{-i2mkz} \mathrm{d}z \ . \tag{A.17}$$

The trick is to use the cosine as the orthogonality check function, and combine the exponentials into a single term:

$$\int_0^{+\infty} \sum_n C_n(t)\, e^{i2(n-m)kz} \cos^2(kz)\, \mathrm{d}z \ . \tag{A.18}$$

Do the same variable change again in z:

$$\int_0^{j} \sum_n C_n(t) \cos^2(2\pi\bar{z})\, e^{i2(n-m)2\pi\bar{z}} j\lambda \mathrm{d}\bar{z} \ . \tag{A.19}$$

Now when $n = m$, the exponential term becomes 1, and we're left with the integral:

$$\int_0^{j} C_m(t) \cos^2(2\pi\bar{z})\, \mathrm{d}\bar{z} = \frac{1}{2} j\lambda C_m(t) \ . \tag{A.20}$$

When $n = m \pm 1$, the exponentials form a cosine sine pair:

$$\int_0^{j} (t) \cos^2(2\pi\bar{z}) \left(\cos(\pm 2 \times 2\pi\bar{z}) + i \sin(\pm 2 \times 2\pi\bar{z})\right) j\lambda \mathrm{d}\bar{z} \ . \tag{A.21}$$

If we multiply out the sine and cosine terms, the sine half of the integral is an odd function, so that side goes to zero. Of the remaining terms, the second remain cosine has twice the frequency of the first, so it looks like another cos^2 when $n = m \pm 1$:

$$\begin{aligned} &\int_0^{j} C_{n=m\pm1}(t) \cos^2(2\pi\bar{z}) \cos(2 \times 2\pi\bar{z}) j\lambda \mathrm{d}\bar{z} = \cdots \\ &\qquad \cdots = \int_0^{j} C_{n=m\pm1}(t) \left[2\cos^4(2\pi\bar{z}) - \cos^2(2\pi\bar{z})\right] j\lambda \mathrm{d}\bar{z} = \cdots \\ &\qquad\qquad \cdots = C_{n=m\pm1}(t)\, j\lambda \left[\frac{3}{4} - \frac{1}{2}\right] = \frac{1}{4} j\lambda C_{n=m\pm1}(t) \ . \end{aligned} \tag{A.22}$$

Plug these all back into the big equation and you get:

$$i\hbar\frac{\partial}{\partial t}j\lambda C_m\left(t\right)=-\frac{\hbar^2}{2m}\left(i2mk\right)^2j\lambda C_m\left(t\right)+...$$
$$...+V_0\left(\frac{1}{4}j\lambda C_{m-1}\left(t\right)+\frac{1}{2}j\lambda C_m\left(t\right)+\frac{1}{4}j\lambda C_{m+1}\left(t\right)\right)\ . \quad \text{(A.23)}$$

Cancel the j, λ and tidy up, and rename the index m to n.

$$\dot{C}_n\left(t\right)=-i\left[\frac{Er^{(2)}n^2}{\hbar}C_n\left(t\right)+\frac{V_0}{4\hbar}\Big(C_{n-1}\left(t\right)+2C_n\left(t\right)+C_{n+1}\left(t\right)\Big)\right]\ . \quad \text{(A.24)}$$

[If the infinity held in j bothers you, notice that you can take the upper limit as some non-infinite number of integer periods $j\lambda$, see that every term picks up a single multiplication of j when you change variables, and then divide through by j *before* you perform any integrals. *Then* take the limit as j tends to infinity (making the periodic assumption hold), and then perform the integrals (which return delta functions because the integral is effectively over an integer number of periods)].

A.3 Atom Gradiometer Theory

If our interferometer is configured such that the excites modes are only the $\pm 2\hbar k$ state, and the pulse sequence is symmetrical in time such that the 'opening time' (T_1) and 'closing time' (T_2) are identical, the interferometer phase is determined entirely by the movement of the atoms in the optical grating [138], leading to a T^2 phase shift due to some potential gradient (such as a gravitational or magnetic gradient). Our derivation follows the method presented in [138]:

We have an initial velocity of v_0. To this we apply a $p=\pm 2\hbar k$ splitter pulse. After a time T_1, we apply a reflection pulse, and after an identical time $T_2=T_1$, we apply an identical splitter pulse to that at $t=0$. We can then calculate the equations of motion for our atoms through time.

Within each interferometer arm we have two energy contributions. If we have a two-arm interferometer with upper arm A and lower arm B, where arms are separated by $\Delta p=4\hbar k$, the first contribution is the velocity of the atoms, $V_0=\hbar k_{eff}/m$, where k_{eff} is the wave-vector of the optical grating. The second is the magnetic potential which generates an acceleration $ma=-\mu_B m_f g_f \frac{\partial B}{\partial z}z(t)$.

We then have a set of state vectors at the time of each pulse.

$$\begin{aligned} v^A(t_1)&=v^B(t_1)=0,\\ z^A(t_1)&=z^B(t_1)=z_0, \end{aligned} \quad \text{(A.25)}$$

$$\begin{aligned}
v^A(t_2) &= +v_0 - at_2, \\
v^B(t_2) &= -v_0 - at_2, \\
z^A(t_2) &= +z_0 + v_0t_2 - \frac{1}{2}at_2^2, \\
z^A(t_2) &= +z_0 - v_0t_2 - \frac{1}{2}at_2^2,
\end{aligned} \tag{A.26}$$

$$\begin{aligned}
v^A(t_3) &= -v_0 - at_2 - at_3, \\
v^B(t_3) &= +v_0 - at_2 - at_3, \\
z^A(t_3) &= +z_0 + v_0t_2 - \frac{1}{2}at_2^2 - v_0t_3 - \frac{1}{2}at_3^2, \\
z^A(t_3) &= +z_0 - v_0t_2 - \frac{1}{2}at_2^2 + v_0t_3 - \frac{1}{2}at_3^2,
\end{aligned} \tag{A.27}$$

We then get our Lagrangian:

$$\begin{aligned}
L =& \frac{1}{2}mv^2 - \mu_B m_f g_f \frac{\partial B}{\partial z} z(t) \\
=& \frac{1}{2}mv^2 - maz(t)
\end{aligned} \tag{A.28}$$

The phase is determined with the classical action along each path:

$$\Delta\Phi_{Path} = \left(S_{cl}^B - S_{cl}^A\right)/\hbar \tag{A.29}$$

where the action is given by

$$S_{cl} = \int_{t_i}^{t_f} \mathrm{d}tL[path] \tag{A.30}$$

We then have

$$\begin{aligned}
L^A(t_2) =& \frac{1}{2}mv(t_2)^2 - maz(t_2) \\
=& \frac{1}{2}m(+v_0 - at_2)^2 - ma(+z_0 + v_0t_2 - \frac{1}{2}at_2^2) \\
=& \frac{1}{2}mv_0^2 - mv_0at_2 + \frac{1}{2}ma^2t_2^2 - maz_0 - mav_0t_2 + \frac{1}{2}ma^2t_2^2 \\
=& \frac{1}{2}mv_0^2 - 2mv_0at_2 + ma^2t_2^2 - maz_0
\end{aligned} \tag{A.31}$$

$$\begin{aligned} L^B(t_2) =& \frac{1}{2}mv(t_2)^2 - maz(t_2) \\ =& \frac{1}{2}m(-v_0 - at_2)^2 - ma(+z_0 - v_0t_2 - \frac{1}{2}at_2^2) \\ =& \frac{1}{2}mv_0^2 + mv_0at_2 + \frac{1}{2}ma^2t_2^2 - maz_0 + mav_0t_2 + \frac{1}{2}ma^2t_2^2 \\ =& \frac{1}{2}mv_0^2 + 2mv_0at_2 + ma^2t_2^2 - maz_0 \end{aligned} \tag{A.32}$$

We then get the action along each path as

$$\begin{aligned} S_{cl}^A(t_2) =& \int_{t1}^{t2} \mathrm{d}t \frac{1}{2}mv_0^2 - 2mv_0a(t_2 - t_1) + ma^2(t_2 - t_1)^2 - maz_0 \\ =& \frac{1}{2}mv_0^2(t_2 - t_1) - mv_0a(t_2 - t_1)^2 + \frac{1}{3}ma^2(t_2 - t_1)^3 - maz_0(t_2 - t_1) \end{aligned} \tag{A.33}$$

$$\begin{aligned} S_{cl}^B(t_2) =& \int_{t1}^{t2} \mathrm{d}t \frac{1}{2}mv_0^2 + 2mv_0a(t_2 - t_1) + ma^2(t_2 - t_1)^2 - maz_0 \\ =& \frac{1}{2}mv_0^2(t_2 - t_1) + mv_0a(t_2 - t_1)^2 + \frac{1}{3}ma^2(t_2 - t_1)^3 - maz_0(t_2 - t_1) \end{aligned} \tag{A.34}$$

Similarly, for the second half of the interferometer from $t_2 \rightarrow t_3$,

$$\begin{aligned} L^A(t_3) =& \frac{1}{2}m\left[v^A\left(t_3 - t_2\right)\right]^2 - ma\left[z^A\left(t_3 - t_2\right)\right] \\ =& \frac{1}{2}m\left[-v_0 - a\left(t_2 - t_1\right) - a\left(t_3 - t_2\right)\right]^2 - \cdots \\ & \cdots - ma\left[+z_0 + v_0t_2 - \frac{1}{2}at_2^2 - v_0t_3 - \frac{1}{2}at_3^2\right] \\ =& \frac{1}{2}mv_0^2 + 2mv_0a\left(t_3 - t_2\right) + ma^2\left(t_3 - t_2\right)^2 + \cdots \\ & \cdots + ma^2\left(t_2 - t_1\right)^2 + ma^2\left(t_3 - t_2\right)\left(t_2 - t_1\right) - maz_0 \end{aligned} \tag{A.35}$$

$$\begin{aligned} L^B(t_3) =& \frac{1}{2}m\left[v^A\left(t_3 - t_2\right)\right]^2 - ma\left[z^A\left(t_3 - t_2\right)\right] \\ =& \frac{1}{2}m\left[+v_0 - a\left(t_2 - t_1\right) - a\left(t_3 - t_2\right)\right]^2 - \cdots \\ & \cdots - ma\left[+z_0 - v_0t_2 - \frac{1}{2}at_2^2 + v_0t_3 - \frac{1}{2}at_3^2\right] \\ =& \frac{1}{2}mv_0^2 - 2mv_0a\left(t_3 - t_2\right) + ma^2\left(t_3 - t_2\right)^2 + \cdots \\ & \cdots + ma^2\left(t_2 - t_1\right)^2 + ma^2\left(t_3 - t_2\right)\left(t_2 - t_1\right) - maz_0 \end{aligned} \tag{A.36}$$

$$
\begin{aligned}
S^A_{cl}(t_3) =& \int_{t1}^{t2} \mathrm{d}t \frac{1}{2} m v_0^2 + 2 m v_0 a \left(t_3 - t_2\right) + m a^2 \left(t_3 - t_2\right)^2 \cdots \\
& \cdots + m a \left(t_2 - t_1\right)^2 + m a \left(t_3 - t_2\right)\left(t_2 - t_1\right) - m a z_0 \\
=& \frac{1}{2} m v_0^2 \left(t_3 - t_2\right) + m v_0 a \left(t_3 - t_2\right)^2 + \frac{1}{3} m a^2 \left(t_3 - t_2\right)^3 + \cdots \\
& \cdots + m a \left(t_2 - t_1\right)^2 \left(t_3 - t_2\right) + \cdots \\
& \cdots + \frac{1}{2} m a \left(t_3 - t_2\right)^2 \left(t_2 - t_1\right) - m a z_0
\end{aligned} \tag{A.37}
$$

$$
\begin{aligned}
S^B_{cl}(t_3) =& \int_{t1}^{t2} \mathrm{d}t \frac{1}{2} m v_0^2 - 2 m v_0 a \left(t_3 - t_2\right) + m a^2 \left(t_3 - t_2\right)^2 \cdots \\
& \cdots + m a \left(t_2 - t_1\right)^2 + m a \left(t_3 - t_2\right)\left(t_2 - t_1\right) - m a z_0 \\
=& \frac{1}{2} m v_0^2 \left(t_3 - t_2\right) - m v_0 a \left(t_3 - t_2\right)^2 + \frac{1}{3} m a^2 \left(t_3 - t_2\right)^3 + \cdots \\
& \cdots + m a \left(t_2 - t_1\right)^2 \left(t_3 - t_2\right) + \cdots \\
& \cdots + \frac{1}{2} m a \left(t_3 - t_2\right)^2 \left(t_2 - t_1\right) - m a z_0
\end{aligned} \tag{A.38}
$$

We then get

$$
\begin{aligned}
& S_{cl}\left(t_2 - t_1\right) = \cdots \\
& \cdots = \left[\frac{1}{2} m v_0^2 (t_2 - t_1) - m v_0 a (t_2 - t_1)^2 + \frac{1}{3} m a^2 (t_2 - t_1)^3 - m a z_0 (t_2 - t_1)\right] - \cdots \\
\cdots - & \left[\frac{1}{2} m v_0^2 (t_2 - t_1) + m v_0 a (t_2 - t_1)^2 + \frac{1}{3} m a^2 (t_2 - t_1)^3 - m a z_0 (t_2 - t_1)\right] \\
& = -2 m v_0 a (t_2 - t_1)^2
\end{aligned} \tag{A.39}
$$

and

$$\begin{aligned}
&S_{cl}\left(t_3-t_2\right)=\cdots\\
&\cdots\Big[\frac{1}{2}mv_0^2\left(t_3-t_2\right)+mv_0a\left(t_3-t_2\right)^2+\frac{1}{3}ma^2\left(t_3-t_2\right)^3+\cdots\\
&\cdots+ma\left(t_2-t_1\right)^2\left(t_3-t_2\right)+\cdots\\
&\quad\cdots+\frac{1}{2}ma\left(t_3-t_2\right)^2\left(t_2-t_1\right)-maz_0\Big]-\cdots\\
\cdots-&\Big[\frac{1}{2}mv_0^2\left(t_3-t_2\right)-mv_0a\left(t_3-t_2\right)^2+\frac{1}{3}ma^2\left(t_3-t_2\right)^3+\cdots\\
&\cdots+ma\left(t_2-t_1\right)^2\left(t_3-t_2\right)+\cdots\\
&\quad\cdots+\frac{1}{2}ma\left(t_3-t_2\right)^2\left(t_2-t_1\right)-maz_0\Big]\\
&=\ +2mv_0a(t_3-t_2)^2
\end{aligned}\tag{A.40}$$

Our phase along the interferometer is then

$$\begin{aligned}
\Delta\Phi&=S_{cl}\left(t_2-t_1\right)+S_{cl}\left(t_3-t_2\right)\\
&=\left(-2mv_0a(t_2-t_1)^2+2mv_0a(t_3-t_2)^2\right)\\
&=0,\quad(\text{if }\left(t_3-t_2\right)=\left(t_2-t_1\right))
\end{aligned}\tag{A.41}$$

Bibliography

[1] P. Hariharan, *Optical interferometry*, Reports on Progress in Physics **54**, 339 (1991).

[2] H. Benson, *University Physics* (Wiley, 1996).

[3] A. A. Michelson and E. W. Morley, *On the relative motion of the Earth and the luminiferous ether*, American Journal of Science **34**, 333 (1887).

[4] A. Einstein, *Zur Elektrodynamik bewegter Körper [AdP 17, 891 (1905)]*, Annalen der Physik **14**, 194 (1905).

[5] K. U. Schreiber and J.-P. R. Wells, *Invited Review Article: Large ring lasers for rotation sensing*, Review of Scientific Instruments **84**, 041101 (2013), http://dx.doi.org/10.1063/1.4798216.

[6] G. E. Stedman, *Ring-laser tests of fundamental physics and geophysics*, Reports on Progress in Physics **60**, 615 (1997).

[7] A. Gauguet, *Foreword*, Comptes Rendus Physique **15**, 787 (2014), The Sagnac effect: 100 years later / L'effet Sagnac : 100 ans après.

[8] B. Abbott *et al.*, *Detector description and performance for the first coincidence observations between {LIGO} and {GEO}*, Nuclear Instruments and Methods in Physics Research Section A: Accelerators, Spectrometers, Detectors and Associated Equipment **517**, 154 (2004).

[9] LIGO Scientific Collaboration and Virgo Collaboration, B. P. Abbott *et al.*, *Observation of Gravitational Waves from a Binary Black Hole Merger*, Phys. Rev. Lett. **116**, 061102 (2016).

[10] A. Einstein, *Die Grundlage der allgemeinen Relativitätstheorie [AdP 49, 769 (1916)]*, Annalen der Physik **14**, 517 (1916).

[11] L. de Broglie, *Waves and quanta*, Nature **112**, 2815 (1923).

[12] M. E. Zawadzki, P. F. Griffin, E. Riis, and A. S. Arnold, *Spatial interference from well-separated split condensates*, Phys. Rev. A **81**, 043608 (2010).

[13] C. Carson, *High contrast interferometry and finite temperature coherence of Bose-Einstein condensates*, PhD thesis, University of Strathclyde, 2015.

[14] O. Carnal and J. Mlynek, *Young's double-slit experiment with atoms: A simple atom interferometer*, Phys. Rev. Lett. **66**, 2689 (1991).

[15] A. D. Cronin, J. Schmiedmayer, and D. E. Pritchard, *Optics and interferometry with atoms and molecules*, Rev. Mod. Phys. **81**, 1051 (2009).

[16] C. Davisson and L. H. Germer, *Diffraction of Electrons by a Crystal of Nickel*, Phys. Rev. **30**, 705 (1927).

[17] I. Estermann and A. Stern, *Beugung von molekularstrahlen (bending of molecular rays)*, Z. Phys. 61, 95. (1930).

[18] L. Marton, *Electron Interferometer*, Phys. Rev. **85**, 1057 (1952).

[19] L. Marton, J. A. Simpson, and J. A. Suddeth, *Electron Beam Interferometer*, Phys. Rev. **90**, 490 (1953).

[20] L. Marton, J. A. Simpson, and J. A. Suddeth, *An Electron Interferometer*, Review of Scientific Instruments **25**, 1099 (1954), http://dx.doi.org/10.1063/1.1770945.

[21] H. Rauch, W. Treimer, and U. Bonse, *Test of a single crystal neutron interferometer*, Physics Letters A **47**, 369 (1974).

[22] R. Colella, A. W. Overhauser, and S. A. Werner, *Observation of Gravitationally Induced Quantum Interference*, Phys. Rev. Lett. **34**, 1472 (1975).

[23] J. A. Leavitt and F. A. Bills, *Single-Slit Diffraction Pattern of a Thermal Atomic Potassium Beam*, American Journal of Physics **37**, 905 (1969), http://dx.doi.org/10.1119/1.1975924.

[24] D. W. Keith, M. L. Schattenburg, H. I. Smith, and D. E. Pritchard, *Diffraction of Atoms by a Transmission Grating*, Phys. Rev. Lett. **61**, 1580 (1988).

[25] D. W. Keith, C. R. Ekstrom, Q. A. Turchette, and D. E. Pritchard, *An interferometer for atoms*, Phys. Rev. Lett. **66**, 2693 (1991).

[26] C. Brand *et al.*, *An atomically thin matter-wave beamsplitter*, Nature Nanotechnology **10**, 845 EP (2015).

[27] P. L. Kapitza and P. A. M. Dirac, *The reflection of electrons from standing light waves*, Mathematical Proceedings of the Cambridge Philosophical Society **29**, 297 (1933).

[28] D. L. Freimund, K. Aflatooni, and H. Batelaan, *Observation of the Kapitza-Dirac effect*, Nature **413**, 142 (2001).

[29] E. M. Rasel, M. K. Oberthaler, H. Batelaan, J. Schmiedmayer, and A. Zeilinger, *Atom Wave Interferometry with Diffraction Gratings of Light*, Phys. Rev. Lett. **75**, 2633 (1995).

[30] D. M. Giltner, R. W. McGowan, and S. A. Lee, *Atom Interferometer Based on Bragg Scattering from Standing Light Waves*, Phys. Rev. Lett. **75**, 2638 (1995).

[31] D. S. Durfee, Y. K. Shaham, and M. A. Kasevich, *Long-Term Stability of an Area-Reversible Atom-Interferometer Sagnac Gyroscope*, Phys. Rev. Lett. **97**, 240801 (2006).

[32] T. L. Gustavson, A. Landragin, and M. A. Kasevich, *Rotation sensing with a dual atom-interferometer Sagnac gyroscope*, Classical and Quantum Gravity **17**, 2385 (2000).

[33] T. L. Gustavson, P. Bouyer, and M. A. Kasevich, *Precision rotation measurements with an atom interferometer gyroscope*, Phys. Rev. Lett. **78**, 2046 (1997).

[34] A. Lenef *et al.*, *Rotation Sensing with an Atom Interferometer*, Phys. Rev. Lett. **78**, 760 (1997).

[35] F. Riehle, T. Kisters, A. Witte, J. Helmcke, and C. J. Bordé, *Optical Ramsey spectroscopy in a rotating frame: Sagnac effect in a matter-wave interferometer*, Phys. Rev. Lett. **67**, 177 (1991).

[36] B. Deissler, K. J. Hughes, J. H. T. Burke, and C. A. Sackett, *Measurement of the ac Stark shift with a guided matter-wave interferometer*, Phys. Rev. A **77**, 031604 (2008).

[37] M. de Angelis *et al.*, *Precision gravimetry with atomic sensors*, Measurement Science and Technology **20**, 022001 (2009).

[38] Y.-J. Wang *et al.*, *Atom Michelson Interferometer on a Chip Using a Bose-Einstein Condensate*, Phys. Rev. Lett. **94**, 090405 (2005).

[39] M. J. Snadden, J. M. McGuirk, P. Bouyer, K. G. Haritos, and M. A. Kasevich, *Measurement of the Earth's Gravity Gradient with an Atom Interferometer-Based Gravity Gradiometer*, Phys. Rev. Lett. **81**, 971 (1998).

[40] A. V. Rakholia, H. J. McGuinness, and G. W. Biedermann, *Dual-Axis High-Data-Rate Atom Interferometer via Cold Ensemble Exchange*, Phys. Rev. Applied **2**, 054012 (2014).

[41] G. Rosi *et al.*, *Measurement of the Gravity-Field Curvature by Atom Interferometry*, Phys. Rev. Lett. **114**, 013001 (2015).

[42] R. Geiger *et al.*, *Detecting inertial effects with airborne matter-wave interferometry*, Nature Communications **2** (2011).

[43] M. Kasevich and S. Chu, *Atomic interferometry using stimulated Raman transitions*, Phys. Rev. Lett. **67**, 181 (1991).

[44] S. M. Dickerson, J. M. Hogan, A. Sugarbaker, D. M. S. Johnson, and M. A. Kasevich, *Multiaxis Inertial Sensing with Long-Time Point Source Atom Interferometry*, Phys. Rev. Lett. **111**, 083001 (2013).

[45] B. Canuel *et al.*, *Six-Axis Inertial Sensor Using Cold-Atom Interferometry*, Phys. Rev. Lett. **97**, 010402 (2006).

[46] A. Arvanitaki, S. Dimopoulos, A. A. Geraci, J. Hogan, and M. Kasevich, *How to Test Atom and Neutron Neutrality with Atom Interferometry*, Phys. Rev. Lett. **100**, 120407 (2008).

[47] M. Prevedelli, L. Cacciapuoti, G. Rosi, F. Sorrentino, and G. M. Tino, *Measuring the Newtonian constant of gravitation G with an atomic interferometer*, Philosophical Transactions of the Royal Society of London A: Mathematical, Physical and Engineering Sciences **372** (2014).

[48] T. Schuldt *et al.*, *Design of a dual species atom interferometer for space*, Experimental Astronomy **39**, 167 (2015).

[49] S. Gupta, K. Dieckmann, Z. Hadzibabic, and D. E. Pritchard, *Contrast Interferometry using Bose-Einstein Condensates to Measure h/m and α*, Phys. Rev. Lett. **89**, 140401 (2002).

[50] P. Cladé *et al.*, *Determination of the Fine Structure Constant Based on Bloch Oscillations of Ultracold Atoms in a Vertical Optical Lattice*, Phys. Rev. Lett. **96**, 033001 (2006).

[51] M. Cadoret *et al.*, *Combination of Bloch Oscillations with a Ramsey-Bordé Interferometer: New Determination of the Fine Structure Constant*, Phys. Rev. Lett. **101**, 230801 (2008).

[52] R. Bouchendira, P. Cladé, S. Guellati-Khélifa, F. Nez, and F. Biraben, *New Determination of the Fine Structure Constant and Test of the Quantum Electrodynamics*, Phys. Rev. Lett. **106**, 080801 (2011).

[53] R. Bouchendira, P. Cladé, S. Guellati-Khélifa, F. Nez, and F. Biraben, *State of the art in the determination of the fine structure constant: test of Quantum Electrodynamics and determination of h/mu*, Annalen der Physik **525**, 484 (2013), 1309.3393.

[54] A. O. Jamison, B. Plotkin-Swing, and S. Gupta, *Advances in precision contrast interferometry with Yb Bose-Einstein condensates*, Phys. Rev. A **90**, 063606 (2014).

[55] A. Sommerfeld, *Zur Quantentheorie der Spektrallinien.*, Annalen der Physik **356**, 1 (1916).

[56] P. A. M. Dirac, *The Quantum Theory of the Electron*, Proceedings of the Royal Society of London A: Mathematical, Physical and Engineering Sciences **117**, 610 (1928), http://rspa.royalsocietypublishing.org/content/117/778/610.full.pdf.

[57] W. E. Lamb and R. C. Retherford, *Fine Structure of the Hydrogen Atom by a Microwave Method*, Phys. Rev. **72**, 241 (1947).

[58] W. E. Lamb and R. C. Retherford, *Fine Structure of the Hydrogen Atom. Part I*, Phys. Rev. **79**, 549 (1950).

[59] H. A. Bethe, *The Electromagnetic Shift of Energy Levels*, Phys. Rev. **72**, 339 (1947).

[60] J. Schwinger, *On Quantum-Electrodynamics and the Magnetic Moment of the Electron*, Phys. Rev. **73**, 416 (1948).

[61] P. J. Mohr and B. N. Taylor, *CODATA recommended values of the fundamental physical constants: 1998*, Rev. Mod. Phys. **72**, 351 (2000).

[62] T. Kinoshita, *The fine structure constant*, Reports on Progress in Physics **59**, 1459 (1996).

[63] I. M. Mills, P. J. Mohr, T. J. Quinn, B. N. Taylor, and E. R. Williams, *Adapting the International System of Units to the twenty-first century*, Philosophical Transactions of the Royal Society of London A: Mathematical, Physical and Engineering Sciences **369**, 3907 (2011), http://rsta.royalsocietypublishing.org/content/369/1953/3907.full.pdf.

[64] D. Hanneke, S. Fogwell, and G. Gabrielse, *New Measurement of the Electron Magnetic Moment and the Fine Structure Constant*, Phys. Rev. Lett. **100**, 120801 (2008).

[65] T. Aoyama, M. Hayakawa, T. Kinoshita, and M. Nio, *Tenth-Order QED Contribution to the Electron $g-2$ and an Improved Value of the Fine Structure Constant*, Phys. Rev. Lett. **109**, 111807 (2012).

[66] J.-P. Uzan, *Varying Constants, Gravitation and Cosmology*, Living Reviews in Relativity **14** (2011).

[67] V. V. Flambaum, D. B. Leinweber, A. W. Thomas, and R. D. Young, *Limits on variations of the quark masses, QCD scale, and fine structure constant*, Phys. Rev. D **69**, 115006 (2004).

[68] P. Jansen, H. L. Bethlem, and W. Ubachs, *Perspective: Tipping the scales: Search for drifting constants from molecular spectra*, The Journal of Chemical Physics **140** (2014).

[69] M. Born, *The Mysterious Number 137*, Proc. Indian Acad. Sci., Sect. A **2**, 533 (1956).

[70] C. J. Hogan, *Why the universe is just so*, Rev. Mod. Phys. **72**, 1149 (2000).

[71] P. J. Mohr, D. B. Newell, and B. N. Taylor, *CODATA recommended values of the fundamental physical constants: 2014*, Rev. Mod. Phys. **88**, 035009 (2016).

[72] B. P. Kibble, I. A. Robinson, and J. H. Belliss, *A Realization of the SI Watt by the NPL Moving-coil Balance*, Metrologia **27**, 173 (1990).

[73] R. L. Steiner, E. R. Williams, R. Liu, and D. B. Newell, *Uncertainty Improvements of the NIST Electronic Kilogram*, IEEE Transactions on Instrumentation and Measurement **56**, 592 (2007).

[74] E. R. Williams, R. L. Steiner, D. B. Newell, and P. T. Olsen, *Accurate Measurement of the Planck Constant*, Phys. Rev. Lett. **81**, 2404 (1998).

[75] I. M. Mills, P. J. Mohr, T. J. Quinn, B. N. Taylor, and E. R. Williams, *Redefinition of the kilogram, ampere, kelvin and mole: a proposed approach to implementing CIPM recommendation 1 (CI-2005)*, Metrologia **43**, 227 (2006).

[76] C. J. Bordé, *Base units of the SI, fundamental constants and modern quantum physics*, Philosophical Transactions of the Royal Society of London A: Mathematical, Physical and Engineering Sciences **363**, 2177 (2005), http://rsta.royalsocietypublishing.org/content/363/1834/2177.full.pdf.

[77] I. C. for Science (ICSU), *Committee on Data of the International Council for Science*, 2017,
`http://www.codata.org/`.

[78] I. A. Robinson, *Towards the redefinition of the kilogram: a measurement of the Planck constant using the NPL Mark II watt balance*, Metrologia **49**, 113 (2012).

[79] G. Trapon, O. Thévenot, J. C. Lacueille, and W. Poirier, *Determination of the von Klitzing constant R K in terms of the BNM calculable capacitor-fifteen years of investigations*, Metrologia **40**, 159 (2003).

[80] G. Trapon *et al.*, *Progress in linking the Farad and the RK value to the SI units at BNM-LCIE*, IEEE Transactions on Instrumentation and Measurement **50**, 572 (2001).

[81] G. W. Small, B. W. Ricketts, P. C. Coogan, B. J. Pritchard, and M. M. R. Sovierzoski, *A new determination of the quantized Hall resistance in terms of the NML calculable cross capacitor*, Metrologia **34**, 241 (1997).

[82] A. M. Jeffery, R. E. Elmquist, L. H. Lee, J. Q. Shields, and R. F. Dziuba, *NIST comparison of the quantized Hall resistance and the realization of the SI OHM through the calculable capacitor*, IEEE Transactions on Instrumentation and Measurement **46**, 264 (1997).

[83] A. Jeffery *et al.*, *Determination of the von Klitzing constant and the fine-structure constant through a comparison of the quantized Hall resistance and the ohm derived from the NIST calculable capacitor*, Metrologia **35**, 83 (1998).

[84] V. Y. Shifrin, P. G. Park, V. N. Khorev, C. H. Choi, and C. S. Kim, *A new low-field determination of the proton gyromagnetic ratio in water*, IEEE Transactions on Instrumentation and Measurement **47**, 638 (1998).

[85] V. Y. Shifrin, P. G. Park, V. N. Khorev, C. H. Choi, and S. Lee, *Determination of the tesla-to-ampere ratio for the KRISS/VNIIM gamma;'P-experiment*, IEEE Transactions on Instrumentation and Measurement **48**, 196 (1999).

[86] E. R. Williams *et al.*, *A low field determination of the proton gyromagnetic ratio in water*, IEEE Transactions on Instrumentation and Measurement **38**, 233 (1989).

[87] F. G. Mariam *et al.*, *Higher Precision Measurement of the hfs Interval of Muonium and of the Muon Magnetic Moment*, Phys. Rev. Lett. **49**, 993 (1982).

[88] W. Liu *et al.*, *High Precision Measurements of the Ground State Hyperfine Structure Interval of Muonium and of the Muon Magnetic Moment*, Phys. Rev. Lett. **82**, 711 (1999).

[89] A. Wicht, J. M. Hensley, E. Sarajlic, and S. Chu, *A Preliminary Measurement of the Fine Structure Constant Based on Atom Interferometry*, Physica Scripta **2002**, 82 (2002).

[90] R. S. V. Dyck, D. B. Pinegar, S. V. Liew, and S. L. Zafonte, *The UW-PTMS: Systematic studies, measurement progress, and future improvements*, International Journal of Mass Spectrometry **251**, 231 (2006), ULTRA-ACCURATE MASS SPECTROMETRY AND RELATED TOPICS Dedicated to H.-J. Kluge on the occasion of his 65th birthday anniversary.

[91] G. Gabrielse, D. Hanneke, T. Kinoshita, M. Nio, and B. Odom, *New Determination of the Fine Structure Constant from the Electron g Value and QED*, Phys. Rev. Lett. **97**, 030802 (2006).

[92] P. J. Mohr, B. N. Taylor, and D. B. Newell, *CODATA recommended values of the fundamental physical constants: 2006*, Rev. Mod. Phys. **80**, 633 (2008).

[93] T. Udem *et al.*, *Phase-Coherent Measurement of the Hydrogen $1S - 2S$ Transition Frequency with an Optical Frequency Interval Divider Chain*, Phys. Rev. Lett. **79**, 2646 (1997).

[94] M. P. Bradley, J. V. Porto, S. Rainville, J. K. Thompson, and D. E. Pritchard, *Penning Trap Measurements of the Masses of ^{133}Cs, $^{87,85}Rb$, and ^{23}Na with Uncertainties ≤ 0.2 ppb*, Phys. Rev. Lett. **83**, 4510 (1999).

[95] B. J. Mount, M. Redshaw, and E. G. Myers, *Atomic masses of* $^{6}\mathrm{Li},^{23}\mathrm{Na},^{39,41}\mathrm{K},^{85,87}\mathrm{Rb}$, *and* $^{133}\mathrm{Cs}$, Phys. Rev. A **82**, 042513 (2010).

[96] B. Estey, C. Yu, H. Müller, P.-C. Kuan, and S.-Y. Lan, *High-Resolution Atom Interferometers with Suppressed Diffraction Phases*, Phys. Rev. Lett. **115**, 083002 (2015).

[97] P. J. Mohr, B. N. Taylor, and D. B. Newell, *CODATA recommended values of the fundamental physical constants: 2010*, Rev. Mod. Phys. **84**, 1527 (2012).

[98] A. Dinkelaker, *Smooth Inductively Coupled Ring Trap for Cold Atom Optics*, PhD thesis, University of Strathclyde, 2013.

[99] B. I. Robertson, *Measurement of the Fine-Structure Constant using Matter-Wave Interferometry*, PhD thesis, University of Strathclyde, 2016.

[100] M. H. Anderson, J. R. Ensher, M. R. Matthews, C. E. Wieman, and E. A. Cornell, *Observation of Bose-Einstein Condensation in a Dilute Atomic Vapor*, Science **269**, 198 (1995).

[101] K. B. Davis *et al.*, *Bose-Einstein Condensation in a Gas of Sodium Atoms*, Phys. Rev. Lett. **75**, 3969 (1995).

[102] C. C. Bradley, C. A. Sackett, and R. G. Hulet, *Bose-Einstein Condensation of Lithium: Observation of Limited Condensate Number*, Phys. Rev. Lett. **78**, 985 (1997).

[103] H. J. Metcalf and P. v. d. Straten, *Laser Cooling and Trapping* (Springer, 1999).

[104] D. A. Steck, *Rubidium 87 D Line Data*, URL http://steck.us/alkalidata/rubidium87numbers.pdf.

[105] C. Foot, *Atomic Physics,* Oxford master series in physics (Oxford University Press, 2005).

[106] E. L. Raab, M. Prentiss, A. Cable, S. Chu, and D. E. Pritchard, *Trapping of Neutral Sodium Atoms with Radiation Pressure*, Phys. Rev. Lett. **59**, 2631 (1987).

[107] Y.-J. Lin, A. R. Perry, R. L. Compton, I. B. Spielman, and J. V. Porto, *Rapid production of* ^{87}*Rb Bose-Einstein condensates in a combined magnetic and optical potential*, Phys. Rev. A **79**, 063631 (2009).

[108] J. Lodewyck, *Gaussian optics simulator*, 2013, `http://gaussianbeam.sourceforge.net`.

[109] W. Ketterle, D. S. Durfee, and D. M. Stamper-Kurn, *Making, probing and understanding Bose-Einstein condensates*, eprint arXiv:cond-mat/9904034 (1999), cond-mat/9904034.

[110] A. O. Jamison, B. Plotkin-Swing, and S. Gupta, *Controlling Interactions in a Yb Bose-Einstein Condensate Interferometer*, ArXiv e-prints (2014), 1404.6028.

[111] S. Gupta, A. Leanhardt, A. Cronin, and D. Pritchard, *Coherent manipulation of atoms with standing light waves*, Comptes Rendus de l'Academie des Sciences - Series IV: Physics, Astrophysics **2**, 479 (2001).

[112] P. Cladé, S. Guellati-Khélifa, F. m. c. Nez, and F. m. c. Biraben, *Large Momentum Beam Splitter Using Bloch Oscillations*, Phys. Rev. Lett. **102**, 240402 (2009).

[113] V. Giovannetti, S. Lloyd, and L. Maccone, *Quantum-Enhanced Measurements: Beating the Standard Quantum Limit*, Science **306**, 1330 (2004), http://science.sciencemag.org/content/306/5700/1330.full.pdf.

[114] D. B. Hume *et al.*, *Accurate Atom Counting in Mesoscopic Ensembles*, Phys. Rev. Lett. **111**, 253001 (2013).

[115] T. L. Gustavson, *Precision Rotation Sensing using Atom Interferometry*, PhD thesis, Stanford University, 2000.

[116] P. Berg *et al.*, *Composite-Light-pulse Technique for High-Precision Atom Interferometry*, Phys. Rev. Lett. **114**, 063002 (2015).

[117] A. F. Bernhardt and B. W. Shore, *Coherent atomic deflection by resonant standing waves*, Phys. Rev. A **23**, 1290 (1981).

[118] P. J. Martin, B. G. Oldaker, A. H. Miklich, and D. E. Pritchard, *Bragg scattering of atoms from a standing light wave*, Phys. Rev. Lett. **60**, 515 (1988).

[119] B. Gadway, D. Pertot, R. Reimann, M. G. Cohen, and D. Schneble, *Analysis of Kapitza-Dirac diffraction patterns beyond the Raman-Nath regime*, Opt. Express **17**, 19173 (2009).

[120] Y.-J. Wang *et al.*, *Atom Michelson Interferometer on a Chip Using a Bose-Einstein Condensate*, Phys. Rev. Lett. **94**, 090405 (2005).

[121] S. Wu, Y.-J. Wang, Q. Diot, and M. Prentiss, *Splitting matter waves using an optimized standing-wave light-pulse sequence*, Phys. Rev. A **71**, 043602 (2005).

[122] O. Garcia, B. Deissler, K. J. Hughes, J. M. Reeves, and C. A. Sackett, *Bose-Einstein-condensate interferometer with macroscopic arm separation*, Phys. Rev. A **74**, 031601 (2006).

[123] K. J. Hughes, B. Deissler, J. H. T. Burke, and C. A. Sackett, *High-fidelity manipulation of a Bose-Einstein condensate using an optical standing wave*, Phys. Rev. A **76**, 035601 (2007).

[124] K. Mattle, M. Michler, H. Weinfurter, A. Zeilinger, and M. Zukowski, *Non-Classical Statistics at Multiport Beam Splitters*, Applied Physics B **60**, S111 (1995).

[125] N. Spagnolo *et al.*, *Three-photon bosonic coalescence in an integrated tritter*, Nat Commun **4**, 1606 (2013).

[126] K. J. Hughes, *Optical manipulation of atomic motion for a compact gravitational sensor with a Bose-Einstein condensate interferometer*, PhD thesis, University of Virginia, 2008.

[127] J. D. Pritchard, A. N. Dinkelaker, A. S. Arnold, P. F. Griffin, and E. Riis, *Demonstration of an inductively coupled ring trap for cold atoms*, New Journal of Physics **14**, 103047 (2012).

[128] D. L. Jenkin *et al.*, *Bose-Einstein condensation of 87Rb in a levitated crossed dipole trap*, The European Physical Journal D **65**, 11 (2011).

[129] F. Harris, *On the use of windows for harmonic analysis with the discrete Fourier transform*, Proceedings of the IEEE **66**, 51 (1978).

[130] S. Dimopoulos, P. W. Graham, J. M. Hogan, M. A. Kasevich, and S. Rajendran, *Gravitational wave detection with atom interferometry*, Physics Letters B **678**, 37 (2009).

[131] N. Ghosh and K. Bhattacharya, *Cube beam-splitter interferometer for phase shifting interferometry*, Journal of Optics **38**, 191 (2009).

[132] M. C. Kandes, R. Carretero-Gonzalez, and M. W. J. Bromley, *Phase-Shift Plateaus in the Sagnac Effect for Matter Waves*, (2013), 1306.1308.

[133] H. C. Lefèvre, *The fiber-optic gyroscope, a century after Sagnac's experiment: The ultimate rotation-sensing technology?*, Comptes Rendus Physique **15**, 851 (2014), The Sagnac effect: 100 years later / L'effet Sagnac : 100 ans après.

[134] B. Barrett *et al.*, *The Sagnac effect: 20 years of development in matter-wave interferometry*, Comptes Rendus Physique **15**, 875 (2014), The Sagnac effect: 100 years later / L'effet Sagnac : 100 ans après.

[135] M. D. Gregoire, I. Hromada, W. F. Holmgren, R. Trubko, and A. D. Cronin, *Measurements of the ground-state polarizabilities of Cs, Rb, and K using atom interferometry*, Phys. Rev. A **92**, 052513 (2015).

[136] J. Hogan, *Towards Precision tests of General Relativity using an Atom Interferometer*, PhD thesis, Stanford University, 2010.

[137] Y. L. Lim and A. Beige, *Multiphoton entanglement through a Bell-multiport beam splitter*, Phys. Rev. A **71**, 062311 (2005).

[138] F. A. Narducci and J. P. Davis, *Gradient Magnetometer Atom Interferometer (United States Patent US 8,289,018 B2)*, 2012.

[139] B. I. Robertson *et al.*, *Detection of Residual Inertial Forces with A Matterwave Magnetic-Gradiometer*, ArXiv e-prints (2017), 1707.07600.

[140] J. A. Stickney, D. Z. Anderson, and A. A. Zozulya, *Increasing the coherence time of Bose-Einstein-condensate interferometers with optical control of dynamics*, Phys. Rev. A **75**, 063603 (2007).

[141] Saers, R., Rehn, M., Scheler, T., Zelán, M., and Kastberg, A., *A set-up for flexible geometry optical lattices*, Eur. Phys. J. Appl. Phys. **42**, 269 (2008).

[142] D. V. Strekalov, A. Turlapov, A. Kumarakrishnan, and T. Sleator, *Periodic structures generated in a cloud of cold atoms*, Phys. Rev. A **66**, 023601 (2002).

[143] W. B. Case, M. Tomandl, S. Deachapunya, and M. Arndt, *Realization of optical carpets in the Talbot and Talbot-Lau configurations*, Opt. Express **17**, 20966 (2009).

[144] I. G. Hughes and T. P. A. Hase, *Measurements and their Uncertainties: A Practical Guide to Modern Error Analysis by Ifan G. Hughes, Thomas P. A. Hase*, International Statistical Review **79**, 280 (2011).

[145] R. Barlow, *Asymmetric Errors*, in *Proceedings of the Conference on Statistical Problems in Particle Physics, Astrophysics and Cosmology [PHYSTAT2003], (Stanford Linear Accelerator Center, Stanford, California, September 8th - 11th, 2003)*, US Department of Energy, 2003.

[146] M. R. Stoneking and D. J. Hartog, *Maximum-likelihood fitting of data dominated by Poisson statistical uncertainties*, Review of Scientific Instruments **68**, 914 (1997).

[147] C. J. Clopper and E. S. Pearson, *The Use of Confidence or Fiducial Limits Illustrated in the Case of the Binomial*, Biometrika **26**, 404 (1934).

[148] J. D'Errico, *Adaptive Robust Numerical Differentiation*, 2014, `http://uk.mathworks.com/matlabcentral/fileexchange/13490-adaptive-robust-numerical-differentiation/content/DERIVESTsuite/jacobianest.m`.

[149] M. Egorov *et al.*, *Measurement of s-wave scattering lengths in a two-component Bose-Einstein condensate*, Phys. Rev. A **87**, 053614 (2013).

[150] Y. Castin and R. Dum, *Bose-Einstein Condensates in Time Dependent Traps*, Phys. Rev. Lett. **77**, 5315 (1996).

[151] F. Dalfovo, S. Giorgini, L. P. Pitaevskii, and S. Stringari, *Theory of Bose-Einstein condensation in trapped gases*, Rev. Mod. Phys. **71**, 463 (1999).

[152] X. Antoine and R. Duboscq, *GPELab, a Matlab toolbox to solve Gross-Pitaevskii equations I: Computation of stationary solutions*, Computer Physics Communications **185**, 2969 (2014).

[153] X. Antoine and R. Duboscq, *GPELab, a Matlab toolbox to solve Gross-Pitaevskii equations II: Dynamics and stochastic simulations*, Computer Physics Communications **193**, 95 (2015).

[154] S. Schmidt, *Interactive Simulation Toolbox for Optics*, 2013, `http://uk.mathworks.com/matlabcentral/fileexchange/40093-interactive-simulation-toolbox-for-optics`.

[155] K. Yee, *Numerical solution of inital boundary value problems involving maxwell's equations in isotropic media*, IEEE Transactions on Antennas and Propagation **14**, 302 (1966).

[156] D. B. Hume *et al.*, *Accurate Atom Counting in Mesoscopic Ensembles*, Phys. Rev. Lett. **111**, 253001 (2013).

[157] S. A. Haine, *Mean-Field Dynamics and Fisher Information in Matter Wave Interferometry*, Phys. Rev. Lett. **116**, 230404 (2016).

[158] S. Haine, Personal communication, 2017.

[159] R. Uppu, T. A. W. Wolterink, T. B. H. Tentrup, and P. W. H. Pinkse, *Quantum optics of lossy asymmetric beam splitters*, Opt. Express **24**, 16440 (2016).